An evaluation of the use of thermal techniques for the non-destructive testing of sprayed coatings and other materials

Saintey, M. B.

Award date:
1995

Awarding institution:
University of Bath

An Evaluation Of The Use Of Thermal Techniques For The Non-Destructive Testing Of Sprayed Coatings And Other Materials

Submitted by M.B. Saintey
for the degree of PhD
of the University of Bath
June 1995

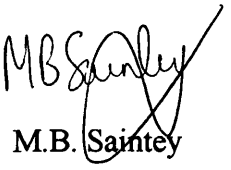

M.B. Saintey

ProQuest LLC
789 East Eisenhower Parkway
P.O. Box 1346
Ann Arbor, MI 48106-1346

Abstract

An investigation has been made into the use of thermal techniques for the non-destructive testing of sprayed coatings and other materials. In particular, tests have been conducted on High Velocity Oxy-Fuel (HVOF), arc, and plasma sprayed coatings. Both modulated and transient heating techniques have been considered, and some success has been shown with the use of these techniques for thermal property determination, coating thickness evaluation and defect detection. The suitability of a particular coating to the use of the thermal techniques has been shown to be highly dependent upon the internal structure of the coating. This is turn has been shown to be dependent upon the spraying technique and the coating material.

A numerical finite difference model to simulate transient experiments has been developed as part of the project, and results from the model compared with experimental data. The model has been found capable of accurately modelling experiment, and is therefore a useful tool in assessing the applicability of the transient technique. The model has been used to investigate the effect of defect characteristics such as depth, diameter and severity on the transient response following pulse excitation. The results have indicated that there is a complex dependence on these parameters, that combine to make accurate interpretation of transient thermography data in terms of the internal structure of a component difficult.

A method of using neural network processing for accurate defect characterisation from transient thermographic data has been developed, and good results have been achieved. The training and test data sets used in the development of the network were generated using the finite difference model.

Acknowledgements

I wish to thank TWI (The Welding Institute) for their sponsorship of this research, George Georgiou for his enthusiasm about the project, and Alan Lank for his work on the heat flow animation software. I would also like to thank Robin Cooke for his valuable advice throughout the project. I am most grateful to the technicians of the School Of Materials Science, in particular Simon Bowman for his assistance in building parts of the test apparatus, and Mark Deven for his considerable help with the metallography of my test samples.

I would especially like to thank Darryl Almond for his encouragement and guidance, and my wife Paulette for supporting my decision to undertake this research.

Finally, special thanks to my parents for all of their support and encouragement throughout the whole of my education.

Contents

List Of Symbols

Latin Symbols

Symbol	Definition	Units
A	Rate Of Internal Heat Generation	W/m^3
b	Effusivity Ratio	
c	Specific Heat Capacity	J/kgK
c	Speed Of Light In Vacuum	m/s
C_{max}	Maximum Thermal Contrast	
d	Thickness	m
d	Neural Network Training Required Output Vector	
f	Flux	W/m^2
h	Surface Heat Transfer Coefficient	W/m^2K
h	Planck's Constant	J s
I_0	Applied Heat Flux	W/m^2
j	Square Root Of Minus 1	
k	Thermal Conductivity	W/mK
k	Boltzmann's Constant	J/K
l_c	Coating Thickness	m
o	Neural Network Calculated Output Vector	
R	Reflection Coefficient	
R_c	Contact Resistance	m^2K/W
t	Time	s
T	Temperature	K
T	Transmission Coefficient	
V	Volume Of Cell Of Finite Difference Grid	m^3
W	Radiative Power	$Wcm^{-2}\mu m^{-1}$
w	Neural Network Weight Vector	
x	Neural Network Training Input Vector	

Greek Symbols

Symbol	Definition	Units
α	Thermal Diffusivity	m^2/s
α	Neural Network Learning Momentum Parameter	

Symbol	Definition	Units
Δ	Spacing Of Finite Difference Grid	m
ε	Thermal Effusivity	$J/m^2Ks^{½}$
ε	Spectral Emissivity	
Γ	Effective Reflection Coefficient	
η	Neural Network Learning Rate Parameter	
φ	Neural Network Activation Function	
λ	Wavelength Of Light	m
μ	Thermal Diffusion Length	m
μ_{eff}	Effective Thermal Diffusion Length	m
θ_i	Angle Of Incidence	radians
θ_r	Angle Of Reflection	radians
θ_t	Angle Of Refraction	radians
ρ	Density	kg/m^3
σ	Complex Thermal Wave Vector	m^{-1}
ω	Angular Modulation Frequency	radians/s

Chapter 1

Introduction

This thesis is concerned with the application of thermal techniques to the non-destructive testing (NDT) of sprayed coatings and other materials. In particular, the testing of high velocity oxy-fuel (HVOF) and arc sprayed coatings is considered. Before discussing specific techniques in detail, it is necessary to specify precisely what is meant by NDT.

1.1 What Is Non-Destructive Testing (NDT) ?

In conducting a test, be it destructive or non-destructive, an attempt is being made to determine if a component is suitable for the purpose for which it is to be used. The key aspect of the NDT of a component, is that the test must cause no damage to the component that would disqualify it from its intended use. NDT techniques range from the very simple, such as visual inspection, through to more advanced methods such as X-ray radiography and ultrasound inspection. NDT techniques have a distinct advantage over destructive testing methods, in that every component can be tested, thereby ensuring that each and every component complies to the necessary quality standard. Using destructive testing, it is only possible to test a small percentage, as the result of conducting the test is a spoiled component. Destructive testing is obviously less thorough, as there is no guarantee that *every* component would meet the required standard, even if the tested components comply. In addition to this, when testing components that are very expensive to manufacture, the cost of throwing away the destructively tested samples is high. It is for these reasons that non-destructive testing is of such importance.

1.2 Applicability Of Existing NDT Techniques To Sprayed Coatings

When testing the integrity of the coating on a component, there are several types of defect that can be present, e.g. clusters of large pores or blow holes, delaminations between the coating and substrate, and delaminations between layers within the coating. Such defects may have considerable impact on the strength and expected service life of the component, as might a region where the coating is not as thick as intended. An

ideal NDT technique for use with coated materials would therefore be able to detect defects such as delaminations, and accurately gauge coating thickness. Sprayed coatings of all types, D-Gun, HVOF, Arc and Plasma (see chapter 2) are all inherently porous, although the amount of porosity is dependent upon the spraying method and coating material. The presence of this porosity is of great importance when considering a suitable testing technique. Ultrasonic testing is perhaps the most widely adopted NDT technique, and attempts have been made to apply it to the testing of coatings [1-4]. The problem is that the small pores within the coating have a dramatic effect on the propagation of ultrasound [5,6], making accurate interpretation of the ultrasonic signals very difficult. Ultrasound is also more usually applied to problems of detecting defects deep within a material. The total thickness of a coating is often less than 250μm, meaning that any reflected signal from a defect within the coating occurs very rapidly after the input pulse, further complicating the problem.

X-ray radiography is also not suitable for the testing of coatings, as the total absorption of the rays on their path through a component is dominated by absorption within the substrate, due to the coating being so thin (generally < 250μm) relative to the substrate (generally several millimetres). Defects within the coating are therefore undetectable.

There are many other NDT techniques that have been developed over the years [7], but none has been found particularly successful for the testing of coatings, due to their inherent surface roughness and porosity. The increasing use of sprayed coatings for safety critical applications, such as for aircraft turbine blades, has lead to the increased need for a suitable NDT technique to be developed.

1.3 Requirements For An NDT Technique

Ideally an NDT technique should fulfil the following requirements :

1. It should be single-sided and non-contactive.

2. For use with sprayed coatings, it should be able to accurately evaluate coating thickness, and to detect defects such as delaminations.

3. It should be capable of use on components with complicated geometries.

4. It should be quick and reliable to apply.

Thermal techniques fulfil most, if not all, of the above requirements.

1.4 Thermal NDT

Broadly speaking, thermal testing can be split into two categories, depending upon how the sample is heated. The first category, known as photothermal techniques, heat the sample with a modulated heating flux, often a modulated laser beam, which gives rise to periodic temperature fluctuations that propagate within the solid as what are known as thermal waves (see chapter 3). The second applies a pulse or step excitation, which gives rise to a thermal transient within the sample. The basic idea behind the use of both categories is the same. The presence of a thermal discontinuity (change in thermal properties) within the sample, causes a perturbation in the pattern of heat flow through the sample. This gives rise to some form of modified temperature field on the surface of the sample that can be measured, and interpreted (inverted) to give the internal structure that caused the perturbation in flow. The thermal discontinuity could be an interface between a coating and substrate or a delamination defect. These two categories of techniques are discussed below.

1.4.1 Photothermal Techniques

Photothermal techniques have stemmed from the discovery of the photoacoustic effect by Alexander Graham Bell [8] in 1880. He found that if he shone a beam of modulated (chopped) sunlight onto the surface of a solid contained within a closed container, if he put his ear to the container he could hear a sound, the pitch of which was dependent upon the frequency at which the light was chopped. It was not until almost one hundred years later (1976) that a paper was published [9] giving a thorough theoretical explanation of the mechanism responsible for the sound production. The theory explained that the sound was caused by the periodic flow of heat from the surface of the solid into the thin layer of air close to the solid surface. This layer of air acted as a piston on the remainder of the gas in the cell, thereby causing periodic pressure variations (sound). The sound can be detected by placing a sensitive microphone in contact with the cell, and analysing the signal from the microphone.

In the late 1970s, and early 1980s, several groups were pioneering work on a technique known as photothermal radiometry (PTR). A modulated laser beam is used to heat a sample, and an infrared (IR) detector used to detect the emitted IR radiation. An early application of the technique was to analyse the absorption spectra of materials [10].

The more of the incident heating flux that the sample absorbed, the higher the periodic fluctuations in surface temperature, and hence the more IR radiation emitted. The technique was also used to measure the thickness of pieces of aluminium [11]. A transmission probing set-up was used for this, where the IR detector was placed on the opposite side of the sample to the heat source. It was also found to be possible to detect shallow defects within a material [12] with the heat source and detector placed on the same side of the sample (single-sided technique). As early as 1981 [13], a technique based on PTR had been developed for the measurement of the relative thickness of a plasma sprayed coating of tungsten carbide.

During the 1980s, interest in photothermal techniques for NDT flourished, with considerable interest shown specifically in their application to plasma sprayed coatings [14-20]. It was shown to be theoretically and experimentally possible to evaluate coating thickness, and detect delamination defects within plasma sprayed coatings. It was also shown to be possible to use the technique for the determination of the thermal properties of coatings [21]. Since the early 1990s however, interest appears to have focused more on transient thermal techniques, although specific applications such as NDT of hydoxyapatite coatings on prosthetic hip replacements, and the evaluation of paint adhesion are still being reported [22, 23]. The drop off in interest in the PTR techniques is mainly due to the very low speed of testing associated with the single point nature of this technique. A new technique known as lock-in thermography, that has many similarities with PTR, but allows for the testing of a large area in a single shot, has been developed over recent years, and is discussed in section 1.4.3.

1.4.2 Transient Techniques

There are several different geometries that have been developed for the generation (excitation) and detection of thermal transients. Single point techniques, where a single point is heated with a pulsed laser, and the subsequent thermal transient detected with a focused single point detector, have been applied to the testing of coated materials and composites [24-26]. These were shown to be able to detect variations in coating thickness and delaminations, but as with PTR, suffer from a very slow speed of testing.

Another technique [27,28] is to scan the heating laser along a line on the sample surface, whilst moving the sample perpendicular to the heating scan. The focus of a single point detector can be scanned along a line parallel to, but behind the heating scan, so that there is a fixed time gap between when a point was heated, and a temperature measurement taken. If the heat propagating into the sample has been perturbed by the presence of a subsurface feature by the time the measurement is taken,

this will appear as a perturbation in the surface temperature, and subsequently appear in the output signal of the detector. Using this technique it is possible to scan areas far more rapidly than using the single point technique. This technique has been developed to the stage where a hand held scanning unit has been produced for use in the field [29,30].

With the availability of cheaper infrared cameras has come great interest in their use for NDT. The most popular set-up used for transient testing was pioneered by Milne and Reynolds [31] in 1982, and is known as pulsed video thermography (PVT). This technique uses a flash tube to heat an area on the surface of a sample, and an IR camera to follow the resulting transient. This set-up has the considerable advantage of testing a large area in a single shot, but the cost of a thermal camera system, even though it has fallen dramatically over the past 10 years, is still very high compared to the equipment required for a PTR system. Other methods of injecting the heat into the system have been investigated, and included the use of hot air blowers (see chapters 5 and 6), induction heating [29,30], hot pads placed in contact with the sample [32], and microwave heating [33].

This technique has been found to be particularly useful for the detection of defects in composite materials [33-45]. These materials are being very widely used in the aircraft industry, where safety standards are very high, and therefore testing procedures must be strictly controlled. These materials have the advantage of being thermally slow (compared to metals) which makes them particularly suited to this form of testing, as the thermal transient is often persistent for many seconds, making defect location a simple task. The aircraft industry has been quick to realise the potential of PVT, with the technique also being successfully applied to the testing of aircraft skins for subsurface corrosion and disbonding [46,47].

Other reported applications have been the use of the technique for such tasks as the inspection of the protective coatings in a flue gas desulphurisation plant (part of a power generation plant) [48], the assessment of the waterproofing of bridges [49], and once again, the NDT of coatings [32,50-52].

Probably the greatest barrier that must be surmounted before the PVT technique can be more widely applied, is the difficulty of interpreting (inverting) the images recorded during the experiment, in terms of the subsurface structure that caused it. Many numerical models have been written to investigate this problem [53-59], and many attempts at devising analytical inversion procedures made [60-74]. Recently, the use of

neural networks for this task has been investigated [75-77], with some considerable success (see chapter 8).

1.4.3 Lock-In Thermography - A Hybrid Technique

Lock-In thermography [78-82] is a relatively new technique that is a hybrid of PTR. It can be thought of in simple terms as conducting a PTR experiment on an area rather than a single point. The surface of a sample is illuminated by a modulated source, such as a sinusoidally modulated halogen lamp, and a sequence of images recorded using a thermal camera. The frequency of the heating modulation must be tuned precisely to the frame rate of the thermal camera, so that a precise multiple of frames (usually greater than 4) is stored during each cycle of the heating modulation. In this way, the temperature-time evolution of a single point (which will be sinusoidal if the heating modulation is sinusoidal) can be compared with the time dependence of the heating modulation, to give the phase and magnitude of the temperature at the point with respect to the heating. This is a very interesting technique, but is perhaps limited in its application to such materials as sprayed coatings, in that only low frequencies (generally < 1 Hz) can be used, due to the limiting factor of the frame rate of the camera, and the need to collect multiple frames of data per modulation cycle. So far the technique has been applied to such tasks as the detection of moisture in wood veneers [82], and other laminate materials [80].

1.5 The Structure And Content Of The Remaining Chapters

The remainder of this thesis has been split into 8 chapters. Chapter 2 gives a description of the different thermal spraying techniques (D-Gun, HVOF, Plasma and Arc), and the uses to which sprayed materials are put. Chapter 3 deals with the analytical treatment of heat flow problems, deriving temperature expressions for the pulse, step and modulated excitation of a solid. Chapter 4 looks at the problem from the numerical prospective, explaining how finite difference techniques can be used. The finite difference model developed as part of the project is described, and images from a heat flow animation generated using the model presented. Chapter 5 describes the equipment and procedures used for the experimental investigations, and concludes with a description of each of the test samples. Chapter 6 presents the results of the experimental work and subsequent data analysis. Chapter 7 investigates the dependence of the depth, diameter, severity and surrounding material of a crack defect,

on the transient response following pulse excitation. Chapter 8 then looks at the problem of characterising defects from transient thermography data. A neural network approach is taken to the solution of this problem, and results of the analysis presented. Chapter 9 concludes the work, and gives a brief discussion of the results, and the conclusions that have been drawn from it.

Chapter 2

Thermal Spraying

Thermal spraying is the name given to a group of processes used to apply surface coatings by propelling molten particles at high velocities onto the surface of a component. On reaching the component, the particles which may be travelling at up to 800 m/s, splat, flatten out, and cool very rapidly, adhering to the component or previously deposited coating layers. To aid the adhesion to the component, before spraying the surface is prepared by degreasing and grit blasting. Typical coating thicknesses range from around 100 to several hundred microns. Common applications of such coatings include: the protection of bare metallic surfaces from corrosion and oxidation using coating materials such as aluminium and zinc, the protection of components from wear using tungsten carbide or other carbide coatings, the thermal insulation of components using materials such as zirconia, and the reclamation of worn parts. A specific example is the use of carbide coatings on aircraft turbine blades for wear resistance; another is the use of thermal barrier coatings on the components of high performance engines, to allow them to run at higher temperatures.

Several techniques have been developed around the simple idea behind thermal spraying, including plasma, arc, high velocity oxy-fuel (HVOF) and detonation gun (D-Gun) spraying. These techniques are briefly described below.

2.1 Arc Spraying

The arc spraying process consists of striking an arc between the tips of two conductive rods by the passing of a high DC current between the tips. The molten tips atomise, and are blown onto the component surface by a jet of compressed air or inert gas [83]. Figure 2.1 shows a schematic diagram of the arc spraying process. As the tips of the wires melt, fresh wire is continuously fed into the arc region by the wire feeders. A limitation of this technique is that only conductive wires can be used, however it is possible to mix non-conductive materials with the conductive wire by making cored wires containing the non-conductive material. Temperatures in excess of 4000°C can be achieved in the arc, which combined with the efficient transfer of this heat to the atomised particles, making it possible to work at high spraying rates. This makes the technique suitable for such applications as the corrosion protection (using zinc or

aluminium) of large structures such as ships or bridges. This technique is inexpensive in comparison with the other techniques, but produces coatings of a lower quality, being generally porous and having a high oxide content. The process is also extremely noisy (110 dB), and generates very high levels of ultraviolet and infrared radiation, requiring special safety precautions to be taken. Vacuum arc spraying can be used to produce coatings of lower porosity and oxide content, but involves the inconvenience of mounting the spraying gun and component within a vacuum chamber, making this variant of the technique only suitable for small components. Micrographs of arc sprayed aluminium/silicon alloy coatings are shown in figures 6.14a and 6.14b.

2.2 Detonation Gun (D-Gun) Spraying

Developed in the 1950s by Union Carbide, the D-Gun process has been primarily used for the application of carbide coatings, specifically to aircraft engine components. The process begins with the combustion chamber of the gun (figure 2.2) being filled with a mixture of oxygen and acetylene. Fine particles of the coating powder are injected into the chamber so that they are suspended in this gas when it is ignited by a spark plug. Temperatures in excess of 3000°C can be achieved, melting the suspended particles and projecting them very rapidly (Mach 3) out of the gun as the burning gas mixture expands. In contrast to the other techniques discussed, this technique is not continuous. Following a detonation, the chamber is refilled with the fuel gas and powder, and the process repeated at a rate of around 8 detonations per second. This technique produces the highest quality coatings. It should be noted that this coating method is only available as a service from Union Carbide.

2.3 Plasma Spraying

Plasma spraying [84] is a rather more complicated process than either arc or D-Gun spraying. The plasma spray gun (figure 2.3) consists of a cone shaped cathode, surrounded by an anode shaped to form the nozzle of the gun. The plasma gas, often a mixture of an inert gas with hydrogen, is fed into the region between the electrodes where it is ionised to form a plasma at temperatures up to 15000°C. To generate and maintain the plasma requires a large amount of energy, typically between 20000 and 80000 Kilowatts. The powdered coating material is fed into the plasma stream near the end of the nozzle, where the particles are accelerated to subsonic velocities, melted, and projected onto the component. Typical coating materials deposited using this technique

include carbides and oxides. The coatings are of a higher quality than arc sprayed and HVOF coatings, but have generally higher porosity and oxide content than D-Gun coatings. Coatings of comparable quality to D-Gun can be obtained using the vacuum plasma spraying technique, where the component and gun are mounted in a vacuum chamber. This has the advantage of a higher particle velocity (Mach 1), causing lower porosity and oxide content in the coatings, but is more expensive and time consuming.

2.4 High Velocity Oxy-Fuel (HVOF) Spraying

The HVOF [85] process was developed in 1982 by J.A. Browning of the Browning Engineering Company, Enfield, New Hampshire. It was initially developed to compete with the Union Carbide D-Gun process for the application of high quality carbide coatings, but has subsequently been used to apply a range of coating materials. A fuel gas, often propylene, acetylene, propane or hydrogen is mixed with oxygen in a mixing chamber before being piped into the combustion chamber where it mixes with the powder and carrier gas (usually an inert gas) (figure 2.4). The mixture is ignited to create a jet of supersonic gas (Mach 4) at temperatures around 3000°C which melts and propels the powder onto the component surface. Coatings deposited using this technique are characterised by their low porosity, low oxide content, and high bond strength. Micrographs of HVOF sprayed tungsten carbide coatings are shown in figures 6.3a, 6.3b, 6.8a and 6.8b.

The spraying techniques are ranked in terms of the quality of the coatings that they produce as follows :

Arc spraying	-	Poor Quality
HVOF spraying		
Plasma spraying	-	High Quality
Vacuum plasma spraying		
D-Gun	-	Very High Quality

Previous investigations into the use of thermal techniques for the NDT of sprayed coatings have concentrated on their use for high quality plasma sprayed coatings. One of the major objectives of this research was to investigate if the techniques were equally applicable to the lower quality arc and HVOF coatings.

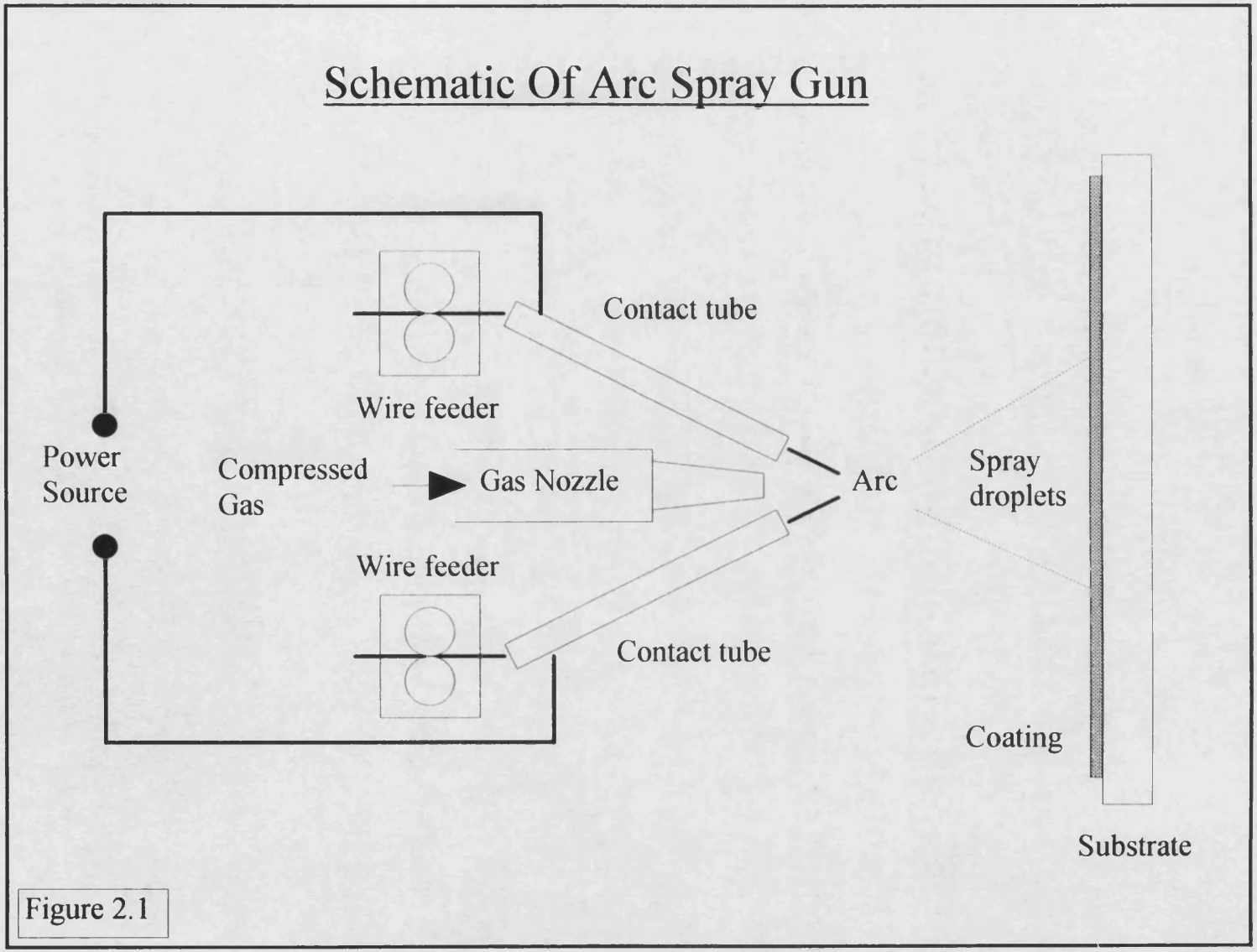
Schematic Of Arc Spray Gun
Contact tube
Wire feeder
Power Source
Compressed Gas
Gas Nozzle
Arc
Spray droplets
Wire feeder
Contact tube
Coating
Substrate

Figure 2.1

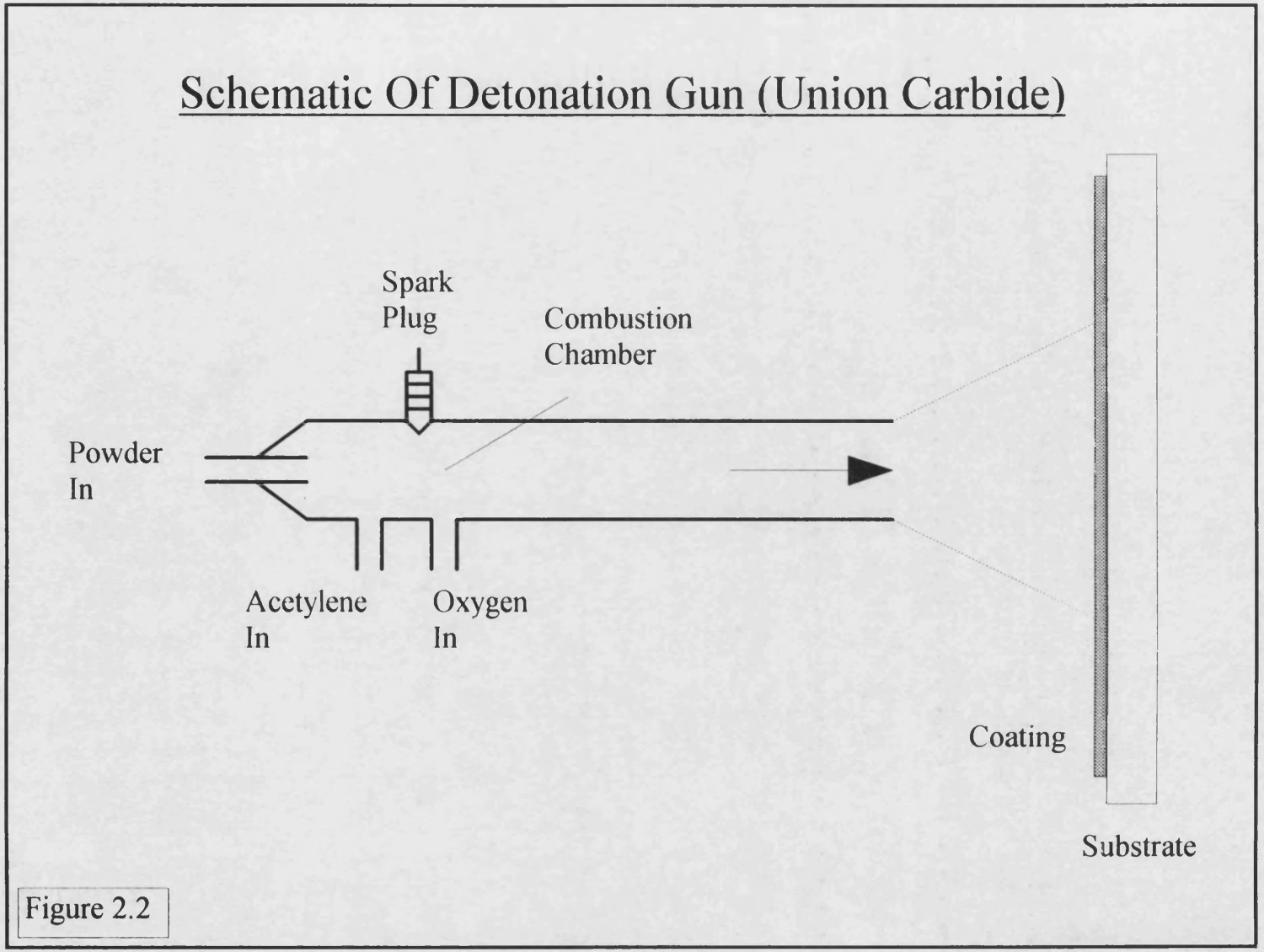
Schematic Of Detonation Gun (Union Carbide)
Spark
Plug
Combustion
Chamber
Powder
In
Acetylene
In
Oxygen
In
Coating
Substrate

Figure 2.2

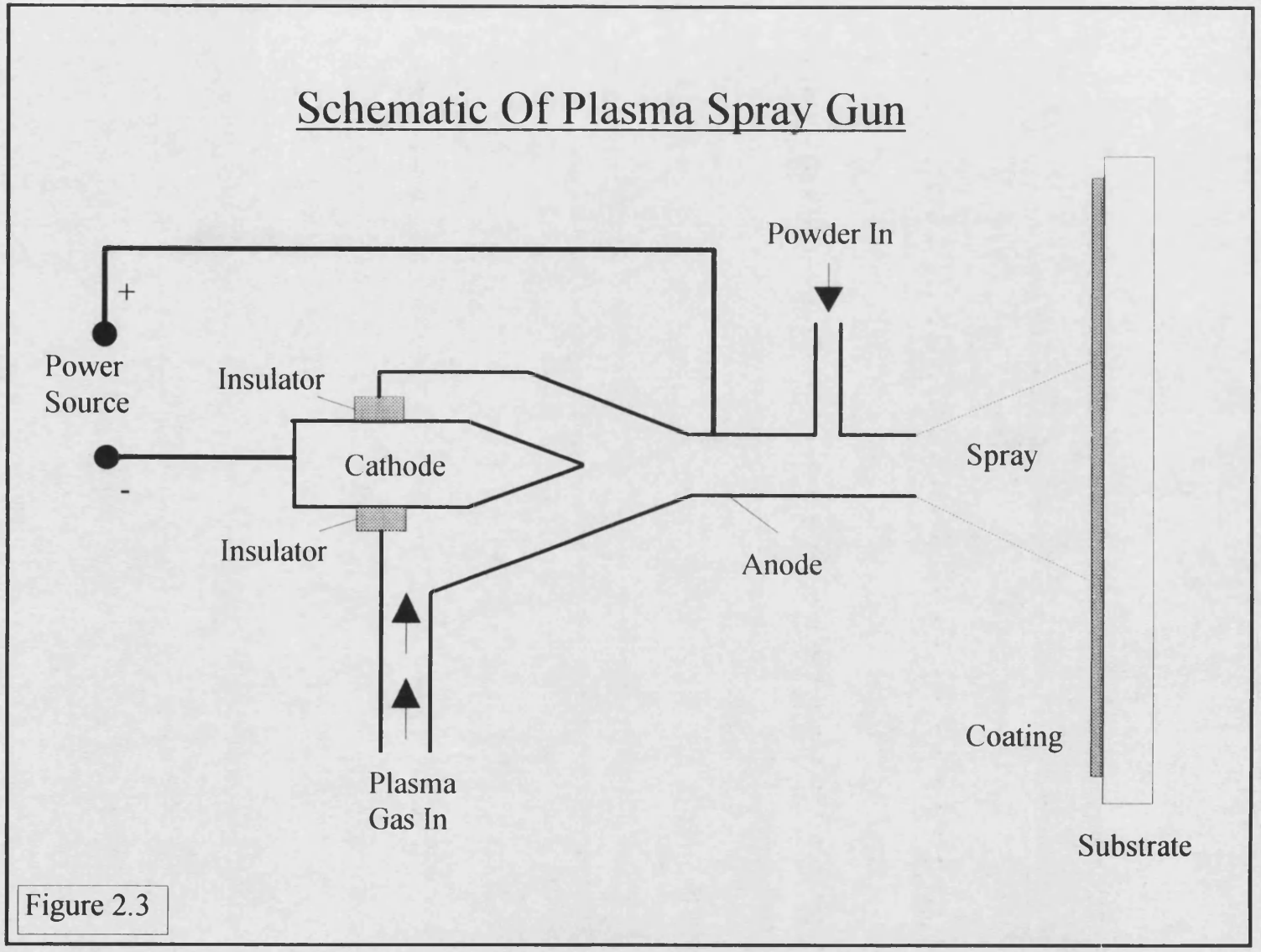
Schematic Of Plasma Spray Gun
Powder In
+
Power
Source
Insulator
Cathode
-
Spray
Insulator
Anode
Coating
Plasma
Gas In
Substrate

Figure 2.3

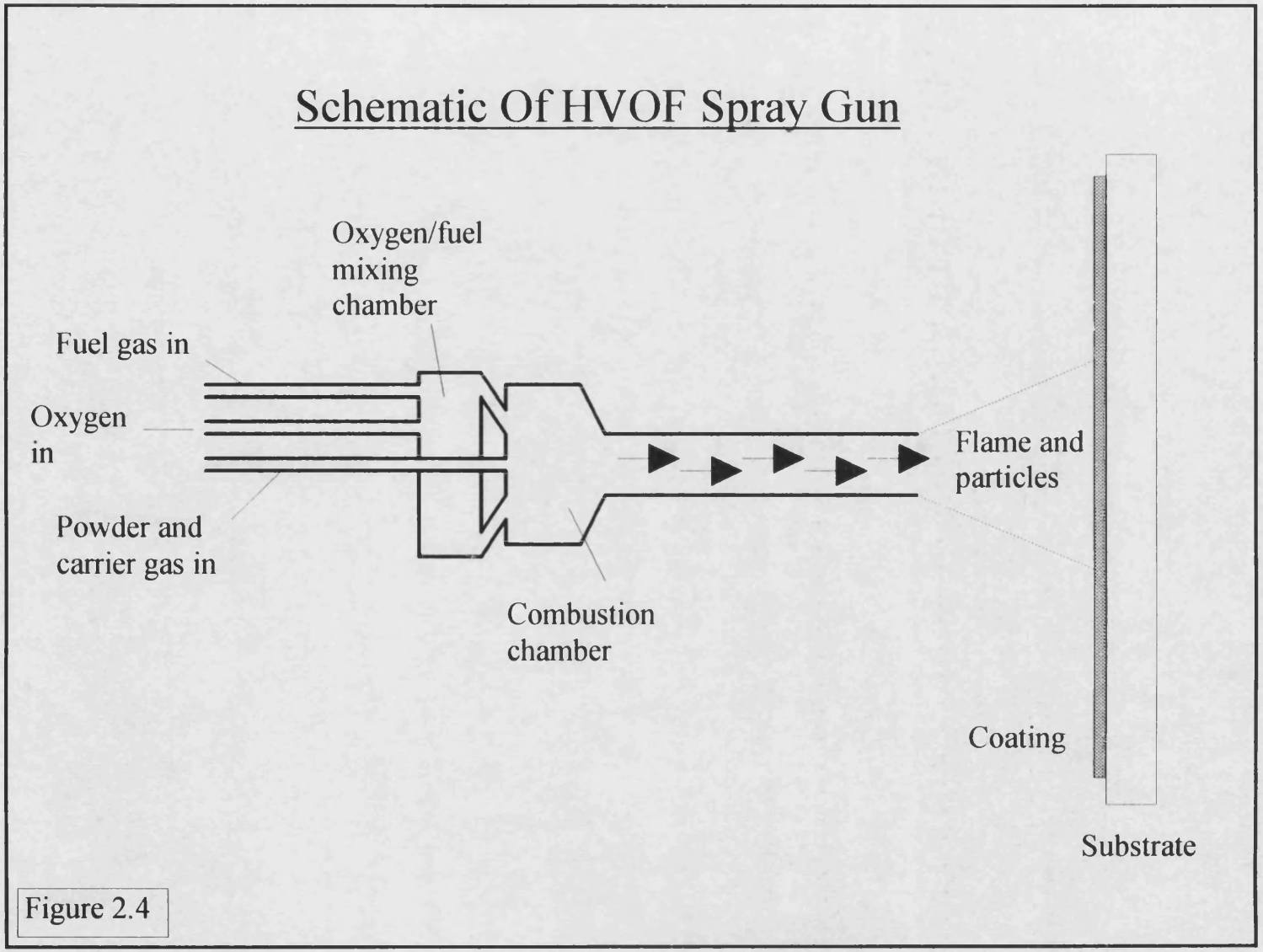
Schematic Of HVOF Spray Gun
Oxygen/fuel mixing chamber
Fuel gas in
Oxygen in
Powder and carrier gas in
Combustion chamber
Flame and particles
Coating
Substrate

Figure 2.4

Chapter 3

The Analytical Treatment Of The Diffusion Of Heat In Solids

There are three methods by which heat energy may be transferred: Conduction, Convection and Radiation. Conduction is the transfer of heat energy through the substance of the body itself. Convection is the transfer of heat energy by the relative motion of parts of the body. Radiation is the transfer of heat energy between parts of a body directly by electromagnetic radiation. In solids, conduction is the dominant method, with convection being wholly absent, and radiation being usually negligible. There are two mechanisms that comprise conduction in a solid: vibrations of the lattice structure, and motion of the free electrons through the lattice. Of these two mechanisms, motion of the free electrons is dominant. The higher thermal conductivity of metals over insulators is explained by this; metals containing free electrons, and insulators not.

3.1 The Theory Of Heat Conduction

The theory of the conduction of heat in solids is founded on the following experiment. Consider a flat plate of material infinite in extent in two dimensions, but of thickness d in the third. The two sides of the plate are held fixed at different temperatures T_1 and T_2 ($T_1 > T_2$). After a long period of time, a steady state is reached at which time the temperature at any point within the plate does not vary with time. It is found that all points lying within a plane parallel to the sides of the plate are at the same temperature (isothermal planes). At the steady state, a constant flux (heat energy per unit area per unit time) crosses the isothermal planes within the plate, directed from hot to cold. The magnitude of this flux is given by:

$$Flux = \frac{k(T_1 - T_2)}{d} \tag{3.1}$$

where:

k = Thermal Conductivity, and is material dependent.

3.1.1 The Differential Equation Of Heat Conduction

Consider a solid in which heat is flowing, and in which heat is being generated. The temperature at a point P(x,y,z,t) within the solid will be a continuous function of position and time, as will the flux. Consider a small control volume, taken for convenience to be of side 2dx, 2dy and 2dz centred on the point P, (See figure 3.1).

Consider first the net influx of heat into the control volume in the x-direction in time δt.

$$Influx_x = 4dydz\left(f_x - \frac{\partial f_x}{\partial x}dx - f_x - \frac{\partial f_x}{\partial x}dx\right)\delta t = -8dxdydz\frac{\partial f_x}{\partial x}\delta t \qquad (3.2)$$

Where f_x is the flux at the point P in the x direction. Similarly in the y and z directions:

$$Influx_y = -8dxdydz\frac{\partial f_y}{\partial y}\delta t \qquad (3.3)$$

$$Influx_z = -8dxdydz\frac{\partial f_z}{\partial z}\delta t \qquad (3.4)$$

If heat is being generated within the solid at the point P at the rate A(x,y,z,t), in the time δt, the energy generated within the control volume is given by:

$$\text{Internal Heat Generated} = 8Adxdydz\ \delta t \qquad (3.5)$$

This gain of energy will give rise to a temperature increase of the control volume. The energy required to raise the temperature of the control volume by δT is given by:

$$Energy = 8dxdydz\,\rho c\delta T \qquad (3.6)$$

where:

ρ = density of the material

c = specific heat capacity of the material

Equating the sum of the right hand sides (RHS) of equations 3.2, 3.3, 3.4, and 3.5 with the RHS of 3.6, cancelling common terms and dividing by δt:

$$-\nabla f + A = \rho c\frac{\delta T}{\delta t} \qquad (3.7)$$

Taking the limit as $\delta t \rightarrow 0$:

$$Lim_{\delta t \rightarrow 0} \frac{\delta T}{\delta t} = \frac{\partial T}{\partial t} \tag{3.8}$$

So:

$$-\nabla f + A = \rho c \frac{\partial T}{\partial t} \tag{3.9}$$

The flux at a point can be expressed in terms of the temperature gradient at the point by Fourier's Law (the single point equivalent of equation 3.1). For heat conduction in the x-direction this is given by:

$$f_x = -k_x \frac{\partial T}{\partial x} \tag{3.10}$$

Substituting this into equation (3.9) and using similar expressions for f_y and f_z, assuming the thermal conductivity of the material is isotropic and homogeneous:

$$\nabla^2 T + \frac{A}{k} = \frac{1}{\alpha} \frac{\partial T}{\partial t} \tag{3.11}$$

where:

$\alpha = k/\rho c$ = Thermal diffusivity of the material.

If there is no internal heat generation, the equation reduces to:

$$\nabla^2 T = \frac{1}{\alpha} \frac{\partial T}{\partial t} \tag{3.12}$$

This is known as Fourier's equation, or the heat diffusion equation.

3.1.2 Related Solutions Of The Differential Equation Of Heat Conduction

Consider equation (3.11) where A is the step-on heating function defined by:

$A = 0$ for $t < 0$, and $A = I_0$ for $t > 0$.

If equation (3.11) is differentiated with respect to time, assuming that the order of differentiation on the left hand side may be reversed:

$$\nabla^2\left(\frac{\partial T}{\partial t}\right)+\frac{1}{k}\frac{\partial A}{\partial t}=\frac{1}{\alpha}\frac{\partial\left(\frac{\partial T}{\partial t}\right)}{\partial t} \tag{3.13}$$

But, the time derivative of the step-on function is simply the Dirac delta pulse function:

$$\frac{\partial A}{\partial t}=\delta(t=0) \tag{3.14}$$

So, the solution of the equation for the conduction of heat in the case of Dirac delta pulse heating, is simply the time derivative of the solution for step on heating. This result will be utilised later in the numerical modelling of heat transfer problems.

3.2 Thermal Waves

Consider now a semi-infinite body with isotropic and homogeneous thermo-physical properties, whose surface (at x=0) is heated by a periodic plane flux given by $I_0e^{j\omega t}$, where I_0 is the flux amplitude, and ω is the angular modulation frequency.

The temperature within the body can be found by solution of the 1-D diffusion equation with the appropriate boundary conditions. The equation within the body is the 1-D equivalent of equation (3.12):

$$\frac{\partial^2 T}{\partial x^2}=\frac{1}{\alpha}\frac{\partial T}{\partial t} \tag{3.15}$$

The steady-state solution (which assumes that the modulated flux has been applied long enough so that the initial transient has died away) can be derived using the method of separation of variables. Assuming the time dependency of the solution to be of the form $e^{j\omega t}$, the solution can be written as:

$$T(x,t)=V(x)e^{j\omega t} \tag{3.16}$$

Substituting this into equation (3.15) a simple equation for V(x) is derived:

$$\frac{d^2V}{dx^2} = \frac{j\omega}{\alpha}V = \sigma^2 V \tag{3.17}$$

Where:

$$\sigma = (1+j)\sqrt{\frac{\omega}{2\alpha}} \tag{3.18}$$

The general solution for T(x,t) is given by:

$$T(x,t) = (Ae^{-\sigma x} + Be^{+\sigma x})e^{j\omega t} \tag{3.19}$$

Where A and B are arbitrary constants. To evaluate these constants, the boundary conditions must be considered. As $x \rightarrow \infty$, the solution must remain finite, hence B must be zero. A is determined by requiring that the flux at the surface is continuous:

$$-k\left.\frac{\partial T}{\partial x}\right|_{x=0} = k\sigma A e^{j\omega t} = I_0 e^{j\omega t} \tag{3.20}$$

Therefore:

$$A = \frac{I_0}{k\sigma} \tag{3.21}$$

The solution for T(x,t) is therefore given by:

$$T(x,t) = \frac{I_0}{k\sigma}e^{-\sigma x + j\omega t} = \frac{I_0}{\sqrt{k\rho c\omega}}e^{-\frac{x}{\mu}}e^{j\left(\omega t - \frac{x}{\mu} - \frac{\pi}{4}\right)} \tag{3.22}$$

Where:

$$\mu = \sqrt{\frac{2\alpha}{\omega}} \text{ is the thermal diffusion length.} \tag{3.23}$$

The solution for T(x,t) is seen to have the form of a damped wave, known as a thermal wave.

3.2.1 Thermal Wave Properties

1. Within one thermal diffusion length of the heated surface, the amplitude of the wave has dropped to 1/e of the value at the surface. Within one thermal

wavelength of the surface ($\lambda=2\pi\mu$), the amplitude has dropped to less than 1/500 of the amplitude at the surface. The waves are extremely heavily damped.

2. From equation 3.23 it is seen that the thermal diffusion length is dependent on the thermo-physical properties of the material (through α), and on the angular modulation frequency ω. The depth of penetration of the wave can therefore be adjusted by changing the modulation frequency of the heat source.

3. At the heated surface, there is a 45° phase lag in the temperature with respect to the phase of the heat source. The phase lag increases linearly with depth below the surface:

$$\text{Phase Lag} = \left(\frac{-x}{\mu} - \frac{\pi}{4}\right) \tag{3.24}$$

4. The phase velocity of a thermal wave is frequency dependent, and so thermal waves are dispersive. A flash excitation of a body will give rise to many Fourier frequency components, which will propagate into the body at differing velocities causing a spatial broadening of the wave packet.

3.2.2 Thermal Wave Reflection And Refraction

Consider a plane containing the boundary between two media (labelled 1 and 2), the boundary lying along the x=0 line. Figure 3.2 shows a thermal wave incident on the boundary, and the associated reflected and refracted waves. Let T_i, T_r and T_t be the incident, reflected and refracted (transmitted) waves respectively. The waves are given by:

$$\begin{aligned} T_i &= Ae^{j\omega t}e^{-\sigma_1 x\cos\theta_i - \sigma_1 y\sin\theta_i} \\ T_r &= RAe^{j\omega t}e^{\sigma_1 x\cos\theta_r - \sigma_1 y\sin\theta_r} \\ T_t &= TAe^{j\omega t}e^{-\sigma_2 x\cos\theta_t - \sigma_2 y\sin\theta_t} \end{aligned} \tag{3.25}$$

Where: $T_i = TAe^{j\omega t}e^{-\sigma_2 x\cos\theta_t - \sigma_2 y\sin\theta_t}$

A = Initial amplitude of the incident thermal wave

R = Reflection Coefficient

T = Transmission Coefficient

Continuity of temperature at the interface x=0 requires that:

$$Ae^{-\sigma_1 y \sin\theta_i} + RAe^{-\sigma_1 y \sin\theta_r} = TAe^{-\sigma_2 y \sin\theta_t} \tag{3.26}$$

This must be true for all y positions on the interface, which requires that the exponents in equation (3.26) must all be equal:

$$\sigma_1 \sin\theta_i = \sigma_1 \sin\theta_r = \sigma_2 \sin\theta_t \tag{3.27}$$

From this, the laws of reflection and refraction can be deduced:

$\theta_i = \theta_r$ Law of reflection

$\frac{\sin\theta_i}{\sin\theta_t} = \sqrt{\frac{\alpha_1}{\alpha_2}}$ Snell's Law

Considering specifically the case of y=0 in equation (3.26) it is found that:

$$1 + R = T \tag{3.28}$$

Continuity of flux at the interface x=0 requires that:

$$k_1\sigma_1 \cos\theta_i - Rk_1\sigma_1 \cos\theta_i = Tk_2\sigma_2 \cos\theta_t \tag{3.29}$$

Combining equations (3.28) and (3.29) equations for R and T are derived only in terms of the angles of incidence and refraction, and the thermo-physical properties of the two media:

$$R = \frac{\cos\theta_i - b\cos\theta_t}{\cos\theta_i + b\cos\theta_t}$$

$$T = \frac{2\cos\theta_i}{\cos\theta_i + b\cos\theta_t} \tag{3.30}$$

Where:

$$b = \frac{k_2\sigma_2}{k_1\sigma_1} = \frac{\sqrt{k_2\rho_2 c_2}}{\sqrt{k_1\rho_1 c_1}} = \frac{(Effusivity)_2}{(Effusivity)_1} \tag{3.31}$$

For normally incident thermal waves, $\theta_i = 0$, and from Snell's Law θ_t is also 0. The expressions for R and T then reduce to:

$$R = \frac{1-b}{1+b} \qquad \text{and} \qquad T = \frac{2}{1+b} \tag{3.32}$$

3.3 The 1-D Single Layer System With CW Excitation

Consider a semi-infinite substrate with a coating on the upper surface. The coated surface is periodically heated with a plane heat flux (continuous wave (CW) excitation) of the form $I_0 e^{j\omega t}$. Properties of the coating and substrate are assumed isotropic and homogeneous and so lateral heat diffusion will not occur. The problem is therefore reduced to only one dimension. See figure (3.3). It will be assumed that the coating is opaque, and that all the incident radiation is instantaneously converted to heat on the coating surface. It is also assumed that the coating looses no heat to the air (i.e. that the reflection coefficient between the coating and air is 1). The solutions to the 1-D diffusion equation in the coating and substrate regions are shown in the figure. Note that in the coating, there are forward and backward propagating solutions, but in the substrate only a forward propagating solution exists. The backward propagating solution within the coating is caused by the discontinuity of thermo-physical properties at the interface between the coating and substrate. No such discontinuity exists within the substrate.

The problem can be solved by requiring that flux and temperature are continuous at the interface between coating and substrate, and that the flux at the heated surface matches that of the applied heating. The steady-state solution is required, and so the time dependence of the temperature in each region will be of the form $e^{j\omega t}$. It is not therefore necessary to work with the full time dependent solution, only the spatial dependence need be considered.

Continuity of flux at the surface requires:

$$-k_c \sigma_c (B - A) = I_0 \tag{3.33}$$

Continuity of temperature at the interface $x = l_c$ requires:

$$Ae^{-\sigma_c l_c} + Be^{+\sigma_c l_c} = Ce^{-\sigma_s l_c} \tag{3.34}$$

Continuity of flux at the interface $x = l_c$ requires:

$$-k_c\sigma_c(Be^{+\sigma_c l_c} - Ae^{-\sigma_c l_c}) = -k_s\sigma_s(-Ce^{-\sigma_s l_c}) \tag{3.35}$$

From the above three equations, expressions for A and B can be found. The time independent solution within the coating is given by:

$$V_c(x) = \frac{I_0}{k_c\sigma_c\left(1-\mathrm{Re}^{-2\sigma_c l_c}\right)}\left(e^{-\sigma_c x} + \mathrm{Re}^{-2\sigma_c l_c}\, e^{+\sigma_c x}\right) \tag{3.36}$$

Where:

R = Reflection Coefficient between coating and substrate and is given by:

$$R = \frac{1-b}{1+b} \qquad \text{and} \qquad b = \frac{\sqrt{k_s\rho_s c_s}}{\sqrt{k_c\rho_c c_c}} \tag{3.37}$$

Specifically at the coating surface x = 0, the solution for the spatial dependence of the temperature is given by:

$$V_c(x=0) = \frac{I_0}{k_c\sigma_c}\left(\frac{1+\mathrm{Re}^{-2\sigma_c l_c}}{1-\mathrm{Re}^{-2\sigma_c l_c}}\right) \tag{3.38}$$

The solution for a semi-infinite coating is given by equation (3.22) by replacing $k\sigma$ by $k_c\sigma_c$, and neglecting the time dependence. If equation (3.38) is divided by the solution for a semi-infinite coating, the result is an expression which gives the phase and magnitude of the temperature at the surface with respect to that of an infinitely thick coating. This expression is given by:

$$R(\omega) = \frac{1+\mathrm{Re}^{-2\sigma_c l_c}}{1-\mathrm{Re}^{-2\sigma_c l_c}} \tag{3.39}$$

This function is dependent on the thermo-physical properties of the coating and substrate through R, on the coating thickness l_c, and the angular frequency of the CW heating through σ_c. It is interesting to plot the magnitude and phase of $R(\omega)$ against the thermal thickness of the coating l_c/μ for various values of the reflection coefficient R. See figures (3.4) and (3.5). If the reflection coefficient is positive, and the coating is thermally thin, waves reflected from the coating/substrate interface arrive in-phase with the direct waves at the coating surface, and interfere constructively producing a value for the $|R(\omega)| > 1.0$. As the coating thickness is increased, the reflected waves arrive more and more out of phase with the direct waves, until the interference becomes destructive, and the value of $|R(\omega)|$ becomes < 1.0. As the coating thickness is

increased still further, the reflected waves have little effect at the surface due to decay, and the sample exhibits the characteristics of a thermally thick coating.

The above analysis of the single layer system made the assumption that the coating was opaque, and that all the incident radiation was converted to heat at the coating surface. A more complete analysis of this problem, taking into account the effects of coating translucency was reported by Bennett and Patty in 1982 [21].

3.4 The 1-D Double Layer System With CW Excitation

The double layer system is important as it allows the modelling of the presence of a corrosion layer or delamination between the coating and substrate. These are the types of defect that are hoped to be found with the thermal testing techniques.

The simplest method of determining the response of a double layer system to CW excitation is to calculate the effective thermal wave reflection coefficient Γ between the coating, and the defect/substrate pair. This can then be used in the equations derived for the single layer system in place of the reflection coefficient R. Figure (3.6) shows a diagram of the system, and the solutions in each region. Once more, plane CW heating is assumed, along with isotropic and homogeneous thermal properties in each region. To determine Γ, the conditions of continuity of flux and temperature at $x = 0$ and $x = l_d$ are used.

Continuity of temperature at $x = 0$ requires:

$$A + B = C + D \tag{3.40}$$

Continuity of flux at $x = 0$ requires:

$$k_c\sigma_c(A - B) = k_d\sigma_d(C - D) \tag{3.41}$$

Continuity of temperature at $x = l_d$ requires:

$$Ce^{-\sigma_d l_d} + De^{+\sigma_d l_d} = Fe^{-\sigma_s l_d} \tag{3.42}$$

Continuity of flux at $x = l_d$ requires:

$$k_d\sigma_d(Ce^{-\sigma_d l_d} - De^{-\sigma_d l_d}) = k_s\sigma_s Fe^{-\sigma_s l_d} \tag{3.43}$$

Eliminating C, D and F from the above equations, it is found that Γ is given by:

$$\Gamma = \frac{B}{A} = \frac{R_{cd} + R_{ds} e^{-2\sigma_d l_d}}{1 + R_{cd} R_{ds} e^{-2\sigma_d l_d}} \tag{3.44}$$

Where:

$$R_{cd} = \frac{1-b}{1+b} \quad \text{and} \quad b = \frac{(Effusivity)_d}{(Effusivity)_c} \tag{3.45}$$

R_{cd} = Reflection coefficient between coating and defect.

and:

$$R_{ds} = \frac{1-c}{1+c} \quad \text{and} \quad c = \frac{(Effusivity)_s}{(Effusivity)_d} \tag{3.46}$$

R_{ds} = Reflection coefficient between defect and substrate.

Note that the effective thermal wave reflection coefficient Γ of the coating-defect pair is frequency dependent, in contrast to the simple reflection coefficient R.

Replacing R with Γ in equation (3.39), the corresponding expression for the double layer system is given by:

$$R(\omega) = \frac{1 + \Gamma e^{-2\sigma_c l_c}}{1 - \Gamma e^{-2\sigma_c l_c}} \tag{3.47}$$

Where Γ given by equation (3.44).

Figures 3.7 and 3.8 show phase plots verses square-root of frequency for air gap defects of thicknesses 1, 10 and 100 μm, 0.5 mm below the surface in mild steel and bakelite respectively.

In the case of the air gaps in mild steel, there is a large effusivity mismatch between the air and the mild steel. In the case of the bakelite, the mismatch is much smaller, and so the subsequent phase changes are much smaller.

An expression similar in form to equation (3.44) can be derived for the effective reflection coefficient of a thermal contact resistance between a coating and a substrate.

Results from both the double layer system , and the contact resistance model have been published by Patel, Almond and Reiter [18].

3.5 The 1-D Single Layer System With Pulse Or Step Excitation

In section 3.3, the steady-state solution of the diffusion equation for the 1-D single layer system was derived for CW heating. In this section the emphasis changes to transient solutions of the diffusion equation. Transient solutions are more complicated in general as the time and spatial components of the solution are not usually separable. The solution in section 3.3 gave the response of the system to a single frequency of excitation ω. If pulse or step heating is used, many Fourier frequency components are released simultaneously. A standard method of deriving the system response to non-periodic heating, when the single frequency response is known, is to use the Laplace transform technique [86].

The surface temperature of the system as a function of time following any form of heating, can be found by the convolution of the transfer function of the system, with the heating function. That is

$$\text{Surface Temp}(t) = \text{Transfer Func}(t) * \text{Heating Func}(t) \tag{3.48}$$

Where:

* signifies the operation of convolution.

Convolution is much simpler to apply in the frequency domain, as it is simply a multiplication operation. Taking Laplace transforms of equation (3.48):

$$L(\text{Surface Temp}) = L(\text{Transfer Func}) \,.\, L(\text{Heating Func}) \tag{3.49}$$

Where:

. signifies ordinary multiplication.

L signifies the taking of the Laplace transform.

Rearranging equation (3.49) the Laplace transform of the transfer function can be found:

$$L(Transfer\_Func) = \frac{L(Surface\_Temp)}{L(Heating\_Func)} \tag{3.50}$$

Equation (3.38) multiplied by $e^{j\omega t}$ is the full time dependent solution for the surface temperature of a 1-D single layer system being heated at a modulation frequency ω. Taking the Laplace transform of this, and dividing it by the Laplace transform of the heating function $I_0 e^{j\omega t}$, the Laplace transform of the transfer function is found to be:

$$L(Transfer\_Func) = \frac{1}{k\sigma}\left(\frac{1+\mathrm{Re}^{-2\sigma_c l_c}}{1-\mathrm{Re}^{-2\sigma_c l_c}}\right) \tag{3.51}$$

It is now possible to find the response of the system to any form of heating by taking the inverse Laplace transform of the product of equation (3.51) with the Laplace transform of the heating function. However, computing the inverse Laplace transform is not straightforward. The Bromwich Integral can be used for the inversion, but a simpler method is to find the inverse transform in a book of mathematical tables.

3.5.1 Pulse Heating Response

The response of the 1-D single layer system to a delta heat pulse is now found using the method described above. The Laplace transform of the Dirac delta heating pulse $I_0\delta(0)$ for a pulse at time t=0 is simply I_0. Multiplying this by equation (3.51) and taking the inverse Laplace transform, the surface temperature is found to be given by:

$$T(t) = \frac{I_0}{\sqrt{\pi\rho ckt}}\left(1+2\sum_{n=1}^{\infty} R^n e^{-\left(\frac{n^2 l_c^2}{\alpha t}\right)}\right) \tag{3.52}$$

Figure 3.9 shows the pulse heating response of a single layer system, with various thicknesses of zirconia on a stainless steel substrate, plotted on a log-log scale. All the curves initially have a gradient of -1/2, the same that is found for a semi-infinite coating. At a time depending on the coating thickness, the gradient deviates from -1/2. This can be understood in terms of thermal waves. At very short times, only thermal waves that propagate at high velocity will have had time to reach the coating/substrate interface, be reflected, and return to the surface. However, fast propagating high frequency thermal waves are highly attenuated. By their return to the surface they have decayed to the extent that they are too weak to effect the surface temperature. At longer times, the waves on return from reflection at the interface will still have large enough amplitude to effect the surface temperature, and so the gradient deviates from -1/2. At very long times, the response is dominated by thermal waves of very low frequency

(long wavelength), as faster, shorter wavelength components have decayed. The gradient then returns to -1/2 because the thickness of the coating layer is very small compared to the penetration depth of these thermal waves, and is effectively invisible, with the response being dominated by the passage of the thermal waves in the semi-infinite substrate, causing the system to act once again as a semi-infinite material.

The temperature of a semi-infinite solid following a Dirac delta heating pulse can be calculated using the same approach as above. In this case, instead of using the transfer function of equation 3.51 (based on equation 3.38, the harmonic solution for a single layer system), a transfer function based on the harmonic solution for a semi-infinite solid (equation 3.22) must be used. The resulting solution is given by [87]:

$$T(x,t) = \frac{I_o}{\sqrt{\pi \rho c k t}} e^{-\frac{x^2}{4\alpha t}} \tag{3.53}$$

From this equation, the effective thermal diffusion length μ_{eff} may be defined. This is the transient analogy of the thermal diffusion length μ for single frequency thermal waves. It is the depth below the surface at which the temperature is 1/e of the value at the surface, i.e. when the exponent in equation (3.53) is equal to -1. It is given by:

$$\mu_{eff} = 2\sqrt{\alpha t} \tag{3.54}$$

It has previously been suggested [26] that the response of a system at a time t after Dirac delta excitation is similar to the response of the system to a thermal wave with a thermal diffusion length equal to the effective thermal diffusion length given in equation (3.54). The idea of the effective thermal diffusion length will be used in section 3.6 to relate frequency-domain and time-domain solutions for three dimensional problems.

3.5.2 Step-On Heating Response

The Laplace transform of a step-On heating pulse of magnitude I_0 at time t = 0 is given by 1/s. Once more, multiplying this by equation (3.51) and taking the inverse Laplace transform, the surface temperature expression for step-on heating is given by:

$$T(t) = \frac{2I_0\sqrt{\alpha t}}{k}\left(\frac{1}{\sqrt{\pi}} + 2\sum_{n=1}^{\infty} R^n ierfc\left(\frac{nl_c}{\sqrt{\alpha t}}\right)\right) \tag{3.55}$$

Where:

$$ierfc(x) = \frac{e^{-x^2}}{\sqrt{\pi}} - x\,erfc(x)$$

$$erfc(x) = 1 - erf(x) \qquad \text{erfc(x) = The complimentary error function}$$

$$erf(x) = \frac{2}{\sqrt{\pi}} \int_0^x e^{-t^2}\,dt \qquad \text{erf(x) = The error function}$$

Figure 3.10 shows the response of a single layer system to step-on heating.

3.6 Finite Sized Defects

Transient experimental investigations on samples containing various sizes of artificial defects have shown that characteristics of the images produced are dependent upon the defect size [88]. A defect of radius 5mm produces a different response to one of radius 1mm. Larger defects are found to give greater thermal contrast, and have a maximum contrast occurring at a later time than smaller defects. These differences are caused by the lateral diffusion of the heat around the defect. If only 1-D heat flow is assumed, it is not possible to model this lateral diffusion process, and a defect of any size is predicted to produce the same contrast-time profile. To accurately predict the response of finite sized defects, it is therefore necessary to work with a 3-D model. The analytical solution of the diffusion equation in 3-D, for the case of finite diameter defects, is not straightforward. An approach taken by Almond and Lau [70,71], in which a solution is first derived in the frequency domain by the use of Wiener-Hopf technique, and is then interpreted in the time domain by the use of the effective thermal diffusion length (equation 3.54 and associated text), is discussed here.

3.6.1 The Wiener-Hopf Solution In The Frequency-Domain

Consider plane thermal waves of angular frequency ω travelling in the negative z direction in a body of infinite extent, impinging on an infinitely thin crack that occupies half of the $z = 0$ plane, for $x > 0$ (figure 3.11). The crack is defined such that no thermal flux may pass through it (a perfect reflecting crack). The first step in the solution is to find the temperature profile on the upper surface of the crack due to the incident thermal waves. This can be formally solved using the Wiener-Hopf technique

[89]. The solution for the scattered thermal field (the additional temperature due to the presence of the crack) T^s, on the upper surface of the crack, for normally incident thermal waves is given by:

$$T^s(x,+0) = 1 - \frac{2}{\pi}\int_0^\infty \frac{e^{j\sigma x(1+s^2)}}{(1+s^2)} ds \tag{3.56}$$

Substituting in equation (3.18) for σ, and separating into real (T_r^s) and imaginary (T_i^s) parts, this becomes:

$$T_r^s(x,+0) = 1 - \frac{2}{\pi}\int_0^\infty \frac{e^{-x\left(\frac{1+s^2}{\mu}\right)}}{(1+s^2)} \cos\left(\frac{x(1+s^2)}{\mu}\right) ds \tag{3.57}$$

$$T_i^s(x,+0) = -\frac{2}{\pi}\int_0^\infty \frac{e^{-x\left(\frac{1+s^2}{\mu}\right)}}{(1+s^2)} \sin\left(\frac{x(1+s^2)}{\mu}\right) ds \tag{3.58}$$

These integrals can be evaluated numerically and are plotted in figure (3.12) against normalised distance (x/μ) from the crack edge. It can be seen that the temperature falls to zero at the crack tip over a distance of approximately the thermal diffusion length μ. This is caused by the flow of heat around the crack tip from the hotter upper surface to the cooler lower surface. The flux flowing to the tip from the upper surface is exactly matched by the flux flowing from the tip to the lower surface.

The thermal contrast at a point above the crack can now be calculated by using Green's functions to propagate the solution on the crack surface to the desired height. The symmetry of the problem means that the crack may be considered as a series of line elements running parallel to the y-axis. The required Green's function for a line source is given by [87]:

$$G(r,\omega) = \frac{1}{2\pi k} K_0\left(r\sqrt{\frac{j\omega}{\alpha}}\right) \tag{3.59}$$

Where:

$$r = \sqrt{(x-x')^2 + (z-z')^2} \tag{3.60}$$

And:

K_0 is the modified Bessel function and is defined by:

$$K_0(x) = \int_0^\infty \frac{\cos(xt)}{\sqrt{(1+t^2)}} dt \qquad \text{for } x > 0. \tag{3.61}$$

To find the resulting temperature at a point (x,z) above the plane due to all the line elements, an integral must be formed:

$$T^s(x,z) = -\alpha \int_{crack} T^s(x,+0) \frac{\partial G(r,\omega)}{\partial z} dx \tag{3.62}$$

Where:

$T^s(x,+0)$ is the sum of equations (3.57) and (3.58)

$G(r,\omega)$ is given by equation (3.59)

Figure (3.13) shows the normalised temperature profiles at a height of 1mm above a straight edged crack in mild steel (α=14x10^{-6}), calculated by numerically evaluating equation 3.62, using thermal waves with diffusion lengths of 0.5, 1.0, 1.5, 2.0 and 2.5mm. The profiles are seen to intercept at a normalised temperature amplitude of 0.5, at approximately 0.23μ in from the crack tip (+ve normalised distance indicates a position directly above the crack). If half normalised temperature amplitude is used as the measure of defect size, the 0.23μ error in the size will be least for high frequency thermal waves (with low thermal diffusion lengths). Imaging the defect with lower frequency thermal waves gives rise to a larger error in defect size as the associated thermal diffusion lengths are longer.

3.6.2 The Wiener-Hopf Solution Adapted For Circular Defects

The Wiener-Hopf analytical solution is strictly only valid for the half plane perfect crack defect described above. However, in the field of NDT, defects of interest will be of finite size. An approximation to the solution for the temperature profile on a circular crack can be made by applying the temperature profile at the edge of the straight crack to concentric rings of the surface of a circular crack. As noted above, the edge effects are only present within approximately one thermal diffusion length of the crack edge, so as long as the diameter of the circular crack is greater than 2μ, the edge effects do not overlap, and the approximation should be relatively good. The thermal contrast at a point above the circular crack can now be calculated as before by using Green's functions to propagate the crack surface solution. The Green's function for a point source of frequency ω is given by [87]:

$$G(r,\omega)=\frac{e^{-\sigma r}}{4\pi kr} \tag{3.63}$$

Where:

$$r=\sqrt{(x-x')^2+(y-y')^2+(z-z')^2}$$

The temperature is now found by forming an integral over the surface of the crack analogous to equation (3.62), using the Green's function of equation (3.63).

Figure 3.14 shows the normalised temperature profiles of a 10mm diameter crack in mild steel (α=14x10^{-6}), at a depth of 1mm, when imaged by thermal waves of diffusion lengths 0.5, 1.0, 1.5, 2.0, and 2.5mm. As was the case for the straight edged crack, the profiles are seen to intercept at a normalised temperature amplitude of 0.5, but in this case at approximately 0.3μ in from the crack edge. Once more, if half normalised temperature amplitude is used as the measure of defect size, the error in the size will be least for high frequency thermal waves.

3.6.3 Interpreting The Wiener-Hopf Solution In The Time-Domain

As mentioned in the introduction to this section on finite sized defects, the idea of the effective thermal diffusion length μ_{eff} is used for the interpretation of the frequency-domain solution in the time-domain. By equating equation (3.54) for μ_{eff} with equation (3.23) for μ, a relationship between the angular frequency ω, and the transient time t can be found:

$$t=\frac{1}{2\omega} \tag{3.64}$$

Using the effective thermal diffusion length it is found that the response of a system at short time corresponds to the frequency-domain solution for high frequency thermal waves, and at long times corresponds to the frequency-domain solution for low frequency thermal waves. This is in agreement with the discussion of section 3.5.1. Relating this to the defect sizing results of figure 3.14, it is seen that the least error in the size of the defect is made if the measurement of the width of the contrast peak is made at a short time after the heating pulse.

3.6.4 Short Comings Of The Wiener-Hopf Solution

It must be stressed that the Wiener-Hopf solution discussed above is only approximate. There are four major ways in which the model is deficient :

1. The edge-effect of a semi-infinite straight edged crack was used as an approximation to the effect at the edge of a circular defect. The error associated with this approximation will be least for large diameter, low curvature defects, but will increase as defect size is reduced. As thermal edge-effects scale with μ, this error will be least for high frequency thermal waves (corresponding to short times after the pulse heating), but will increase for lower frequency waves (and elapsed time). Consequently, the curvature of any defect can be regarded as small for high frequency waves (short time), but may become large for low frequency waves (longer times). In the transient regime, the net effect will be an increase in the significance of this error with elapsed time.

2. The edge-effect around the circumference of a circular defect extends from the crack tip inwards to the centre of the defect. If the defect radius is smaller than, or comparable to μ, the edge-effects from opposite sides of the defect will overlap. If this occurs, the analytical solution for the effect at the edge of a semi-infinite half plane ceases to resemble the true edge-effect on the circular defect. This leads to significant errors in the analytical predictions for small diameter defects at short times, and in the larger diameter defects at longer times.

3. The surface temperature contrast was calculated by a Green's function projection of the defect thermal profile to a plane above the defect. This corresponded to simple reflection by the defect. However, for a planar defect a small distance beneath the surface, reverberations of the between the defect and surface planes may occur. These reverberations would cause a spreading of the thermal energy and lead to further deviations from the predictions of the basic analytical model. For high frequency waves (short times) these reverberations are unimportant because μ is small compared to defect depth and the wave has decayed before the first reverberation reaches the surface. For lower frequency waves (longer times), μ exceeds defect depth and the effect of reverberation cannot be ignored.

4. The transient time domain solution was derived from the frequency domain solution by the use of the notion of an effective thermal diffusion length μ_{eff}. The Dirac heating pulse releases thermal waves of all frequencies, and so it is a crude

approximation to assume that the transient solution at a given time can be characterised by a single frequency component.

The general result from the analytical treatment of this problem, that the diameter of a defect imaged using Dirac delta pulse heating should decrease with elapsed time after the pulse has been validated by experiment [70].

3.7 Applicability Of Solutions To Sprayed Coatings

All of the analytical analysis of this chapter has assumed the properties of all materials to be isotropic and homogeneous. It has also been assumed that a sample is heated in a planar fashion, with the entire surface of the sample receiving the same flux input, be it modulated or pulse. In reality, neither of these two assumptions are strictly valid, but if care is taken, the results are still useful.

Spray coatings are inherently inhomogeneous, containing for example unmelted particles and porosity. The interface between the coating and the substrate is grit blasted before spraying to aid adhesion, causing a rough coating/substrate interface in addition to the rough finish of the coating. The solutions derived in this chapter will still be valid if the characteristic dimensions of the roughness and inhomogeneities is small compared to the diffusion length of the thermal wave. In the transient case, this corresponds to times when the temperature is dominated by thermal wave components with an effective thermal diffusion length much greater than the size of these defects. Care should therefore be taken when using high frequency modulation (short thermal diffusion length thermal waves), and in analysing very short-time transient responses (dominated by short thermal diffusion length thermal waves).

The validity of the assumption of planar heating is a particular problem in the case of modulated heating. Experimentally, thermal waves are generated by the use of a modulated laser beam, typically with a 1/e diameter of around 1mm. It has been found [20] that for the heat flow solutions developed in this chapter to be valid, the diameter of the beam should be greater than 14 times the depth of the coating/substrate or coating/defect interface. This is a serious problem, and is a one that cannot always be surmounted. Quantitative interpretation of harmonic heating results are therefore not exact, although general features can be deduced.

Control Volume Used For The Derivation Of The Heat Conduction Equation

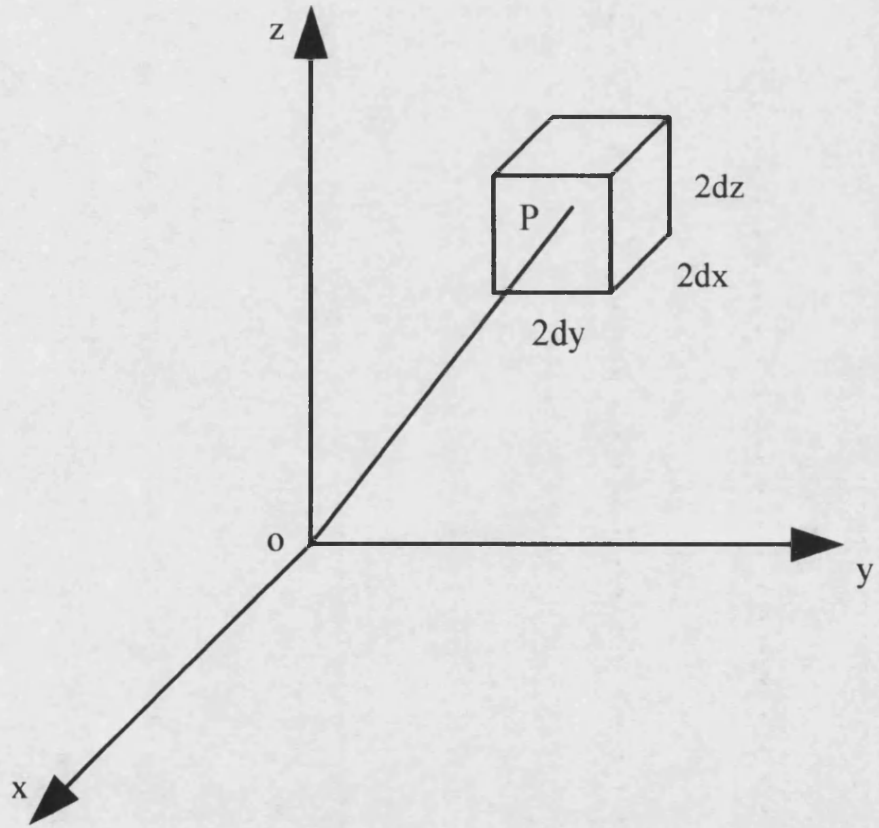

Figure 3.1

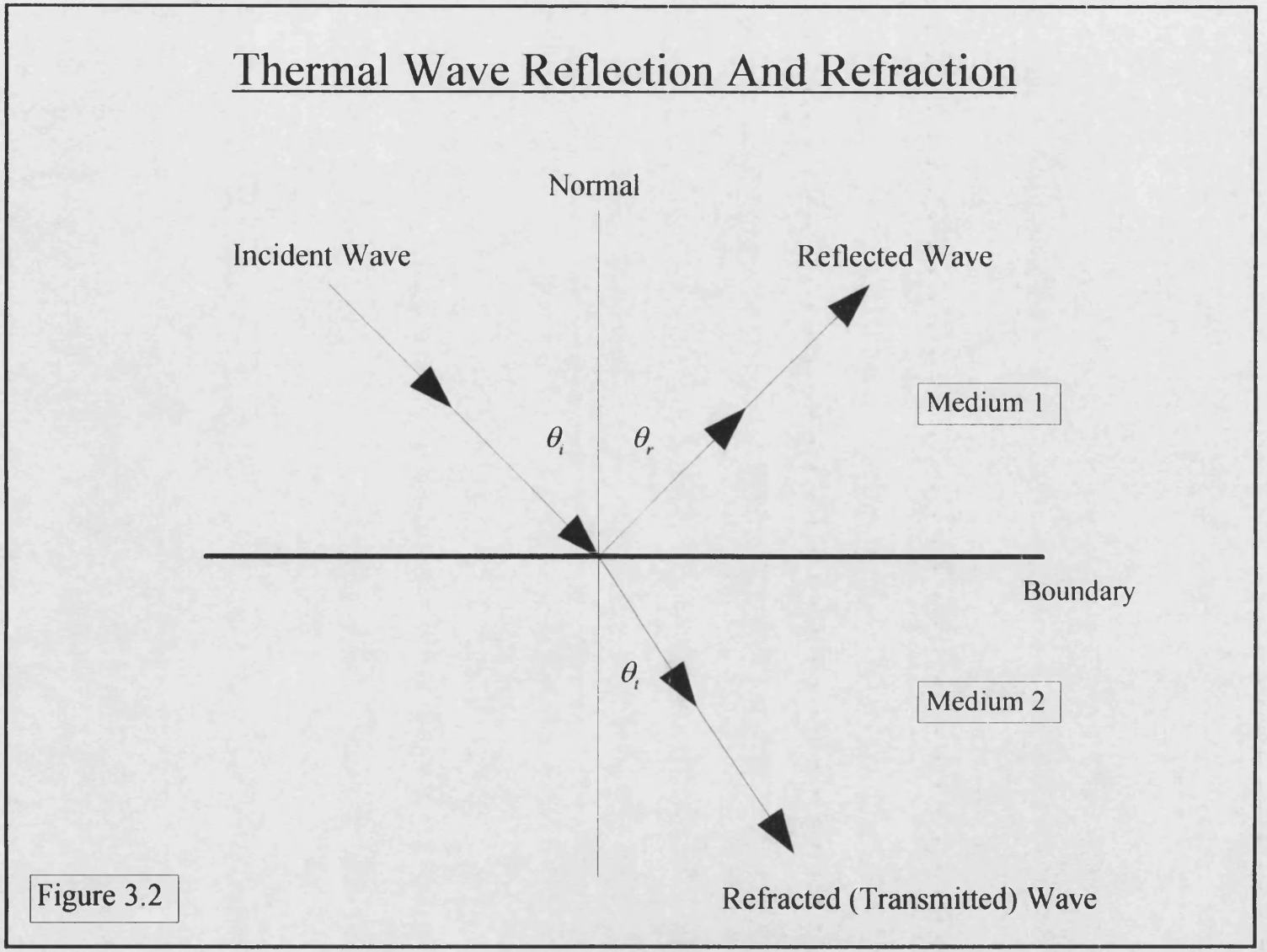
Thermal Wave Reflection And Refraction
Normal
Incident Wave
Reflected Wave
Medium 1
θ_i
θ_r
Boundary
θ_t
Medium 2
Refracted (Transmitted) Wave

Figure 3.2

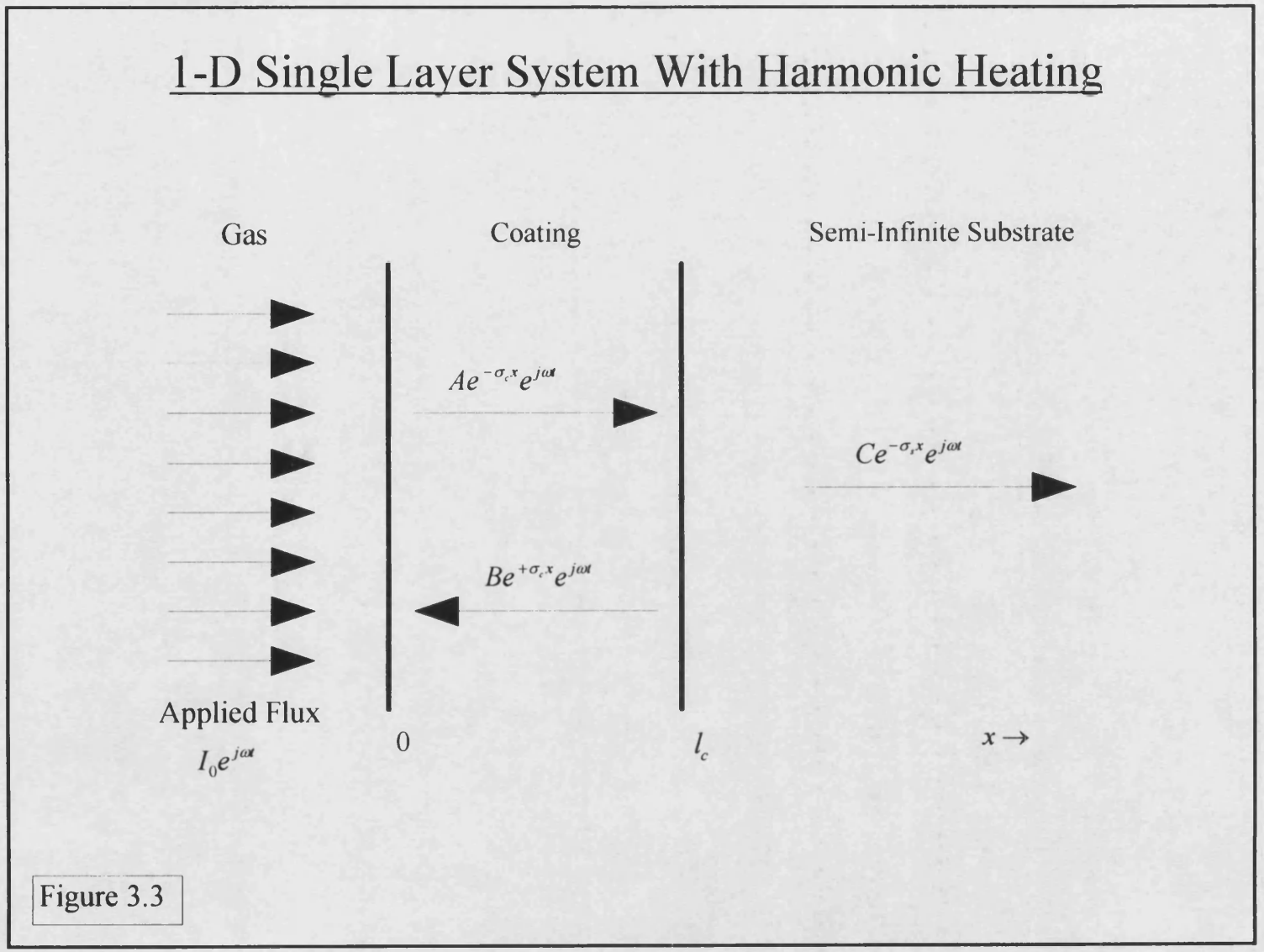
1-D Single Layer System With Harmonic Heating
Gas
Coating
Semi-Infinite Substrate
$Ae^{-\sigma_c x}e^{j\omega t}$
$Ce^{-\sigma_s x}e^{j\omega t}$
$Be^{+\sigma_c x}e^{j\omega t}$
Applied Flux
$I_0 e^{j\omega t}$
0
l_c
$x \rightarrow$

Figure 3.3

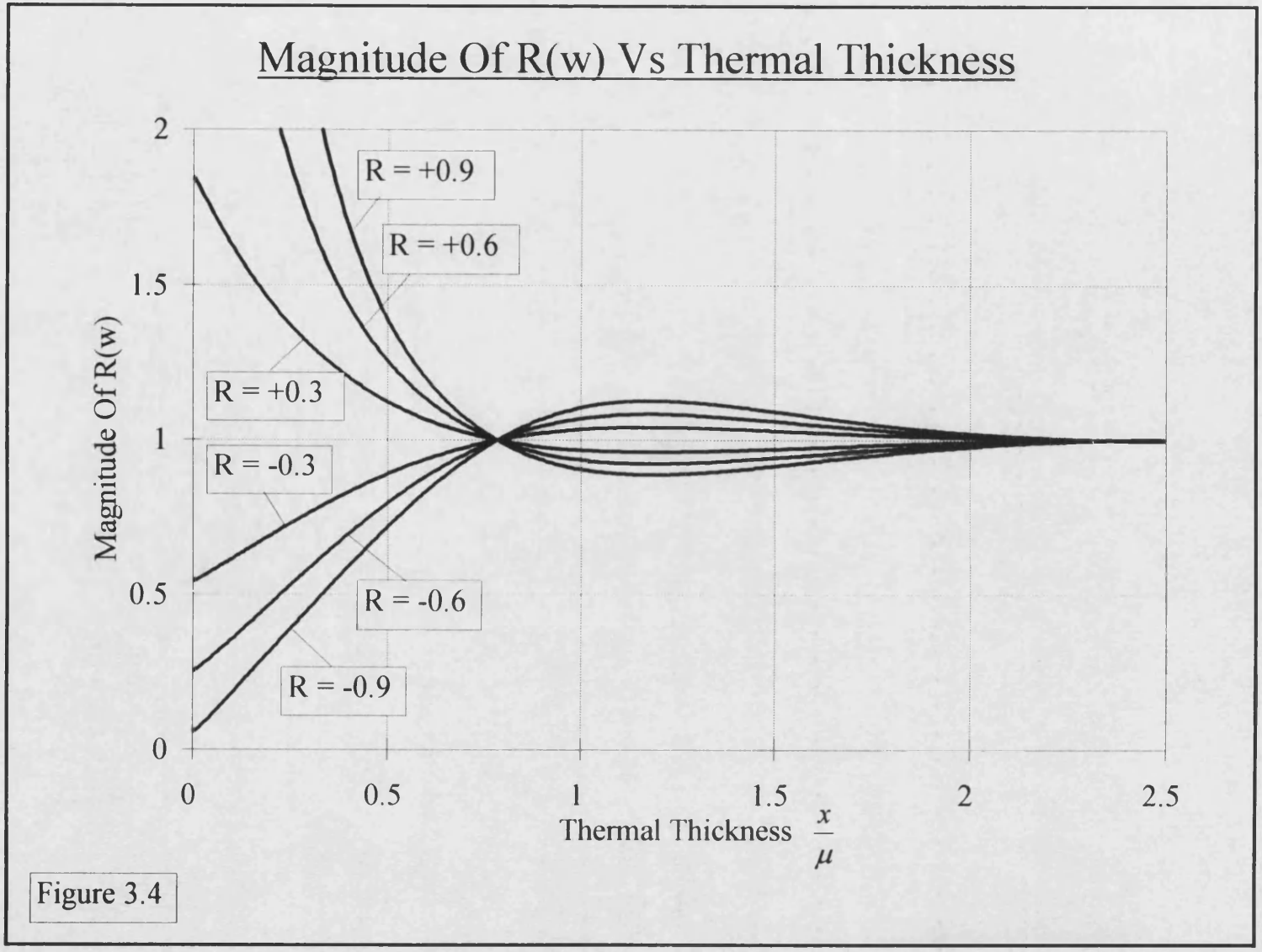
Magnitude Of R(w) Vs Thermal Thickness
Magnitude Of R(w)
Thermal Thickness x/μ
R = +0.9
R = +0.6
R = +0.3
R = -0.3
R = -0.6
R = -0.9
0
0.5
1
1.5
2
2.5

Figure 3.4

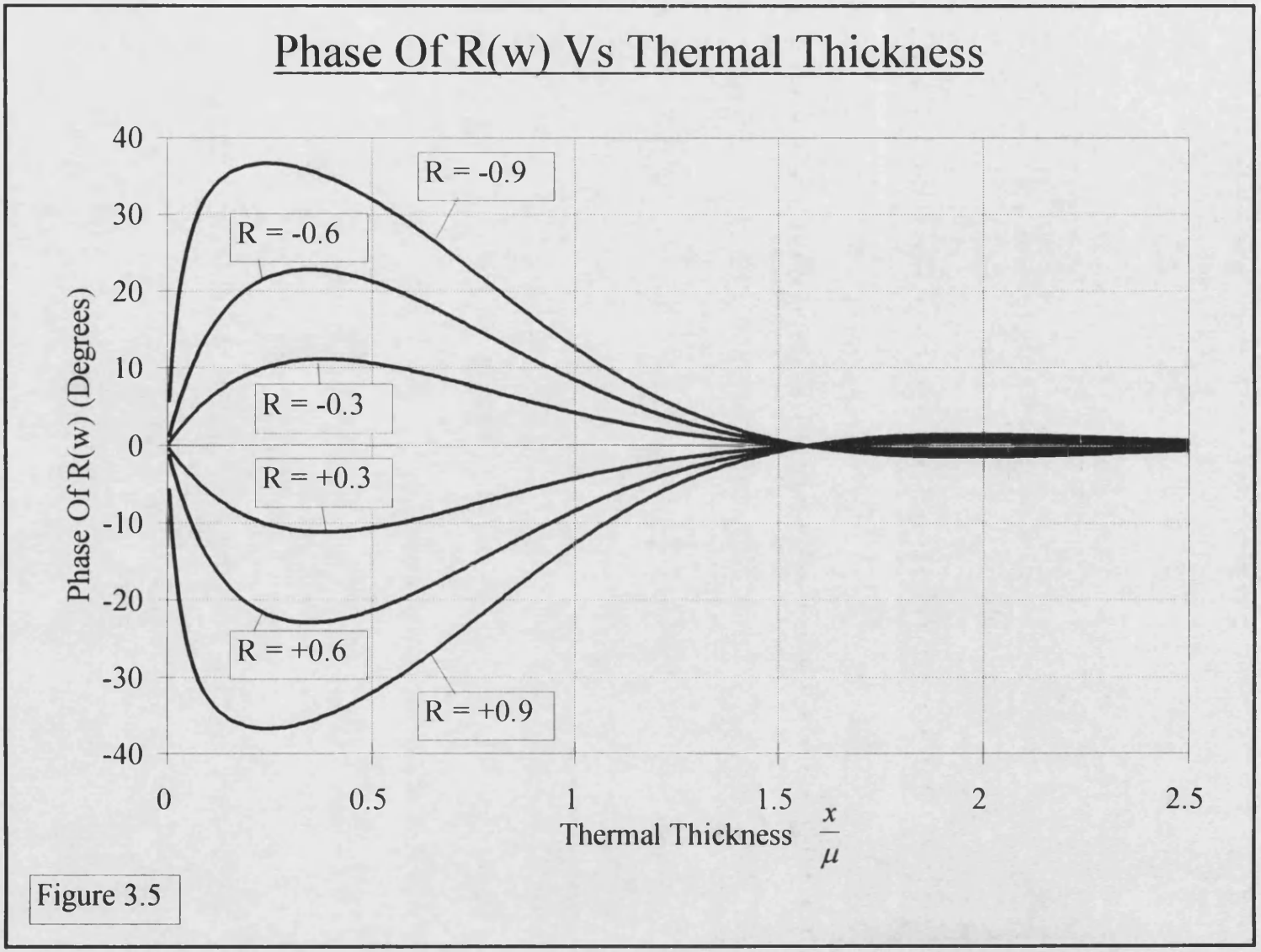
Phase Of R(w) Vs Thermal Thickness
40
30
20
10
0
-10
-20
-30
-40
Phase Of R(w) (Degrees)
R = -0.9
R = -0.6
R = -0.3
R = +0.3
R = +0.6
R = +0.9
0
0.5
1
1.5
2
2.5
Thermal Thickness x/μ

Figure 3.5

1-D Double Layer System With Harmonic Heating

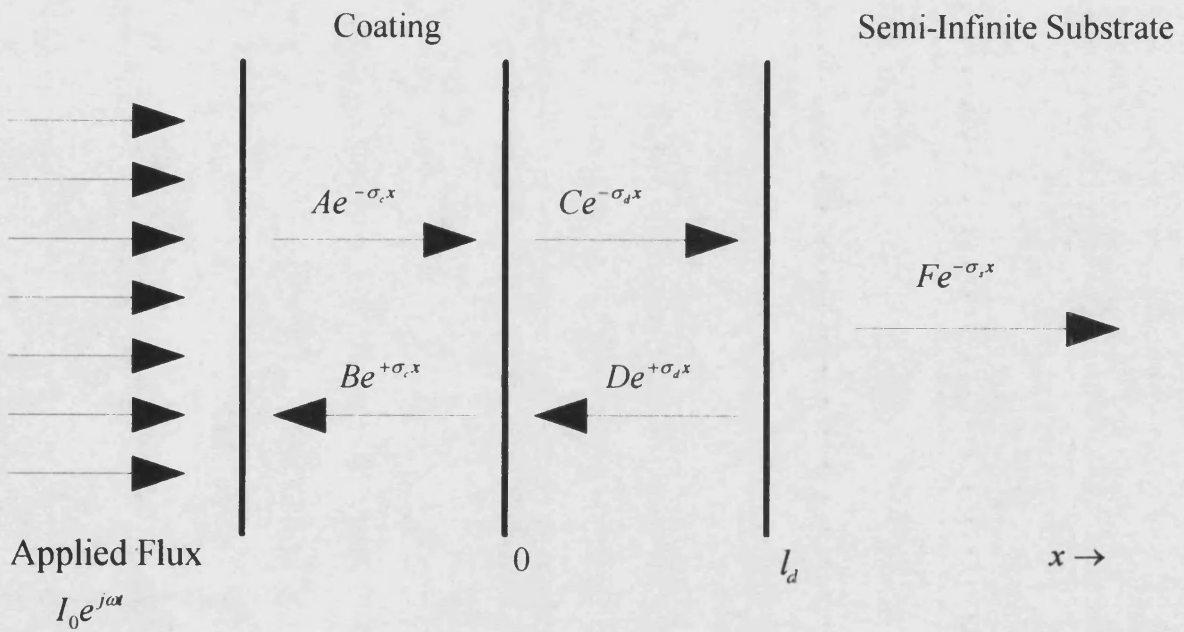

Figure 3.6

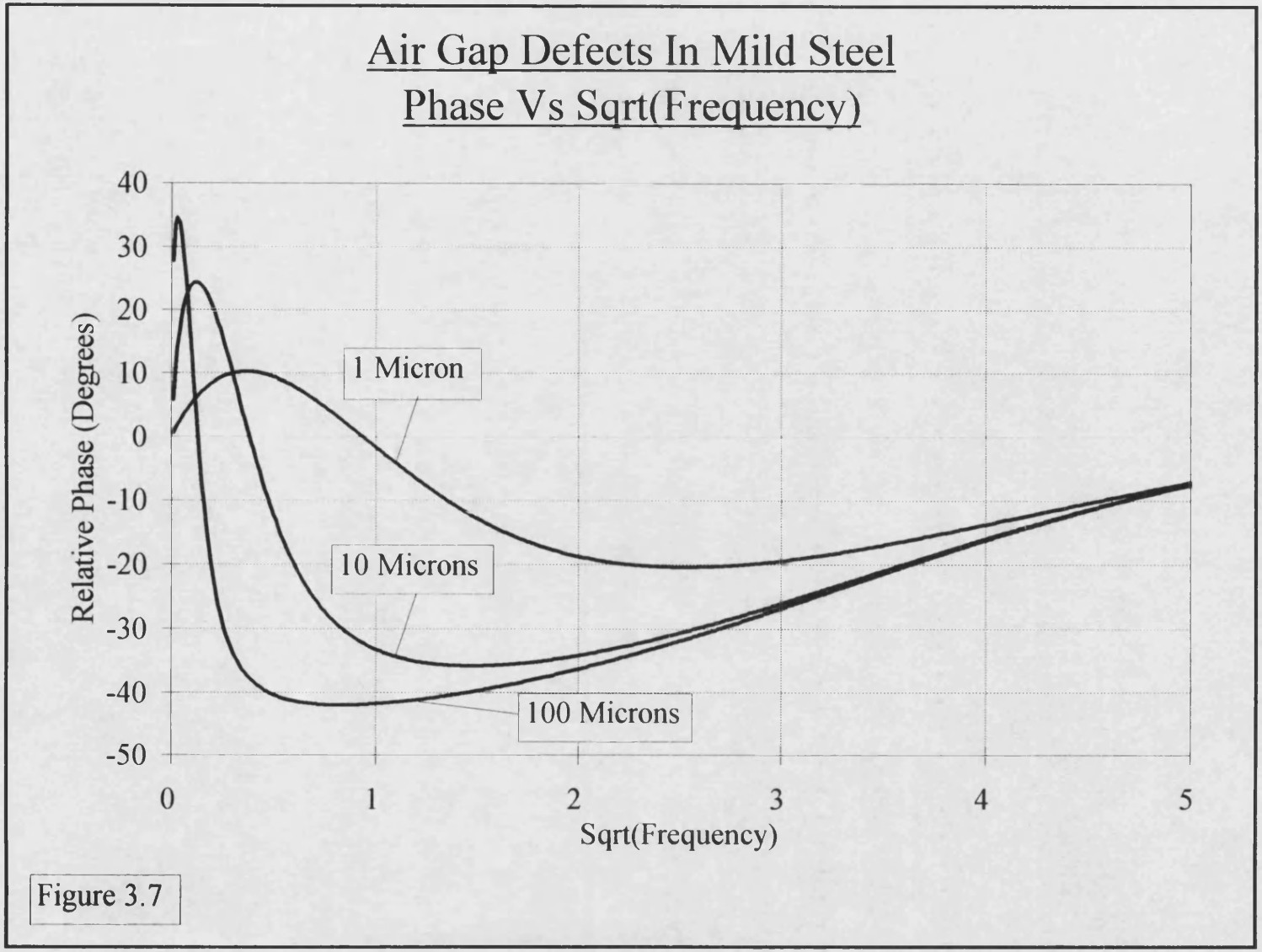
Air Gap Defects In Mild Steel
Phase Vs Sqrt(Frequency)
Relative Phase (Degrees)
40
30
20
10
0
-10
-20
-30
-40
-50
0
1
2
3
4
5
Sqrt(Frequency)
1 Micron
10 Microns
100 Microns

Figure 3.7

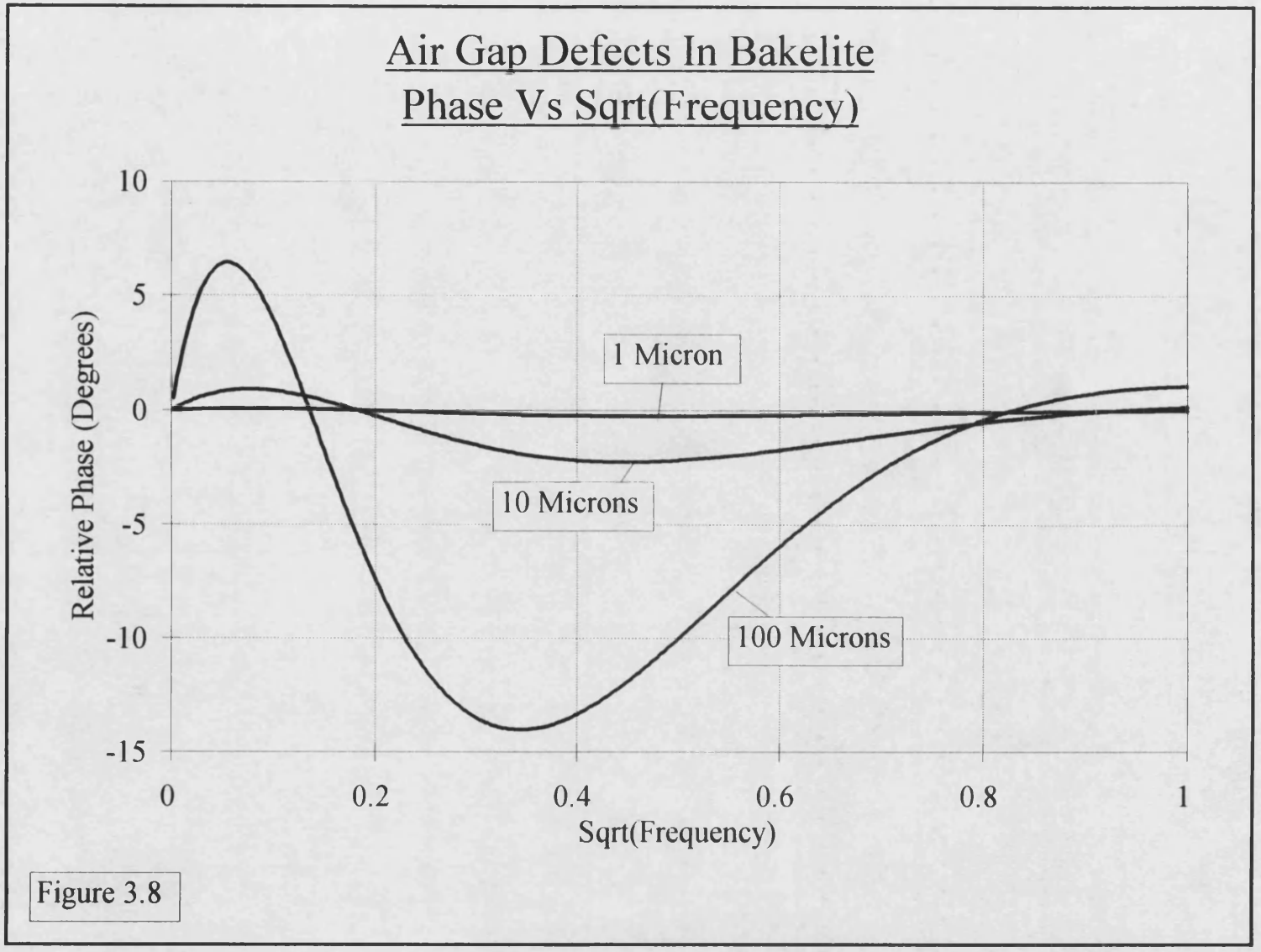
Air Gap Defects In Bakelite
Phase Vs Sqrt(Frequency)
10
5
0
-5
-10
-15
Relative Phase (Degrees)
1 Micron
10 Microns
100 Microns
0
0.2
0.4
0.6
0.8
1
Sqrt(Frequency)

Figure 3.8

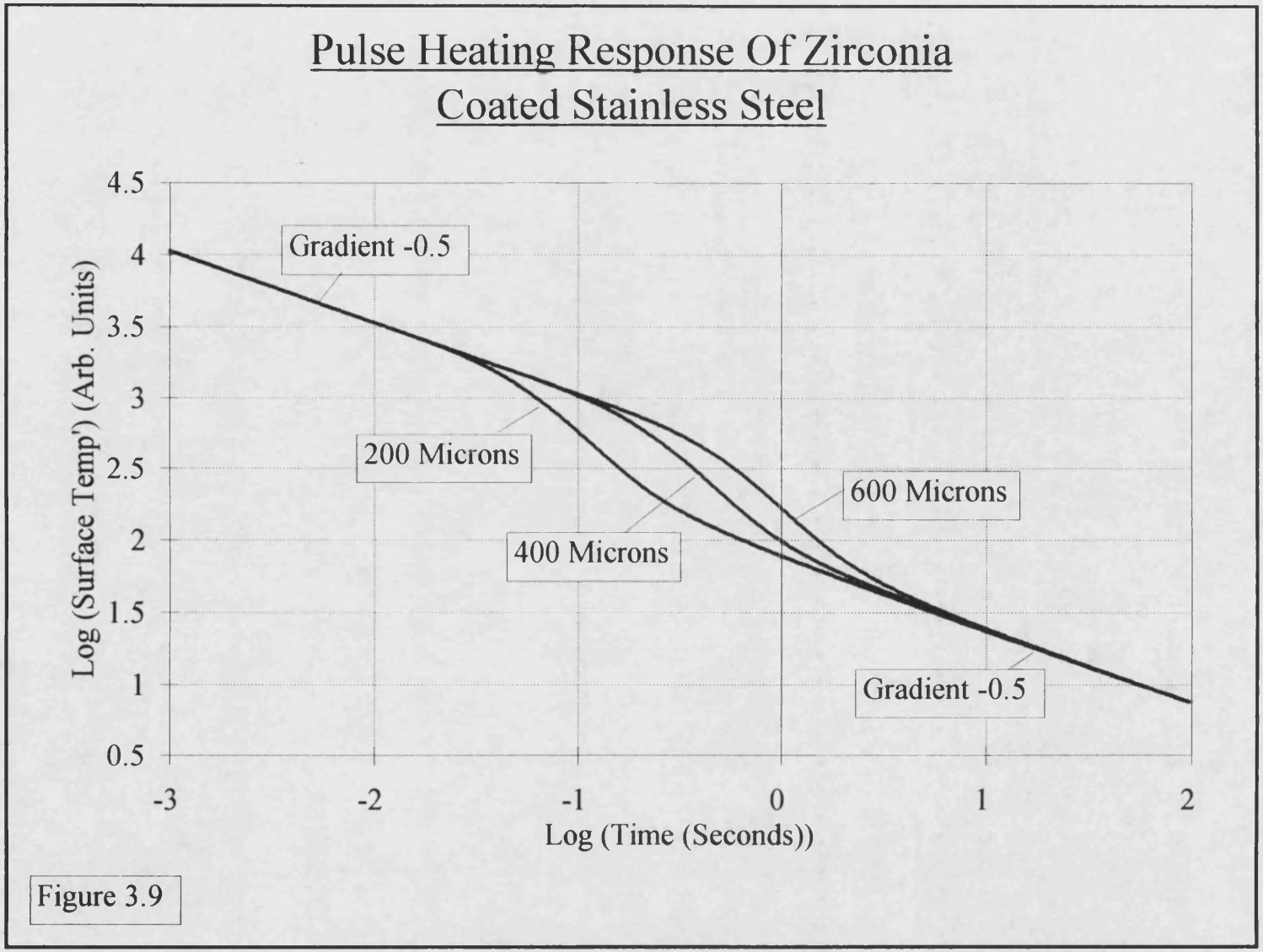
Pulse Heating Response Of Zirconia Coated Stainless Steel
Log (Surface Temp') (Arb. Units)
4.5
4
3.5
3
2.5
2
1.5
1
0.5
-3
-2
-1
0
1
2
Log (Time (Seconds))
Gradient -0.5
200 Microns
400 Microns
600 Microns
Gradient -0.5

Figure 3.9

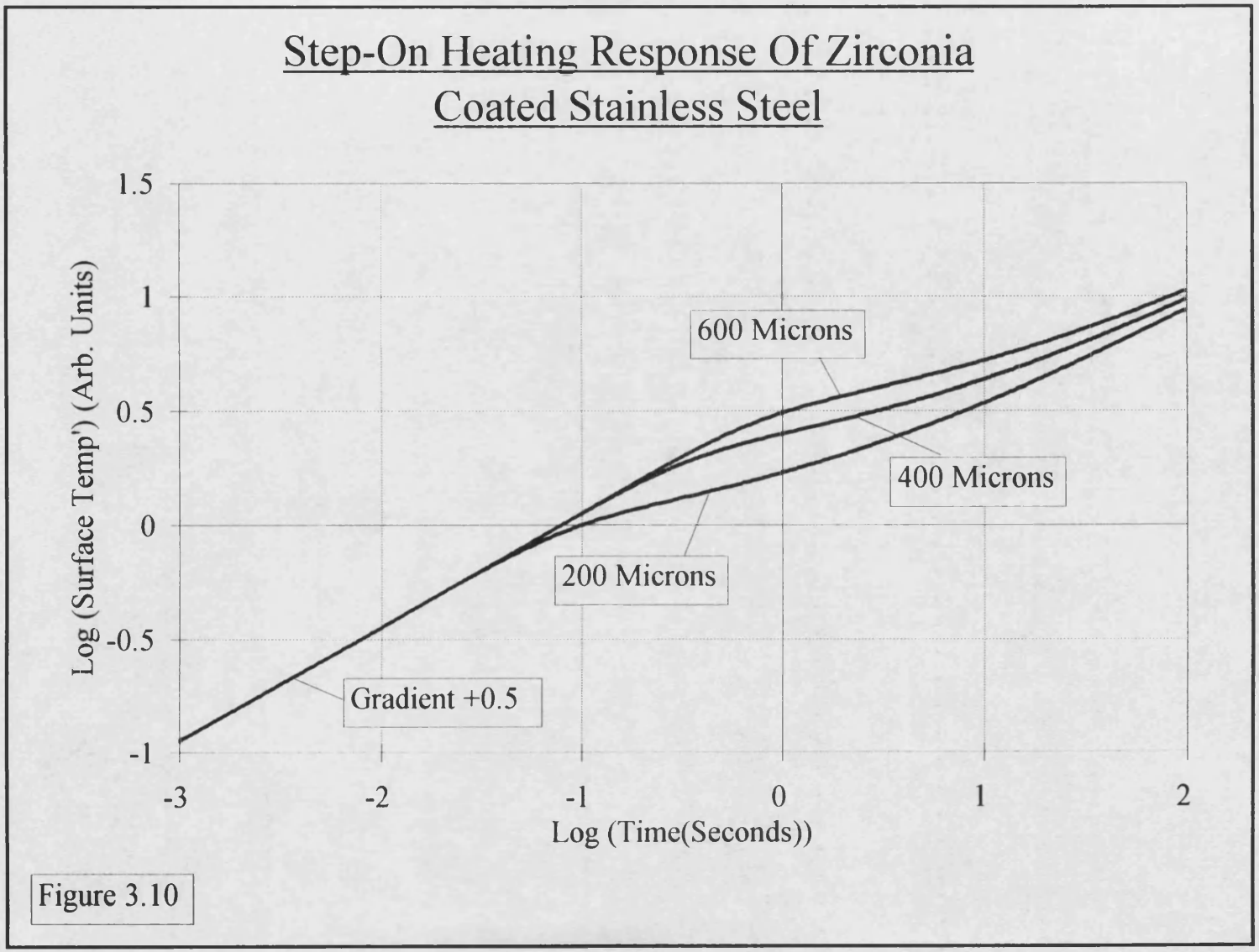
Step-On Heating Response Of Zirconia Coated Stainless Steel
1.5
1
0.5
0
-0.5
-1
Log (Surface Temp') (Arb. Units)
600 Microns
400 Microns
200 Microns
Gradient +0.5
-3
-2
-1
0
1
2
Log (Time(Seconds))

Figure 3.10

Geometry For The Wiener-Hopf Half-Plane Solution

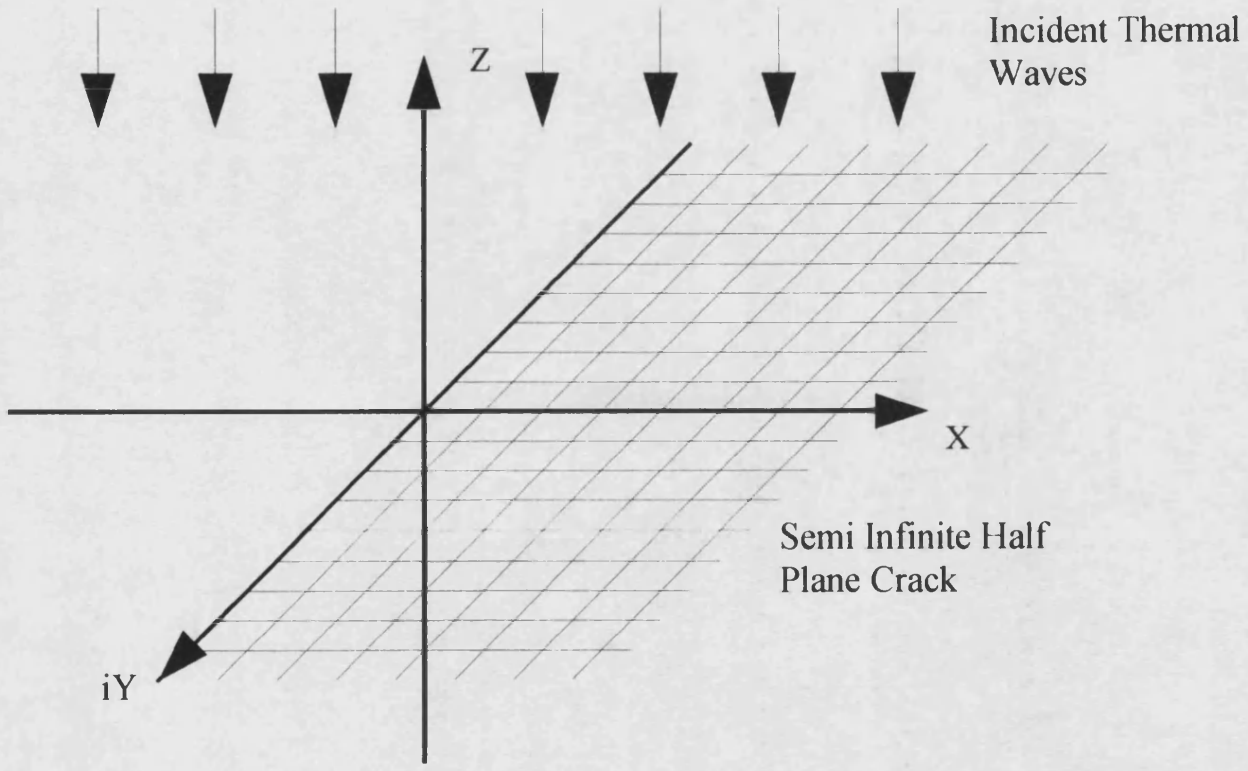

Figure 3.11

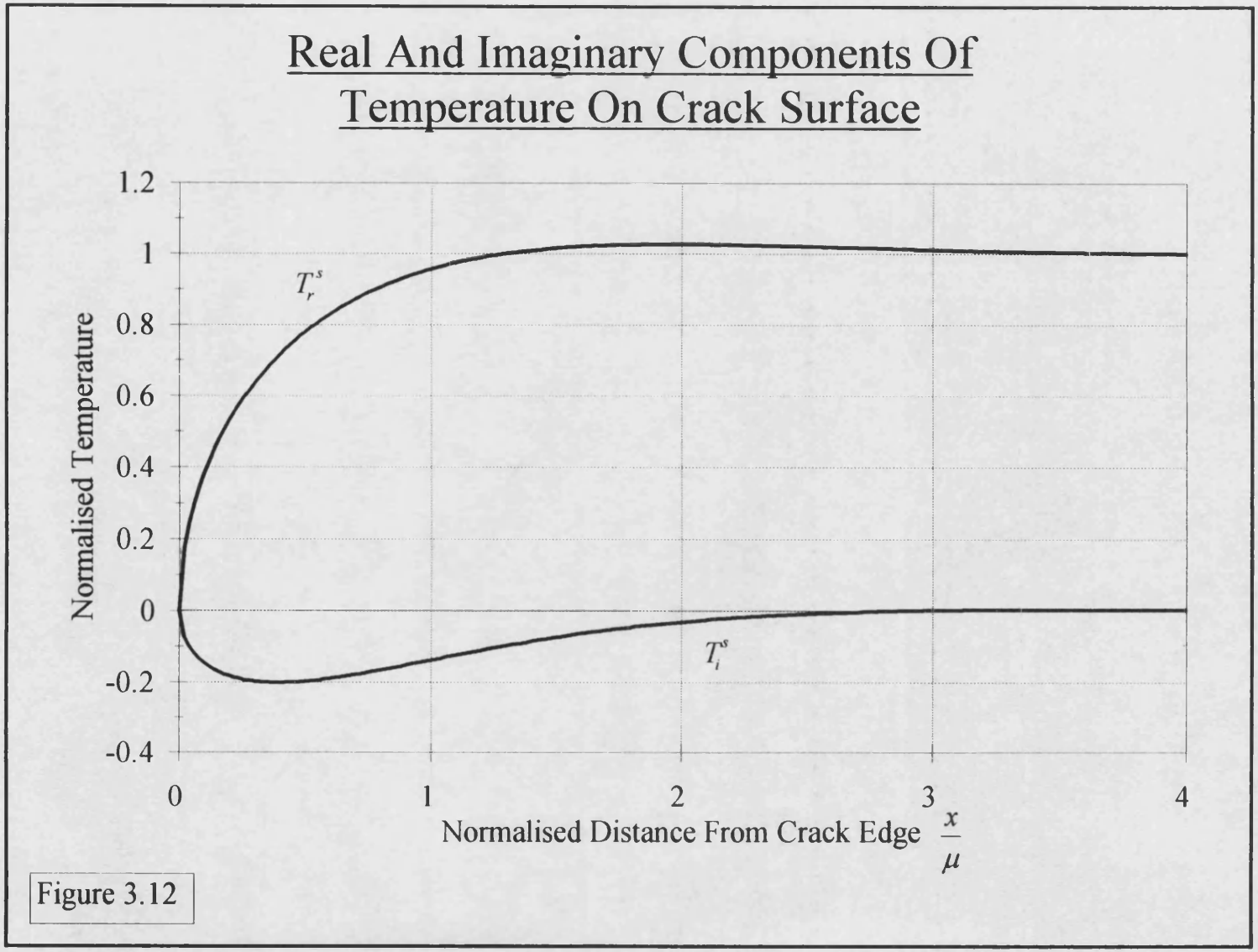
Real And Imaginary Components Of
Temperature On Crack Surface
1.2
1
0.8
0.6
0.4
0.2
0
-0.2
-0.4
Normalised Temperature
T_r^s
T_i^s
0
1
2
3
4
Normalised Distance From Crack Edge $\frac{x}{\mu}$

Figure 3.12

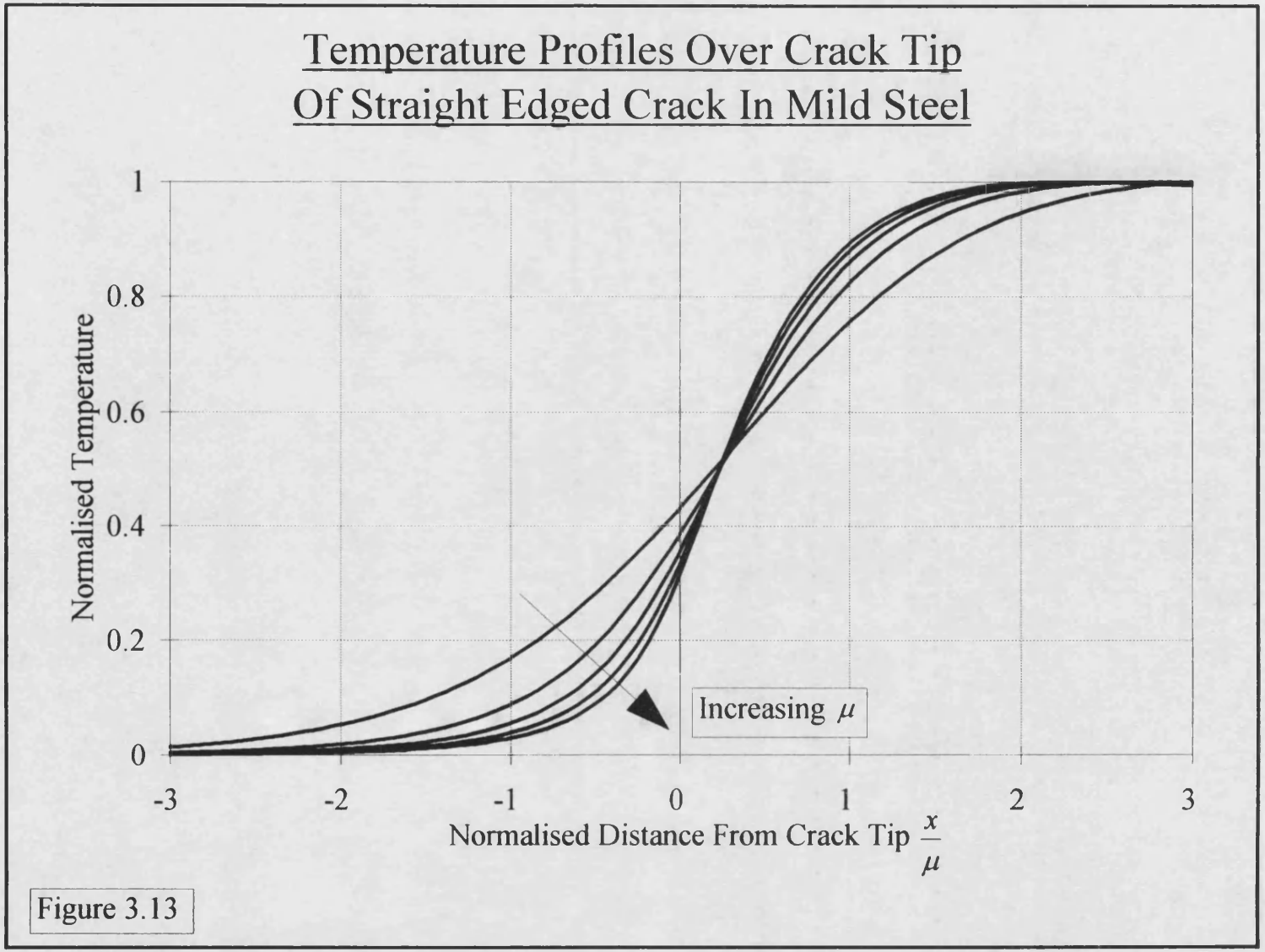
Temperature Profiles Over Crack Tip
Of Straight Edged Crack In Mild Steel
Normalised Temperature
1
0.8
0.6
0.4
0.2
0
-3
-2
-1
0
1
2
3
Increasing μ
Normalised Distance From Crack Tip $\frac{x}{\mu}$

Figure 3.13

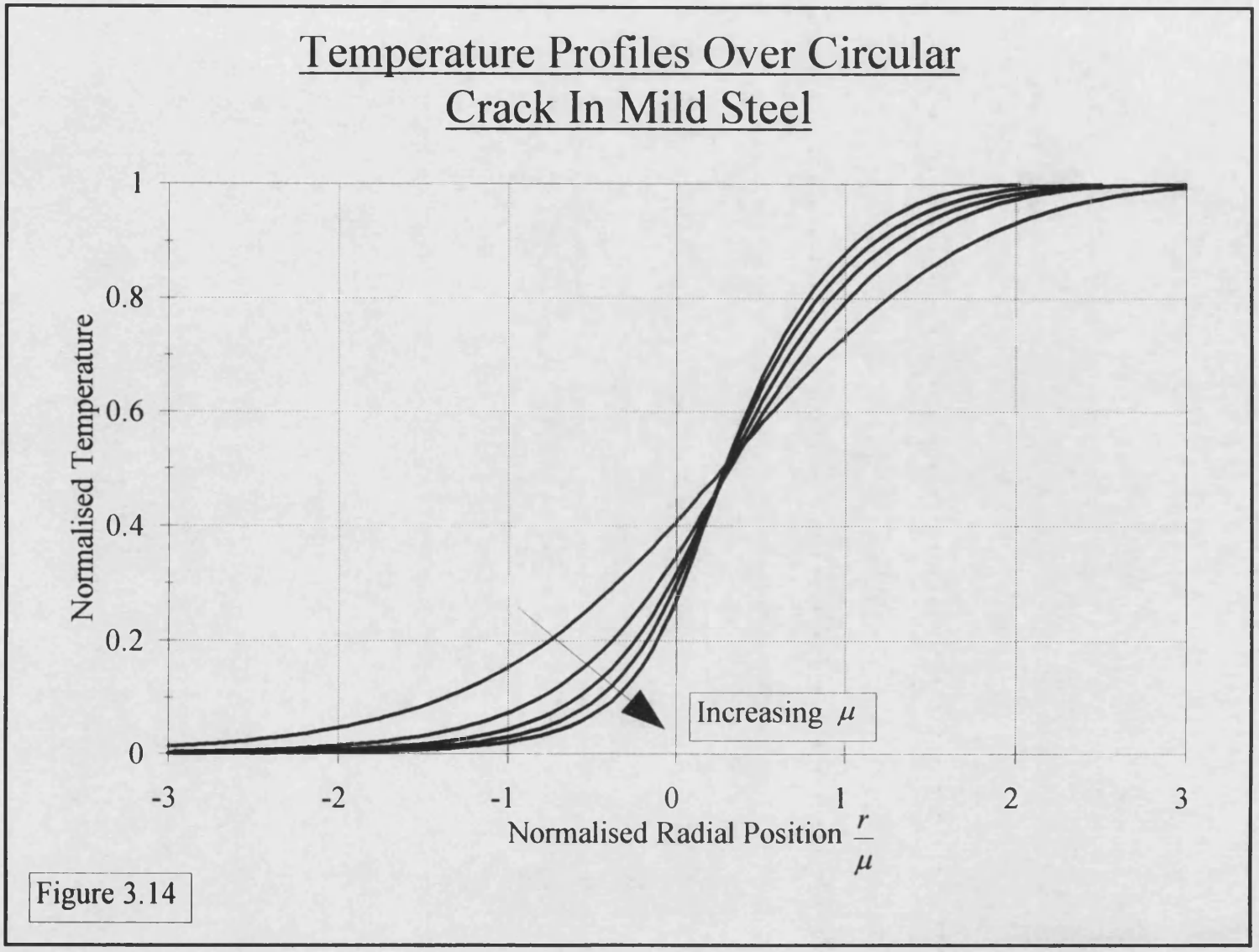
Temperature Profiles Over Circular Crack In Mild Steel
Normalised Temperature
1
0.8
0.6
0.4
0.2
0
-3
-2
-1
0
1
2
3
Normalised Radial Position r/μ
Increasing μ

Figure 3.14

Chapter 4

The Numerical Treatment Of The Diffusion Of Heat In Solids

As can be seen by reference to chapter 3, the analytical solution of heat flow problems with even fairly simple geometries requires the use of heavy-weight mathematical techniques, and often does not result in simple closed form solutions. It was mentioned at the end of the section on the analytical solution of heat flow problems for finite sized defects, that the solutions developed had several important shortcomings to do with the simplifications made in their development. Improving the analytical solutions to overcome the shortcomings was deemed to be extremely difficult and time consuming, and so an alternate route was taken involving the solution of transient heat flow problems using numerical methods. Many researchers in the field of heat flow analysis have resorted to the use of numerical techniques for the solution of their problems, the finite difference method being very widely used due to its simplicity. A simple introduction to the subject of heat transfer calculations using finite differences is given by Croft and Stone [90]. A more complete treatment of the numerical solution of partial differential equations is given by Smith [91].

4.1 The Finite Difference Method

A finite difference solution, in contrast to an analytical solution, does not produce a continuous temperature distribution. Instead, only the temperatures at a set of discrete points, termed lattice points, are calculated. If the temperature at a position between lattice points is required, interpolation can be used.

Consider a 2-D region R overlaid with a Cartesian grid with spacing Δx in the x-direction, and Δy in the y-direction. The points of intersection of the grid provide the lattice points. At each lattice point, energy balance considerations can be used to determine the temperature at that point, in terms of the temperatures at neighbouring points. Once this has been done for every lattice point within the region, a set of simultaneous linear equations are produced. These are then solved to find the temperatures at the lattice points.

The techniques described in this section are for the solution of transient heat flow problems. At the outset (time $t = 0$), the temperature of the body is at a known constant

temperature throughout. A heat flux is then applied to the surface of the body, and it is required to calculate the transient temperature change that takes place within the body due to the applied flux. The solution propagates forward in time from time t to time (t+ Δt) by calculating the temperature at each lattice point at time (t+Δt) in terms of the temperatures at time t.

4.2 Forming Finite Difference Equations Using The Energy Balance Approach

Consider a point P in the interior of a 2-D region, surrounded by neighbouring points N (North), E (East), S (South) and W (West) (see figure 4.1). For simplicity, the spacing between the points in both the x and y directions is taken to be Δ. The temperature at the point P is taken to be representative of the small volume surrounding it. (In less than 3 dimensions, the term volume is still used, the third dimension of the volume is taken to have unit length). This small volume surrounding the point, known as the control cell or control volume, is formed by the series of lines bisecting the lines that connect P to its neighbours.

Consider the rate of energy flow into the control cell over the northern face. This will be given by the flux over the northern face multiplied by the area of the face. From Fourier's law, the flux in the y-direction is given as:

$$Flux_y = -k\frac{\partial T}{\partial y} \tag{4.1}$$

The partial derivative can be approximated as the difference in temperature between points N and P, divided by the distance between the points. That is:

$$\frac{\partial T}{\partial y} \approx \frac{T_P - T_N}{\Delta} \tag{4.2}$$

The area of the face is Δ (Δx1), and so the rate of flow of energy into the control cell over the northern face is given approximately by:

$$Energy_{N\to P} = \frac{k\Delta(T_N - T_P)}{\Delta} \tag{4.3}$$

Notice that if $T_N > T_P$ energy flows into the cell as expected. Approximations for the rates of flow of energy into the cell over the other three faces are derived in the same way, and are given by:

$$Energy_{E\to P} = \frac{k\Delta(T_E - T_P)}{\Delta} \tag{4.4}$$

$$Energy_{S\to P} = \frac{k\Delta(T_S - T_P)}{\Delta} \tag{4.5}$$

$$Energy_{W\to P} = \frac{k\Delta(T_W - T_P)}{\Delta} \tag{4.6}$$

The sum of the right hand sides of equations (4.3), (4.4), (4.5), and (4.6) can be equated to the rate of change of energy within the control cell. This is given by:

$$\rho c V \frac{\Delta T_P}{\Delta t} \tag{4.7}$$

Where:

V is the volume of the control cell, and is equal to Δ^2.

ΔT_P is the change in temperature of the control cell in time Δt.

Expression (4.7) may be approximated by:

$$\rho c \Delta^2 \frac{(T_P' - T_P)}{\Delta t} \tag{4.8}$$

Where:

T_P is the temperature at the point P at time t.

T_P' is the temperature at the point P at time $(t+\Delta t)$.

The full energy balance equation for the control cell surrounding the point P is therefore given by:

$$\frac{k\Delta(T_N - T_P)}{\Delta} + \frac{k\Delta(T_S - T_P)}{\Delta} + \frac{k\Delta(T_E - T_P)}{\Delta} + \frac{k\Delta(T_W - T_P)}{\Delta} = \frac{\rho c \Delta^2 (T_P' - T_P)}{\Delta t} \tag{4.9}$$

Equation (4.9) can be applied to any internal point, but further consideration needs to be given to points on a boundary.

4.3 Dealing With Boundary Nodes

4.3.1 Applied Heat Flux Boundary Condition

Consider a lattice point P on the western boundary of a region that is being heated on its western face with a constant heat flux I_0 (see figure 4.2). Notice that the control cell in this instance has half the volume of the control cell used above. The rate of heat flow into the control cell through the side exposed to the heating is simply given by the product of the applied heat flux with the area. This is given by:

$$Energy_{W\to P} = I_0\Delta \tag{4.10}$$

The energy flow into the control cell from the East has the form given in equation (4.4). The energy flow into the cell from the North and South are half of that given in equations (4.3) and (4.5) since the areas of the northern and southern faces are $\Delta/2$ instead of Δ. The full energy balance equation for the control cell surrounding the point B is given by:

$$I_0\Delta + \frac{k\Delta(T_E - T_P)}{\Delta} + \frac{k\Delta(T_N - T_P)}{2\Delta} + \frac{k\Delta(T_S - T_P)}{2\Delta} = \frac{\rho c\Delta^2(T_P' - T_P)}{2\Delta t} \tag{4.11}$$

4.3.2 Convective Boundary Condition

Consider a lattice point P on the western boundary of a region, the boundary in this case being convective into an atmosphere at ambient temperature T_A, see figure 4.3. The rate of convection at the surface is governed by the surface heat transfer coefficient h. This is the rate of energy transfer through the surface per unit area of the surface, per degree difference in temperature between the surface and the ambient temperature. The rate of energy transfer through the convective western face into the control cell is given by:

$$Energy_{W\to P} = h\Delta(T_A - T_P) \tag{4.12}$$

The rates of energy transfer through the other three faces are as for the applied heat flux boundary condition above. The full energy balance equation for the control cell surrounding the point P is given by:

$$h\Delta(T_A - T_P) + \frac{k\Delta(T_E - T_P)}{\Delta} + \frac{k\Delta(T_N - T_P)}{2\Delta} + \frac{k\Delta(T_S - T_P)}{2\Delta} = \frac{\rho c\Delta^2(T_P' - T_P)}{2\Delta t} \quad (4.13)$$

It should be noted that if I_0 and h are set to 0 in equations (4.11), and (4.13) respectively, the equations are then as required for an insulated boundary.

4.3.3 A Node Above A Boundary Between Two Media

Consider a lattice point P within material A, just above a boundary between materials A and B (figure 4.4). The complication of dealing with this node is that heat will be conducted from the cell centred on S, along a path partly in material B, before entering material A at the boundary. It is therefore necessary to determine an effective thermal conductivity between the lattice points P and S. The simplest way to do this is to use the idea of the thermal resistance of a slab of material.

Thermal Resistance

In the case of steady 1-D flow in a slab of material of thermal conductivity k, and of thickness d, whose surfaces are kept at constant temperatures T_1 and T_2, the constant flux flowing at any point within the slab is given by equation 3.1 as :

$$Flux = \frac{k(T_1 - T_2)}{d} \quad (4.14)$$

By analogy to Ohm's law, which relates the electrical potential (V) and electric current (I) by the electrical resistance (R), a quantity called the thermal resistance R of the slab can be defined by :

$$R = \frac{d}{k} \quad (4.15)$$

Using this, the equation for the flux reduces to :

$$Flux = \frac{(T_1 - T_2)}{R} \qquad \left\{\text{like : } I = \frac{(V_1 - V_2)}{R} \text{ of Ohm's Law}\right\} \quad (4.16)$$

This idea can be applied to a composite wall, consisting of layers of material of different thicknesses, and different thermal conductivitys. Considering the composite

wall shown in figure 4.5, the total resistance of the wall is given by the sum of the resistances of the individual layers of the wall :

$$\text{Total Resistance R} = \sum_i R_i \tag{4.17}$$

Where : $R_i = \frac{d_i}{k_i} =$ the resistance of layer i

and : d_i = the thickness of layer i

k_i = the thermal conductivity of layer i

If the total thickness of the whole wall is D, from a rearrangement of equation 4.15 it is possible to define an effective thermal conductivity of the whole wall by :

$$k_{eff} = \frac{D}{R} \tag{4.18}$$

This can now be applied to the problem of the conduction of heat from lattice point S to lattice point P of figure 4.4. By applying the ideas above, the total thermal resistance between points P and S is given by :

$$R = \frac{\Delta}{2k_A} + \frac{\Delta}{2k_B} \tag{4.19}$$

Using equation 4.18, the effective thermal conductivity between P and S is therefore given by :

$$k_{eff} = \frac{2k_A k_B}{(k_A + k_B)} \tag{4.20}$$

With this expression for the effective thermal conductivity, it is simple to evaluate the rate of energy transfer across the boundary between the two media :

$$Energy_{S \to P} = \frac{k_{eff}\Delta(T_S - T_P)}{\Delta} \tag{4.21}$$

Combining this expression with the usual expressions for the rate of energy transfer from the other directions N, W and E, the full energy balance in the case of a node above a boundary between two media is given by :

$$\frac{k_A\Delta(T_N-T_P)}{\Delta}+\frac{k_{eff}\Delta(T_S-T_P)}{\Delta}+\frac{k_A\Delta(T_E-T_P)}{\Delta}+\frac{k_A\Delta(T_W-T_P)}{\Delta}=\frac{\rho_A c_A\Delta^2(T_P'-T_P)}{\Delta t} \quad (4.22)$$

Where k_{eff} is given by equation 4.20.

A similar expression for a node below a boundary between two media can easily be deduced from this.

Thermal Contact Resistance

An extension of the above is the inclusion of a thermal contact resistance at the boundary between the two media. That is an infinitely thin layer that represents a resistance to the flow of heat over the boundary, but occupies no volume. This is a simple way of simulating very narrow cracks, that does not require the generation of an extremely fine lattice in the region of the crack.

If at the boundary between two media A and B (see figure 4.6), there exists a thermal contact resistance of R_c, the total thermal resistance between P and S is now given by :

$$R=\frac{\Delta}{2k_A}+R_c+\frac{\Delta}{2k_B} \quad (4.23)$$

This gives an effective thermal conductivity between P and S of :

$$k_{eff}=\frac{2\Delta k_A k_B}{(\Delta k_A+2R_c k_A K_B+\Delta k_B)} \quad (4.24)$$

This expression for k_{eff} can be substituted into equation 4.22 to give the energy balance equation for the case of a node above a boundary between two media, with the inclusion of a thermal contact resistance at the boundary.

4.4 Finite Difference Techniques

In this section, four techniques of applying the finite difference method are discussed. So far it has not been stated at which time step, t or (t+Δt), the rates of flow of energy through the faces of the control cell should be evaluated. It is in this respect that the four techniques differ.

4.4.1 The Explicit Technique

The explicit technique is by far the simplest to apply. The rates of flow of energy through the faces of the control cell are evaluated at time t (at which time the temperatures at every lattice point are already known). Equation (4.9) therefore becomes:

$$\frac{k\Delta(T_N - T_P)}{\Delta} + \frac{k\Delta(T_S - T_P)}{\Delta} + \frac{k\Delta(T_E - T_P)}{\Delta} + \frac{k\Delta(T_W - T_P)}{\Delta} = \frac{\rho c\Delta^2(T_P' - T_P)}{\Delta t} \qquad (4.25)$$

Unprimed temperatures are evaluated at time t, and primed temperatures are evaluated at time (t+Δt). Equation (4.25) has only one unknown, that being T_P', the temperature at lattice point P at time (t+Δt). The equation can therefore be rearranged to give T_P' directly in terms of known temperatures. To propagate the solution forward by a time step Δt, it is only necessary to evaluate such an equation for each lattice point.

There are however problems with the stability of the technique. The technique is only stable for restricted values of the lattice point spacing Δ, and the time step Δt. If a dense set of lattice points are required, it is found that the time steps needed to make the calculation stable are extremely small. It therefore takes a great many time steps to propagate the solution forward a reasonable period of time.

4.4.2 The Implicit Technique

In the implicit technique, the rates of flow of energy through the faces of the control cell are evaluated at time (t+Δt) (at which time the temperatures at the lattice points are unknown). Equation (4.9) therefore becomes:

$$\frac{k\Delta(T_N' - T_P')}{\Delta} + \frac{k\Delta(T_S' - T_P')}{\Delta} + \frac{k\Delta(T_E' - T_P')}{\Delta} + \frac{k\Delta(T_W' - T_P')}{\Delta} = \frac{\rho c\Delta^2(T_P' - T_P)}{\Delta t} \qquad (4.26)$$

In this case, there are many unknowns in the finite difference equation for each lattice point. This means that a set of highly interlinked simultaneous equations is formed. The solution can only propagated forward from time t, to time (t+Δt) by the solution of such a set. The implicit technique has the advantage of being stable for any selection of the grid spacing Δ, and the time increment Δt, but the computational power required to solve such sets of simultaneous equations limits its application.

4.4.3 The Crank-Nicolson Technique

Consider the rates of flow of energy into the control cell being evaluated as a weighted average of the rates at time t and time (t+Δt). For the case of energy flow through the northern face of the cell, equation 4.3 is replaced with:

$$(1-\lambda)\frac{k\Delta(T_N - T_P)}{\Delta} + \lambda\frac{k\Delta(T_N' - T_P')}{\Delta} \tag{4.27}$$

Where:

λ is between 0 and 1.

If the same is done for the energy flow through the other 3 faces, the full energy balance equation becomes:

$$\begin{aligned}&(1-\lambda)\left\{\frac{k\Delta(T_N - T_P)}{\Delta} + \frac{k\Delta(T_S - T_P)}{\Delta} + \frac{k\Delta(T_E - T_P)}{\Delta} + \frac{k\Delta(T_W - T_P)}{\Delta}\right\}\\ &+\lambda\left\{\frac{k\Delta(T_N' - T_P')}{\Delta} + \frac{k\Delta(T_S' - T_P')}{\Delta} + \frac{k\Delta(T_E' - T_P')}{\Delta} + \frac{k\Delta(T_W' - T_P')}{\Delta}\right\}\\ &= \frac{\rho c\Delta^2(T_P' - T_P)}{\Delta t}\end{aligned} \tag{4.28}$$

If equation (4.28) is evaluated for λ=0, the explicit equation (4.25) is derived; for λ=1, the implicit equation (4.26) is derived. If equation (4.28) is evaluated for λ=0.5, the Crank-Nicolson [92] equation is derived. This, like the fully implicit equation, has the advantage of being stable for any selection of grid spacing Δ, and time step Δt, but once again the solution can only propagate forward each time step by the solution of a set of highly interlinked simultaneous equations.

If the Crank-Nicolson or fully implicit methods are applied to a 1-D heat flow problem, a set tri-diagonal equations are formed at each step. These equations have the form:

$$\begin{bmatrix} D_1 & A_1 & & & \\ B_2 & D_2 & A_2 & & \\ & B_3 & D_3 & A_3 & \\ & & \vdots & \vdots & \\ & & & B_n & D_n \end{bmatrix}\begin{bmatrix} T_1 \\ T_2 \\ T_3 \\ \vdots \\ T_n \end{bmatrix} = \begin{bmatrix} C_1 \\ C_2 \\ C_3 \\ \vdots \\ C_n \end{bmatrix} \tag{4.29}$$

Where:

The D_i's are the diagonal terms.

The B_i's are the below diagonal terms.
The A_i's are the above diagonal terms.

The solution of such a set can be calculated simply, and to a good accuracy, by using a direct elimination method known as the tri-diagonal matrix algorithm [90]. In more than 1-D, the equations are no longer tri-diagonal, and the solution must be tackled by another method. Matrix inversion, or the use of Cramer's determinant may be used, but these methods are extremely time consuming. The preferred method is by an iterative technique such as Jacobi or Gauss-Seidel iteration. These iterative techniques are also time consuming, and shall not be discussed here as they have not been used in this research.

4.4.4 The Alternating Direction Implicit (ADI) Technique

The ADI technique [93] takes a rather different approach to propagating the solution forward in time. Instead of moving forward a complete time step Δt in one go, the step is split into two equal steps of $\Delta t/2$. The equations used for the first half step have implicit type expressions for the rate of flow of energy into the control cell in the x direction (from East and West), and explicit type expressions for the rate of flow in the y direction (North and South):

$$\frac{k\Delta(T_N - T_P)}{\Delta} + \frac{k\Delta(T_S - T_P)}{\Delta} + \frac{k\Delta(T_E' - T_P')}{\Delta} + \frac{k\Delta(T_W' - T_P')}{\Delta} = \frac{\rho c\Delta^2(T_P' - T_P)}{\Delta t/2} \qquad (4.30)$$

A set of tri-diagonal equations are produced which are solved to propagate the solution forward by $\Delta t/2$. The second half time step is then evaluated using explicit expressions in the x direction and implicit in the y direction:

$$\frac{k\Delta(T_N' - T_P')}{\Delta} + \frac{k\Delta(T_S' - T_P')}{\Delta} + \frac{k\Delta(T_E - T_P)}{\Delta} + \frac{k\Delta(T_W - T_P)}{\Delta} = \frac{\rho c\Delta^2(T_P' - T_P)}{\Delta t/2} \qquad (4.31)$$

In this way, the solution of a 2 dimensional problem propagates forward a full time step Δt by the solution of 2 sets of tri-diagonal matrices, rather than the solution of a more complex interlinked set of simultaneous equations as would be produced using the fully implicit or Crank-Nicolson techniques. Due to the simple nature of the solution of tri-diagonal sets of equations, this is found to be computationally efficient. The ADI technique is stable for any values of Δ and Δt so long as the direction of implicit terms is alternated each half time step.

All of the equations so far have been derived for simplicity using a Cartesian grid of lattice points. It should be noted that the techniques can be used for any set of lattice points, characterised by any form of co-ordinate system.

4.5 Finite Difference Models

Several models have been written as part of this project, but as the latest model is able to simulate all the conditions dealt with by the earlier models, only the latest model will be discussed.

A model using the alternating direction implicit (ADI) method was written to simulate the conductive heat flow through a sample containing a circular crack-like defect (radiation and convection across the crack were not modelled). The thermo-physical properties of the material in which the crack was embedded were assumed to be isotropic and homogeneous. The plane containing the crack was parallel to the upper surface of the sample. Due to the axi-symmetric nature of the problem, by using the cylindrical polar co-ordinate system, it was possible to reduce the model to 2 dimensions by modelling a single radius. The applied heating was assumed to be absorbed at the upper surface with 100% efficiency. Convective heat losses from the upper and lower surfaces of the sample have been included. The ADI technique was chosen, as the sets of simultaneous equations that result are tri-diagonal, and therefore quick and easy to solve (see section 4.4.4). The crack-like defect was modelled as a thermal contact resistance between two layers of nodes.

Figure 4.7 shows a schematic of the lattice structure of the model. Three different sets of thermal properties (A, B and C) can be used, in the positions shown in the figure. The contact resistance extends in radius from the axis to the boundary between materials B and C. With this set-up it is possible to model several scenarios of interest :

1. With the thermal properties of A, B and C all set equal, and a finite value for the contact resistance, a homogeneous sample containing a circular crack defect can be simulated.

2. With the thermal properties of materials A and B set equal, and the properties of material C set to those for air, it is possible to simulate a sample with a back drilled hole. (The thermal contact resistance should be set to zero in this case).

3. With the thermal properties of material A set to those for a coating material, and those of B and C set to a substrate material, it is possible to simulate a coating on a substrate. With a non zero value for the contact resistance, it is possible to simulate a circular crack/delamination defect between the coating and substrate. (A different z-axis nodal spacing is used in the region of material A, to allow for the modelling of very thin coatings without using such a small z-axis spacing for the whole model).

The model has been designed to simulate both Dirac delta pulse, and finite duration heating pulses applied to the upper surface of a sample. In the case of Dirac pulse heating, the solution of the thermal diffusion equation is simply the time derivative of the solution for step-on heating (see section 3.1.2 on the related solutions of the thermal diffusion equation). Using this approach, the temperature distribution is first calculated with heat being applied at a constant rate from time t=0, and then differentiated numerically with respect to time to calculate the pulse response.

Model Validation

Validation of the numerical model has been undertaken in three ways. Firstly, simulations have been made of problems for which a simple analytical solution exists, and results compared with these solutions. Secondly, comparison has been made with results generated using another finite difference code, developed completely independently by J.-C. Krapez [62]. Thirdly, comparison has been made between experimental and simulation results (see chapter 6).

Modelling Language, Platform And Compiler

FORTRAN 77 was used to code the model, using Microsoft Powerstation FORTRAN version 1.0. The Powerstation compiler is a 32-bit IBM compatible PC compiler, enabling full advantage to be taken of the 32-bit architecture of the later PCs. A typical calculation using a grid of 150 by 100 nodes, and 1000 time steps, takes approximately 5 minutes to execute on a 486 DX2/66 machine. The code was also ported to Silicon Graphics (UNIX) workstations of my sponsor, TWI. These were used for the generation of computer animations of heat flow through samples with crack defects and back drilled holes.

Appendix A contains a source code listing of the model, and the format of the control file used to run the model.

Control Cell For An Internal Node In A 2-D Cartesian Lattice

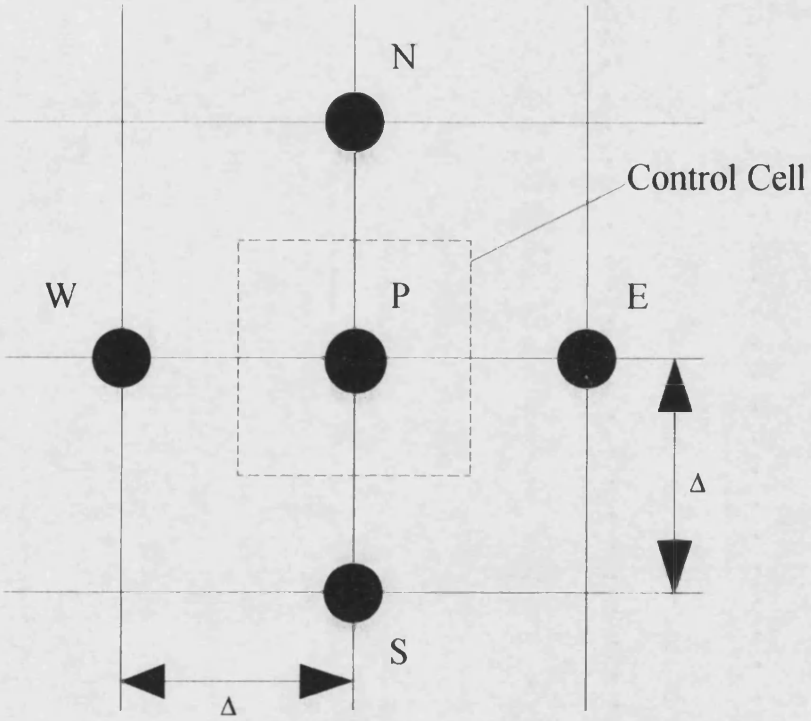

Figure 4.1

Control Cell For The Applied Heat Flux Boundary Condition

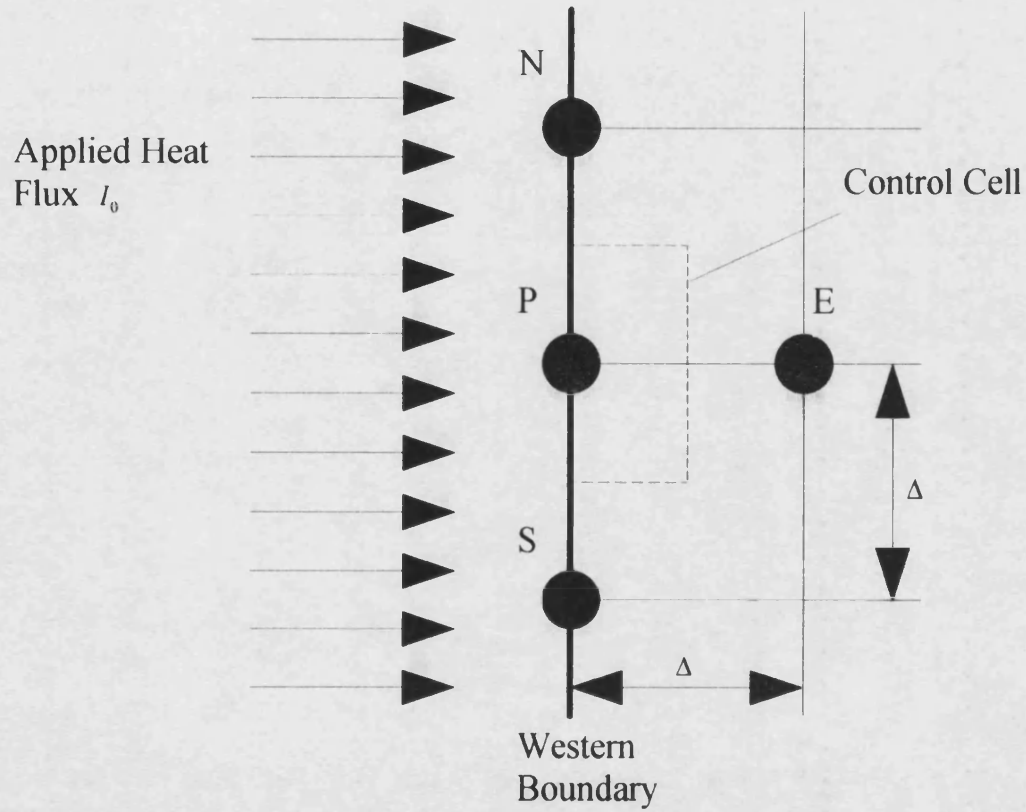

Figure 4.2

Control Cell For The Convective Boundary Condition

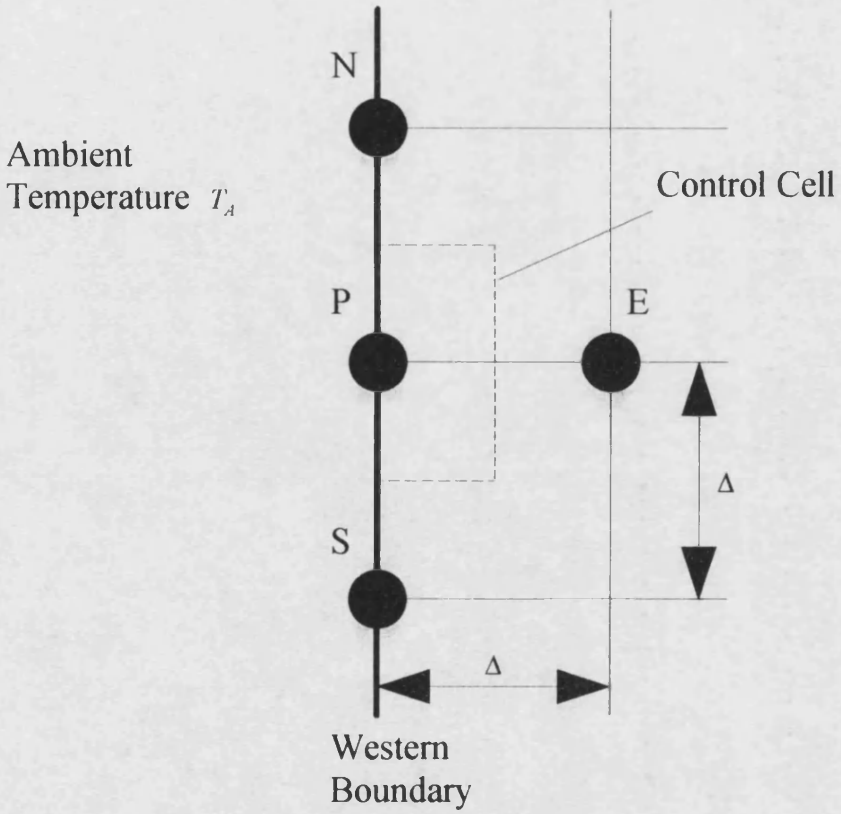

Figure 4.3

Control Cell For A Node Above A Boundary Between 2 Media

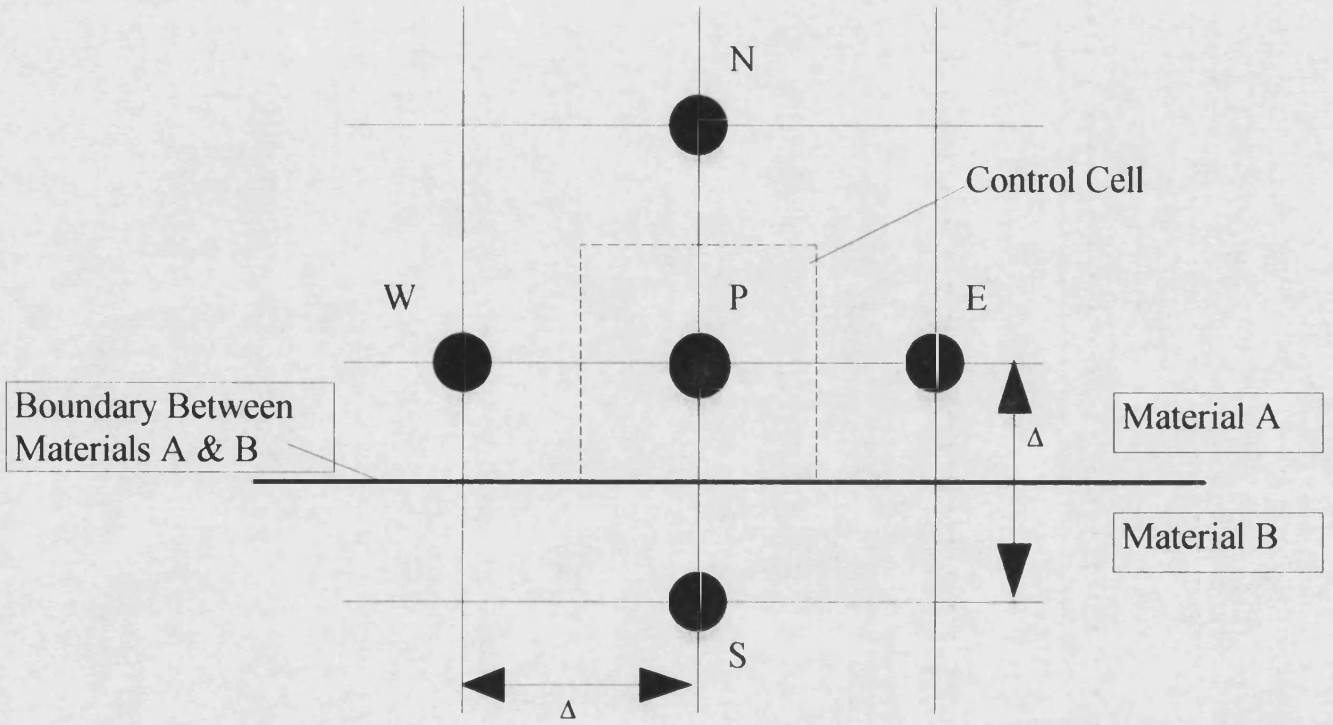

Figure 4.4

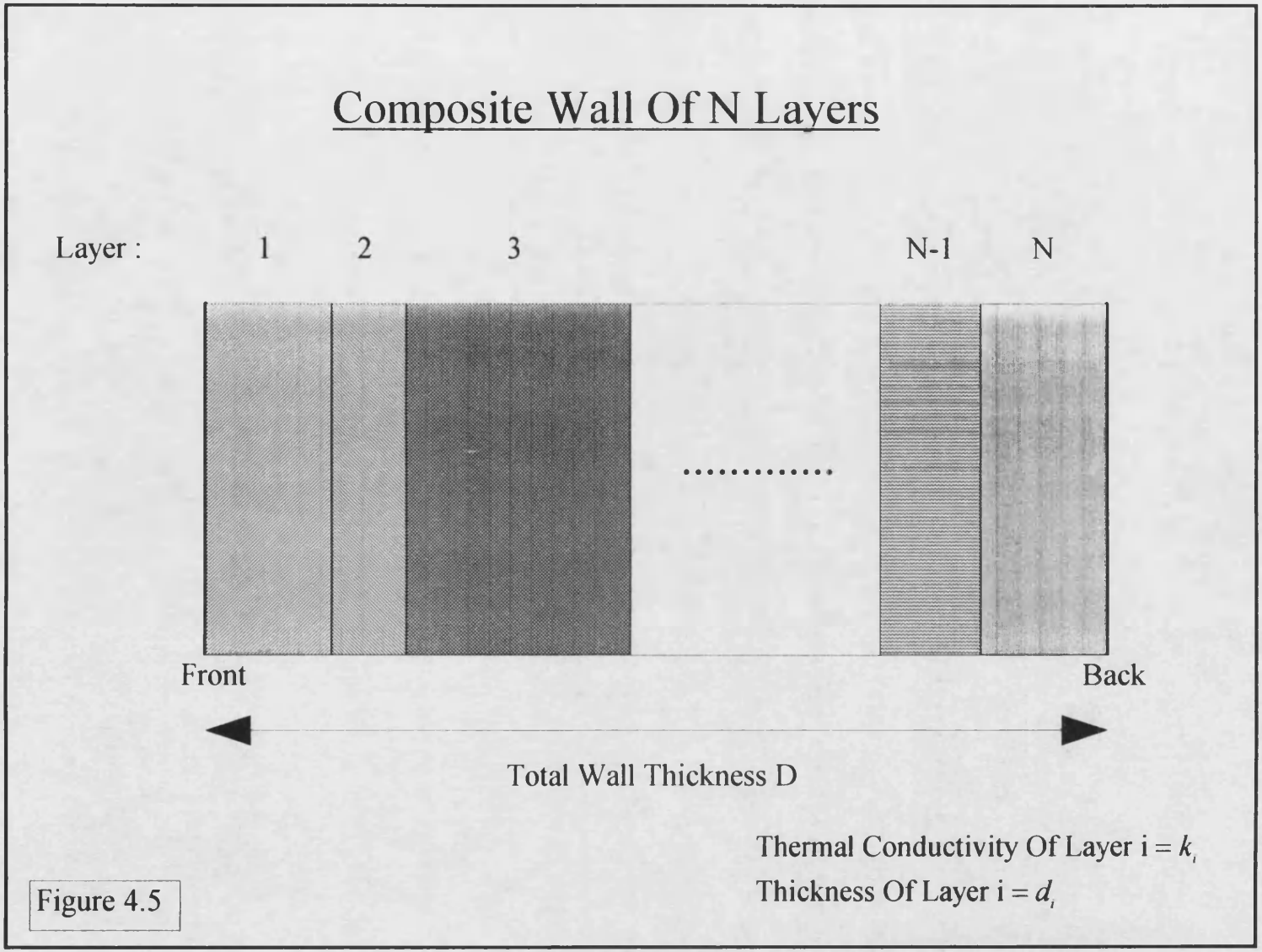
Composite Wall Of N Layers
Layer :
1
2
3
N-1
N
Front
Back
Total Wall Thickness D
Thermal Conductivity Of Layer i = k_i
Thickness Of Layer i = d_i

Figure 4.5

Control Cell For A Node Above A Boundary Between 2 Media With The Inclusion Of A Contact Resistance

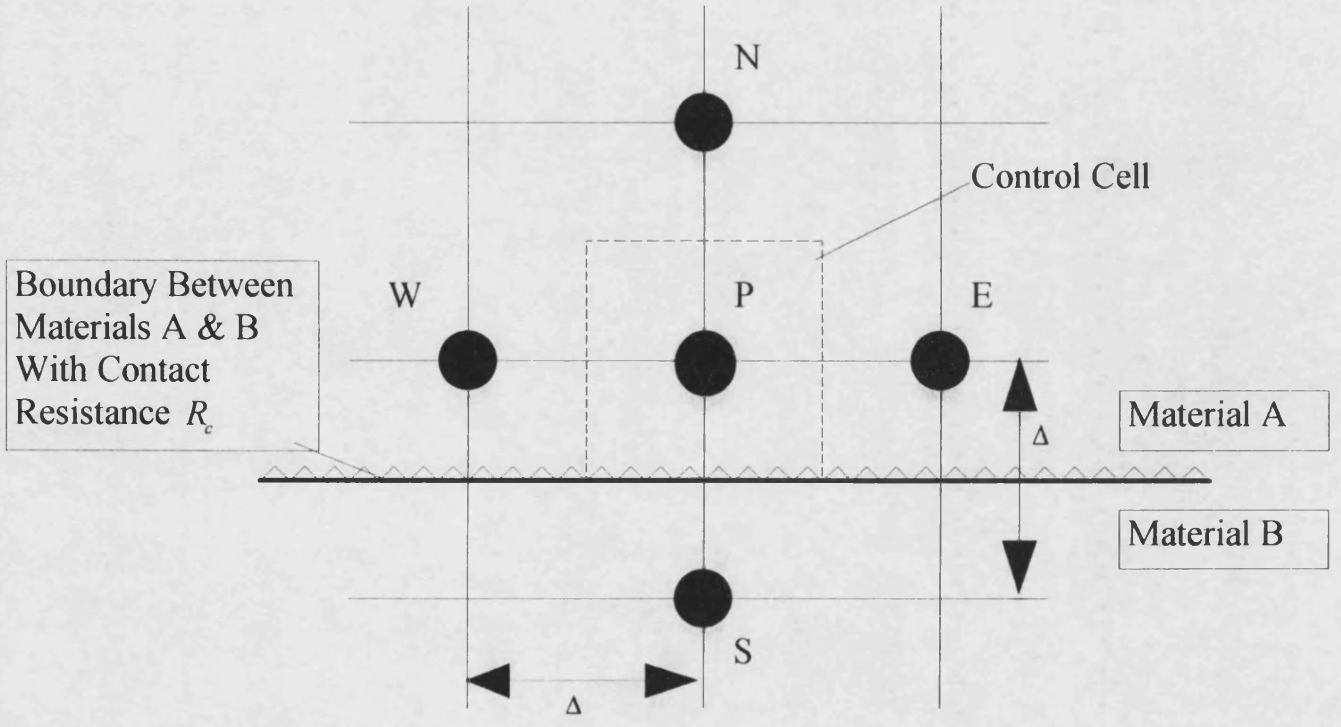

Figure 4.6

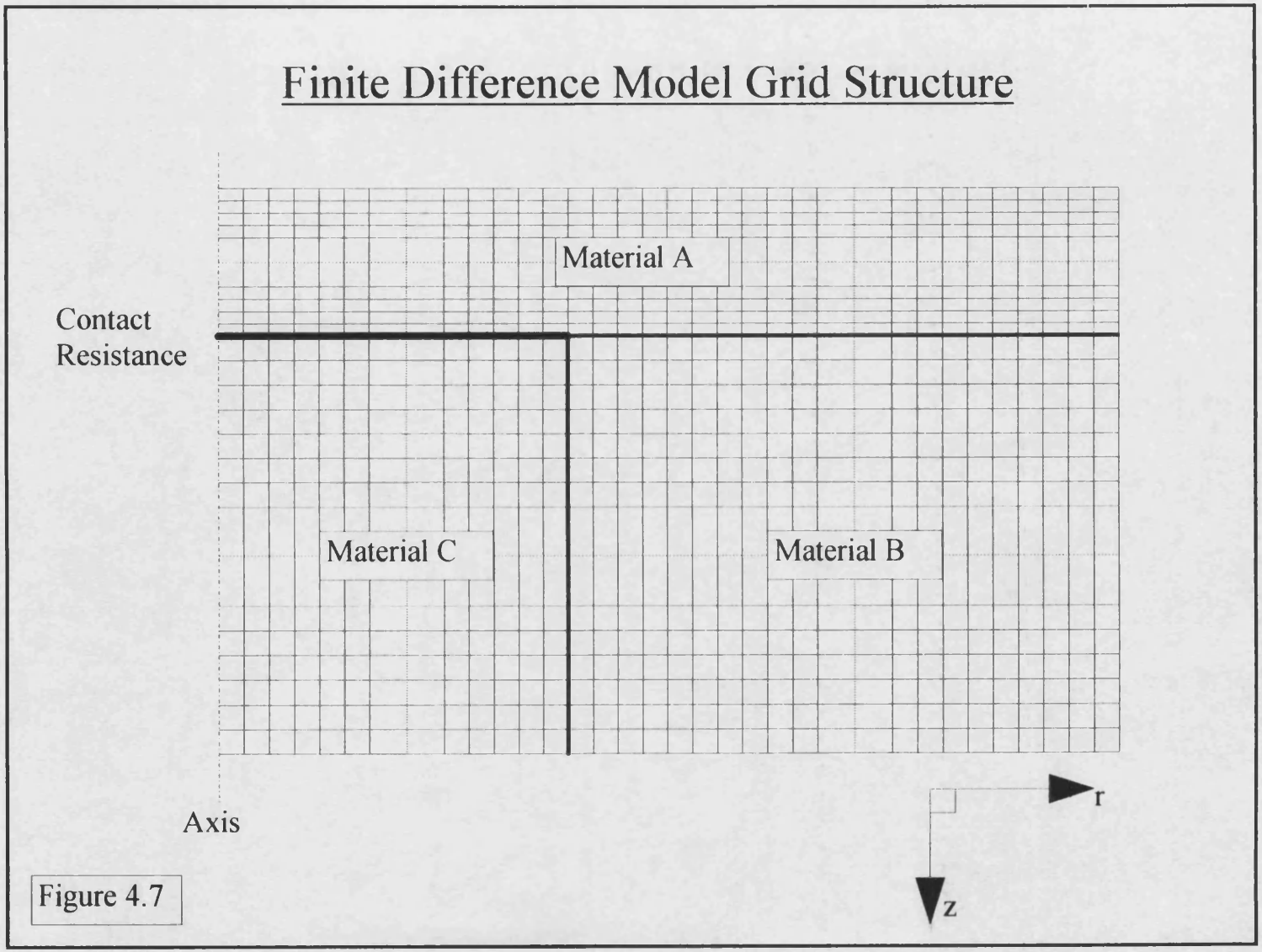
Finite Difference Model Grid Structure
Material A
Contact
Resistance
Material C
Material B
Axis
r
z

Figure 4.7

Chapter 5

Experimental Equipment, Procedures And Samples

Before discussing in detail the experimental equipment and procedures used for the testing of the samples, it is necessary to give an overview of the emission, transmission and detection of infrared radiation.

5.1 Emission Of Infrared (IR) Radiation

Infrared radiation is emitted constantly by all objects. The amount and wavelength dependence of the emitted radiation depends upon the spectral emissivity $\varepsilon(\lambda)$ of the object, and on its temperature T. For a black body emitter ($\varepsilon(\lambda)=1 \ \forall \ \lambda$), that is an emitter that radiates the maximum amount of energy for a given temperature, the radiance at a given temperature T, at a given wavelength λ, is given by Planck's radiation function [94]:

$$W(T,\lambda) = \frac{2\pi hc^2}{\lambda^5}\left\{\frac{1}{e^{\left(\frac{hc}{\lambda kT}\right)}-1}\right\} \text{ W cm}^{-2}\ \mu\text{m}^{-1} \qquad (5.1)$$

Where :

h = Planck's Constant ($6.62559\text{x}10^{-34}$ J s)
c = Velocity Of Light ($2.997925\text{x}10^{10}$ cm s^{-1}) (Values taken from [95])
k = Boltzmann's Constant ($1.38054\text{x}10^{-23}$ J K^{-1})

Figure 5.1 shows a plot of this function against wavelength λ for an object at temperatures around ambient room temperature (300K). The maximum radiance is seen to be in the 8-13 μm range. In a photothermal experiment, it is necessary to detect changes in the emitted radiation caused by changes in the object's temperature. It is therefore necessary to look at the change of Planck's radiation function with temperature, i.e. $\partial W(\lambda,T)/\partial T$:

$$\frac{\partial W(\lambda,T)}{\partial T} = \frac{2\pi h^2 c^3}{\lambda^6 kT^2} e^{\left(\frac{hc}{\lambda kT}\right)}\left\{\frac{1}{e^{\left(\frac{hc}{\lambda kT}\right)}-1}\right\}^2 \text{ W cm}^{-2}\ \mu\text{m}^{-1}\ \text{K}^{-1} \qquad (5.2)$$

Figure 5.2 shows a plot of equation 5.2, the maximum change in the radiation emitted, per degree change in temperature around ambient, lies in the 8-10 μm range. For the experiments it will therefore be necessary to use an infra-red detector that operates in this wavelength band.

5.2 Atmospheric Transmission Of Infrared Radiation

Before it is possible to measure the emitted radiation, it must travel through the atmosphere to the detector. On its path to the detector, the radiation is attenuated by scattering and absorption processes. In the infrared region of the radiation spectrum, the most important attenuation process is the absorption of the radiation by gas molecules. Of the gases in the atmosphere, carbon dioxide and water vapour are the two most important contributors to this absorption. Water vapour absorbs infrared radiation in a band between 5-8 μm, and carbon dioxide absorbs radiation of wavelengths greater than approximately 13 μm, and of less than 3 μm. This restricts the transmission of infrared radiation to two bands : 3-5 μm, and 8-13 μm. From above it is noted that the 8-13 μm band offers greater sensitivity to changes in temperature around ambient, and is the preferred band to work with.

5.3 Detection Of Infrared Radiation - The Pyroelectric Detector

The basic requirement for an infrared detector is that it should be made from a material which exhibits a temperature dependent property. This property might be its electrical resistance (bolometer), optical properties (some liquid crystals), or in the case of pyroelectric detectors, its electrical polarisation. Absorption of infrared radiation causes the pyroelectric material to heat up, changing its electrical polarisation, and causing an external electric field which can be measured as a voltage across the material. This type of detector can only be used for the measurement of changing temperatures as the resulting external electrical field is soon neutralised by the movement of electrons to counterbalance the field. Materials used for pyroelectric detectors include triglycine sulphate (TGS), lithium tantalate (LT) and ceramic lead zirconate titanate (PZT).

5.4 The Single-Sided CW-PTR Technique

The equipment required for the CW-PTR technique consists of six essential components:

(1) A Laser heat source.
(2) An IR Detector.
(3) A Laser beam modulator.
(4) A lock-in amplifier.
(5) A scanning sample mount.
(6) A controlling computer.

Figure 5.3 shows a schematic diagram of the equipment. The use of each component is discussed below.

5.4.1 Laser Heat Source

A Laser is used to deposit energy on the surface of the sample under investigation. A bench mounted Coherent Innova 90 Argon-Ion laser was used, operating in the visible region of the spectrum, tuneable between 488-514nm (bright green). The laser produces a beam with a $1/e^2$ diameter of approximately 1.3 mm at the usual working distance (approximately 1 metre), equivalent to a beam divergence of 0.005 radians. The power output from the Argon-Ion laser can be in excess of four watts, so extreme care must be taken when using it. The equipment is arranged so that the sample, detector and laser head are enclosed within a light tight cabinet. When setting up the experiment it is necessary to have the cabinet open, and so goggles are worn to protect the eyes. The goggles attenuate the laser radiation by a factor of 10^{13}, making it safe to work near the beam, even so, it is important not to look directly into the beam. Care must also be taken to avoid placing any part of the body (e.g. hands) into the path of the beam, so as to avoid burns.

5.4.2 IR Detector

The IR detector is used to detect the IR radiation given off at the surface of the sample. A highly sensitive Mullard 825CPY [96] triglycine sulphate (TGS) detector has been used for the experiments, the operation of which depends upon the pyroelectric effect discussed above. This detector has a fairly flat modulation frequency response between 1-30 Hz, and so is suitable for this application. The detector has a 2x2 mm element,

positioned behind a bloomed germanium window. The window is used to transmit radiation in the infrared region, but to block out any visible laser radiation reflected from the sample surface. An ellipsoidal collector is often used in conjunction with the TGS detector to improve performance.

5.4.3 Laser Beam Modulator

The laser beam modulator is used to modulate the laser beam at the required frequency. The beam is modulated by a sectored blade mechanical chopper, producing square wave modulation. Typical modulation frequencies for this application range from around 2 Hz to 30 Hz.

5.4.4 Lock-In Amplifier

The lock-in amplifier is used to demodulate the signal from the IR detector. The lock-in amplifier has two inputs, a reference signal from the beam modulator, supplying the frequency at which the laser beam is modulated, and the signal from the IR detector. The lock-in detects the component of the detector signal that has the same frequency as the reference, and outputs the amplitude and phase of that component to the controlling computer over an IEEE 488 interface. The phase of the component is measured with respect to the reference input. An EG&G 5210 lock-in amplifier was used.

5.4.5 Scanning Sample Mount

The scanning sample mount is used to move the sample through the stationary modulated laser beam. The mount receives instructions over the IEEE 488 interface from the controlling computer, and can move horizontally and vertically with high precision.

5.4.6 Controlling Computer

The computer controls the experiment. It is fitted with an IEEE 488 interface card which enables communication with the scanning sample mount, and the lock-in amplifier. Phase and signal values are read from the lock-in, and can be plotted to the computer screen, and saved to floppy disk for later analysis. The CW-PTR system, and the software to control the experiment, was initially developed by a former student Pravin Patel [97].

Testing Procedure

The sample to be tested is mounted on the scanning sample mount. The modulation frequency to be used for the scan is set on the mechanical chopper, and is confirmed by checking the frequency of the reference signal input into the lock-in amplifier. With goggles on, the laser is powered up, and the sample positioned at the starting point for the scan by driving the sample mount via the computer. The light tight box surrounding the sample and laser head can then be closed, and goggles removed. The length of scan, resolution (points per mm) and dwell time at each point are then entered into the computer, and the scan commences. When the scan is complete, the data is saved to disk for later analysis. Before opening the light tight box to switch the laser off and remove the sample, goggles must be put back on.

5.5 Pulsed Video Thermography (PVT)

The PVT equipment used for this work consisted of the following components :

(1) An IR camera.
(2) A camera/computer interface.
(3) A computer with a frame grabber board to store data from the camera.
(4) Heat sources and guillotines.
(5) A heat source/timer interface.
(6) A computer to control the time of heating, and to start data acquisition.

Figure 5.4 shows a schematic diagram of the PVT equipment, each item is discussed below.

5.5.1 IR Camera

The IR camera was a Thermovision 750 manufactured by Agema Infrared Systems. The camera has an Indium Antimonide detector, sensitive to IR wavelengths between 2-5.6 microns, and is cooled by liquid nitrogen. The camera has a field rate of 25 Hz, with four fields being interlaced to produce a complete frame at a rate of 6.25 Hz. Care must be taken when handling liquid nitrogen, with gloves and goggles being worn to prevent burns and splashes into the eye.

5.5.2 Camera/Computer Interface

The camera was connected via an interface box to a PC. The interface was used to strip out the frame sync pulses from the raw video data from the camera, and to feed these to the frame grabber board to allow it to synchronise itself to the incoming video data. The interface also fed the raw video signal into another input on the frame grabber board.

5.5.3 Thermal Computer

The computer was a 486DX2/66 IBM compatible PC. This was fitted with a 3Mb frame grabber board, capable of storing up to a maximum of 24 frames of data (approximately 3.84 seconds of data when storing every frame from the camera). By storing only every N^{th} frame, it was possible to collect data over a longer period (approximately 3.84xN seconds), but with obviously lower time scale resolution. Each frame was digitised to give 256 pixels horizontally, and 400 pixels vertically (only 248 of which contained useful data), the digitisation being to 8 bit resolution (0-255 grey levels). Once the data had been digitised and stored on the frame grabber board, it was possible to save the sequence to disk for later analysis. The modulation transfer function (MTF) [98-102] of the camera system had been previously experimentally determined by 2 other researchers at Bath, P. Delpech and R. Hamzah. It was found that the transfer function of the camera only had a significant effect on high frequency spatial Fourier components, and would have no effect on the type of images generated during a PVT experiment on the samples analysed as part of this project.

5.5.4 Heat Sources And Guillotines

Two types of heat sources were tried. The first was a pair of 500 Watt tungsten filament lamps, the second a 1600 Watt hot air gun of the type used for paint stripping. In both case the heat sources were positioned behind guillotine type structures, designed to drop a shutter between the heat source and sample after the desired heating time. This was done to avoid heating the sample longer than the required time as both the lamp filaments and hot air gun remain hot after the power to them is switched off. The heating time and dropping of the guillotine shutters was controlled by the acquisition control computer, via the heat source/timer interface.

5.5.5 Heat Source/Timer Interface

This component was connected to both the acquisition control computer, and the heaters and guillotines. On command of the computer, the heat sources were switched on for the required (user selectable) time, at the end of which the heaters where switched off, and the guillotine blades dropped.

5.5.6 Acquisition Control Computer

The acquisition control computer was used to allow the user to enter the required heating time, to control the heaters and guillotines, and to send a signal to the frame grabber board to start data acquisition at the end of the heating period.

Testing Procedure

The sample is mounted in front of the camera and heating system, and the focus of the camera set to the plane containing the front of the sample. The output level of the camera is adjusted, as is the temperature range of the camera. The duration of the heating is entered into the computer controlling the timing and data acquisition. Once all is set, the experiment is started from the timing computer, and the frames stored on the computer with the frame grabber board. The data is then stored on the hard-disk of the computer for later analysis.

5.6 Profilometry Of Samples

Coating thickness profiles of the samples were made using a dial gauge. The measurements were complicated by the fact that the substrates onto which the coatings had been deposited had not remained flat after spraying, but had become curved due to the residual stresses within the coatings. To try to remove the curvature from the readings, the samples were first clamped on to a movable mount with their uncoated surfaces uppermost, and run length wise beneath a dial gauge, to measure the curvature. The samples were then turned over, and run beneath the dial gauge coating side up. It was then possible to subtract the uncoated side measurements from the coated side measurements in an attempt to remove the effects of substrate curvature. All but two of the samples had an area of the coated side with no coating, allowing the thickness of the substrate to be subtracted from the results, enabling true coating thicknesses to be calculated. For the two samples that did not have an uncoated area, an estimate was

made of the substrate thickness, based on microscopy of the coatings, to allow calculation of absolute coating thickness measurements. The results presented using this technique assume that the substrate thickness is consistent along the entire length of the sample, something that was impossible to verify. Figure 5.5 shows a schematic of the testing apparatus.

5.7 Sample Metallography

The step coated samples (samples 1, 2, 3 and 4 (see below)) were polished along a length wise edge to reveal the thickness and structure of the coatings. After polishing, the samples were micrographed, and measurements taken from the micrographs for use in the determination of the coating thermo-physical properties. It was extremely difficult to polish these samples as they were large (approximately 250mm in length), but it was decided not to section them so that they could be reused in the future.

Two separate procedures were used for the polishing of the samples, these are described below. All the polishing was conducted on a Buehler Motopol 12 grinding/polishing machine.

Tungsten Carbide Coatings (Samples 1 and 2)

1. The samples were mounted as a pair in a clamping system, with the length wise edges to be polished aligned as accurately as possible so that they would be in the plane of the grinding disk when offered up to the machine.

2. The initial task of grinding the edges back to undamaged material was undertaken using a Buehler Metlap system with a surface 10 finish, and 30 micron diamond in an oil based suspension.

3. A surface 4 finish with 9 micron diamond in an oil based suspension.

4. A Texmet cloth with a 1 micron diamond in a water based suspension.

5. The final polish was undertaken using a Chemomet cloth, with 0.06 micron colloidal silica.

6. After polishing, the samples were placed in an ultrasonic bath containing acetone, and cleaned for 30 minutes.

Aluminium/Silicon Alloy Coatings (Samples 3 and 4)

1. The samples were mounted as specified for the tungsten carbide coatings above.

2. The initial task of grinding the edges back to undamaged material was undertaken using 240 grit silicon carbide papers.

3. The remainder of the procedure was as for the tungsten carbide coatings (3)-(6) above.

Sample 6 was also polished and micrographed. This sample consisted of 5 separate pieces, the third of which was sectioned along its centre line, and then sectioned perpendicular to the first cut to produce 4 separate pieces. These pieces were placed into 30mm moulds, evacuated, and impregnated under vacuum with Epothin (an ultra low viscosity epoxy resin) so as to fill the pores in the coating. The moulds were placed in an oven to set for 24 hours before polishing. The polishing procedure is described below, a water free polishing route had to be taken to avoid reaction with the zinc coating. Once again the polishing was conducted on a Buehler Motopol 12 grinding/polishing machine.

Zinc Coating (Sample 6)

1. The samples were mounted in a special mount designed to take 30mm epoxy resin samples.

2. The rough edges of the castings were removed, and the initial polish made with 240 grit silicon carbide papers.

3. A perforated Texmet with 30 micron diamond in an oil based suspension.

4. A Texmet cloth with 3 micron diamond in an oil based suspension.

5. The final polish was made with a Met cloth and 0.25 micron diamond in an oil based suspension.

6. After polishing, the samples were placed in an ultrasonic bath containing acetone, and cleaned for 30 minutes.

Microscopy

The micrographs were taken using a Zeiss ICM 405 inverted metallographic microscope, fitted with a 35mm camera attachment.

5.8 Test Samples

Ten test samples were examined as part of this project, descriptions of each sample are given below. Each sample has been numbered to allow easy referencing in the following chapters. The coating thicknesses stated in the sample descriptions below, were the thicknesses that were intended to be deposited. Microscopy examination of the samples showed that these intended thicknesses were rarely, if ever, accurately achieved. All the test pieces, with the exception of the plasma sprayed samples, were manufactured by the sponsors of this project, TWI.

5.8.1 *Sample 1* - HVOF Sprayed Tungsten Carbide Step Coating On Mild Steel

The sample consisted of a 254 x 51 x 6mm thick mild steel substrate, onto which had been HVOF sprayed a step coating of tungsten carbide with 12% cobalt. The coating steps were sprayed to be approximately 50, 100, 150, 200 and 250μm in thickness, and each step was approximately 51mm in length. Figure 5.6 shows a diagram of the sample.

5.8.2 *Sample 2* - HVOF Sprayed Tungsten Carbide Step Coating On Stainless Steel

This sample is identical to sample 1, with the exception that the substrate in this case is stainless steel. Refer to figure 5.6 for dimensions of the sample.

5.8.3 *Sample 3* - HVOF Sprayed Aluminium/Silicon Alloy Step Coating On Mild Steel

This sample consisted of a 254 x 50 x 6mm thick mild steel substrate, onto which had been HVOF sprayed a step coating of aluminium with 5% silicon. This sample had an

uncoated region approximately 10mm in length adjacent to the thinnest coating thickness step. As before, the coating steps were sprayed to be approximately 50, 100, 150, 200 and 250μm in thickness. Each step was approximately 49mm in length. Figure 5.7 shows a diagram of the sample.

5.8.4 *Sample 4* - Arc Sprayed Aluminium/Silicon Alloy Step Coating On Mild Steel

This sample is the arc sprayed partner to sample 3. The dimensions and coating thicknesses are as shown in figure 5.7.

5.8.5 *Sample 5* - Arc Sprayed 13% Chrome Steel Step Coating On Mild Steel

This sample has the dimensions and coating thicknesses of sample 3, but in this case, has an arc sprayed step coating of 13% chrome steel. For dimensions refer to figure 5.7.

5.8.6 *Sample 6* - Arc Sprayed Zinc Coating On Mild Steel

This sample was in 5 separate pieces, each piece consisted of a 50 x 50 x 6mm thick mild steel substrate, onto which arc sprayed coatings of zinc had been deposited. Each piece had a different coating thickness : 50, 100, 150, 200 and 250μm.

5.8.7 *Sample 7* - HVOF Sprayed Aluminium On Mild Steel With Copper Inserts

This sample was produced as an attempt to manufacture a defect-like sample to test the sensitivity of the testing procedures. The sample consisted of a 150 x 50 x 6mm thick substrate of mild steel, through which holes of varying diameter from 10 to 0.5mm had been drilled. These holes were plugged with copper, the sample grit blasted, and HVOF sprayed on one surface with a 250μm thick coating of aluminium. Figure 5.8 shows a diagram of this test sample.

5.8.8 *Sample 8* - Arc Sprayed Aluminium On Mild Steel With Adhesion Defects

This sample, as for sample 7, was produced as an attempt to manufacture a defect-like sample. In this case it was attempted to create adhesion defects of varying diameters between a mild steel substrate, and a 250μm thick arc sprayed aluminium coating. The sample consisted of a 150 x 50 x 4mm thick substrate of mild steel, onto one surface of which were stuck patches of sticky tape of varying diameters. The sample was then grit

blasted on the side with the patches, the patches removed, and the sample arc sprayed with the aluminium coating. The idea of this procedure is that patches protect the surface beneath them, and so the coating does not adhere to these areas when sprayed. The positioning and sizes of the adhesion defects were as for the copper inserts of sample 7, except that in this case a 0.5mm diameter defect was not included.

5.8.9 *Sample 9* - Plasma Sprayed LC1B Step Coating On Stainless Steel

This sample consisted of a 254 x 25 x 6.7mm thick stainless steel substrate, onto which had been plasma sprayed a step coating of nickel chrome carbide (LC1B). This sample had an uncoated region approximately 11mm in length at both ends. The coating thickness steps were considerably thicker than previously described samples, and were measured (by micrometer screw gauge) to be <100, 260, 380, 500, 650 and 820μm (with an accuracy of ± 10μm). Each step was approximately 39mm in length. Measuring the thickness of the coating of this sample was not hampered by curvature - the substrate had remained flat after spraying. Figure 5.9 shows a diagram of the sample.

5.8.10 *Sample 10* - Plasma Sprayed LC1B On Stainless Steel With Back Drilled Holes

This sample was identical with sample 9 before having holes drilled from the uncoated side, to as close as possible to the coating/substrate interface. The holes were drilled in the centre of each coating thickness step, and were of 10mm in diameter. The holes were circular in cross section, and had flat tops. Figure 5.10 shows a schematic diagram of this sample.

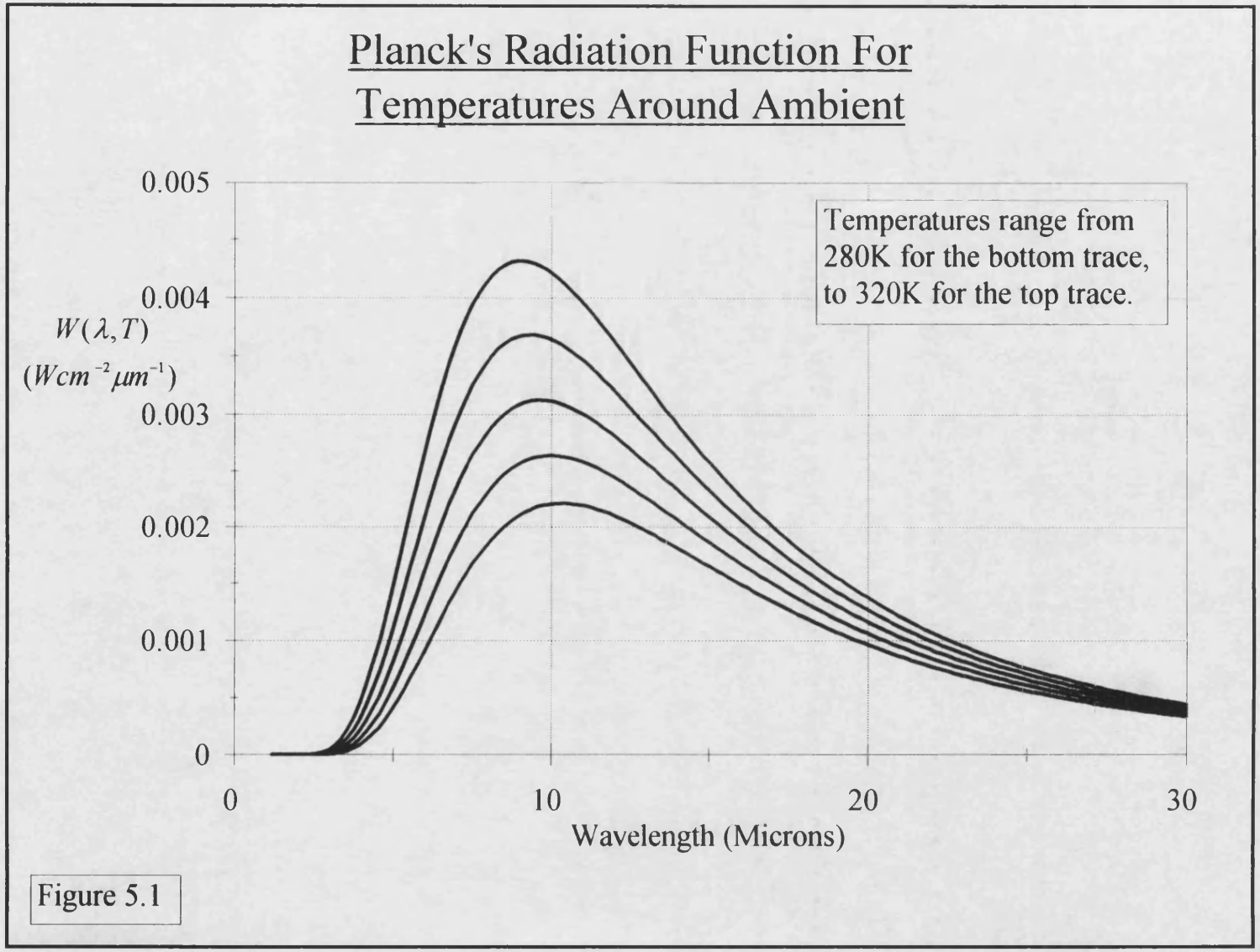
Planck's Radiation Function For
Temperatures Around Ambient
0.005
0.004
$W(\lambda,T)$
$(Wcm^{-2}\mu m^{-1})$
0.003
0.002
0.001
0
0
10
20
30
Wavelength (Microns)
Temperatures range from
280K for the bottom trace,
to 320K for the top trace.

Figure 5.1

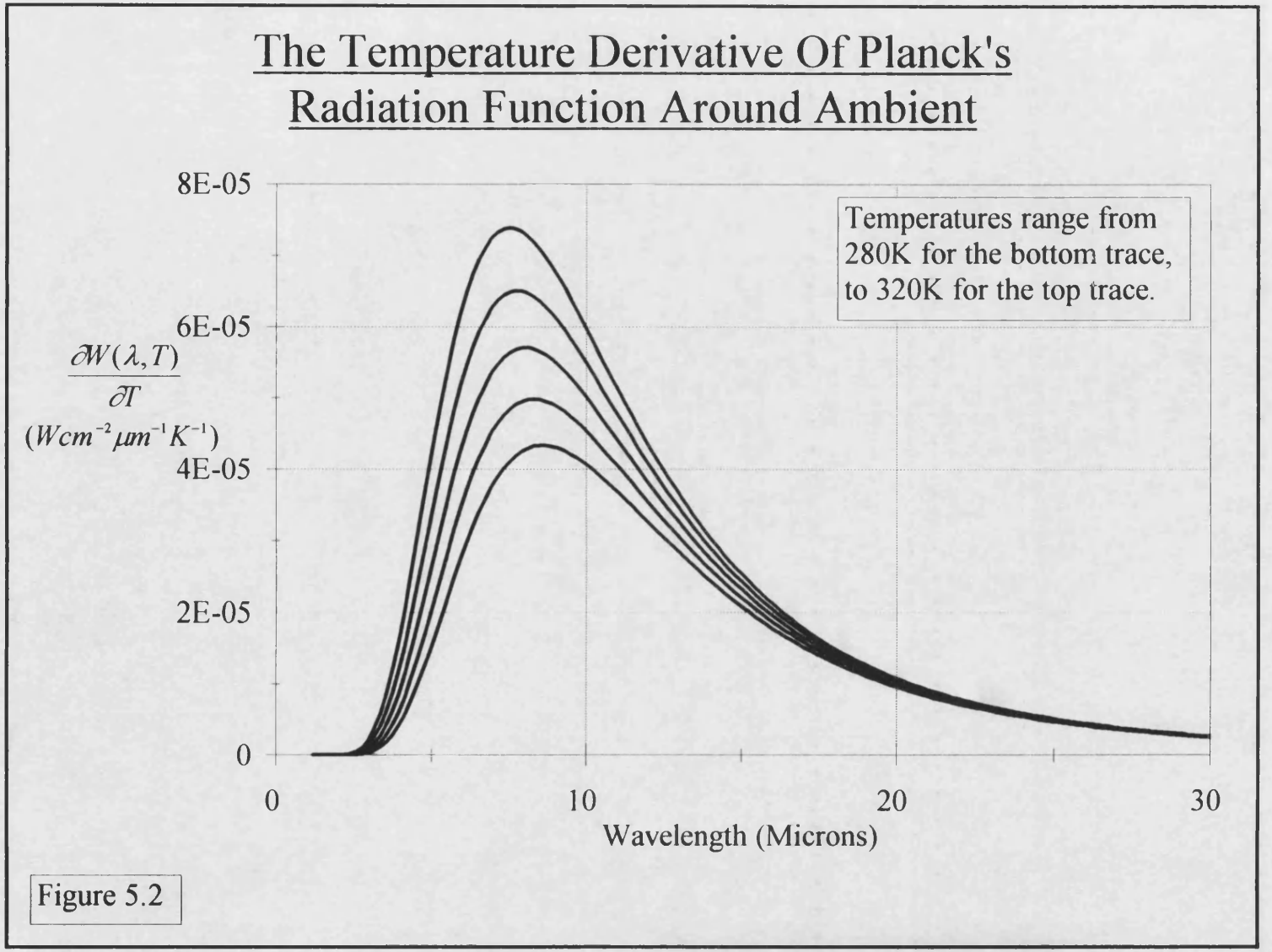
The Temperature Derivative Of Planck's Radiation Function Around Ambient
8E-05
6E-05
4E-05
2E-05
0
$\frac{\partial W(\lambda,T)}{\partial T}$
$(Wcm^{-2}\mu m^{-1}K^{-1})$
Temperatures range from 280K for the bottom trace, to 320K for the top trace.
0
10
20
30
Wavelength (Microns)

Figure 5.2

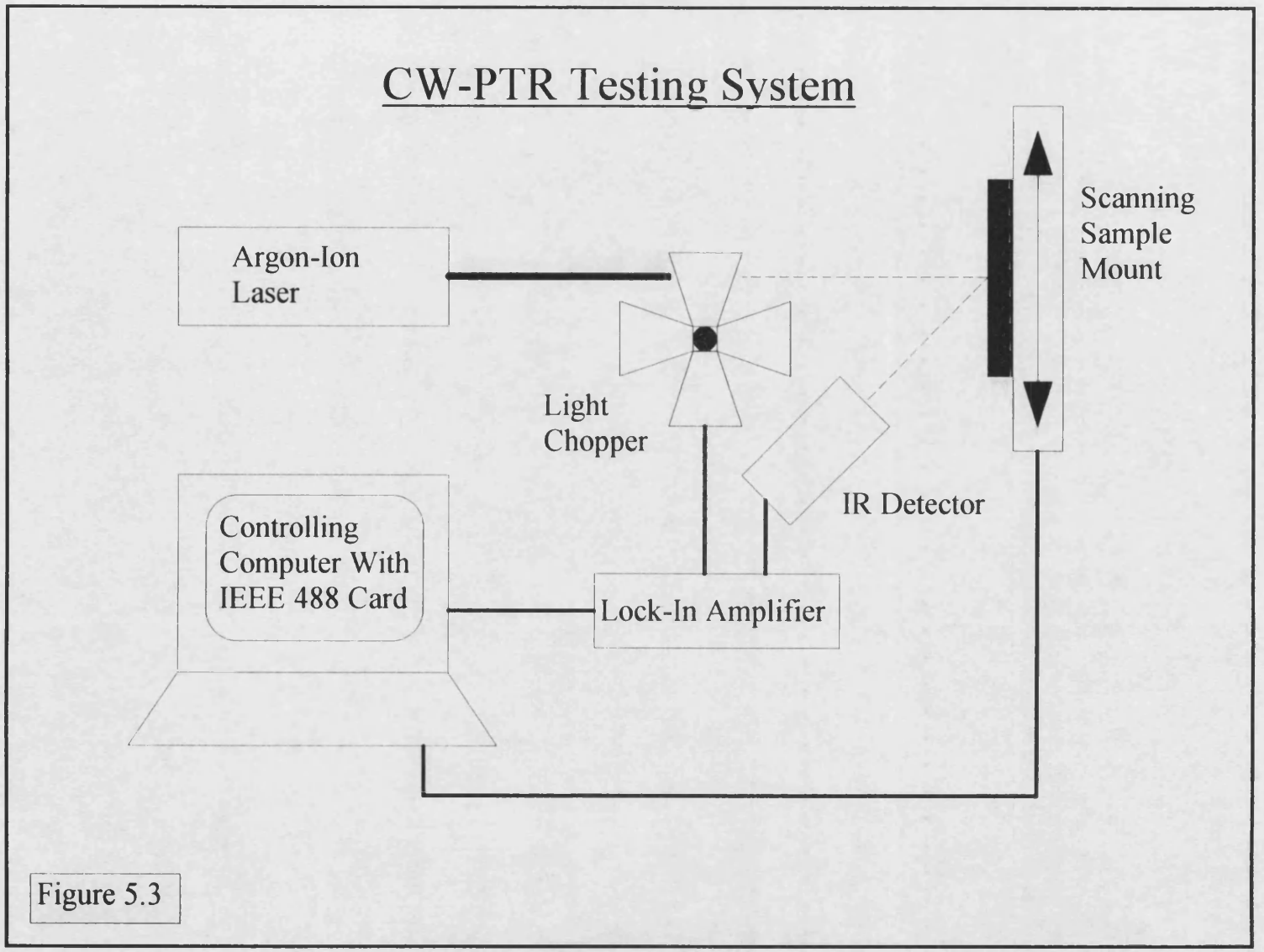
CW-PTR Testing System
Argon-Ion Laser
Scanning Sample Mount
Light Chopper
IR Detector
Controlling Computer With IEEE 488 Card
Lock-In Amplifier

Figure 5.3

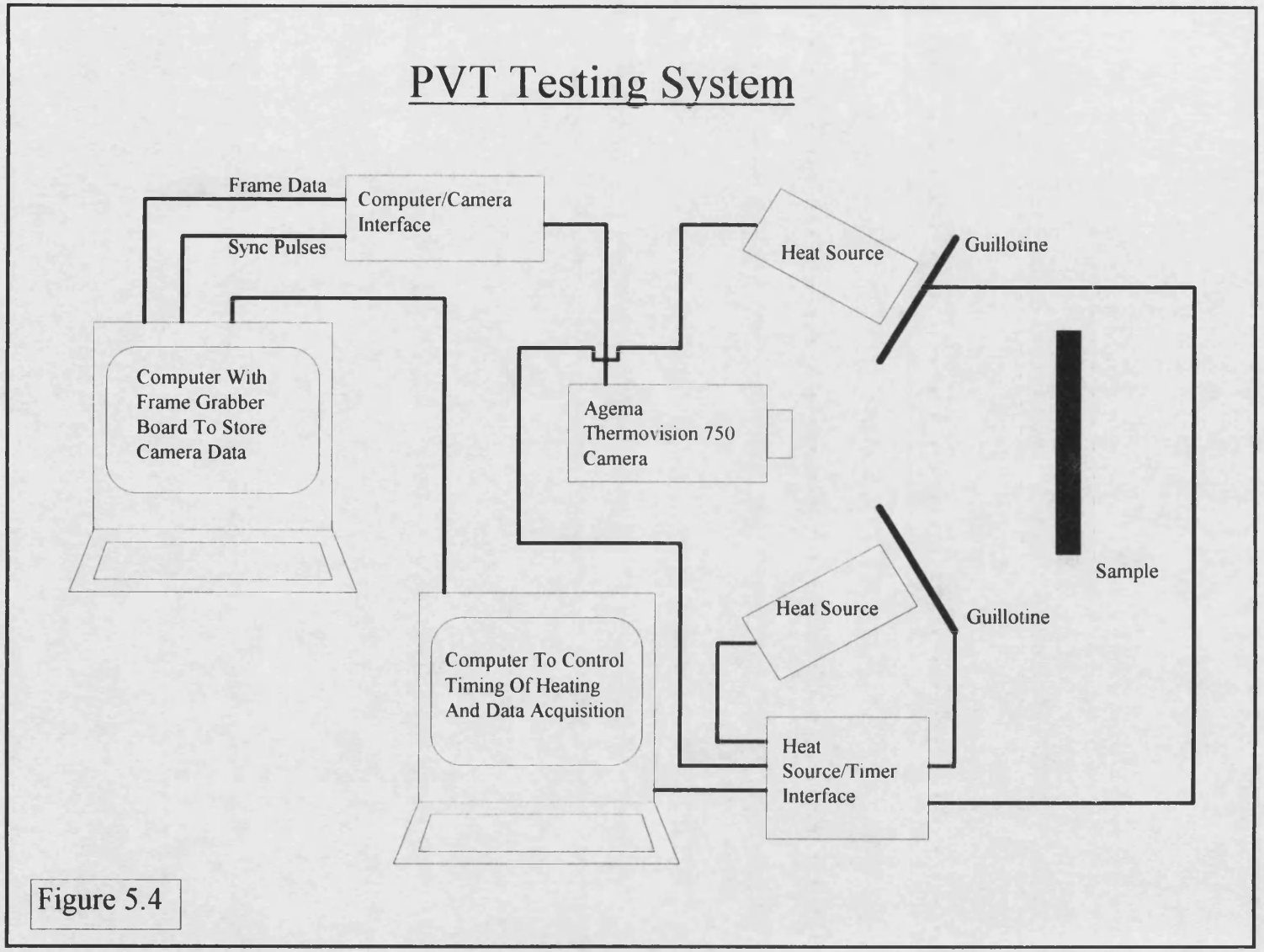
PVT Testing System
Frame Data
Computer/Camera Interface
Sync Pulses
Heat Source
Guillotine
Computer With Frame Grabber Board To Store Camera Data
Agema Thermovision 750 Camera
Sample
Heat Source
Guillotine
Computer To Control Timing Of Heating And Data Acquisition
Heat Source/Timer Interface

Figure 5.4

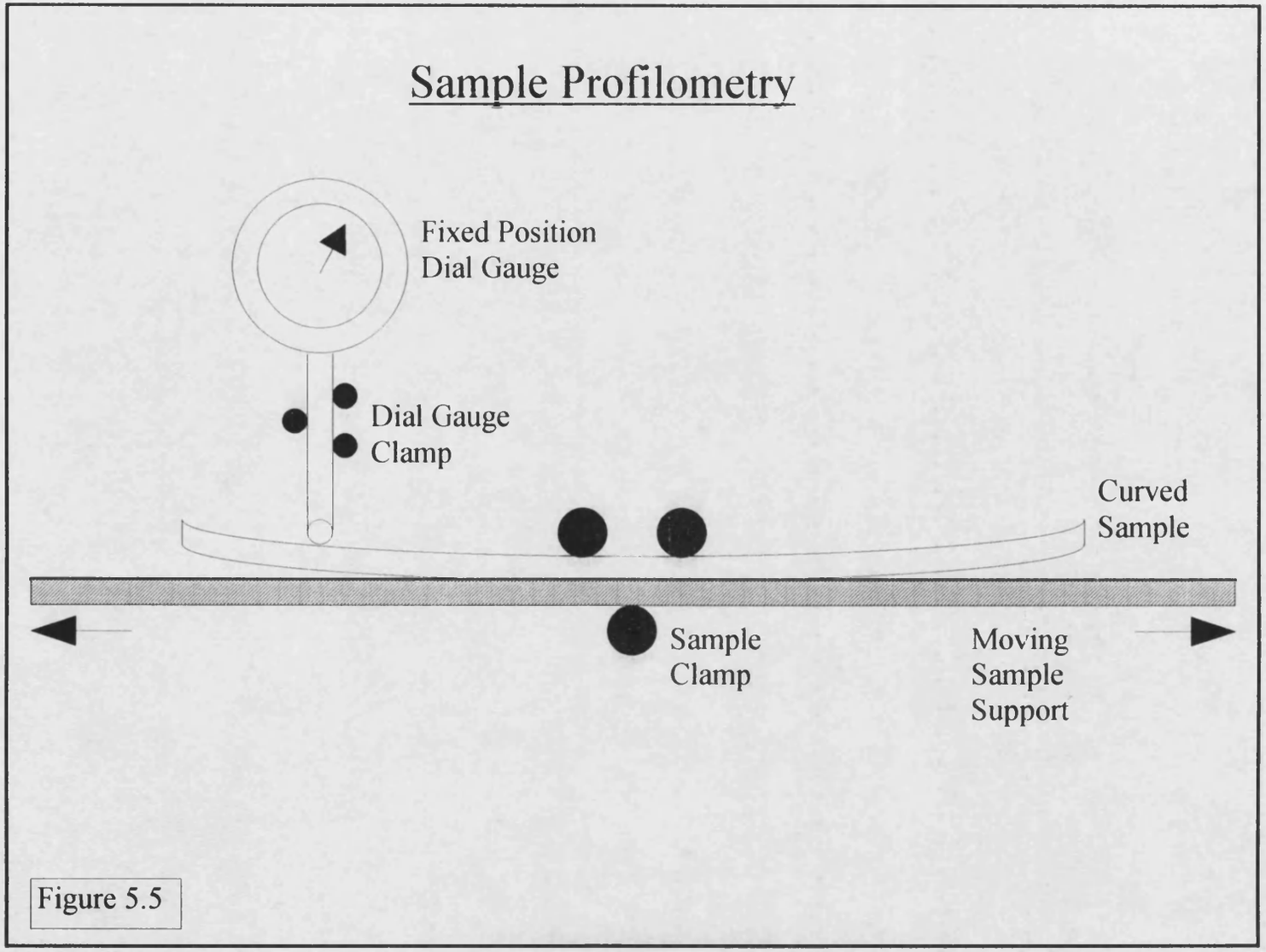
Sample Profilometry
Fixed Position
Dial Gauge
Dial Gauge
Clamp
Curved
Sample
Sample
Clamp
Moving
Sample
Support

Figure 5.5

Sample 1 : HVOF Sprayed Tungsten Carbide On Mild Steel

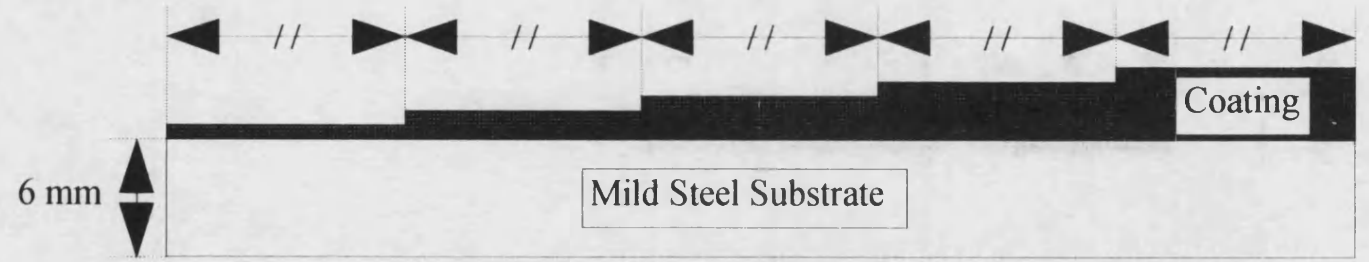

Side View

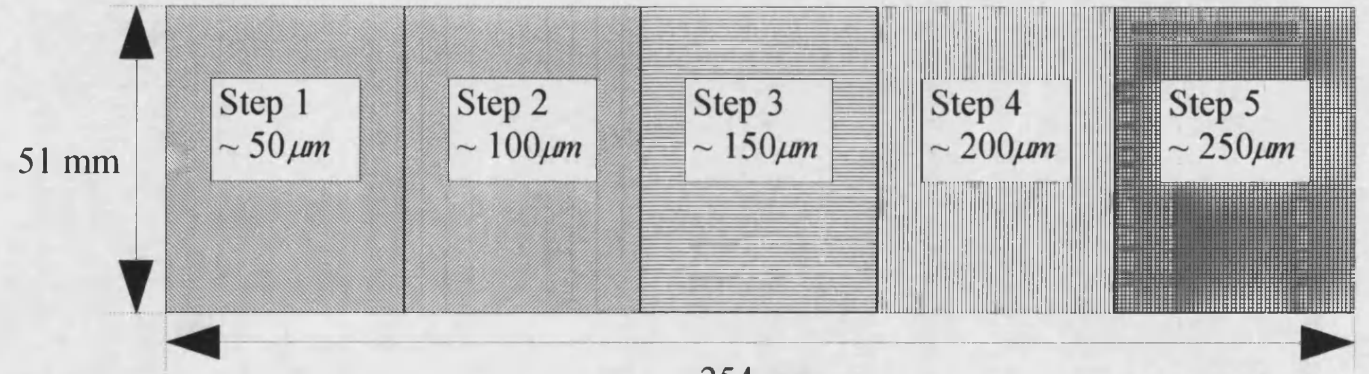

Plan View

Figure 5.6

Not To Scale

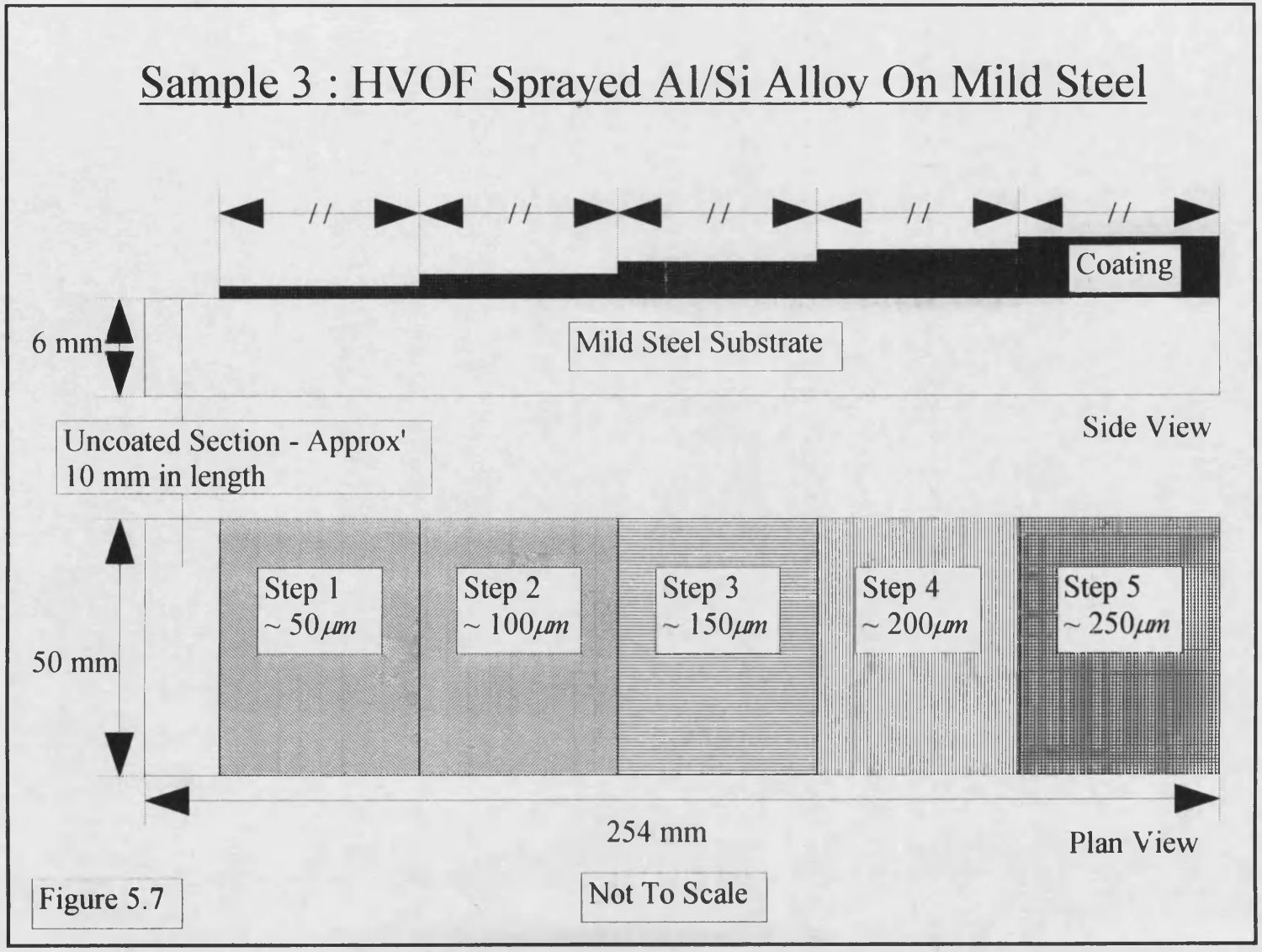
Sample 3 : HVOF Sprayed Al/Si Alloy On Mild Steel
Coating
6 mm
Mild Steel Substrate
Side View
Uncoated Section - Approx'
10 mm in length
Step 1
~ 50μm
Step 2
~ 100μm
Step 3
~ 150μm
Step 4
~ 200μm
Step 5
~ 250μm
50 mm
254 mm
Plan View
Figure 5.7
Not To Scale

Sample 7 : Copper Insert Defect Sample

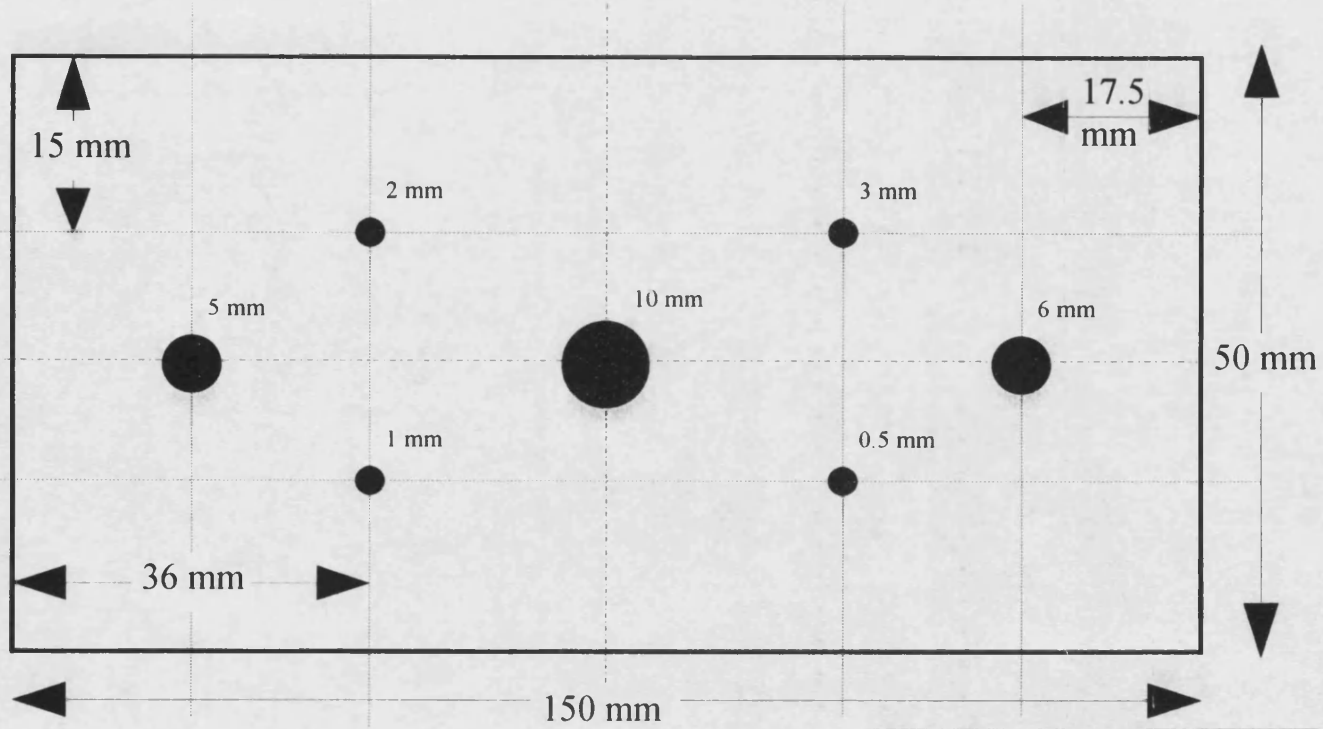

Sizes by the inserts are the copper insert diameter. The positions are shown as if viewed through the coating.

Figure 5.8

Not To Scale

Sample 9 : Plasma Sprayed LC1B On Stainless Steel

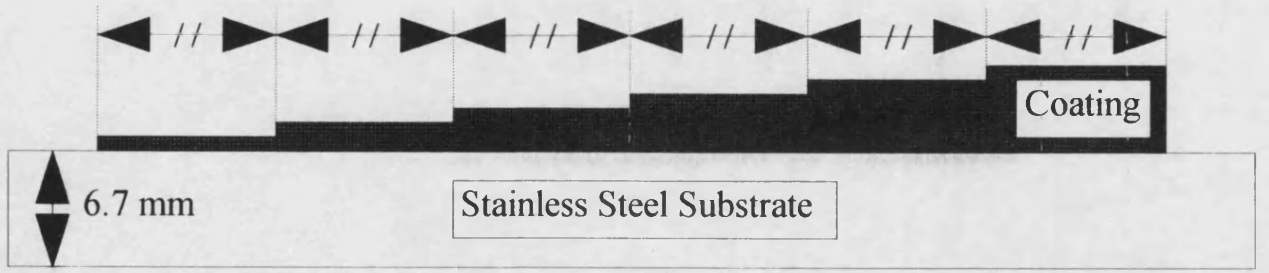

Side View

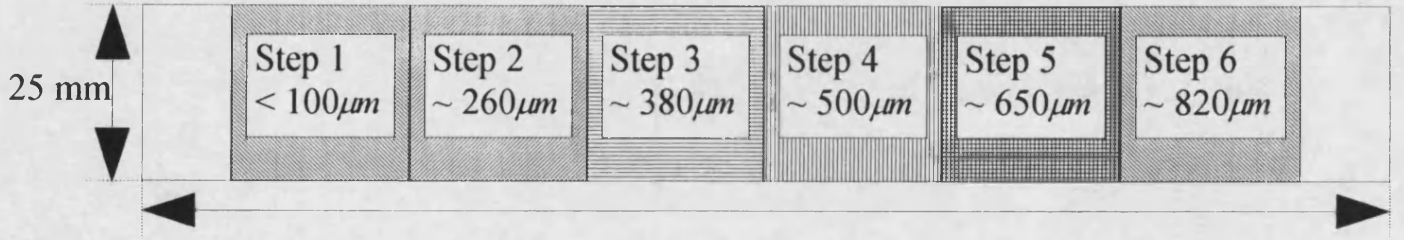

Plan View

Figure 5.9

Not To Scale

Sample 10 : Plasma Sprayed LC1B With Back Drilled Holes

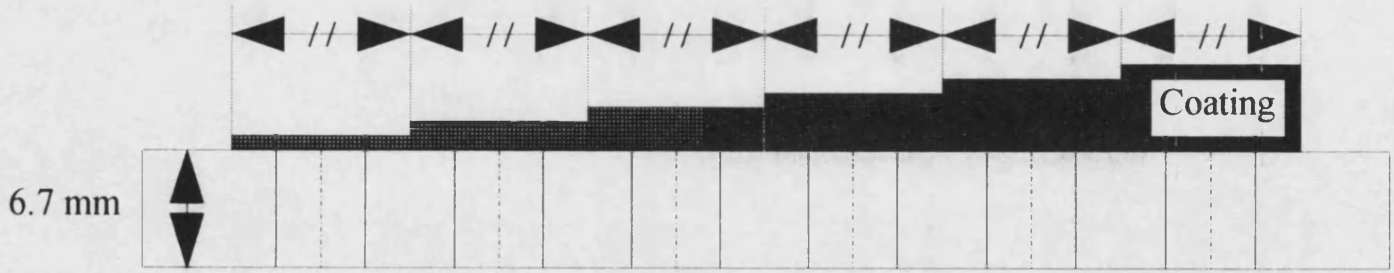

Side Section Through Centre Line Of Back Drilled Holes.

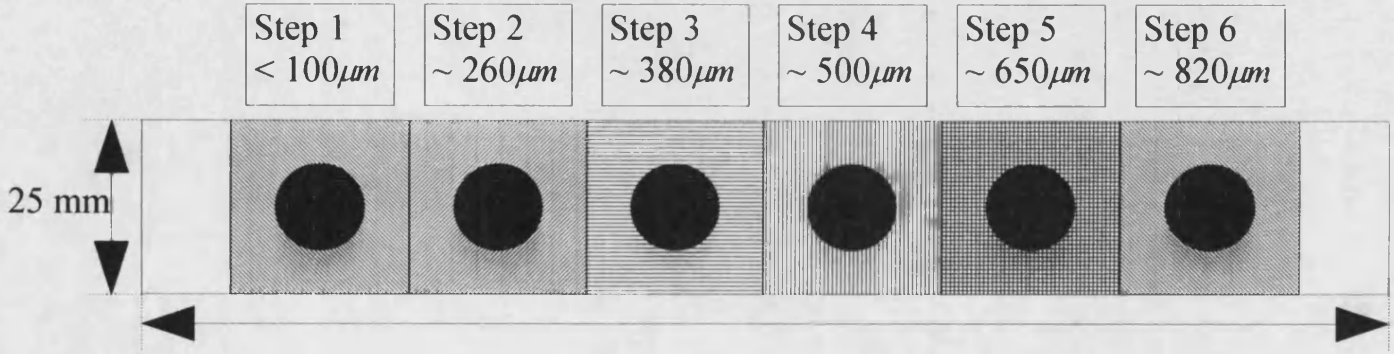

Plan View

Figure 5.10

Not To Scale

Chapter 6

Experimental Results And Analysis

The experimental investigations and subsequent analysis conducted on each specimen described in section 5.8 are the subject of this chapter.

6.1 *Sample 1* - HVOF Sprayed Tungsten Carbide Step Coating On Mild Steel

1. The sample was scanned length-wise along its centre line using CW-PTR, at modulation frequencies of 5, 10, 12, 15, 20 and 25 Hz. The argon-ion laser was used, in conjunction with the TGS detector and ellipsoidal collector. Figure 6.1 shows the result of the 12 Hz scan. The centre line was scanned twice at each frequency, the results of each pair of scans being compared to ensure reproducible data had been recorded. The steps in the coating thickness should occur approximately at the 50mm intervals in the figure. It is seen that there is no obvious step profile, although there is a general fall in phase along the length of the sample. A prominent feature is the region of high phase in the centre of the third coating thickness step (between 100 and 150mm). The rise in phase is indicative of a thinning of the coating in that region, a discovery that was later confirmed by microscopy. An area scan of the sample was also made at a frequency of 12 Hz, and is shown in figure 6.2. It is seen from this figure that the coating seems to be fairly consistent from side to side of the sample, but is not consistent within the coating thickness steps. The prominent feature in the third step (centred around 130mm on the graph) is seen to extend right across the sample.

2. The sample was polished along a length-wise edge, and micrographs taken of the coating at regular spatial intervals. Four micrographs were selected and coating thickness measurements taken from them. The full width of the micrographs at the utilised magnification (~95x) shows approximately 1.2mm of the sample. Ten regularly spaced positions across the width of the selected micrographs were marked, and the coating thickness measured at these points. A mean thickness was calculated from the measurements, along with the standard deviation about the mean. The table below shows the results of these measurements. Figures 6.3a and 6.3b show a selection of micrographs from the sample, the scale of the micrographs is shown in the figures. The micrograph from step 2 shows the extremely rough nature of the coating. The micrographs from steps 3, 4 and 5 show a more

homogeneous coating structure. Small vertical and horizontal cracks are evident in the micrograph from step 4, and gross horizontal delamination is evident in step 5. It is impossible to determine if the cracks were present before the polishing, or were caused by it.

Position Along Sample (mm)	Average Coating Thickness (μm)	Standard Deviation In Coating Thickness (μm)
37 mm	26 μm	10 μm
87 mm	63 μm	8 μm
164 mm	147 μm	14 μm
217 mm	235 μm	13 μm

3. CW-PTR scans were made across the width of the sample at positions corresponding to the thickness measurements taken from the micrographs. This assumes that the coating thickness at the edge of the sample is an accurate measure of the thickness across the whole width, something that appears to be a reasonable assumption from the area scan of the sample. Once again, the scans were made at frequencies of 5, 10, 12, 15, 20 and 25 Hz. Once this had been done, a relative phase value could be associated with each of the 4 coating thicknesses, at each of the 6 frequencies, giving a total of 24 experimental points with which to fit the thermal properties to theory.

4. The thermal properties of the coating/substrate pair were calculated using a program developed to find the least squares fitting of the experimental measurements to the theory discussed in section 3.3 of chapter 3. This process was complicated by the fact that the experimental measurements are for relative phase, and not the absolute phase predicted by the theory. It was therefore necessary to shift the data sets for each frequency relative to one another to fit the data. The errors were estimated by fitting the data with the standard deviations added and subtracted from the average data. The final properties were found to be :

Reflection Coefficient	$R = -0.58 (\pm 9\%)$
Coating Diffusivity	$\alpha = 8.7 \times 10^{-7} (\pm 46\%)$ m²/s

Figure 6.4 shows a graph of the fitting of the data. The x-axis of the graph ($l\sqrt{f}$) is linearly related to the thermal thickness of the coating (l_c / μ). The shape of the fitting curve is seen to have the same form as that of figure 3.5, showing the relationship between the thermal thickness of a coating and the phase for different reflection coefficients. The large error in diffusivity is attributed to the

inhomogeneity of the coating structure and thickness, and errors in the measurements. These errors appear to have relatively little effect on the accuracy of the reflection coefficient, giving a very satisfying accuracy of less than ± 10%. (It should be noted that the method of fitting the data by shifting the different frequency scan data sets relative to each other contributes to the minimisation of the error in the reflection coefficient). [103] is a recent paper on the use of thermal wave interferometry for the evaluation of coating thermal properties.

With knowledge of the reflection coefficient R and diffusivity α, it is possible to determine the coating thermal conductivity k and effusivity ε. To do this, it is necessary to have values for the thermal properties of the substrate material. The following values have been used for the thermal properties of mild steel substrate [97],

Substrate Thermal Conductivity	$k = 63.6$ W/mK
Substrate Density	$\rho = 7850$ kg/m^3
Substrate Specific Heat Capacity	$c = 580$ J/kgK
Substrate Diffusivity	$\alpha = 14 \times 10^{-6}$ m^2/s
Substrate Effusivity	$\varepsilon = 17070$ J/m^{2}Ks^{½}

Using these values, the coating thermal conductivity and effusivity were found to be:

Coating Thermal Conductivity	$k = 4.2$ W/mK
Coating Effusivity	$\varepsilon = 4520$ J/m^{2}Ks^{½}

5. Using the calculated thermal properties of the coating/substrate pair, phase data from the length-wise scans of the sample was inverted to give coating thickness readings. This procedure is complicated by the fact that for every phase value there corresponds at least 2 coating thicknesses (i.e. the inverting function is not single valued - see figure 3.5). Some knowledge of the sample, such as the sample gets thicker from end to end is of use here, as monotonicity and continuity of the coating thickness can be applied during the inversion procedure. This is obviously of no help in regions of rapid fluctuations in coating thickness, and so could not be relied upon for wholly uncharacterised samples. The inversion was made at each frequency, with the inversions averaged to produce the final result.

6. The coating thickness was measured using a dial gauge along the centre line of the sample. This measurement was compared to the thickness inversion made from the

phase scan data. Figure 6.5 shows this comparison. The large ± error in the calculated diffusivity of the coating is the cause of the wide upper and lower band on the inverted phase scan data. It is seen that the inverted phase data always lies below the dial gauge reading. This is expected as the dial gauge had a rounded head of approximately 5mm diameter, and so was unable to penetrate into any structures on the coating surface smaller than this. There is good general agreement between the plots, with many features picked up in both. In particular, the prominent thinning of the coating in the third coating thickness step is found in both traces.

6.2 *Sample 2* - HVOF Sprayed Tungsten Carbide Step Coating On Stainless Steel

The analysis undertaken on sample 2 was identical to that for sample 1. For more details of the experimental and analysis method, refer to the relevant step in the results section of sample 1.

1. CW-PTR scans were made along the length of the sample at frequencies of 5, 10, 12, 15, 20 and 25 Hz. Figure 6.6 shows the average result of the 12 Hz phase scans. As was the case with sample 1, there is no obvious step nature to the trace, but again a general drop in phase along the length of the sample is seen. A region of high phase in the centre of the third coating thickness step is once again present. The similarities of the scans of samples 1 and 2 indicated that they were most likely sprayed at the same time, leading to the same coating thickness irregularities. The maximum phase change in the scan of sample 2 is less than that for sample 1, as the thermal mismatch (and hence reflection coefficient) between the coating and substrate is less for sample 2. An area scan of the sample was made at a frequency of 12 Hz, and is shown in figure 6.7. From the phase scan data, it is seen that the coating appears fairly consistent side to side of the sample, but is again inconsistent along the coating thickness steps.

2. The sample was polished along a length-wise edge, and micrographs taken. Four micrographs were selected and coating thickness measurements made. A mean thickness was calculated from the measurements, along with the standard deviation about the mean. The table below shows the results of these measurements. Figures 6.8a and 6.8b show a selection of micrographs from the sample, the scale of the micrographs is shown in the figures. The micrograph from step 3 was taken in the region of the peak in phase, and shows the coating thickness to be considerably thinner than the intended thickness. The thicker coating thickness steps, in contrast to sample 1, do not show the presence of so much cracking.

Position Along Sample (mm)	Average Coating Thickness (μm)	Standard Deviation In Coating Thickness (μm)
29 mm	33 μm	16 μm
79 mm	92 μm	16 μm
179 mm	161 μm	7 μm
219 mm	239 μm	12 μm

3. CW-PTR scans were made across the width of the sample at positions corresponding to the thickness measurements taken from the micrographs. Scans were made at frequencies of 5, 10, 12, 15, 20 and 25 Hz.

4. The thermal properties of the coating/substrate pair were calculated from the experimental data using the least squares fitting program. The final properties were found to be :

Reflection Coefficient	$R = -0.33 (\pm 8\%)$
Coating Diffusivity	$\alpha = 8.1 \times 10^{-7} (\pm 44\%)\ m^2/s$

Figure 6.9 shows a graph of the fitting of the data. It is pleasing to note that the values for the diffusivity of the tungsten carbide coatings from samples 1 and 2 agree to within 7%, far less than the bounds of the experimental error. This gives more confidence in the use of the quoted figures for the phase scan data inversion procedure.

Once again, the coating thermal conductivity k and effusivity ε were evaluated. The following values have been used for the thermal properties of stainless steel substrate [97],

Substrate Thermal Conductivity	$k = 13.4\ W/mK$
Substrate Density	$\rho = 8238\ kg/m^3$
Substrate Specific Heat Capacity	$c = 468\ J/kgK$
Substrate Diffusivity	$\alpha = 3.5 \times 10^{-6}\ m^2/s$
Substrate Effusivity	$\varepsilon = 7190\ J/m^2Ks^{½}$

Using these values, the coating thermal conductivity and effusivity were found to be:

Coating Thermal Conductivity	$k = 3.5\ W/mK$

Coating Effusivity $\varepsilon = 3700\ J/m^2Ks^{½}$

These are close, but not identical to the values deduced for the coating from the analysis of sample 1. One possible reason for the discrepancy (other than experimental error) is the fact that there is no guarantee that the values used for the thermal properties of the substrates accurately reflected the properties of these samples.

5. Using the calculated thermal properties of the coating/substrate pair, phase data from the length-wise scans of the sample was inverted to give coating thickness readings.

6. The coating thickness was measured using a dial gauge along the centre line of the sample. This measurement was compared to the thickness inversion made from the phase scan data. Figure 6.10 shows this comparison. As for sample 1, there is good general agreement between the plots, with the prominent thinning of the coating in the third coating thickness step found in both traces.

6.3 *Sample 3* - HVOF Sprayed Aluminium/Silicon Alloy Step Coating On Mild Steel

It was intended to analyse this sample in the same way as for samples 1 and 2, however the quality of the coating was insufficient to enable the thermal properties to be deduced, and so inversion of the phase scan data was impossible.

1. CW-PTR scans were made along the length of the sample at frequencies of 5, 10, 12, 15, 20 and 25 Hz. Figure 6.11 shows the average result of the 12 Hz phase scans. The scan shows no evidence of the steps in the coating thickness, and is extremely irregular. There is barely 10 degrees of phase between the highest and lowest point on the trace, implying that the reflection coefficient between the coating and substrate is small. An area scan was not made of this sample.

2. The sample was polished along a length-wise edge, and micrographs taken. Four micrographs were selected and coating thickness measurements made. A mean thickness was calculated from the measurements, along with the standard deviation about the mean. The table below shows the results of these measurements. Figures 6.12a and 6.12b show a selection of micrographs from the sample, the scale of the

micrographs is shown in the figures. All the micrographs show the coating to have much higher porosity and inhomogeneity than the tungsten carbide coatings of samples 1 and 2, and all show a rough upper surface to the coating. Blow holes as large as 50 μm in diameter can be seen in the micrographs from the thicker coating thickness steps. These are probably due to the re-melting of the aluminium when a second or subsequent pass is made over the sample, as the melting point of aluminium is very low (660 °C). Such large features in the coating structure clearly make the application of the simple theory based on homogeneous materials inapplicable.

Position Along Sample (mm)	Average Coating Thickness (μm)	Standard Deviation In Coating Thickness (μm)
55 mm	35 μm	7 μm
115 mm	72 μm	7 μm
175 mm	102 μm	10 μm
195 mm	165 μm	8 μm

3. CW-PTR scans were made across the width of the sample at positions corresponding to the thickness measurements taken from the micrographs. Scans were made at frequencies of 5, 10, 12, 15, 20 and 25 Hz. These scans showed that the coating thickness/properties were not consistent from side to side of the sample, as had been the case for samples 1 and 2. This made it impossible to reliably assign a relative phase value to a given coating thickness, and hence calculating the thermal properties was not possible. No further analysis was undertaken of this sample.

6.4 *Sample 4* - Arc Sprayed Aluminium/Silicon Alloy Step Coating On Mild Steel

This sample, the arc sprayed equivalent of sample 3, showed even greater inhomogeneity in the coating structure, and so once again only a limited analysis was possible.

1. CW-PTR scans were made along the length of the sample at frequencies of 5, 10, 12, 15, 20 and 25 Hz. Figure 6.13 shows the average result of the 12 Hz phase scans. The trace is irregular, with very little change along its length except for the spike in the third coating thickness step. A dial gauge measurement was made on

this sample, but this feature could not be found in the data, indicating that the spike is probably attributable to a cluster of blow holes or other such inhomogeneities.

2. The sample was polished along a length-wise edge, and micrographs taken. Figures 6.14a and 6.14b show a selection of micrographs from the sample, the scale of the micrographs is shown in the figures. Little needs to be said about these, the coating structure and thickness are so inconsistent that the CW-PTR signal is swamped by these inhomogeneities, and is unable to distinguish the grosser features of the coating.

6.5 *Sample 5* - Arc Sprayed 13% Chrome Steel Step Coating On Mild Steel

This sample, being arc sprayed, showed similar characteristics in its coating structure to that of sample 4. As very little was possible with sample 4, no analysis was carried out on this sample.

6.6 *Sample 6* - Arc Sprayed Zinc Coating On Mild Steel

1. The five separate pieces were butted together, and mounted in the CW-PTR system for scanning at frequencies of 5, 10, 15, 20 and 25 Hz. As with all previous arc sprayed samples, the scans showed very irregular phase, with no trend in the data. Figure 6.15 shows the average of two 10 Hz phase scans along the samples. Near the centre of the third coating thickness step (between 100 and 150mm), a peak and trough is seen in the phase. A more finely spaced scan of this step was made, again at 10 Hz, and is shown in figure 6.16. (In this figure, 0mm is equivalent to 100mm in figure 6.15).

2. The third coating thickness step was sectioned close to the line of the phase scan shown in figure 6.16. This sample was then resin mounted and polished back to the line of the scan, before being micrographed in an attempt to find features in the coating structure that could account for the irregularities in the phase (this has previously been done for ultrasonic testing of coatings [5]). From figure 6.16, there should be a significant difference in the coating between positions around 20mm from the start of the third step, and positions around 35mm, as there is greater than 6° difference in phase between the two. Figure 6.17 shows micrographs taken from these two areas. The micrograph 1 (from 20mm) shows large planar flaws in the

coating which are not seen in micrograph 2 (35mm). This could explain the reduced phase recorded at 20mm, as a thermal wave reflected from a coating/air interface caused by a defect could give lower phase than reflection from a coating/substrate interface.

6.7 *Sample 7* - HVOF Sprayed Aluminium On Mild Steel With Copper Inserts

Figure 5.8 shows a schematic diagram of this sample, marking the positions and sizes of the copper inserts.

1. CW-PTR scans were made along a horizontal line directly over the sites of the three largest diameter inserts. Scans were made at frequencies of 5, 10, 15, 20 and 25 Hz. The positions of these inserts were found at all frequencies as peaks in phase. Figure 6.18 shows the average result of two 15 Hz phase scans, the peaks are clearly visible at positions 17.5, 75 and 132.5mm along the sample. The widths of these peaks give a reasonable estimate of the size of the inserts, and the relative heights of the peaks are in order of insert size. Other structure on the trace is attributable to coating thickness variations or coating structure irregularities.

2. An area scan was made of the whole sample at a frequency of 15 Hz. The scan resolution was 1 point per millimetre in both the x and y directions. Figure 6.19 shows the result of this scan. The 5, 10 and 6mm diameter inserts are clearly seen in the figure, with the region around the site of the 3mm diameter insert showing signs of its presence. The smaller defects are clearly not visible, but at this resolution they would be difficult to see. The large variations in phase over the sample clearly show that the coating is very variable. There is a general trend in the phase data from low (dark blue) at the left hand side of the figure, to high (green/yellow) at the right hand side.

3. As the resolution of the whole sample scan was not high enough to determine if it was possible to detect the smaller inserts, detailed high resolution scans were made over them. Each of the scans was made at 15 Hz, at a resolution of 4 points per millimetre in both the x and y directions. Figure 6.20 shows the area scan over the site of the 3mm diameter insert. A region of high phase, relatively circular in shape is clearly visible. Figure 6.21 shows the area scan over the 2mm diameter insert, which again is clearly seen. The positioning of this scan was not very accurate, with the insert positioned to the left hand edge of the scan. Figure 6.22 shows the scan over the 1mm diameter insert. An area of high phase is detected, not very circular

in shape, and quite large compared to the true size of the insert. It seems likely that this can be attributed to the insert. The area scan over the site of the 0.5mm diameter defect did not reveal anything, setting a limit of 1mm in diameter for detectable inserts at this frequency and resolution of scan.

4. A series of high resolution line scans were made over the a diameter of the 10mm insert, at frequencies ranging from 5 to 45 Hz. The idea was to determine the effect of the modulation frequency on the apparent size of the insert. Figure 6.23 shows the results of these scans, the 5 Hz trace is at the top, increasing in frequency to the 45 Hz trace at the bottom. From this figure, the widths of the phase peaks at half maximum height were measured, and are plotted as a function of modulation frequency in figure 6.24. The exponential fit to the data shows a decrease in the apparent diameter with increasing frequency. This is in strict contrast to the increase in apparent size with increasing frequency expected from the frequency domain Wiener-Hopf solution discussed in chapter 3. The Wiener-Hopf solution is however based on a crack type defect in a homogeneous material. In this case we have a high conductivity insert below a coating. The important difference is that the copper insert has the effect of 'pulling' the heat down into itself due to its extremely high conductivity, whereas a crack defect forces the heat to flow around it.

5. The sample was tested using the transient thermography (thermal camera) system to see if it were possible to detect the presence of the inserts through the coating. As mentioned in chapter 5, the camera has a relatively slow capture rate, and so was unable to detect the inserts. This was not surprising as aluminium has a high diffusivity, and so any thermal transient would decay very rapidly.

6.8 *Sample 8* - Arc Sprayed Aluminium On Mild Steel With Adhesion Defects

This sample was tested using both CW-PTR, and transient thermography. No defects were found with either technique. In the case of CW-PTR, this could be due to the inserts being hidden in the familiar noise in the phase scan data associated with arc sprayed coatings. However, it could be that the method of producing the defects did not work. Without sectioning the sample, this could not be established.

6.9 *Sample 9* - Plasma Sprayed LC1B Step Coating On Stainless Steel

1. CW-PTR scans were made of this sample at frequencies of 3, 4, 5 and 7 Hz. Low frequencies were needed as the coating thicknesses of this sample far exceed those for the other step coated samples, and so deep penetrating - long thermal diffusion length thermal waves were needed. Only the thickest 5 coating thickness steps were scanned, a total of 180mm in length, as the coating on the thinnest step was damaged. Figure 6.25 shows the average of two 3 Hz scans along the sample, the left hand end of the trace corresponding to the 820μm thick step, the right hand end to the 260μm step. The positions of the steps in the coating thickness are clearly visible.

2. The thicknesses of each of the 5 thickest steps were measured by micrometer screw gauge, the results of which are presented in the table below.

Step Along Sample - Thickest First	Average Coating Thickness (μm)	Standard Deviation In Coating Thickness (μm)
1	820 μm	8 μm
2	650 μm	7 μm
3	500 μm	10 μm
4	380 μm	6 μm
5	260 μm	6 μm

3. CW-PTR scans were made across the width of the sample at frequencies of 3, 4, 5 and 7 Hz, at positions corresponding to the thickness measurements in the table above. The thermal properties of the coating/substrate pair were then calculated using the least squares fitting program, and were found to be :

Reflection Coefficient	$R = -0.38$ ($\pm$ 10%)
Coating Diffusivity	$\alpha = 1.85 \times 10^{-6}$ ($\pm$ 10%) m^2/s

Figure 6.26 shows a graph of the curve fitting. An error of ± 10% in both reflection coefficient and coating diffusivity is extremely good, and reflects the superior nature of this coating compared to the HVOF and arc sprayed coatings of samples 1-8. The thermal properties of this coating/substrate pair were evaluated so that they could be used in the computer simulation of the transient thermography experiments conducted on sample 10.

6.10 *Sample 10* - Plasma Sprayed LC1B On Stainless Steel With Back Drilled Holes

1. The sample was mounted in front of the thermal camera and heating equipment, so that the field of view of the camera was centred on the area above the back drilled hole below the thickest (0.82mm) thick coating. Initially, tungsten filament lamps were tried as the heat source, but they failed to provide enough heat energy to produce detectable contrast on the sample surface. A hot air blower was used in place of the lamps, and produced excellent results. A heating time of 6 seconds was used, as this was found to provide the best images. Figures 6.27 and 6.28 show a sequence of 18 frames from the camera. The first frame in the sequence is number 2, as frame number 1 was saturated. The frames were grabbed at a rate of 6.25 Hz, the maximum rate for the camera. The first frame in figure 6.27 is at a time of 320 ms after the heating has stopped, subsequent frames are at 160 ms intervals. The location of the hole is still just visible in frame 19.

2. Measurements of the diameter of the contrast peak at half maximum contrast (FWHM) were made from the images. A computer simulation of the experiment was made using the model described in section 4.5, and using the thermal properties for the coating/substrate pair calculated from sample 9. Figure 6.29 shows the comparison of the measured FWHM from the experiment and the simulation for times between 0 and 4 seconds after the heating had finished. It is seen that the results compare very well.

3. Similar experiments were conducted for the back drilled holes below the 0.65, 0.5 and 0.38mm thick coatings. Figure 6.30 to 6.32 show the comparison of the experimental data to computer simulations of the experiments. The data agrees very well for the holes below the 0.65 and 0.38 mm thick coatings, but not so well for the 0.5 mm thick coating. On closer inspection it was found that the hole below the 0.5 mm coating had not been drilled as accurately as the other holes, leaving a thickness of steel between the top of the hole and the coating. This added thickness has the effect of making the experimental data appear to be for a deeper hole (thicker coating) than that modelled. This has the effect of reducing the rate at which the FWHM decreases with time as compared to the simulated data, explaining the positioning of the experimental data points above the simulated data. The excellent agreement between the simulated and experimental data gives confidence in the ability of the computer model to accurately simulate experiment.

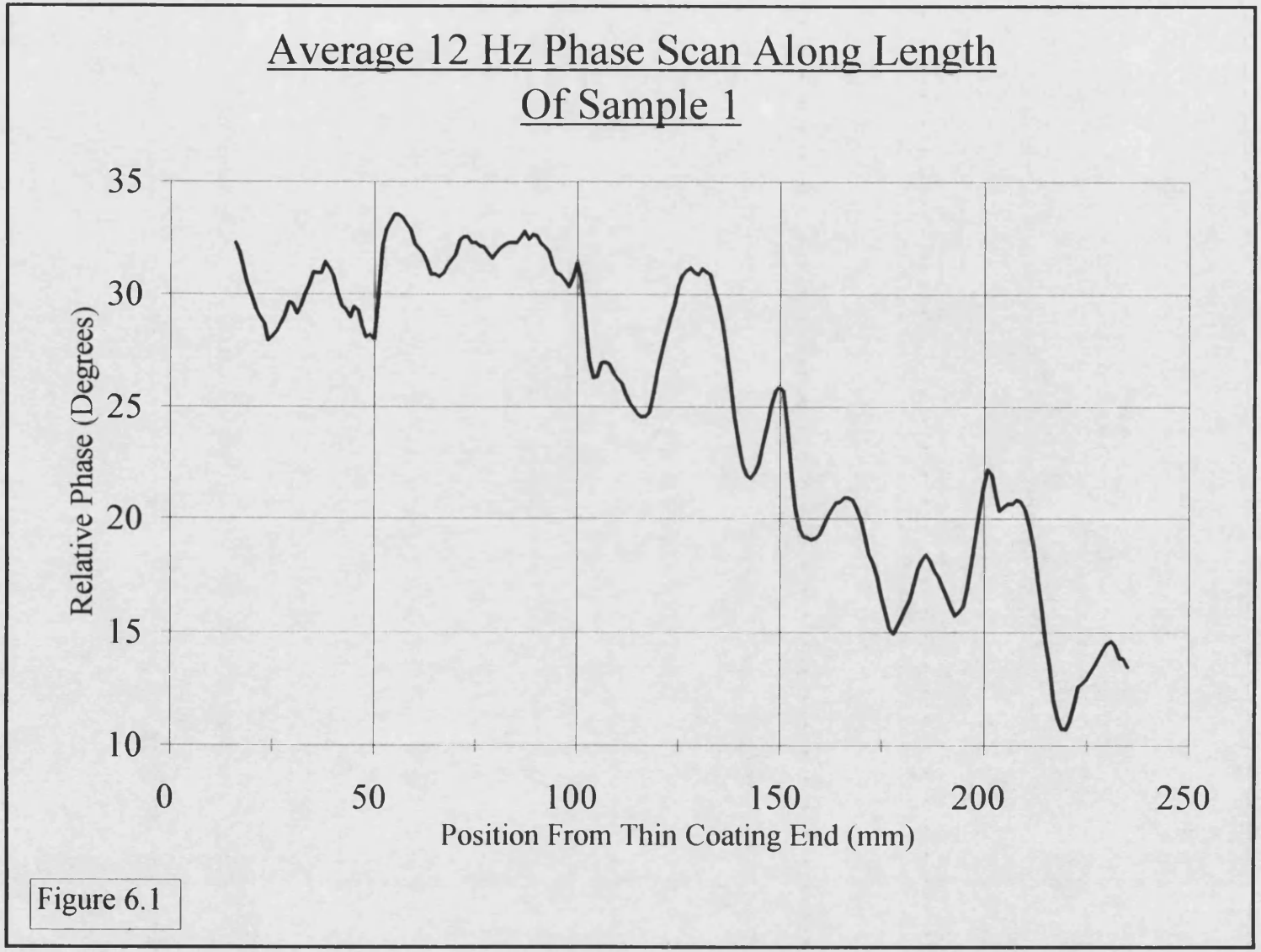
Average 12 Hz Phase Scan Along Length Of Sample 1
Relative Phase (Degrees)
35
30
25
20
15
10
0
50
100
150
200
250
Position From Thin Coating End (mm)

Figure 6.1

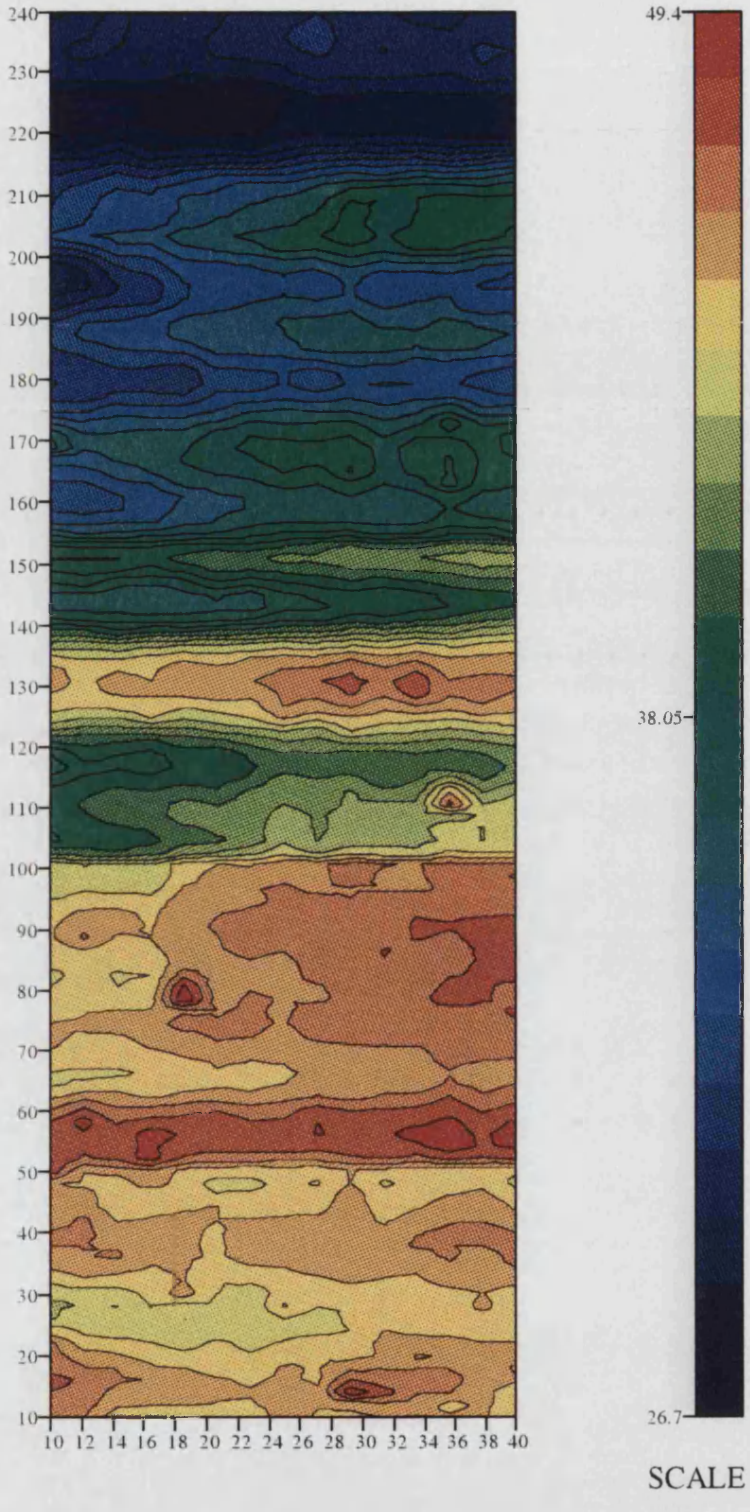

Area Phase Scan Of Sample 1

Figure 6.2

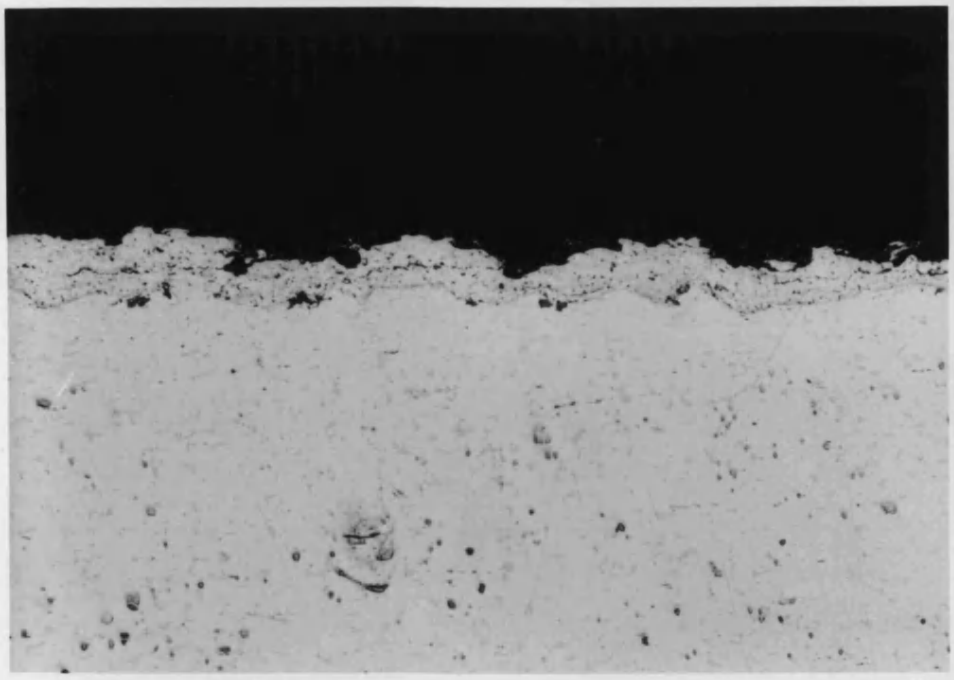

Micrograph 1 : Step 2

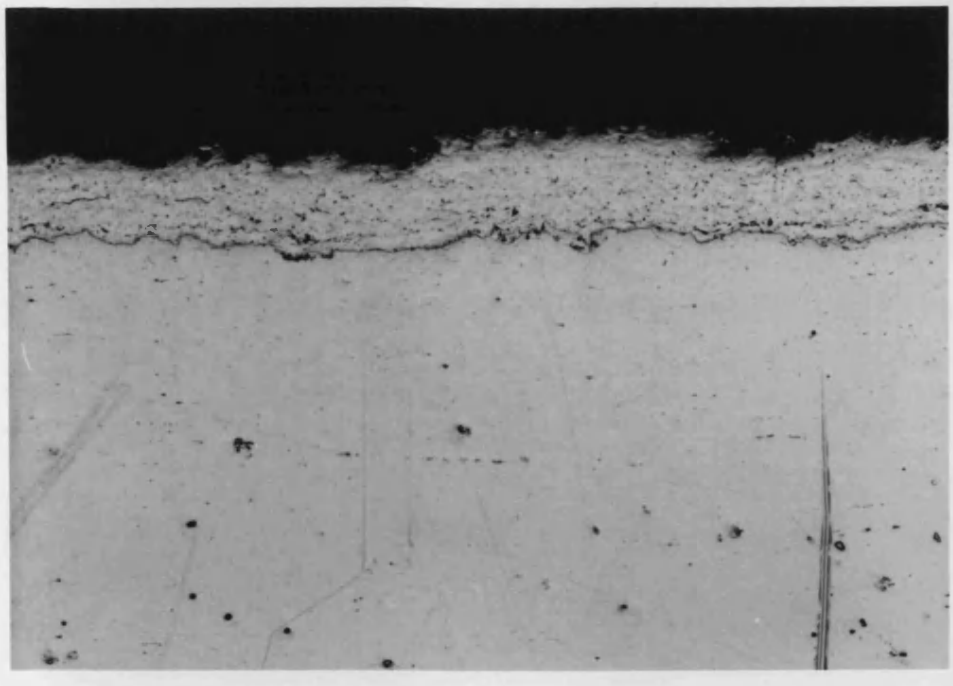

Micrograph 2 : Step 3

Scale :
100μm

Figure 6.3a

Micrographs Of Sample 1

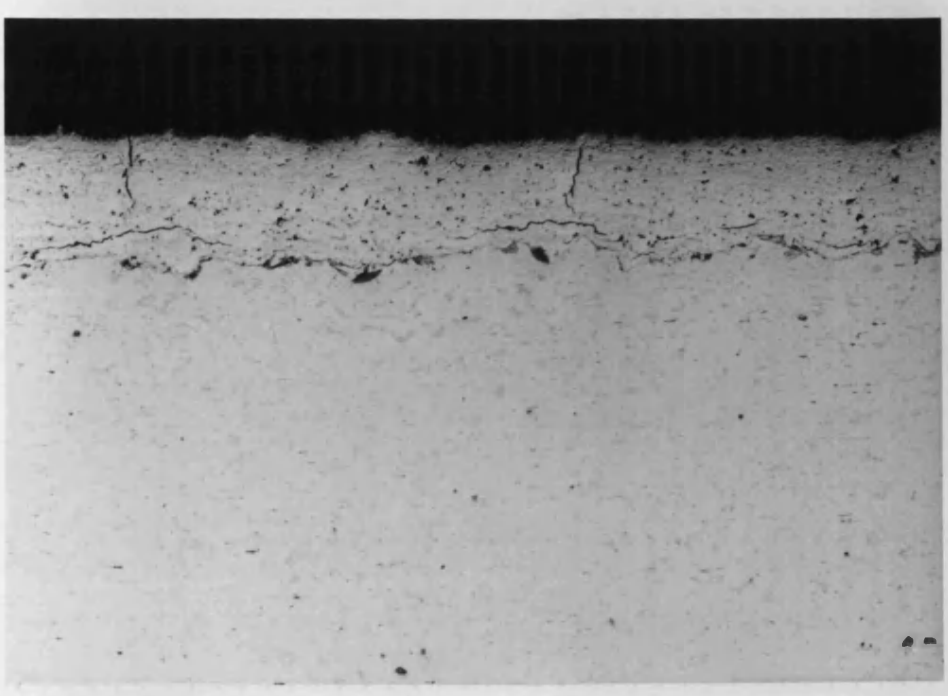

Micrograph 3 : Step 4

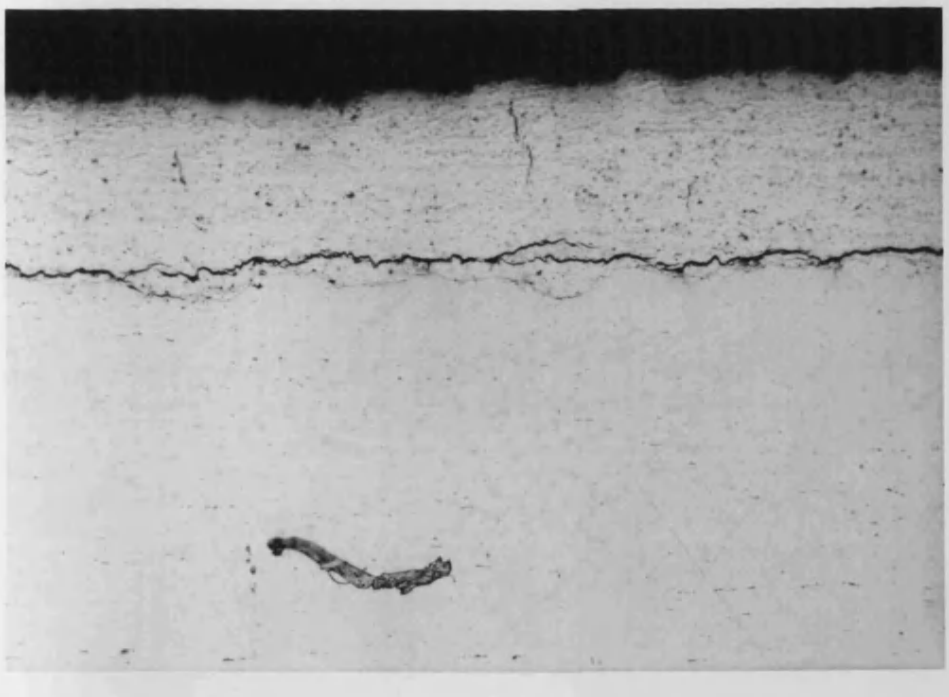

Micrograph 4 : Step 5

Scale :
100μm

Figure 6.3b

Micrographs Of Sample 1

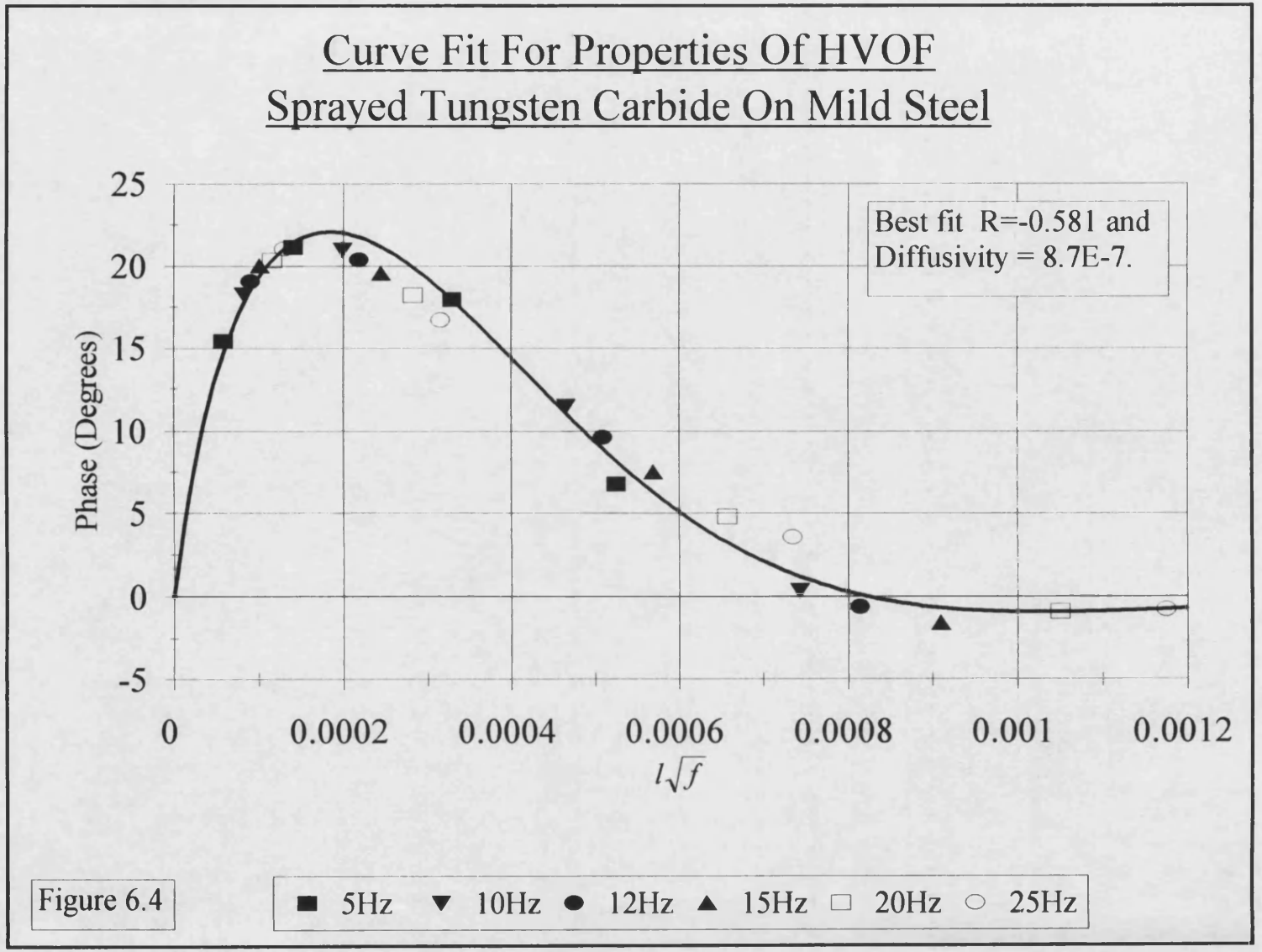
Curve Fit For Properties Of HVOF
Sprayed Tungsten Carbide On Mild Steel
Best fit R=-0.581 and
Diffusivity = 8.7E-7.
Phase (Degrees)
25
20
15
10
5
0
-5
0
0.0002
0.0004
0.0006
0.0008
0.001
0.0012
$l\sqrt{f}$
5Hz
10Hz
12Hz
15Hz
20Hz
25Hz

Figure 6.4

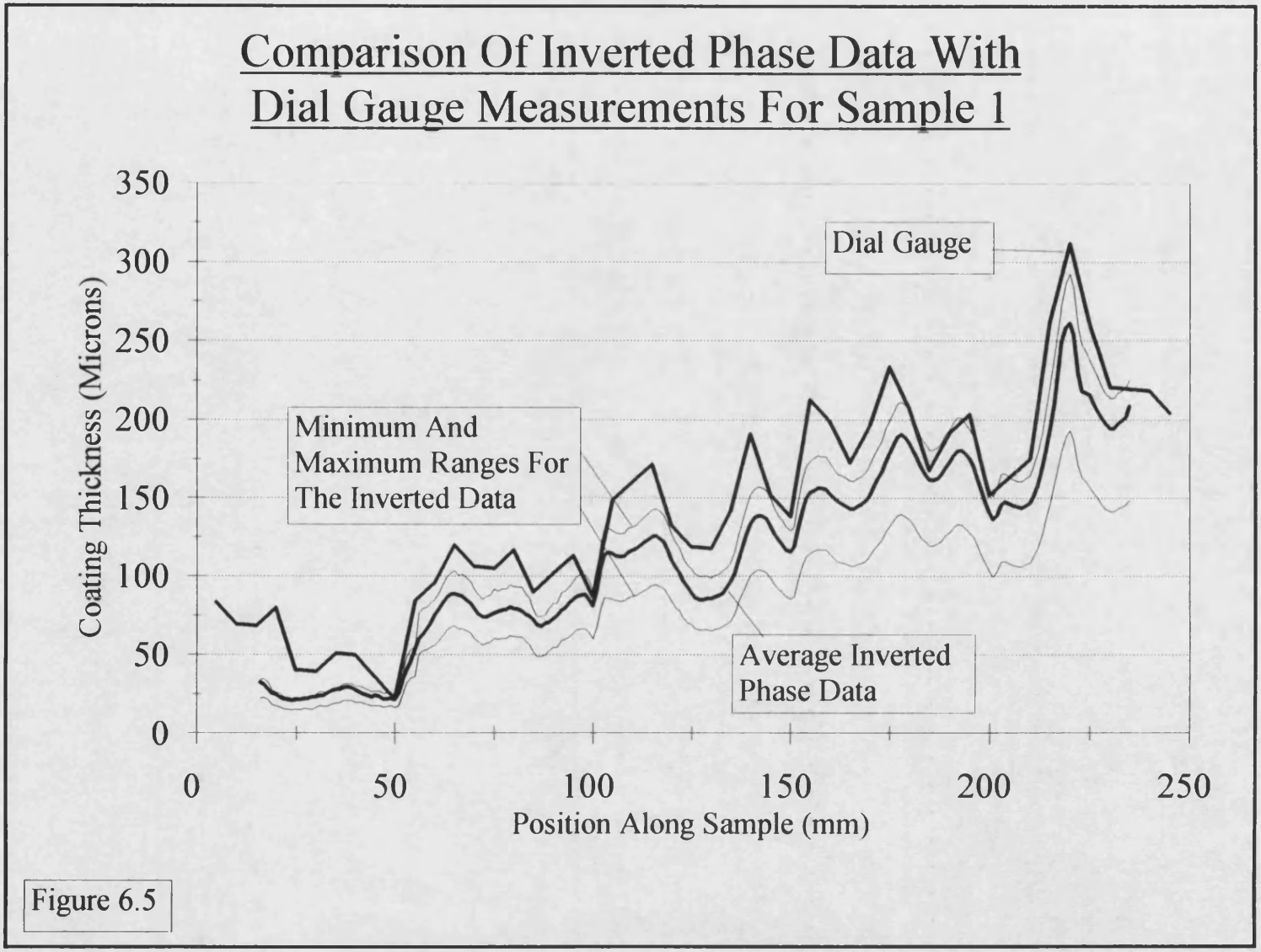
Comparison Of Inverted Phase Data With
Dial Gauge Measurements For Sample 1
Coating Thickness (Microns)
350
300
250
200
150
100
50
0
0
50
100
150
200
250
Position Along Sample (mm)
Dial Gauge
Minimum And
Maximum Ranges For
The Inverted Data
Average Inverted
Phase Data

Figure 6.5

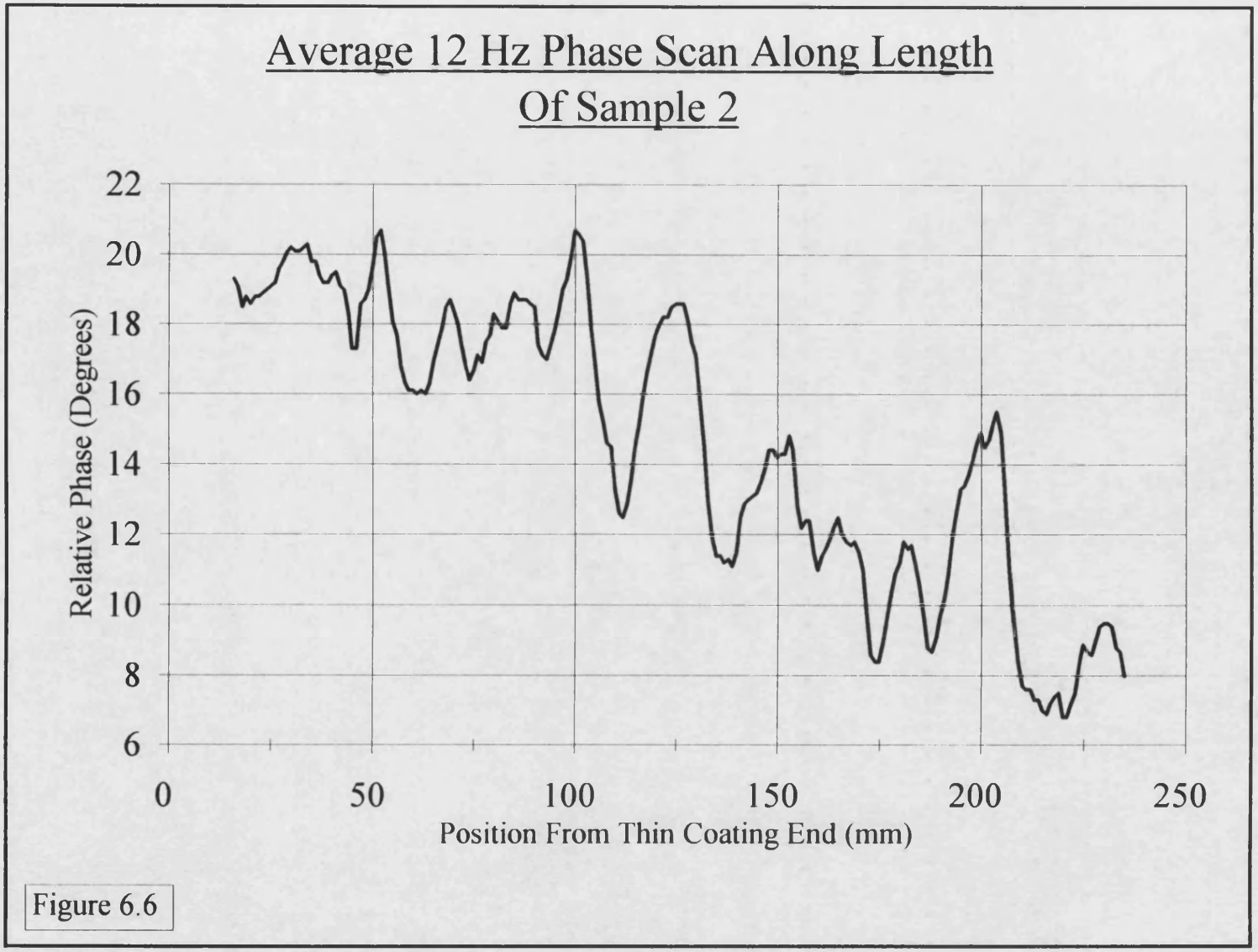
Average 12 Hz Phase Scan Along Length Of Sample 2
Relative Phase (Degrees)
22
20
18
16
14
12
10
8
6
0
50
100
150
200
250
Position From Thin Coating End (mm)

Figure 6.6

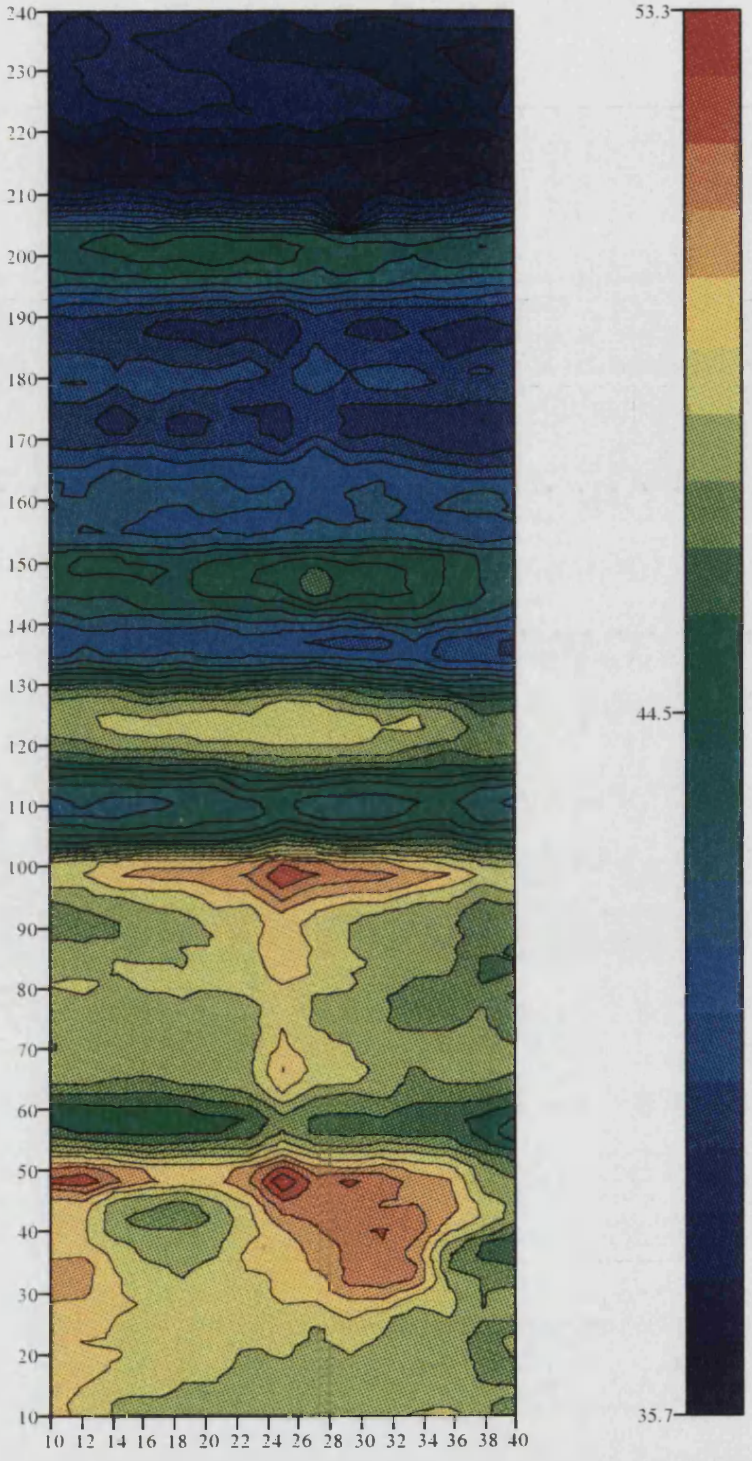

Area Phase Scan Of Sample 2

Figure 6.7

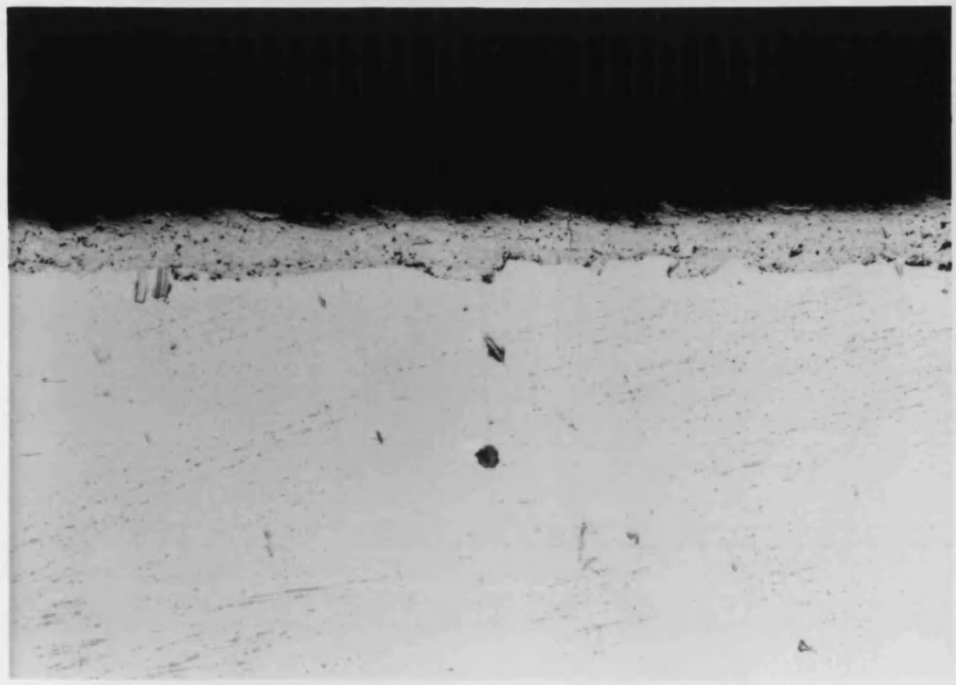

Micrograph 1 : Step 2

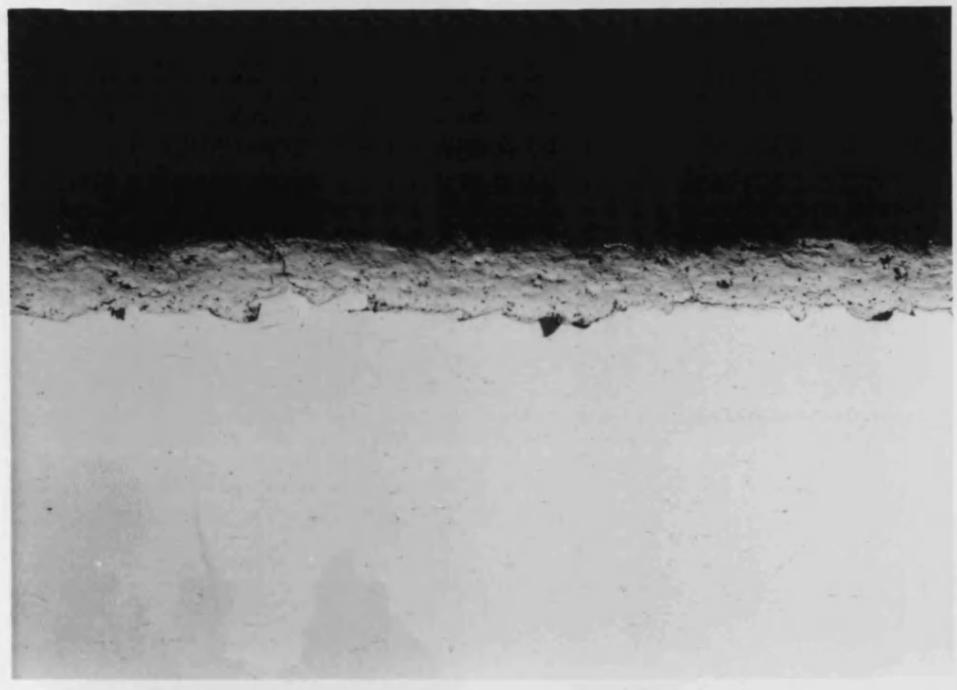

Micrograph 2 : Step 3

Scale :
100μm

Figure 6.8a

Micrographs Of Sample 2

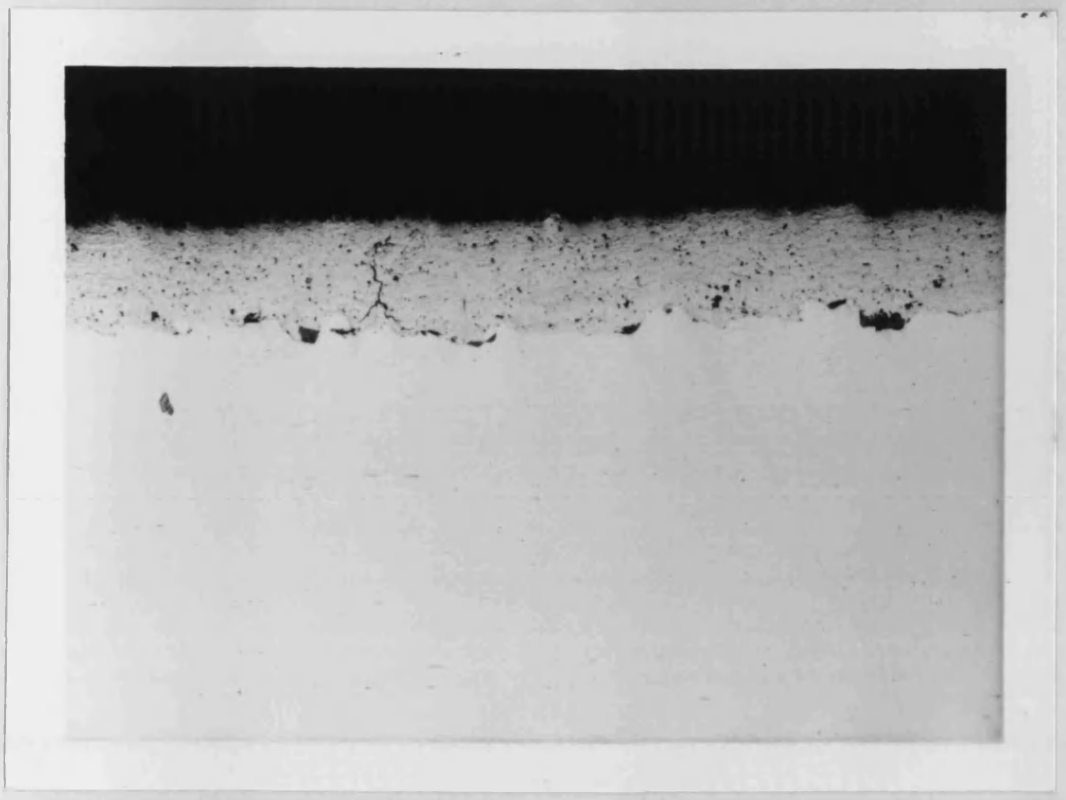

Micrograph 3 : Step 4

Micrograph 4 : Step 5

Scale :
100μm

Figure 6.8b

Micrographs Of Sample 2

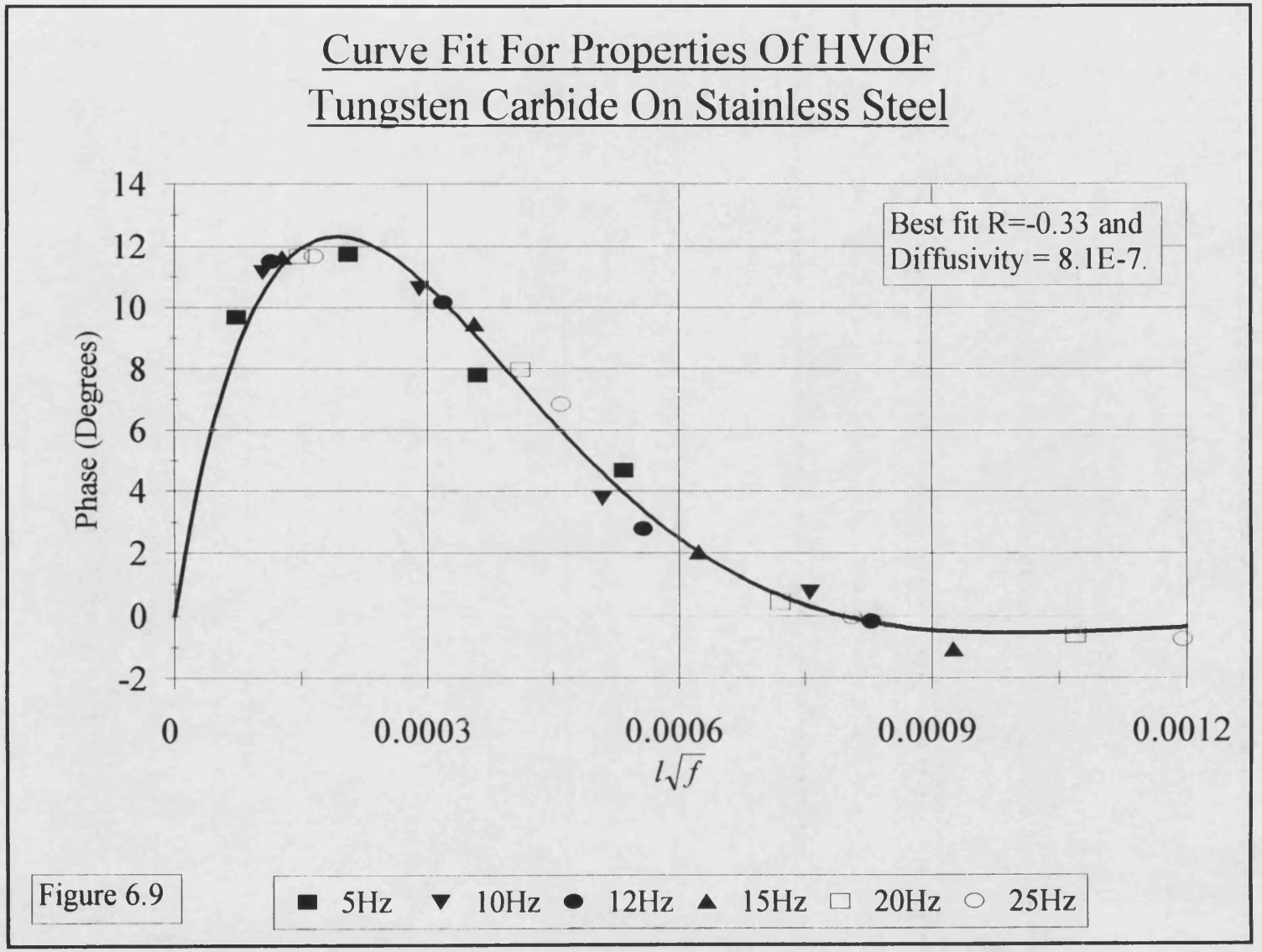
Curve Fit For Properties Of HVOF
Tungsten Carbide On Stainless Steel
Best fit R=-0.33 and
Diffusivity = 8.1E-7.
Phase (Degrees)
14
12
10
8
6
4
2
0
-2
0
0.0003
0.0006
0.0009
0.0012
$l\sqrt{f}$
5Hz
10Hz
12Hz
15Hz
20Hz
25Hz

Figure 6.9

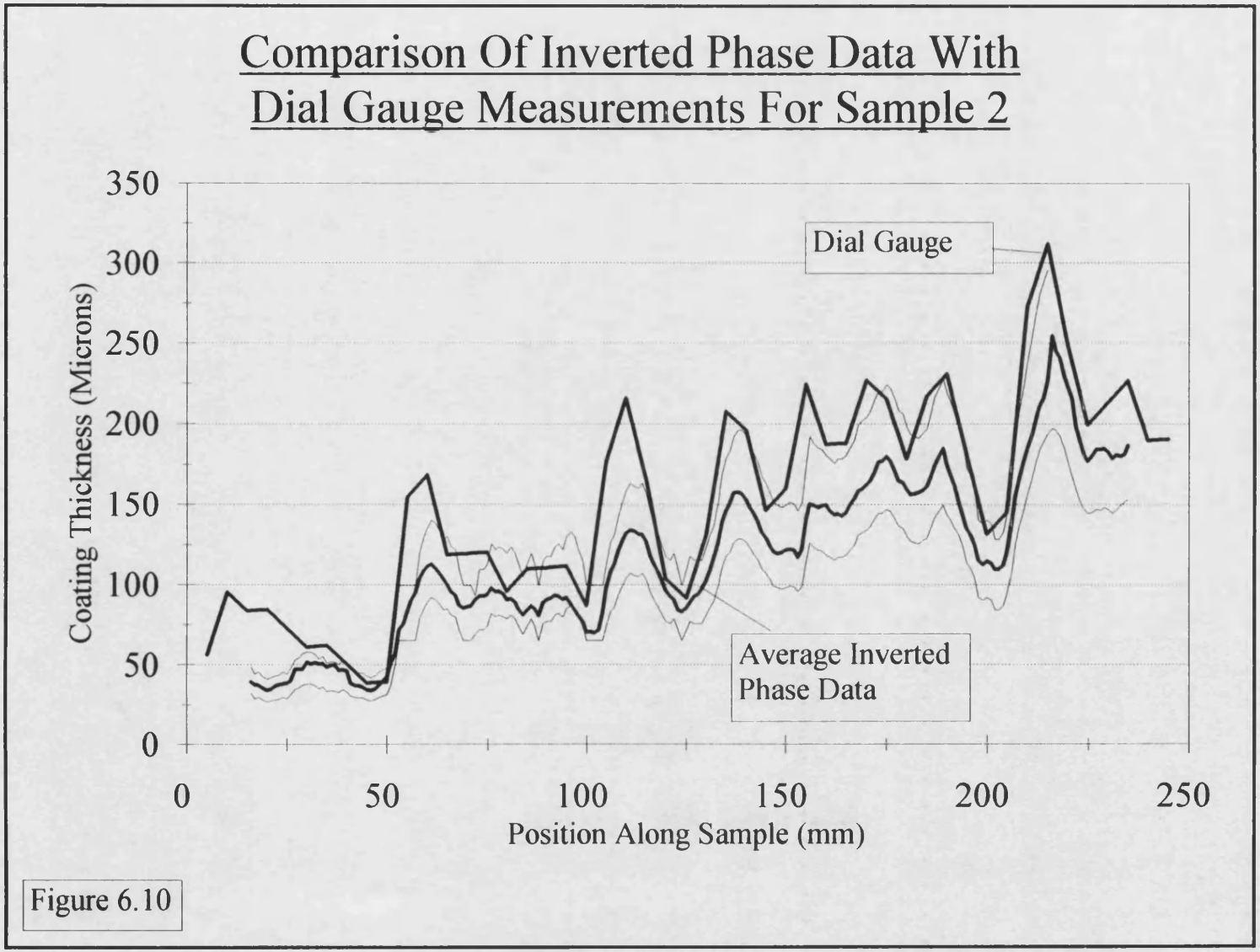
Comparison Of Inverted Phase Data With
Dial Gauge Measurements For Sample 2
Coating Thickness (Microns)
350
300
250
200
150
100
50
0
0
50
100
150
200
250
Position Along Sample (mm)
Dial Gauge
Average Inverted
Phase Data

Figure 6.10

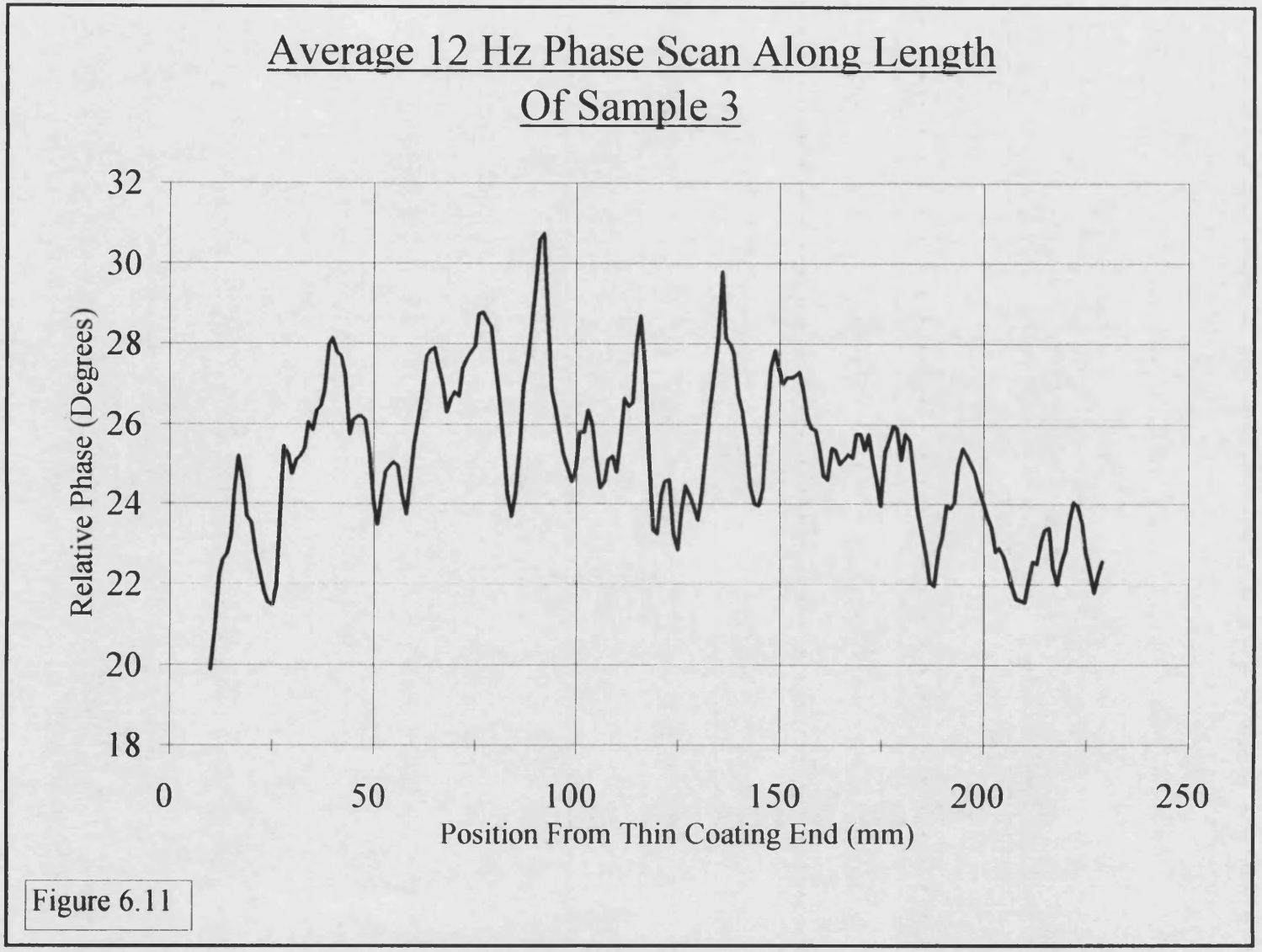
Average 12 Hz Phase Scan Along Length Of Sample 3
Relative Phase (Degrees)
32
30
28
26
24
22
20
18
0
50
100
150
200
250
Position From Thin Coating End (mm)

Figure 6.11

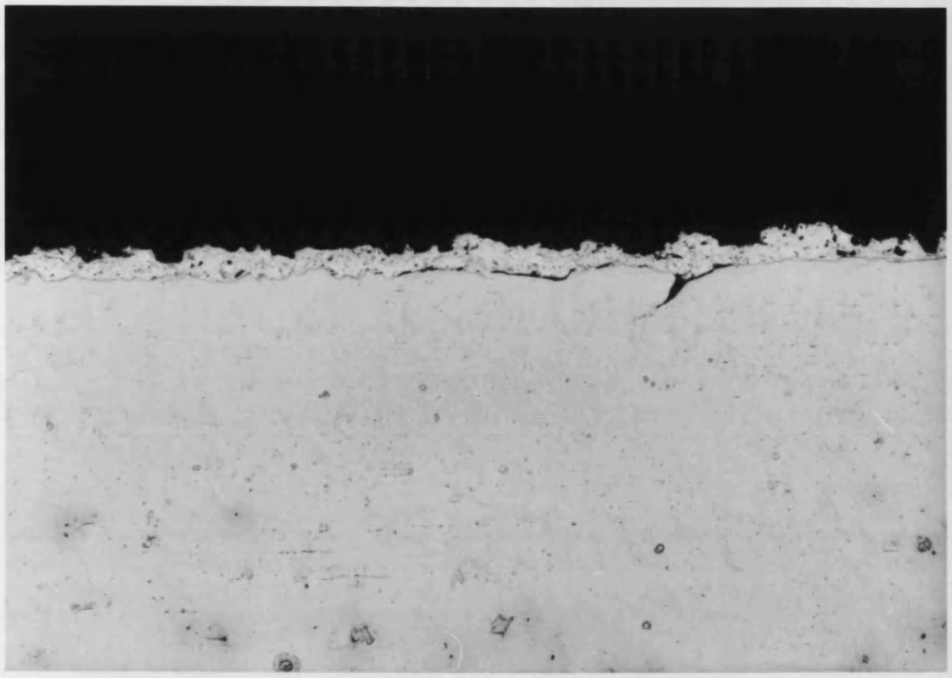

Micrograph 1 : Step 2

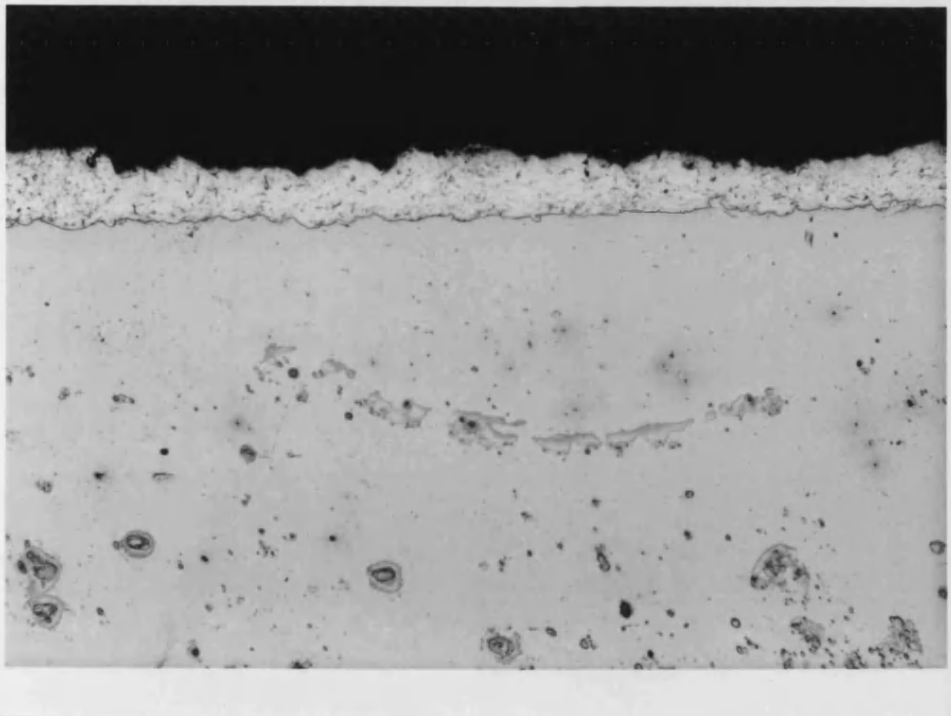

Micrograph 2 : Step 3

Scale :
100μm

Figure 6.12a

Micrographs Of Sample 3

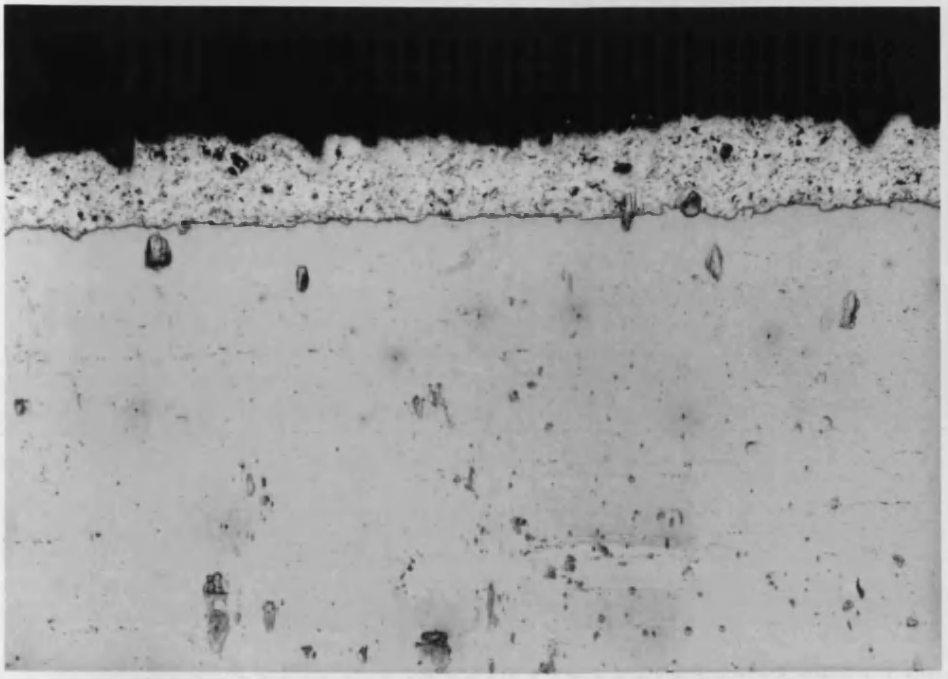

Micrograph 3 : Step 4

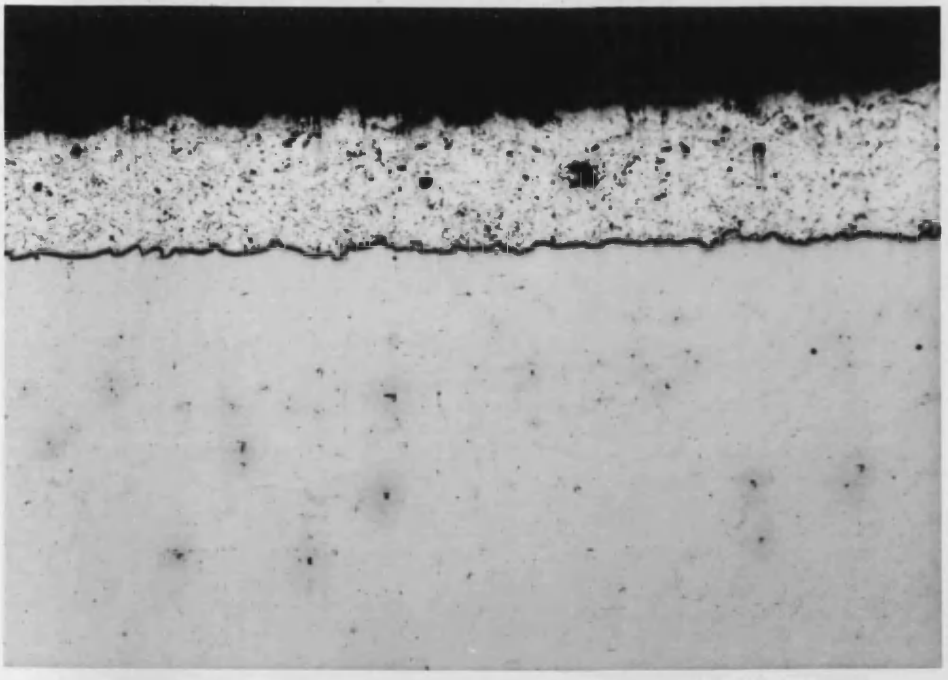

Micrograph 4 : Step 5

Scale :
100μm

Figure 6.12b

Micrographs Of Sample 3

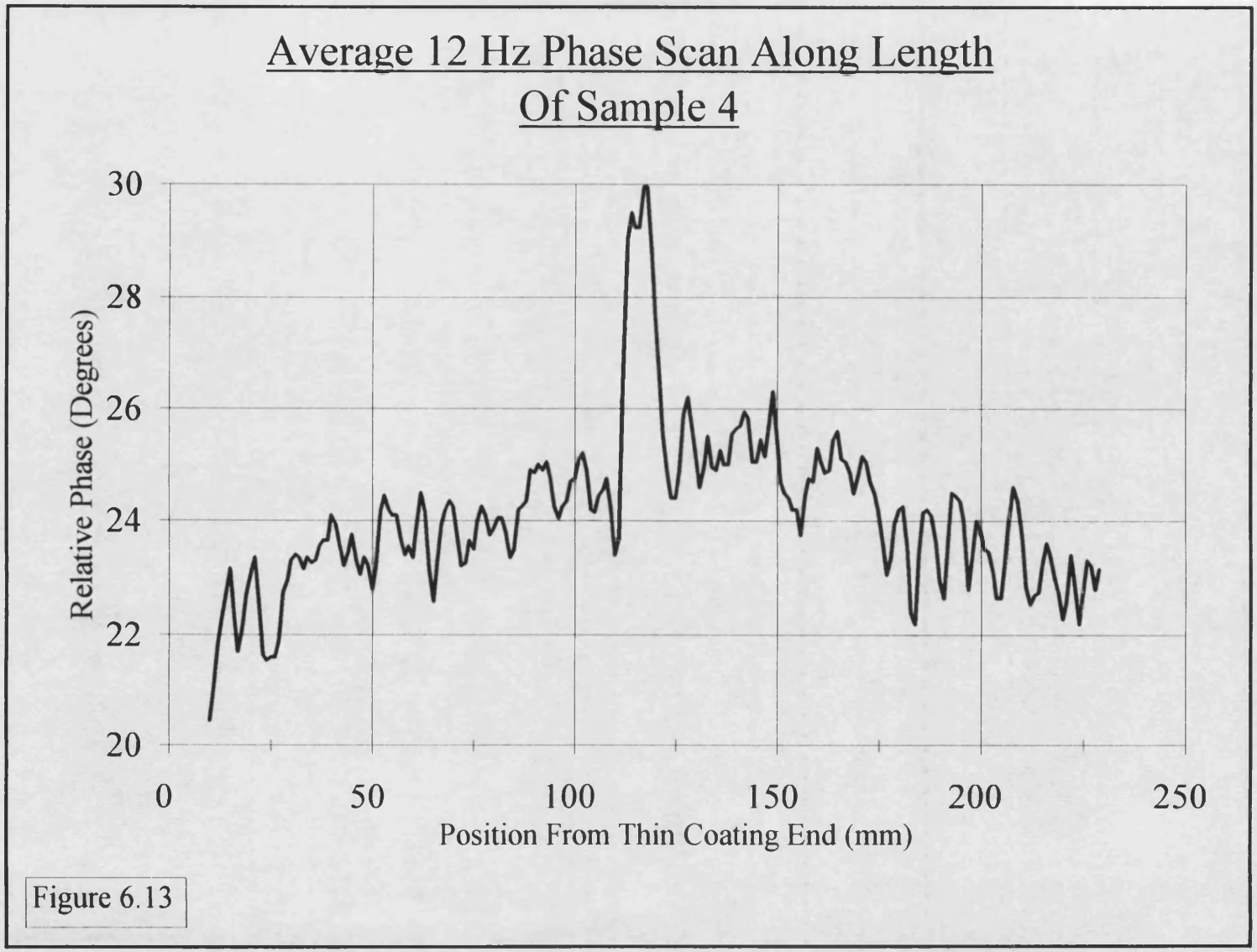
Average 12 Hz Phase Scan Along Length
Of Sample 4
Relative Phase (Degrees)
30
28
26
24
22
20
0
50
100
150
200
250
Position From Thin Coating End (mm)

Figure 6.13

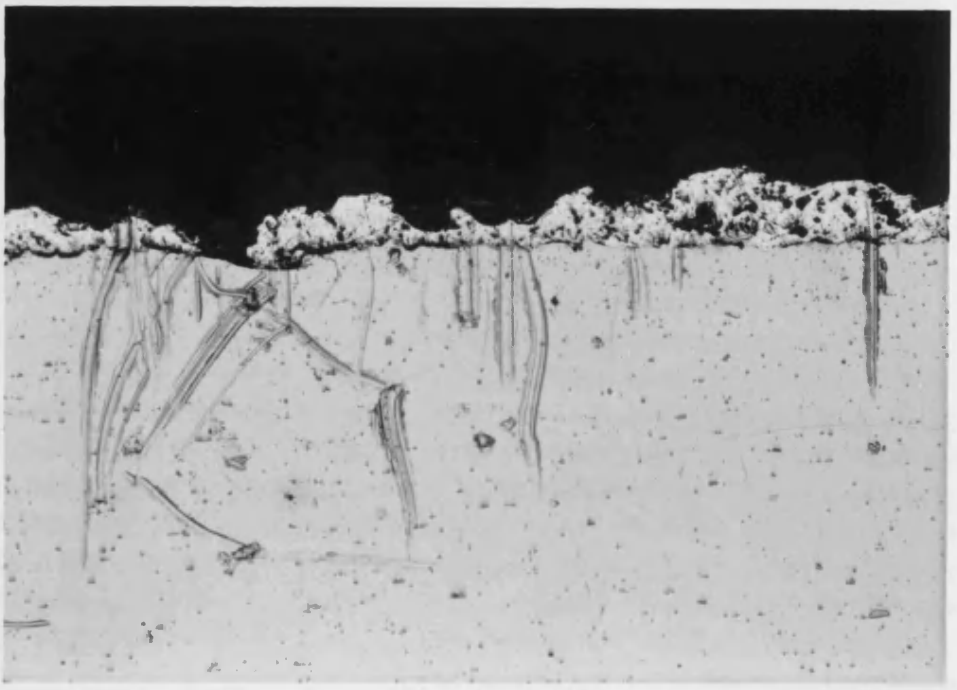

Micrograph 1 : Step 2

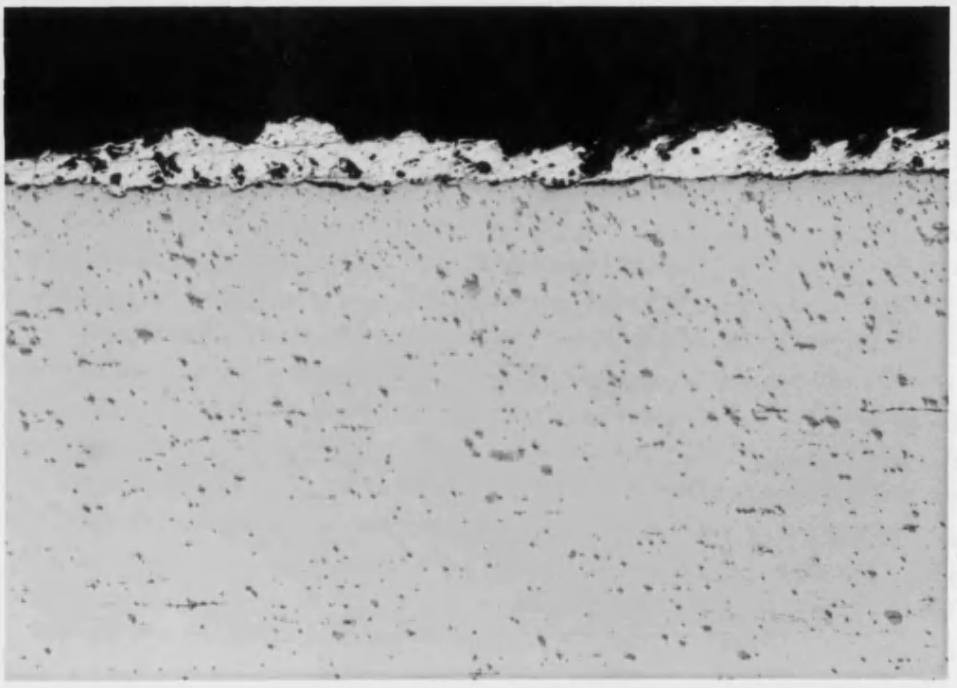

Micrograph 2 : Step 3

Scale :
100μm

Figure 6.14a

Micrographs Of Sample 4

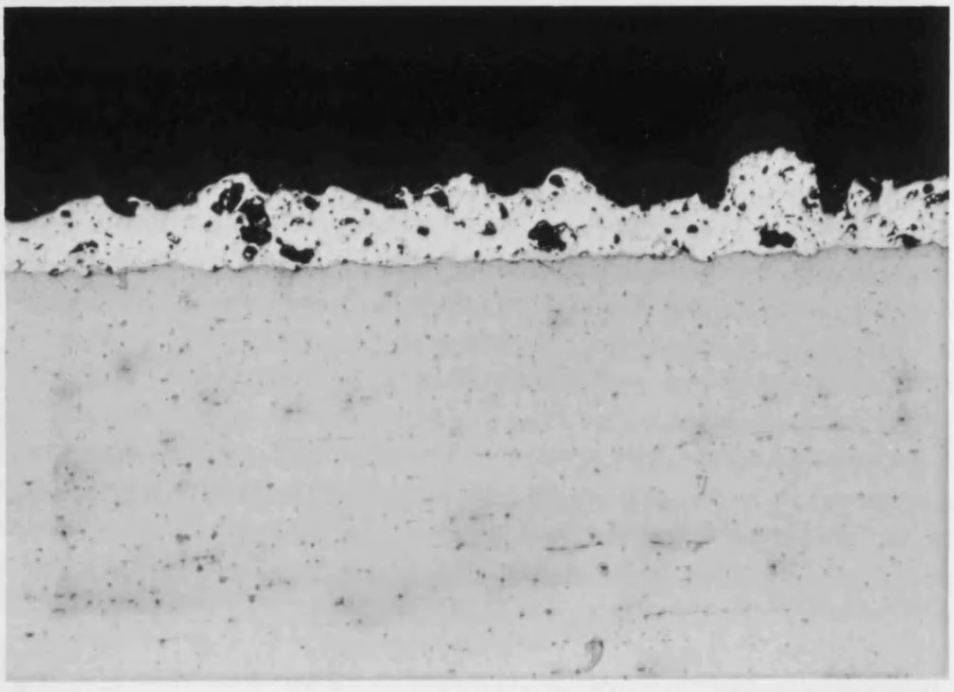

Micrograph 3 : Step 4

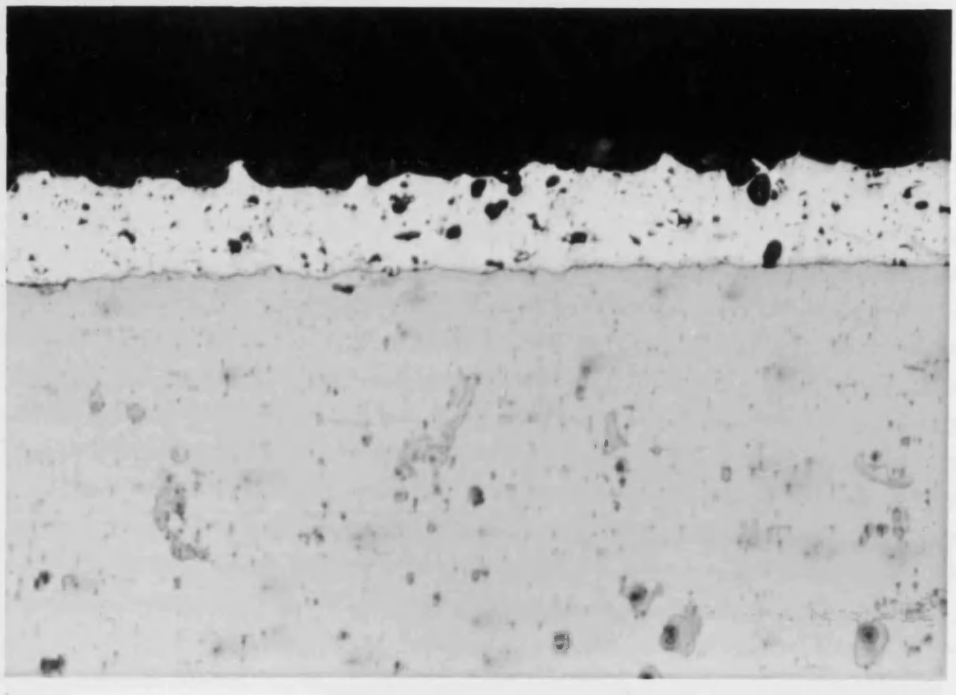

Micrograph 4 : Step 5

Scale :
100μm

Figure 6.14b

Micrographs Of Sample 4

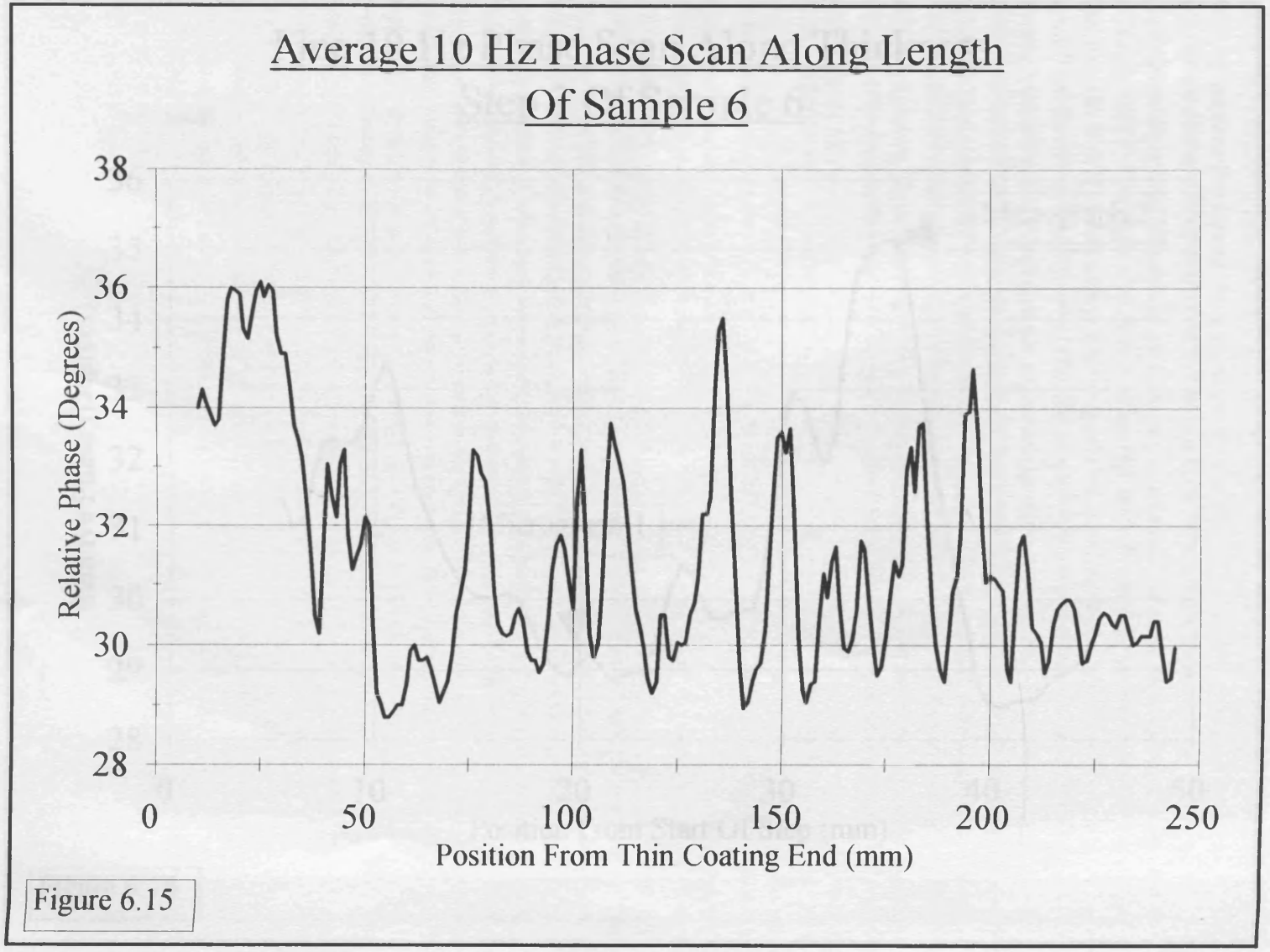
Average 10 Hz Phase Scan Along Length Of Sample 6
Relative Phase (Degrees)
38
36
34
32
30
28
0
50
100
150
200
250
Position From Thin Coating End (mm)

Figure 6.15

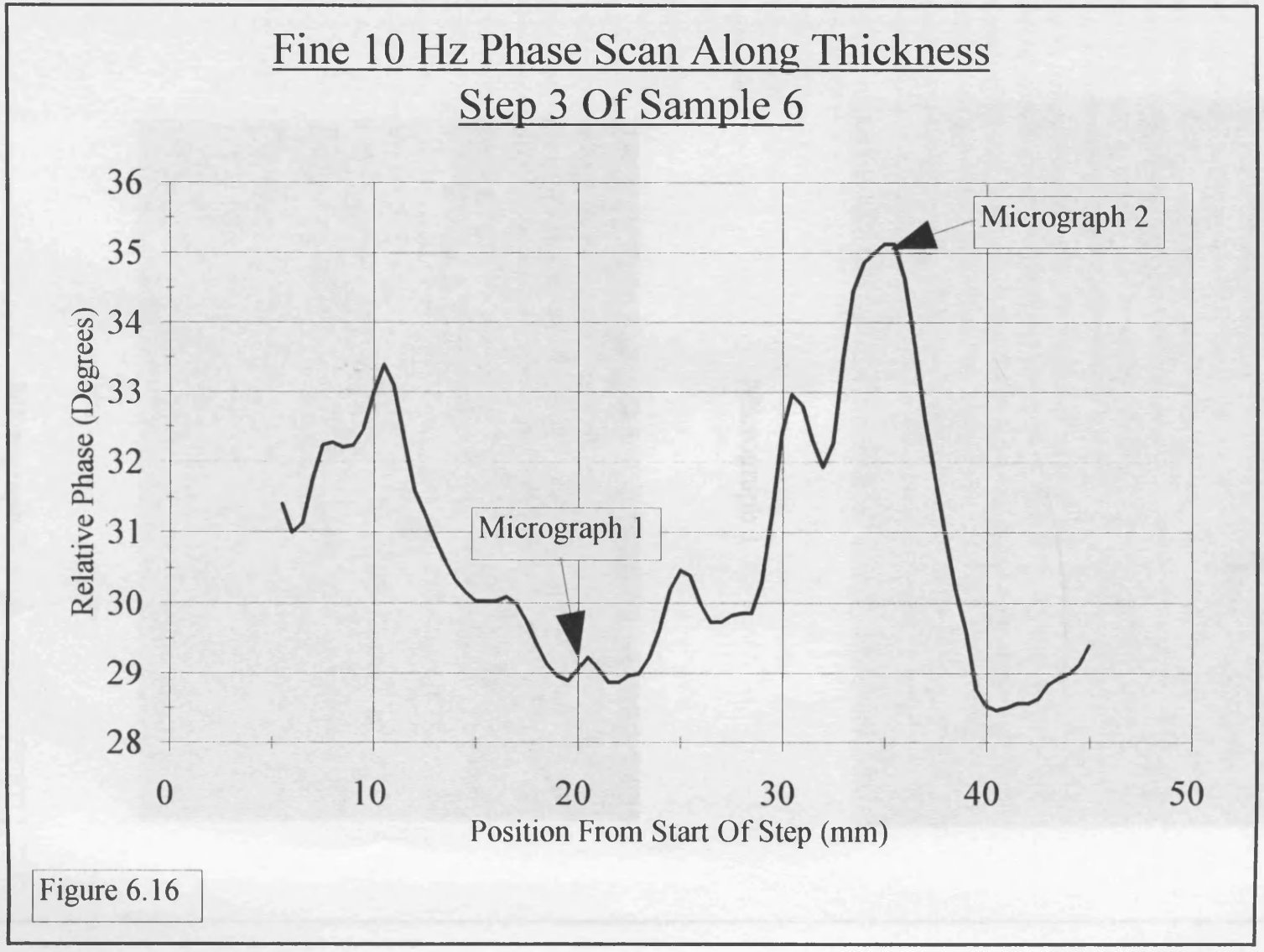
Fine 10 Hz Phase Scan Along Thickness
Step 3 Of Sample 6
Relative Phase (Degrees)
36
35
34
33
32
31
30
29
28
0
10
20
30
40
50
Position From Start Of Step (mm)
Micrograph 1
Micrograph 2

Figure 6.16

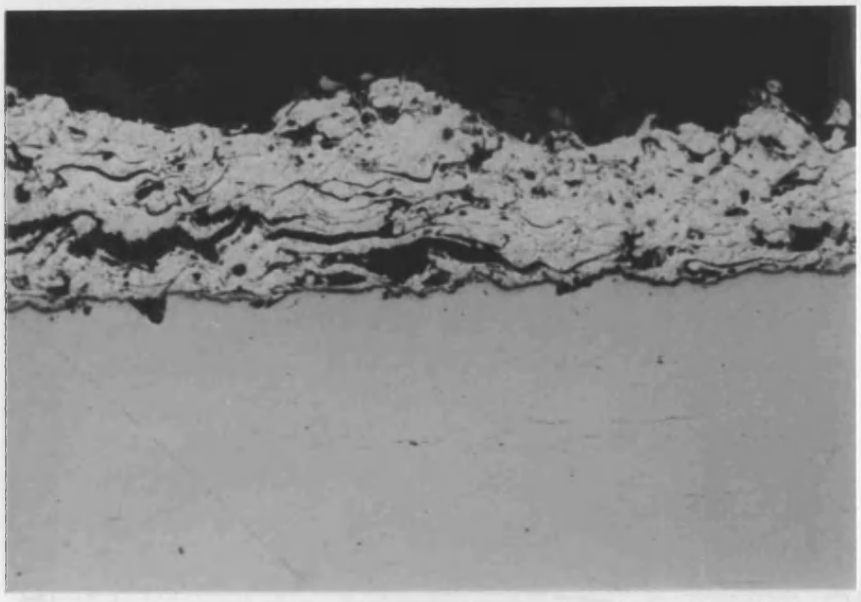

Micrograph 1

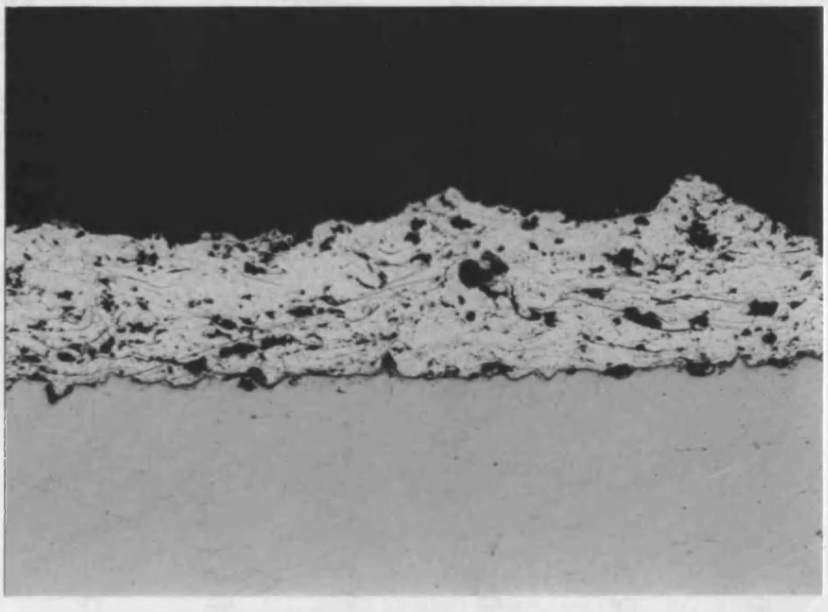

Micrograph 2

Figure 6.17

Micrographs Of Sample 6

Scale :
50μm

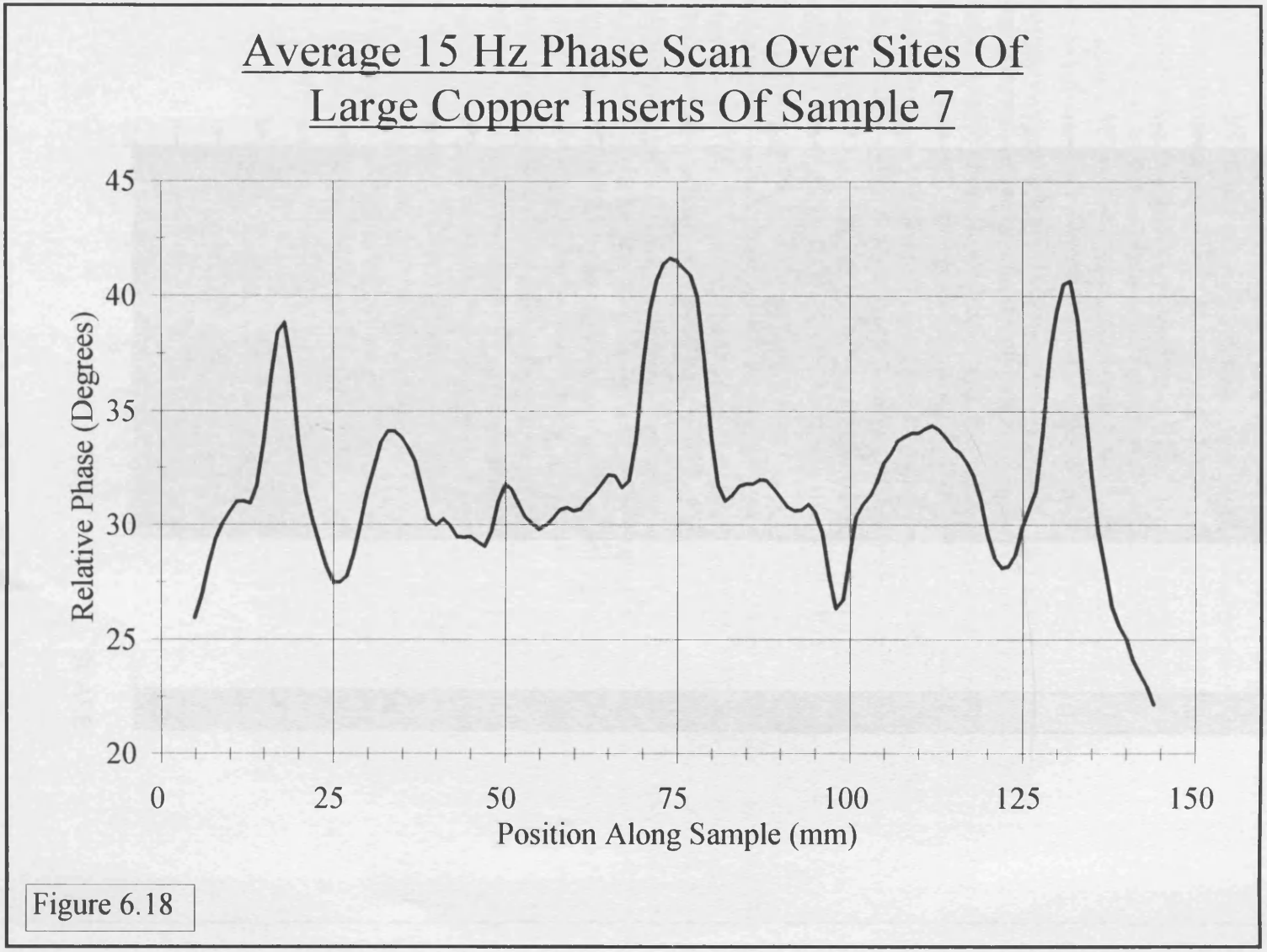
Average 15 Hz Phase Scan Over Sites Of
Large Copper Inserts Of Sample 7
Relative Phase (Degrees)
45
40
35
30
25
20
0
25
50
75
100
125
150
Position Along Sample (mm)

Figure 6.18

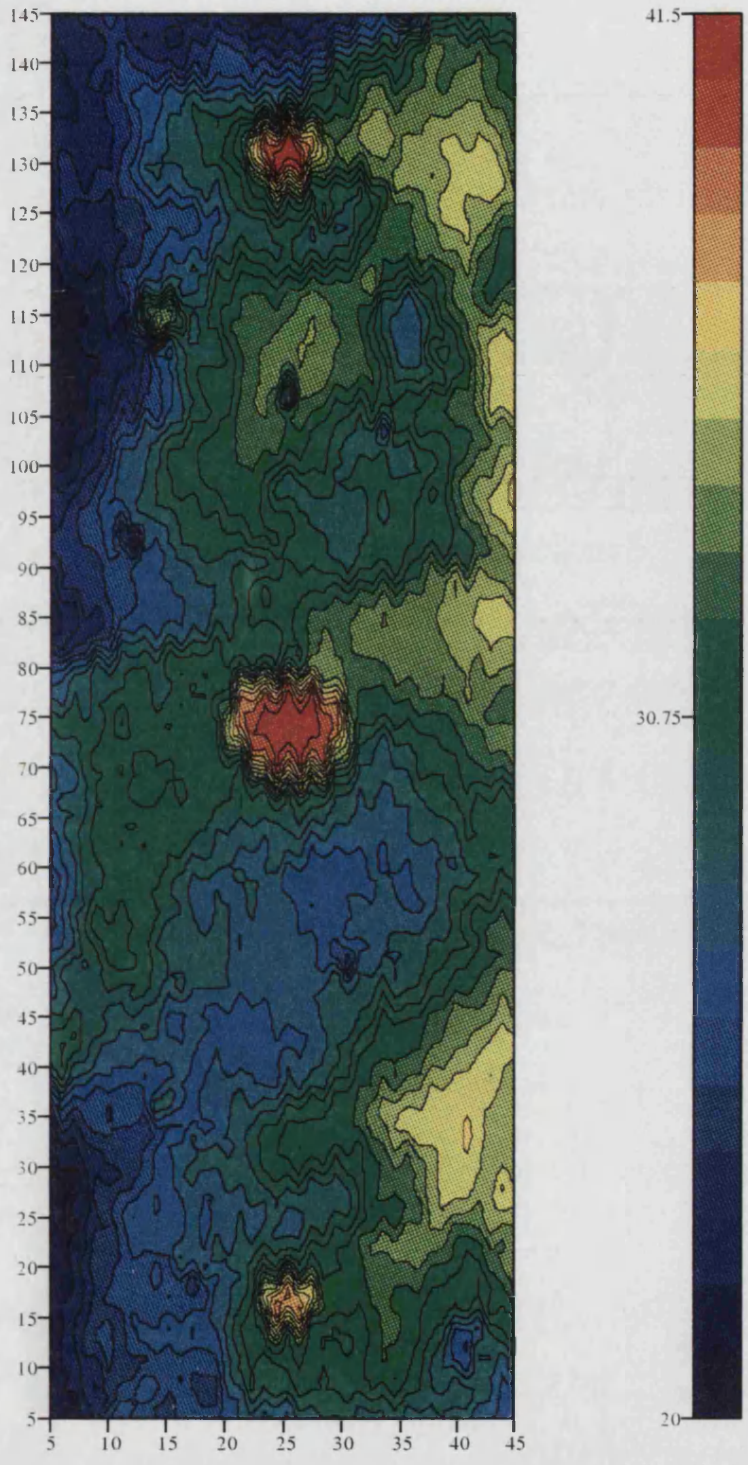

Area Phase Scan Of Sample 7

Figure 6.19

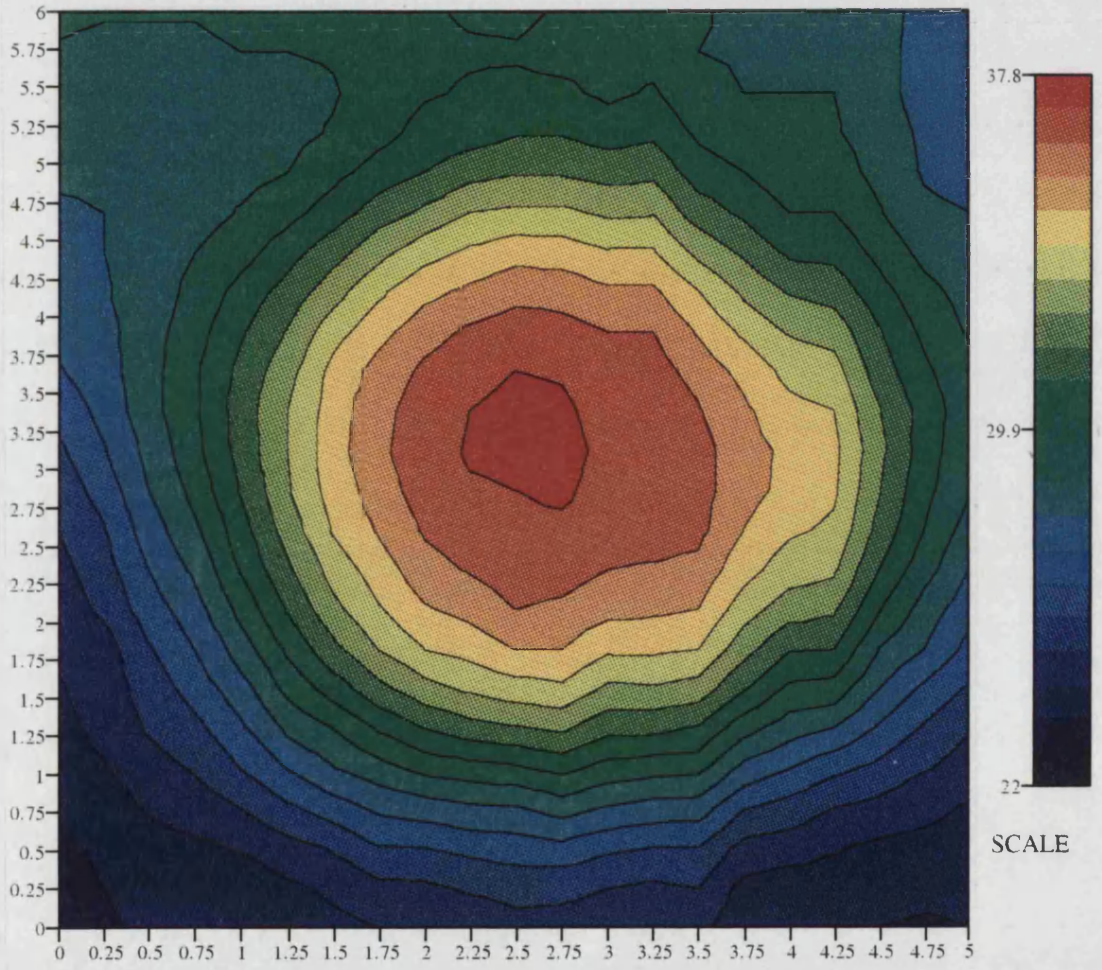

Area Scan Over Site Of 3mm Diameter

Copper Insert Of Sample 7

Figure 6.20

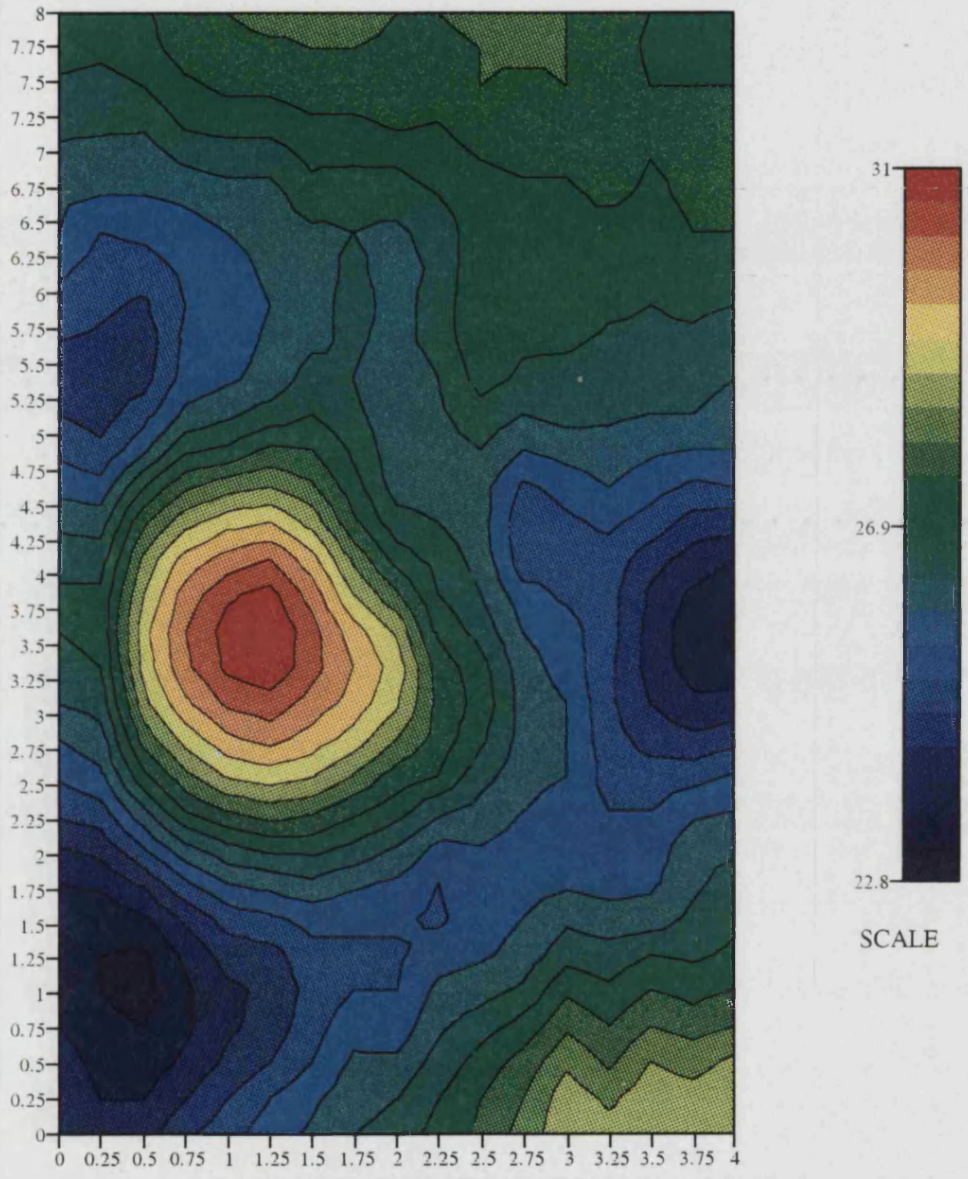

Area Scan Over Site Of 2mm Diameter

Copper Insert Of Sample 7

Figure 6.21

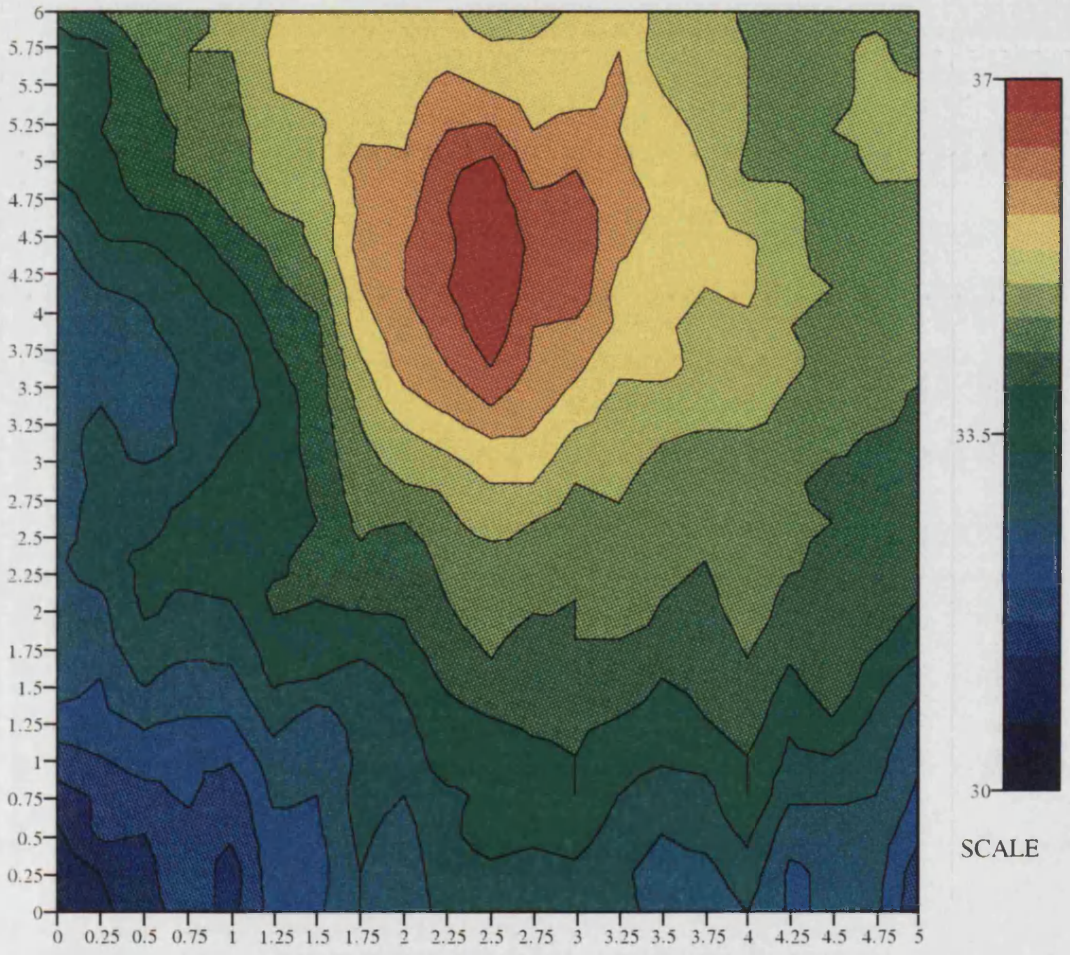

Area Scan Over Site Of 1mm Diameter

Copper Insert Of Sample 7

Figure 6.22

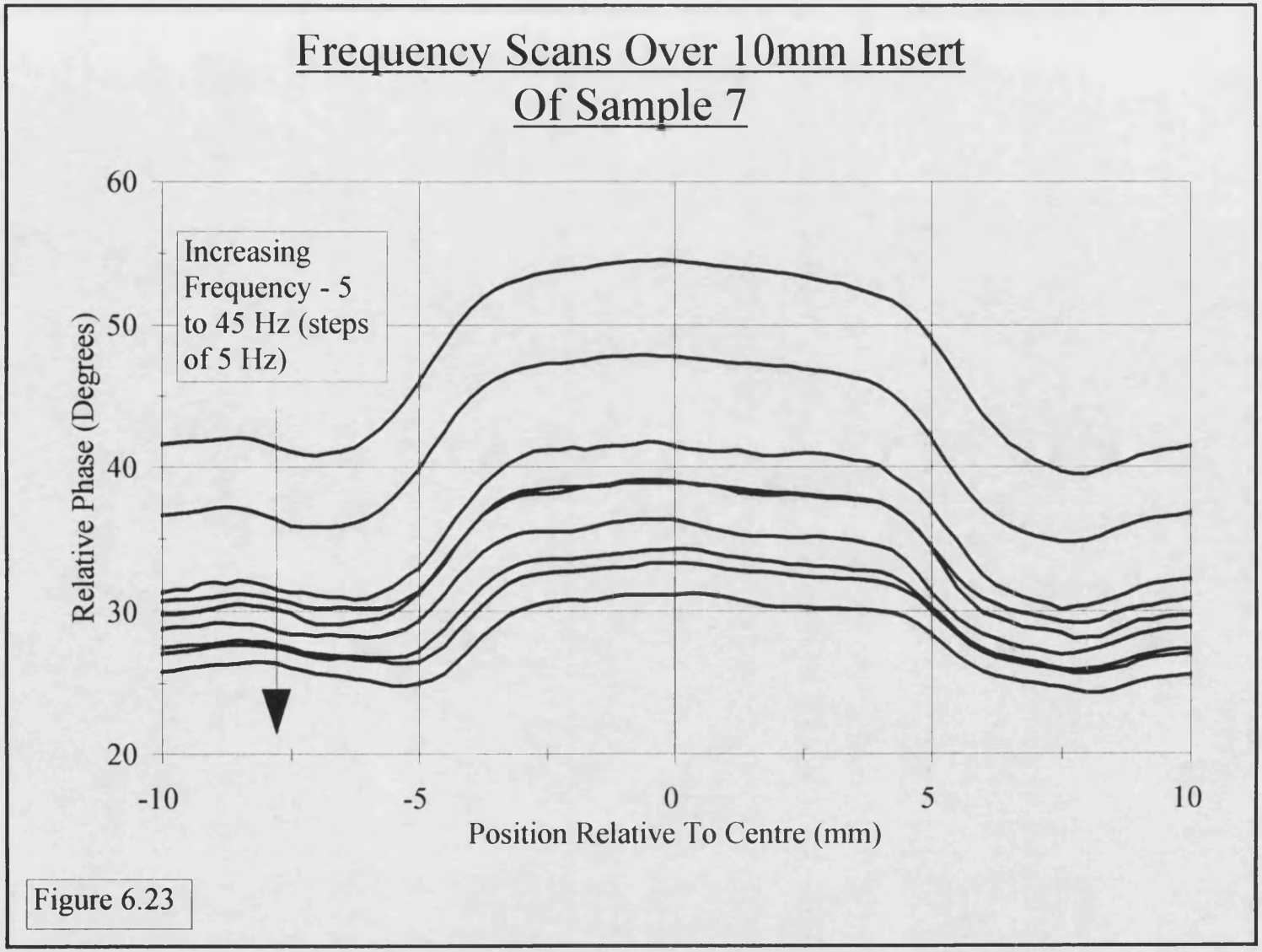
Frequency Scans Over 10mm Insert Of Sample 7
Increasing Frequency - 5 to 45 Hz (steps of 5 Hz)
Relative Phase (Degrees)
60
50
40
30
20
-10
-5
0
5
10
Position Relative To Centre (mm)

Figure 6.23

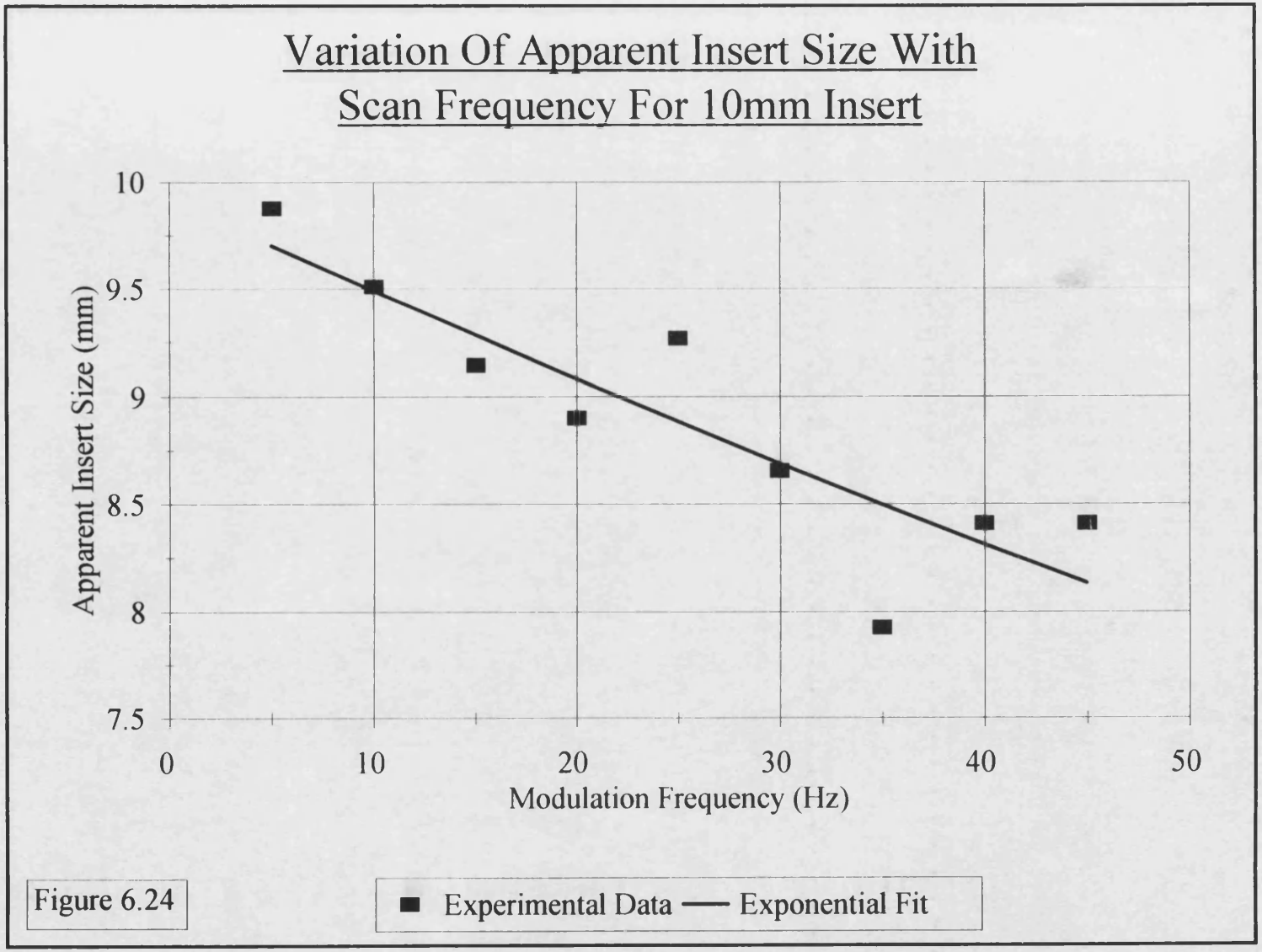
Variation Of Apparent Insert Size With Scan Frequency For 10mm Insert
Apparent Insert Size (mm)
10
9.5
9
8.5
8
7.5
0
10
20
30
40
50
Modulation Frequency (Hz)
Experimental Data
Exponential Fit

Figure 6.24

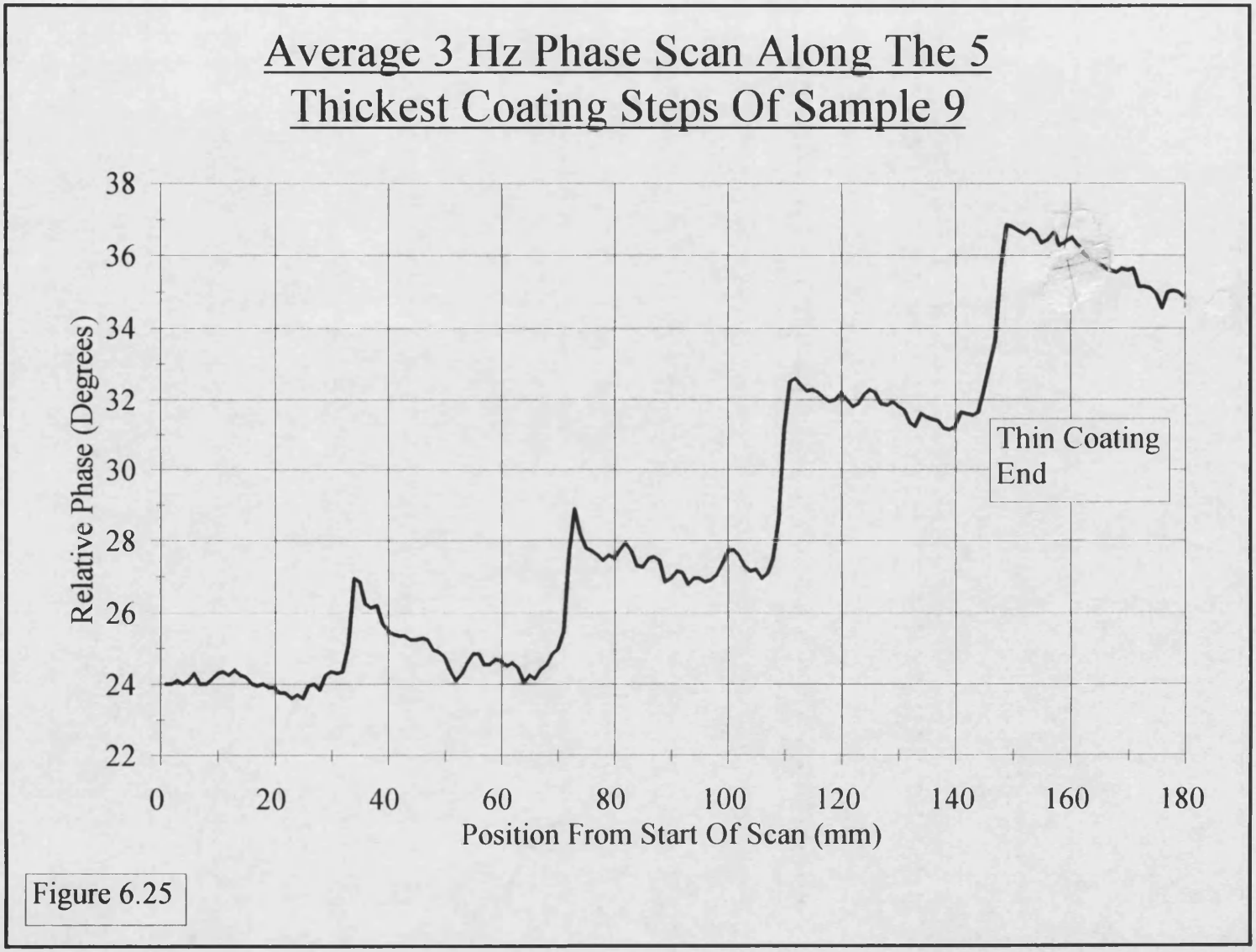
Average 3 Hz Phase Scan Along The 5 Thickest Coating Steps Of Sample 9
Relative Phase (Degrees)
38
36
34
32
30
28
26
24
22
0
20
40
60
80
100
120
140
160
180
Position From Start Of Scan (mm)
Thin Coating End

Figure 6.25

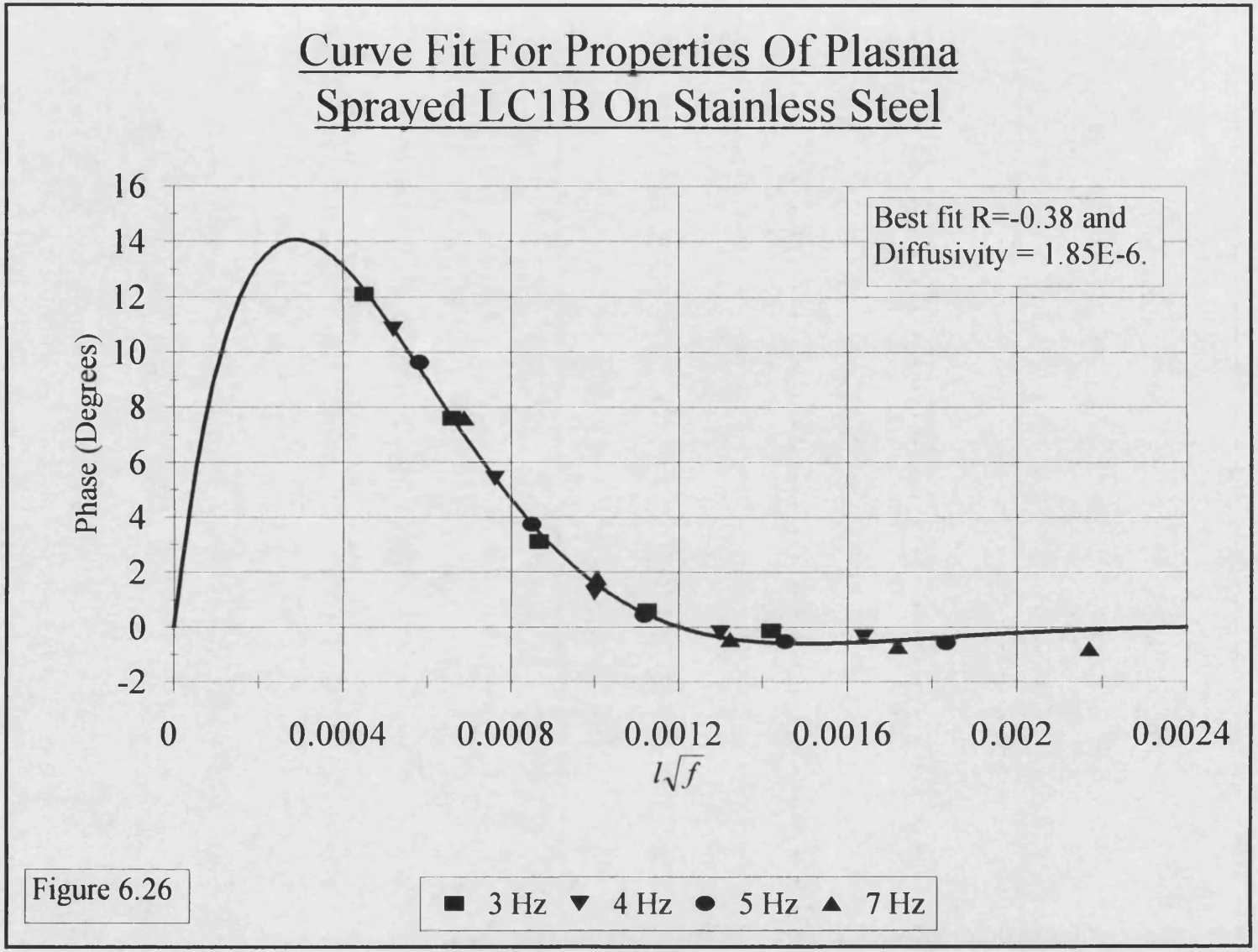
Curve Fit For Properties Of Plasma Sprayed LC1B On Stainless Steel
Best fit R=-0.38 and Diffusivity = 1.85E-6.
Phase (Degrees)
16
14
12
10
8
6
4
2
0
-2
0
0.0004
0.0008
0.0012
0.0016
0.002
0.0024
$l\sqrt{f}$
3 Hz
4 Hz
5 Hz
7 Hz

Figure 6.26

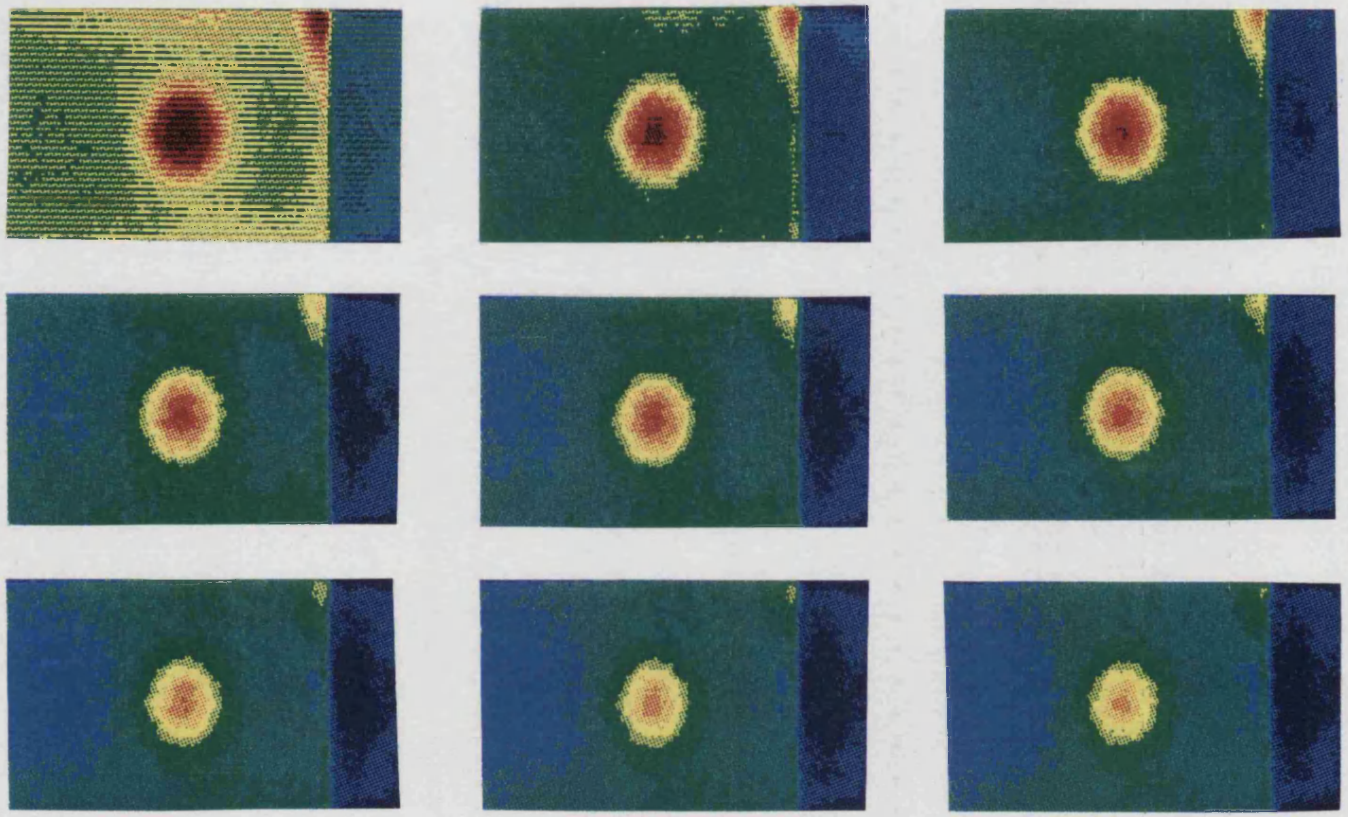

Frames 2-10 Of Transient Experiment
On Sample 10

Figure 6.27

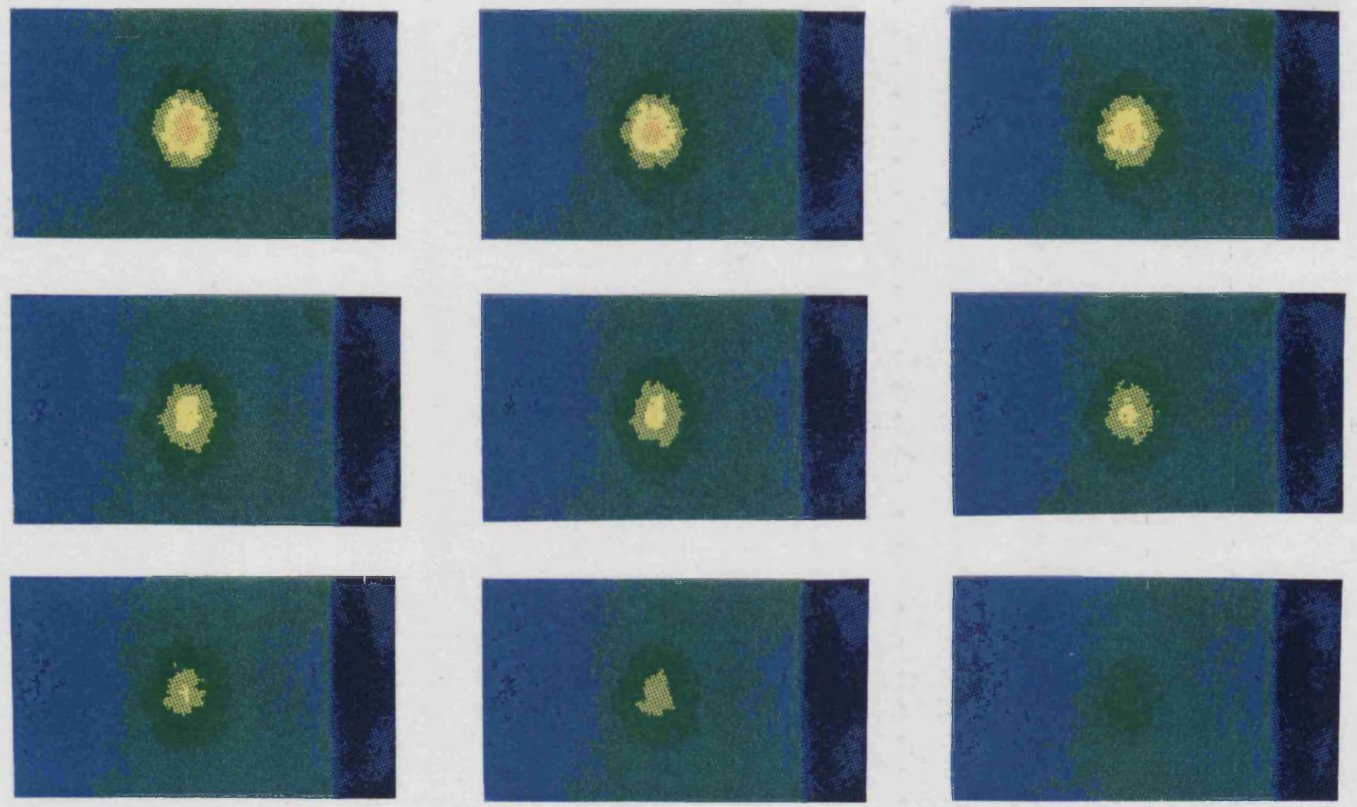

Frames 11-19 Of Transient Experiment
On Sample 10

Figure 6.28

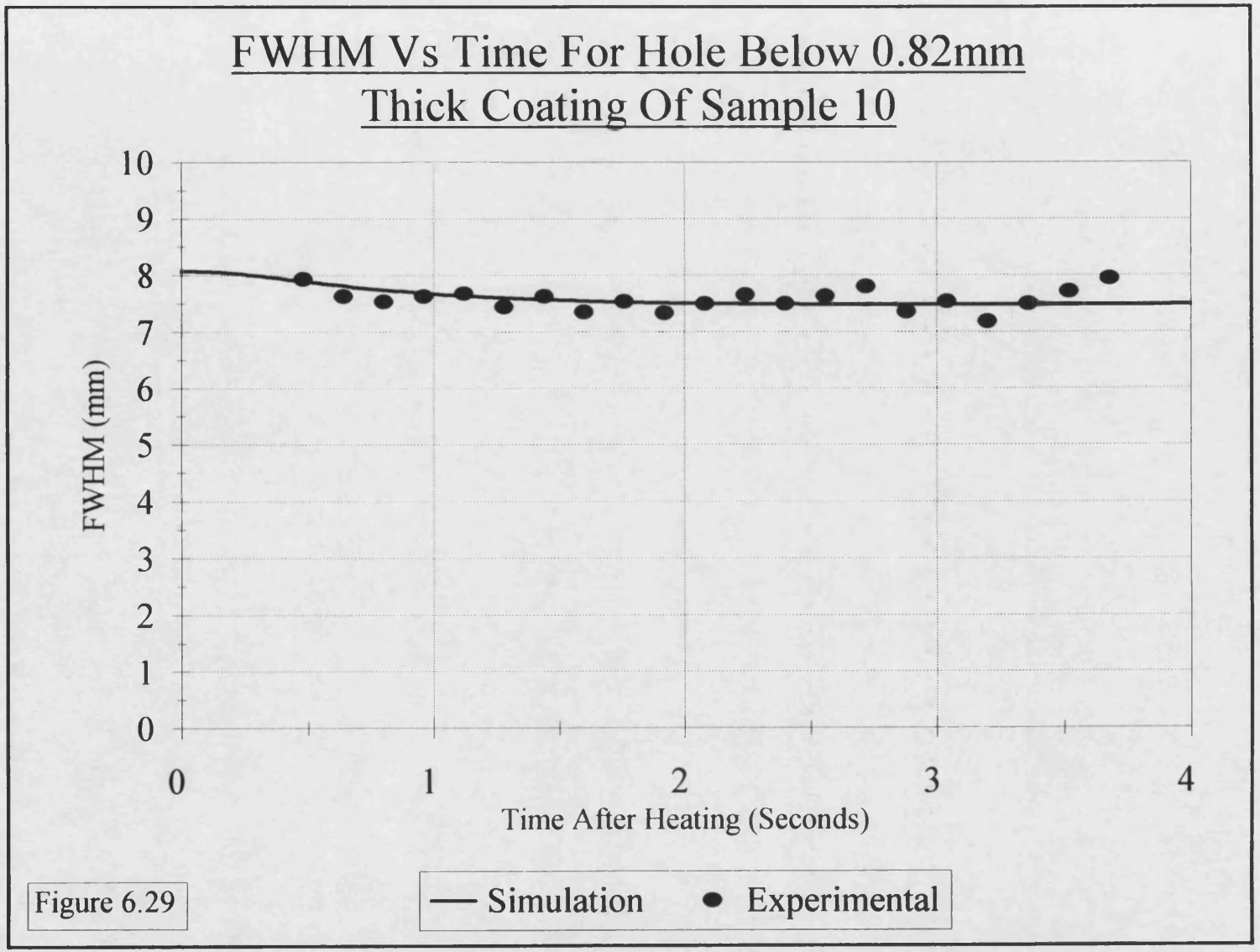
FWHM Vs Time For Hole Below 0.82mm Thick Coating Of Sample 10
FWHM (mm)
10
9
8
7
6
5
4
3
2
1
0
0
1
2
3
4
Time After Heating (Seconds)
Simulation
Experimental

Figure 6.29

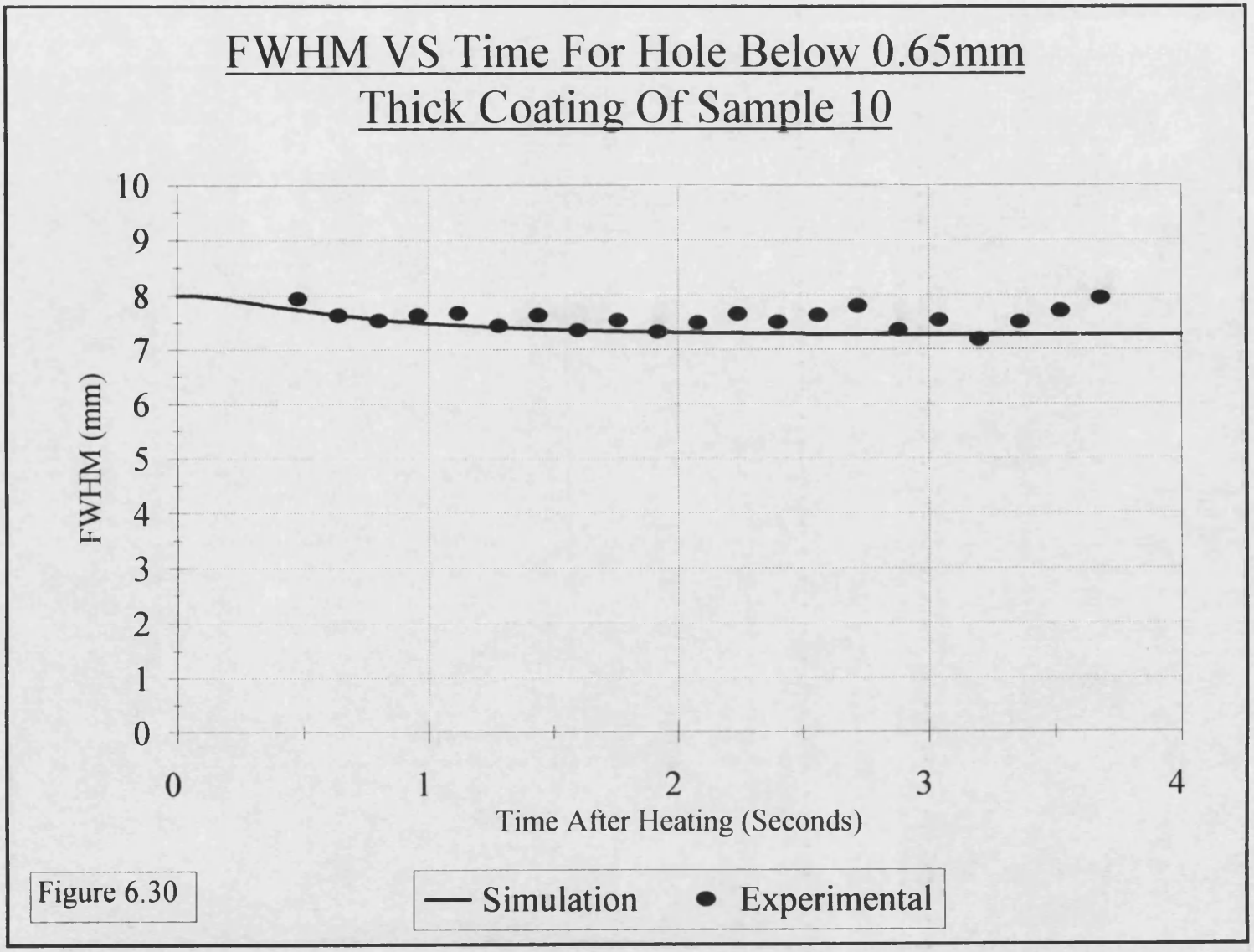
FWHM VS Time For Hole Below 0.65mm Thick Coating Of Sample 10
FWHM (mm)
10
9
8
7
6
5
4
3
2
1
0
0
1
2
3
4
Time After Heating (Seconds)
Simulation
Experimental

Figure 6.30

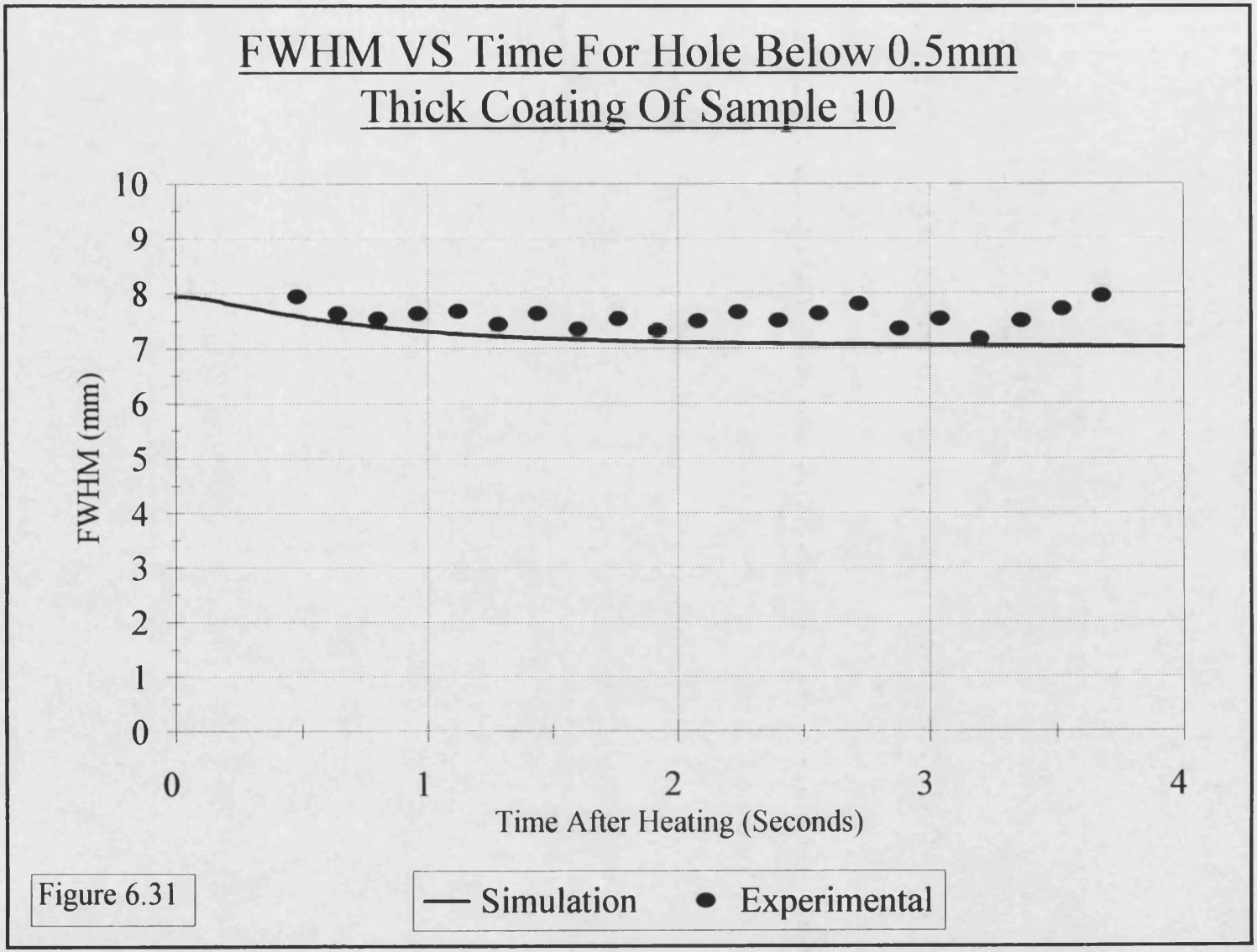
FWHM VS Time For Hole Below 0.5mm Thick Coating Of Sample 10
FWHM (mm)
10
9
8
7
6
5
4
3
2
1
0
0
1
2
3
4
Time After Heating (Seconds)
Simulation
Experimental

Figure 6.31

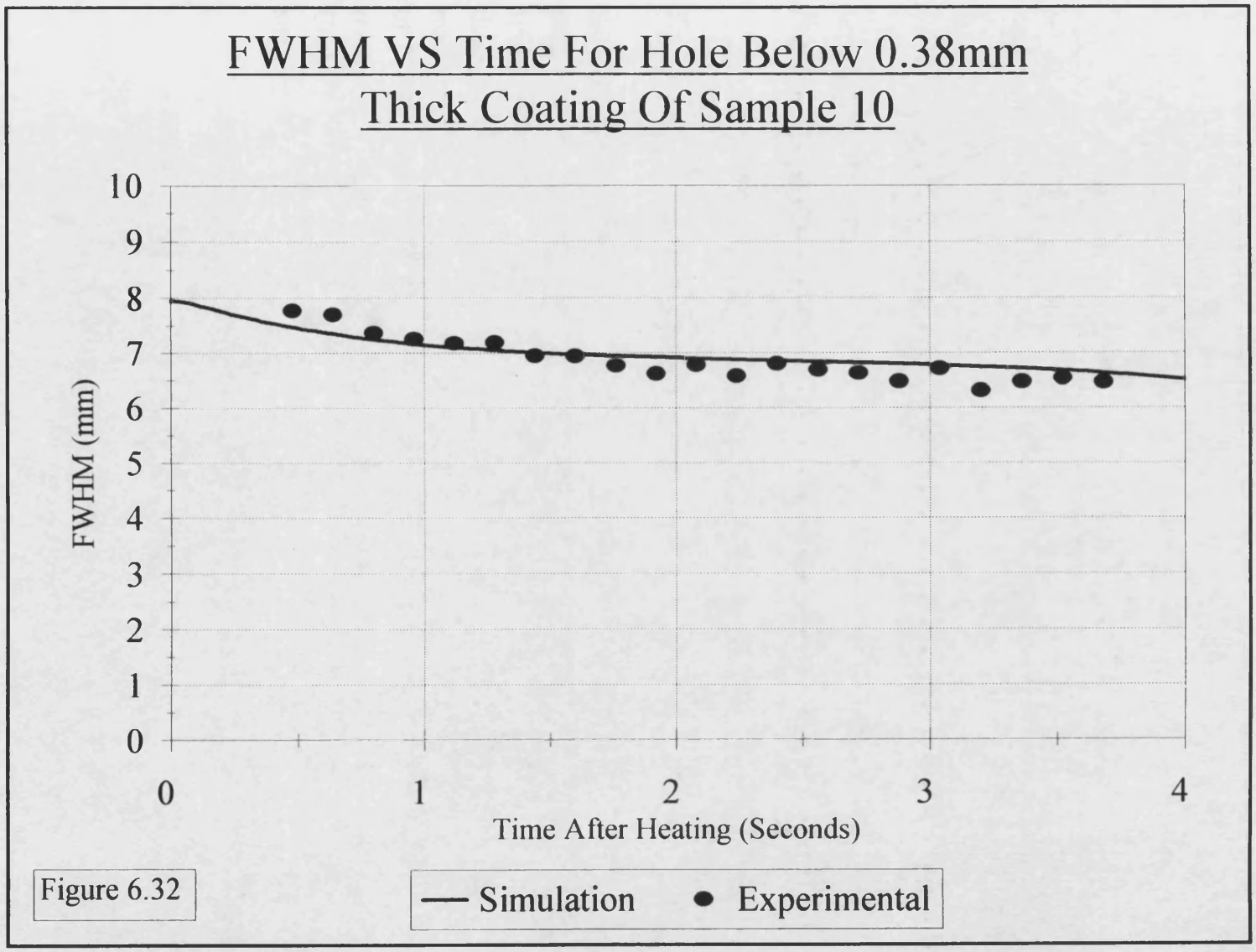
FWHM VS Time For Hole Below 0.38mm
Thick Coating Of Sample 10
FWHM (mm)
10
9
8
7
6
5
4
3
2
1
0
0
1
2
3
4
Time After Heating (Seconds)
Simulation
Experimental

Figure 6.32

Chapter 7

Numerical Modelling

This chapter presents the results of a study into the effects that defect parameters such as diameter, depth, severity and material have on transient thermographic response. This is of great importance if transient thermography is to be widely adopted, as accurate interpretation of experimental results in terms of the defect parameters (inversion) is the prime objective of NDE. All the results presented here are for crack or back drilled holes in a homogeneous material. This restriction has been made as it is necessary to understand the thermal image formation process in the simplest case, before considering more complicated (e.g. multi-layer) scenarios. The numerical finite difference model described in section 4.5 has been used to generate the data. All the results are for Dirac pulse heating of the samples, with a total energy of the pulse of 10 kJ/m^2.

7.1 The Perfect Crack

Section 3.6 describes the Wiener-Hopf solution for the transient response of finite sized defects, and the short comings due to the simplifications made in the model. A situation in which the analytical solution is most likely to be valid, is the case of a large diameter crack at short times after the heating pulse. To test this, a simulation was made of the pulse response of a sample containing a 40 mm diameter crack, at a depth of 1 mm, in mild steel. The crack had a contact resistance of 1.0, equivalent to the resistance of a 2.5 cm wide air gap, and so could be considered a 'perfect' crack. Convective heat losses from the surfaces of the sample were not considered for simplicity. The thermal properties of the mild steel were taken to be:

$k = 64$ W/mK (Thermal conductivity)
$\rho = 7850$ kg/m^3 (Density)
$c = 580$ J/kgK (Specific heat capacity)
$\alpha = 14 \times 10^{-6}$ m^2/s (Diffusivity)

Figure 7.1 shows radial temperature profiles in the plane of the crack, for times up to 1 second after the heating pulse, at intervals of 0.1 seconds (10 profiles). The crack tip is

located at radial position 0, a negative x-axis value indicating a position on the crack surface, -20 being at the crack centre. It can be seen in all of the profiles that the temperature at the crack tip falls very close to the temperature of the surrounding material. This has previously been seen in the results of an earlier finite difference simulation of this problem [62]. Comparing this to figure 7.2, showing the analytical solution of the temperature profile in the crack plane for harmonic heating, they are seen to have a similar form. Figure 7.3 shows radial temperature profiles on the upper surface of the sample, once again for times up to 1 second. The full width at half maximum (FWHM) contrast is used as a measure of the defect size, figure 7.4 shows a typical thermal profile over the diameter of a defect with the FWHM shown. Figure 7.5 shows the variation of FWHM with time for the 40 mm diameter crack, it is seen to decrease with time, as was predicted by the analytical model.

The basic features of the analytical model are correct, the temperature contrast in the plane of the crack falls abruptly to zero at the crack tip, and the FWHM at the sample surface decreases with time. The rounding of the temperature profiles with increasing elapsed time after the pulse, in the plane of the crack, and subsequently at the sample surface, is caused by the flow of heat from the crack surface. Some of this energy flows around the crack tip to the cool underside of the crack.

7.2 Size Effects

Simulations have been made to investigate the effects of crack diameter on the resulting FWHM measurements following pulse heating. Cracks of diameters 20, 10, 5 and 2 mm, all at a depth of 1 mm have been modelled. As before, the cracks were embedded in mild steel, and had a contact resistance such that they could be considered 'perfect' cracks. In these simulations, convective heat losses were included, with a surface heat transfer coefficient of 20 W/m^2K. Figure 7.6 shows the FWHM of the surface temperature contrast over the cracks against time, the lowest trace corresponding to the 2 mm diameter crack, the highest to the 20 mm diameter crack.

The FWHM of the 20 mm diameter crack decreases with time for the full second. The 10 mm diameter crack has an FWHM that flattens out after a short time. The 5 and 2 mm diameter cracks have FWHMs that behave very strangely. The behaviour of the largest crack is as expected from the analytical model, but the others clearly deviate from the simple notion of a decreasing FWHM with time. These clearly lie outside of the range of validity of the analytical model.

In the cases of the smallest cracks, the edge effects from opposite sides of the crack have met in the middle, causing the crack contrast profile to broaden, and hence the increase in the FWHM. For the larger defect, in the time span of the simulation, the edge effects have not come together, and so the FWHM decreases throughout the period.

It is seen in the figure that if it were possible to make a measurement of the FWHM at extremely short time after the heating pulse, for any defect size, the measurement would provide a very accurate indication of the true defect size. However, this may not be possible in practice as the contrast at such an early time after the flash may be too small for measurement (figure 7.7 shows the contrast time curves, the uppermost curve for the 20 mm diameter crack, the lowest curve for the 2 mm diameter crack). It should be noted that for the largest defect, taking measurements at longer times after the flash always results in a larger error in the estimate of the defect size. This is not the case for the smaller defects. For example, in the case of the 5 mm diameter defect, the maximum error (minimum FWHM) occurs at approximately 0.1 seconds after the pulse (approximately maximum contrast), a measurement at this time would give a greater error than one taken later, say at 1 second. For the larger defects, a series of FWHM measurements could be linearly extrapolated back to the time of the heating pulse to give a better estimate of true defect size. This is in agreement with the defect sizing method proposed in [71].

7.3 Depth Effects

Simulations of 10 mm diameter cracks in mild steel, at depths of 0.25, 0.5, 1.0, 2.0 and 4.0 mm were made to investigate the effects of crack depth on the changes of FWHM with time. Once more, the cracks were 'perfect', and convective heat losses were included.

Figure 7.8 shows the variation of the FWHM with time for each of the cracks. It is interesting, and surprising to note, that the shallowest crack, the one that most would assume to be the simplest to size correctly, has an FWHM that deviates most rapidly, and by the largest amount from the true size of the crack. The effect of depth is seen to lessen the extent to which the FWHM reduces. Once more it is seen that a measurement at a very early time after the heating would result in a very good estimate of true defect size. Experimentally the measurement of the FWHM for a deep crack is more difficult, as the contrast on the surface is less (figure 7.9).

For the cracks very close to the heated surface, the heat above the crack is trapped in a very small volume. This causes the material directly above the crack to be elevated rapidly to high temperature, creating large temperature gradients between this volume and the neighbouring material. This causes high rates of flux flow from the crack surface, rounding its temperature profile, and causing the large and rapid decrease in FWHM. For the deeper cracks, the temperature gradients are much less, as the 'trapping' volume is larger, allowing the material above the crack to remain cooler.

7.4 Thermal Resistance Effects

The effect of the severity of the crack was next investigated. 10 mm diameter cracks, all at a depth of 1 mm in mild steel were modelled, with contact resistances equivalent to 2.5 cm (the so called 'perfect' crack used in all the simulations previously discussed), 100 μm, 10 μm and 1 μm of air (resistances of 1.0, $4x10^{-3}$, $4x10^{-4}$ and $4x10^{-5}$ respectively).

Figure 7.10 shows the FWHM verses time for each of the cracks. The FWHM for the 100 μm crack is very close to that of the 'perfect' crack (as is the contrast time curve in figure 7.11). The FWHM for the 10 μm crack is also very similar to that for the 'perfect' crack, showing that cracks of the order of 10 μm cause marked disturbances in heat flow in mild steel. The FWHM for the 1 μm crack is also seen to be very close to that for the 'perfect' crack at short times, but deviates markedly at longer times. The maximum thermal contrast of the 1 μm crack (the lowest curve of figure 7.11) is less than half that for the 'perfect' and 100 μm cracks.

7.5 Material Effects

So far, all the results have been for cracks in mild steel, a high thermal conductivity material. To study the effects of the material in which the cracks were embedded, simulations were also made of 10 mm diameter cracks in materials with the following thermal properties :

Material 1 : $k = 6.4$ W/mK (Thermal conductivity)
$\rho = 7850$ kg/m^3 (Density)
$c = 580$ J/kgK (Specific heat capacity)
$\alpha = 1.4x10^{-6}$ m^2/s (Diffusivity)

Material 2 : $k = 0.64$ W/mK (Thermal conductivity)
$\rho = 7850$ kg/m^3 (Density)
$c = 580$ J/kgK (Specific heat capacity)
$\alpha = 0.14 \times 10^{-6}$ m^2/s (Diffusivity)

Material 1 has a diffusivity a factor of 10 lower than that for mild steel, and material 2 a diffusivity a factor of 10 lower than for material 1. As the speed of the thermal response is related to the diffusivity, these simulations were run over an extended period, up to 100 seconds after the heating pulse, to allow the slower materials to exhibit the full transient response.

Simulations were made for 'perfect' cracks, and cracks equivalent to air gaps of 100, 10 and 1 μm. Figure 7.12 shows the surface temperature contrast over the centre of each crack verses log time for materials 1 and 2, and for a sample made from mild steel for comparison. In the case of the mild steel, only the trace for a 'perfect' crack is shown, but for materials 1 and 2, the traces for cracks of each severity (air gap) are shown. It is seen that the maximum contrast in the case of a 'perfect' crack for the mild steel and material 1 samples have similar magnitude (same value for ρc pair), but occurs a decade later for the lower diffusivity material. The contrast peak for a 'perfect' crack in material 2 is reduced in magnitude due to convective heat losses, and occurs almost a decade after that for material 1. It should be noted that although the shapes of the contrast peaks are very similar, they extend over very different time periods (note the log scale).

Considering now the more realistic cracks (100, 10 and 1 μm), it is seen that a 100 μm crack in material 1 causes a maximum contrast approximately 90% that of a 'perfect' crack, but in material 2 the same severity crack causes a contrast of only around 50% that of a 'perfect' crack. This effect is even more pronounced in the lower severity cases, with the 1 μm crack in material 2 causing an immeasurably small contrast.

Figure 7.13 shows the variation of FWHM against log time for each material, at times for which the contrast was greater than 0.1 K. Once again, the shapes of the curves are similar, but shifted by a decade from each other as the thermal conductivity, and hence thermal diffusivity, decreases by a factor of 10. It is interesting to note that if the FWHM were measured for each sample with a 'perfect' crack at the time of maximum contrast, they would all have a similar value.

7.6 Back Drilled Hole

A requirement for the development of an NDE technique, is the ability to produce experimental test samples on which the technique can be assessed. It is notoriously difficult to produce good quality crack defects of known severity and extent, and so back drilled hole samples are often substituted for real crack defects due to their relative ease of manufacture. It is therefore interesting to compare the response of a sample with a back drilled hole to one with a crack, to see if this is valid. A simulation was made of a sample containing a 10 mm diameter flat topped back drilled hole in a piece of mild steel for comparison with the results for a 10 mm diameter crack. Figure 7.14 shows the FWHM plotted against time for both the back drilled hole and the crack. It is seen that the FWHM for the back drilled hole does not decrease as fast or a far as for the crack. This is because for the crack, a large amount of heat from the crack surface flows around the crack tip, to the cooler underside of the crack. This is not possible for a back drilled hole, where the energy can flow only down the side wall of the hole. This reduces the rate at which heat can escape from the upper surface of the hole, which reduces the rate at which the hole surface temperature contrast is rounded, and hence reduces the rate of decrease in the FWHM. Another effect of this is that the contrast over a back drilled hole is higher than for a crack (figure 7.15) of a similar size and depth, as the heat is more effectively trapped over the hole.

7.7 Discussion

It has been shown that the analytical prediction of a reduction in FWHM with time is true for large defects, but fails for small defects, or medium sized defects at long times. It is seen that a measurement should be made as early as possible after the heating pulse to gain the most accurate estimate of defect size, but that care must be taken especially with small defects. For the larger defects, a good estimate of the true size of a defect can be found by extrapolating a time series of FWHMs back to the time at which the Dirac heating pulse was applied. Further obvious difficulties in the accurate sizing of small defects arise from the reduced thermal contrast above small cracks, when compared to larger cracks of the same severity (contact resistance) and depth.

It is seen that shallow defects have FWHMs that change more rapidly, and by a larger amount, than deeper defects. Sizing of such defects is therefore more difficult than might be imagined.

Comparing the back drilled hole and crack, it is interesting to note the marked difference in the FWHM traces. The back drilled hole presents a much greater obstruction to the flow of heat through the sample than a crack, and produces a greater thermal contrast than a crack at long times. It also has an FWHM that does not decrease as far as for a crack, therefore reducing errors in defect sizing. It should be noted that, when evaluating thermal NDE for crack and delamination detection, back drilled holes should not be used as substitutes for these defects.

The finite difference modelling of this problem has exhibited the complex dependency of the FWHM measurements on crack depth, diameter, severity and material thermal properties. These simulations were made assuming the simplification of homogeneous and isotropic thermal properties, an assumption invalid for such materials as carbon fibre composites, on which thermal NDE is often used. Even with these assumptions, accurately interpreting transient thermographic data in terms of defect characteristics is extremely difficult. Due to this complexity, attempts are now being made to apply neural networks to the interpretation of transient thermographic images [75,76]. Results so far in this area of research are extremely encouraging, and more is certain to follow. Chapter 8 gives details of the work on the use neural networks that has been conducted as part of this project.

7.8 Computer Animation

To aid in the understanding of the heat flow through defective samples, computer animations of pulse heating experiments on samples containing crack defects in mild steel were made. The finite difference model was transferred to the Silicon Graphics Indigo workstations of my sponsors (TWI). The model was used to generate the raw temperature and thermal flux data that was input into an animation program written specifically for the task by Alan Lank (TWI). A video of the computer generated animations was made, and has been screened at two international conferences [72,104].

One of the animations that was made was of the Dirac-delta pulse heating of a mild steel sample containing a 'perfect' crack of radius 5mm, at a depth of 1mm. The total size of the modelled sample was 15mm in radius, and 10mm in depth. Figures 7.16 and 7.17 show a series of 10 frames from the animation, the first frame taken at 100ms after the pulse, with the subsequent frames at 100ms intervals. Each frame shows the temperature profile of a radius of the sample, the left hand edge of the frame is the central axis of the crack. The heat is clearly seen to be trapped in the volume above the crack in the first 3 frames (red, orange, yellow colours), but due to the high diffusivity

of mild steel, by frame 10 (only 1 second after the heating pulse) the sample has very nearly a uniform temperature distribution.

Note : Sections 7.1-7.7 of this chapter have been submitted for publication [105] as a follow up to the earlier paper [71].

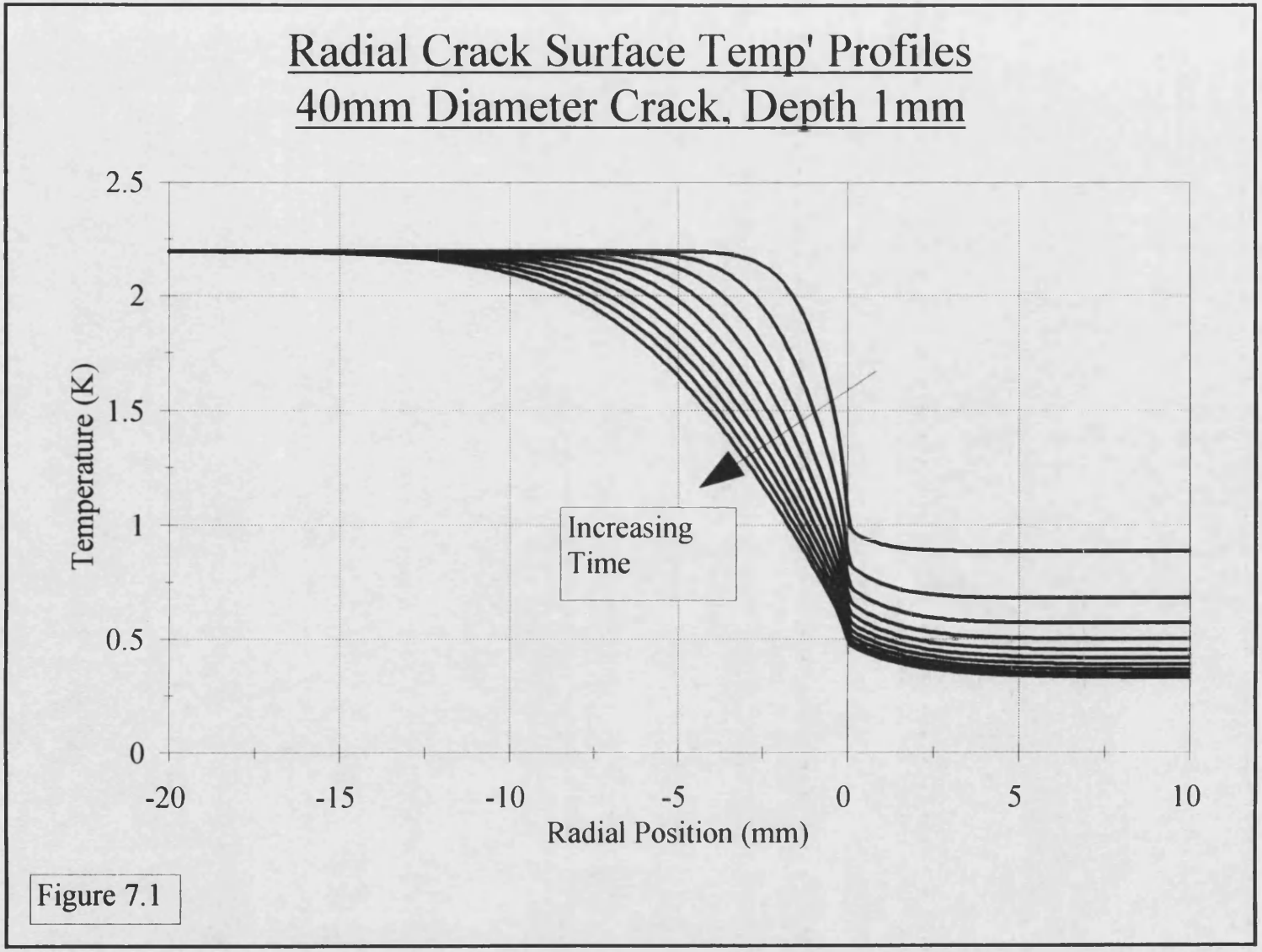
Radial Crack Surface Temp' Profiles
40mm Diameter Crack, Depth 1mm
Temperature (K)
2.5
2
1.5
1
0.5
0
-20
-15
-10
-5
0
5
10
Radial Position (mm)
Increasing
Time

Figure 7.1

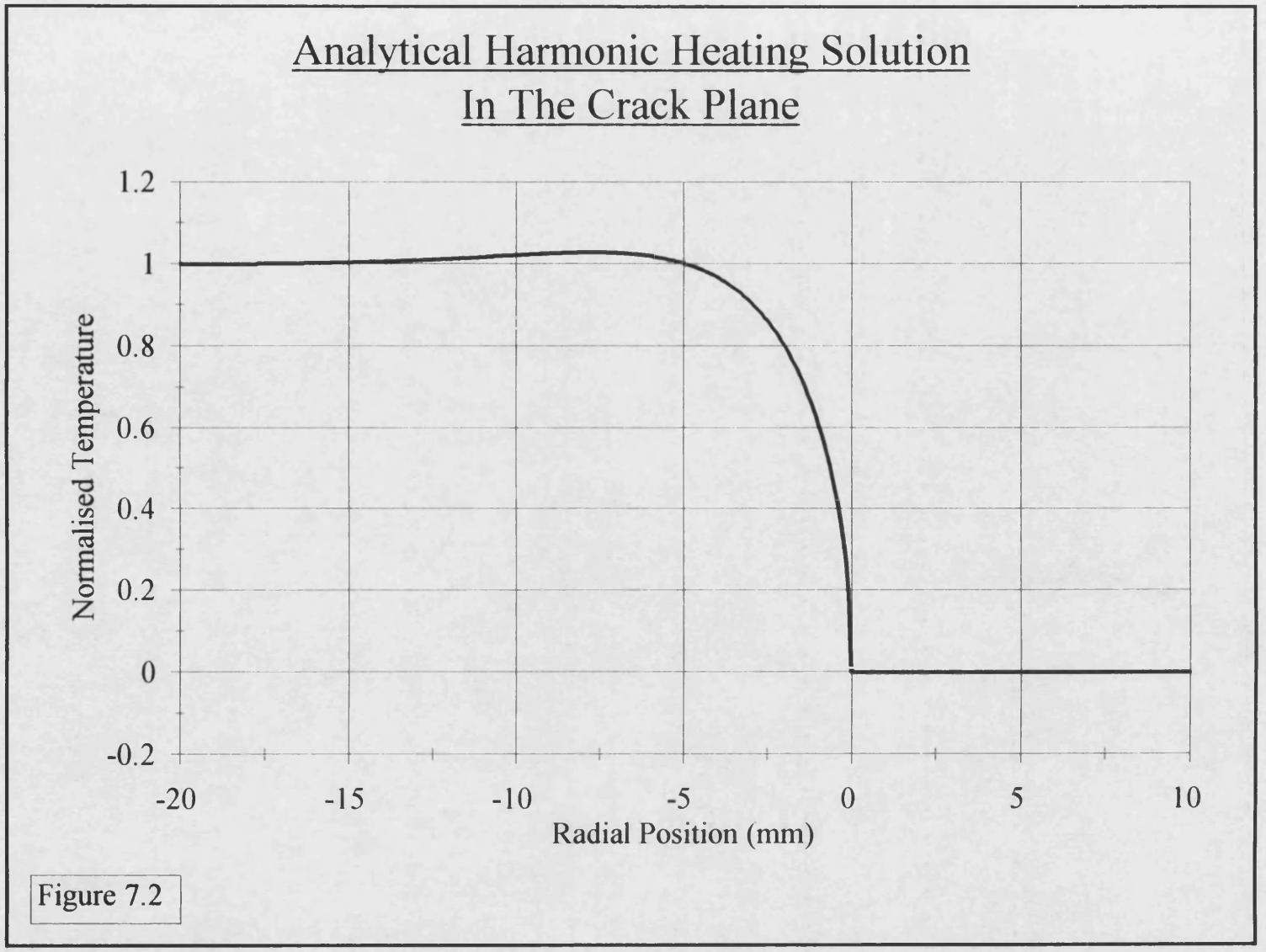
Analytical Harmonic Heating Solution
In The Crack Plane
Normalised Temperature
1.2
1
0.8
0.6
0.4
0.2
0
-0.2
-20
-15
-10
-5
0
5
10
Radial Position (mm)

Figure 7.2

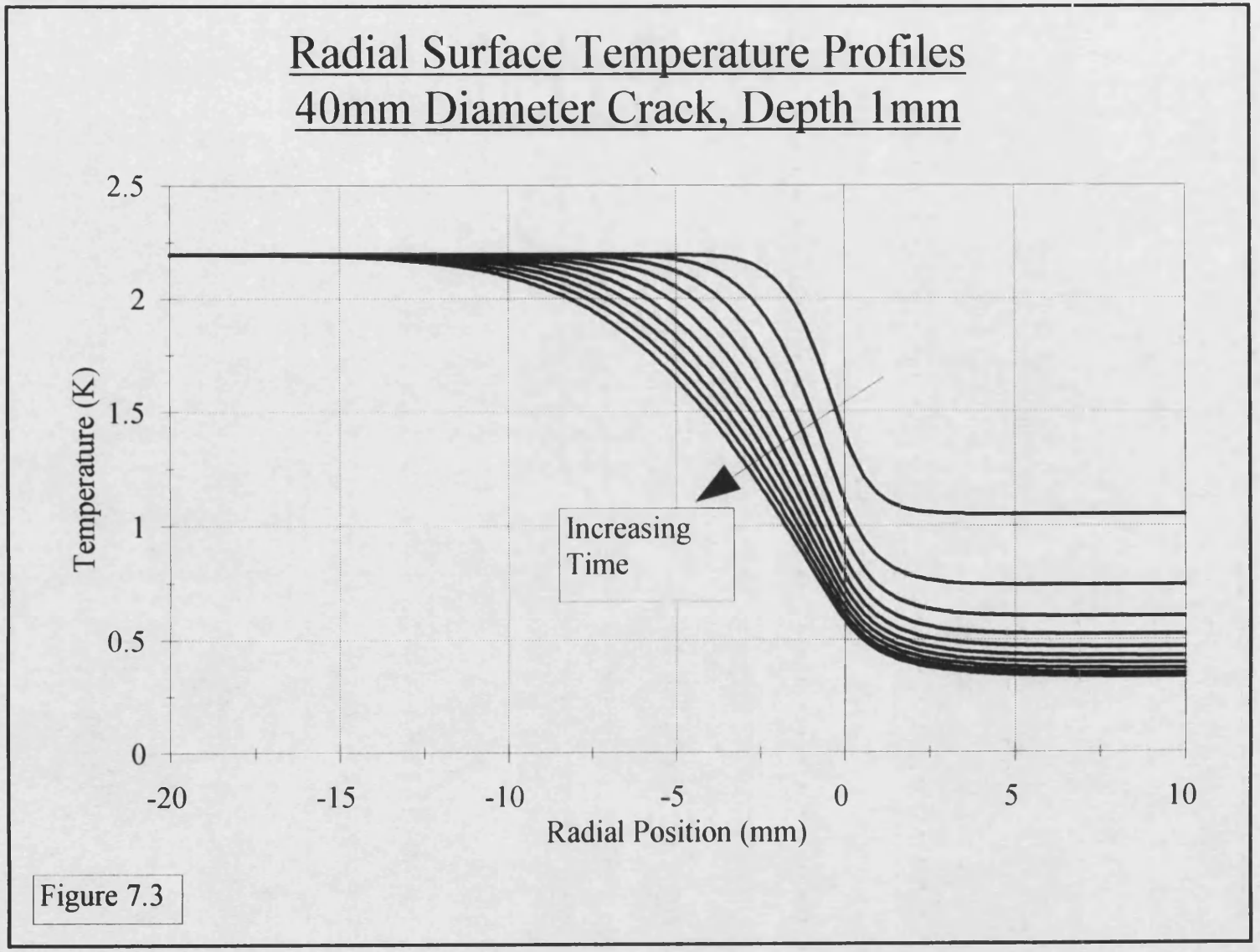
Radial Surface Temperature Profiles
40mm Diameter Crack, Depth 1mm
Temperature (K)
2.5
2
1.5
1
0.5
0
-20
-15
-10
-5
0
5
10
Radial Position (mm)
Increasing
Time

Figure 7.3

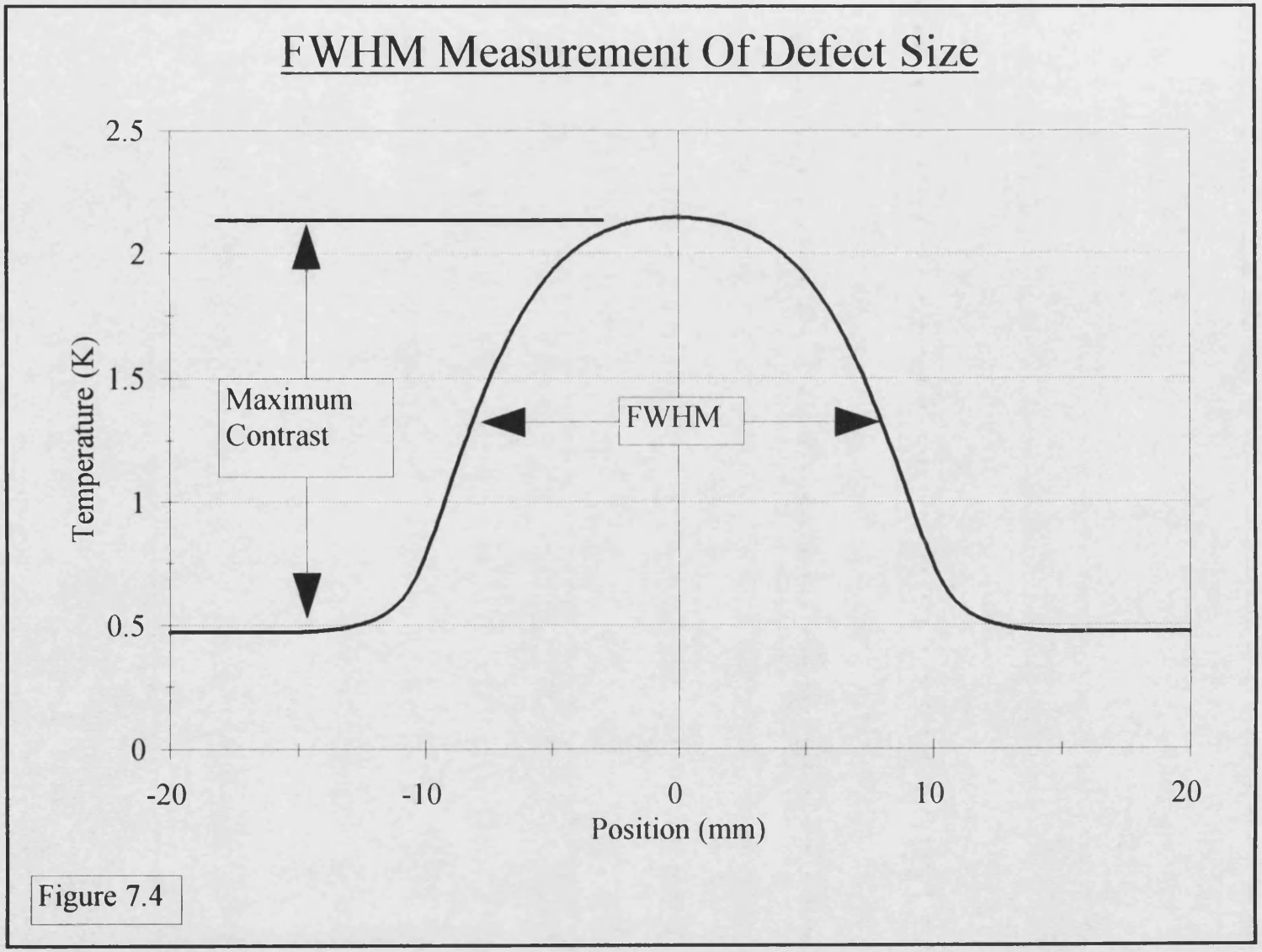
FWHM Measurement Of Defect Size
2.5
2
1.5
1
0.5
0
Temperature (K)
Maximum Contrast
FWHM
-20
-10
0
10
20
Position (mm)

Figure 7.4

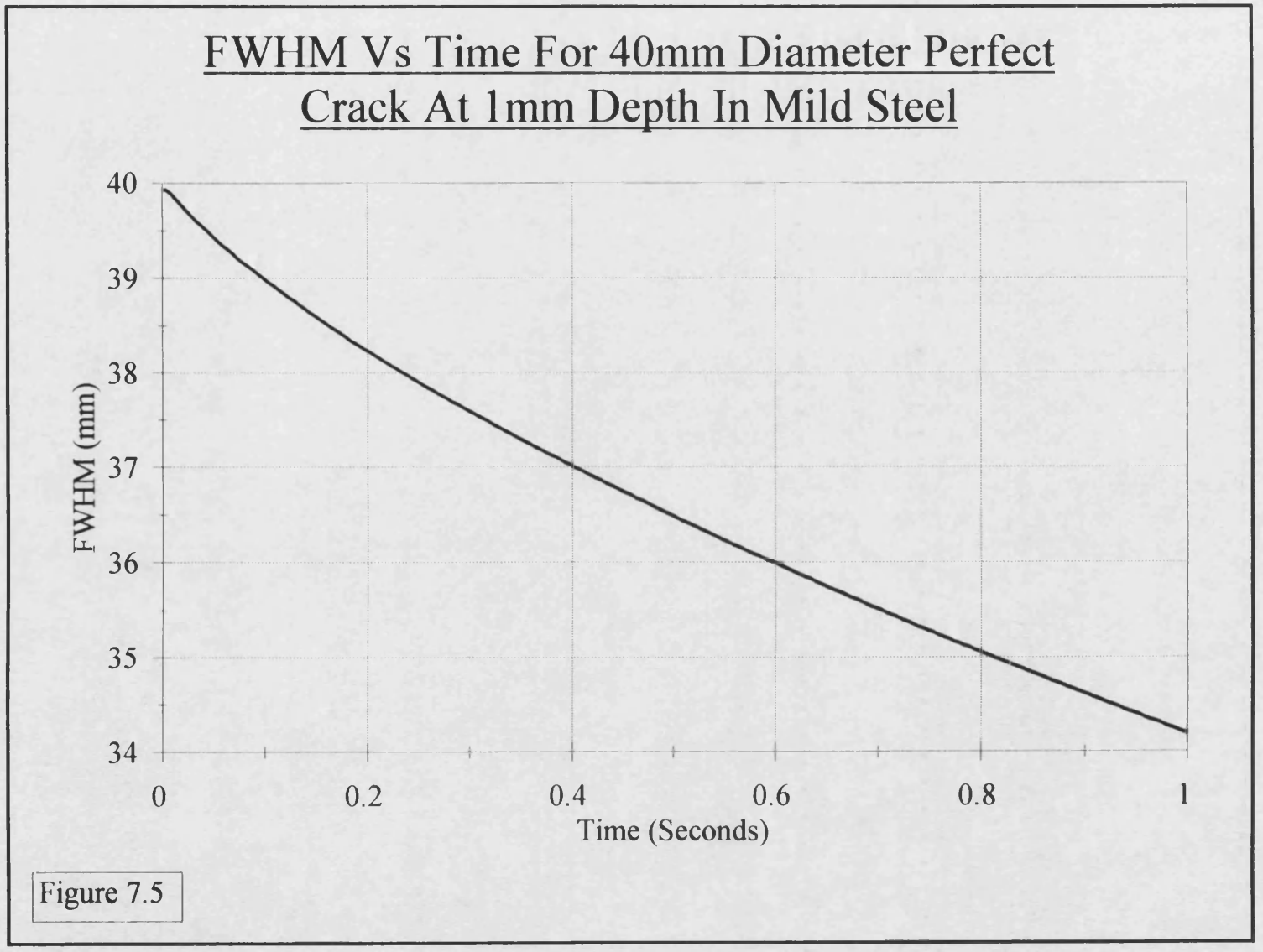
FWHM Vs Time For 40mm Diameter Perfect Crack At 1mm Depth In Mild Steel
FWHM (mm)
40
39
38
37
36
35
34
0
0.2
0.4
0.6
0.8
1
Time (Seconds)

Figure 7.5

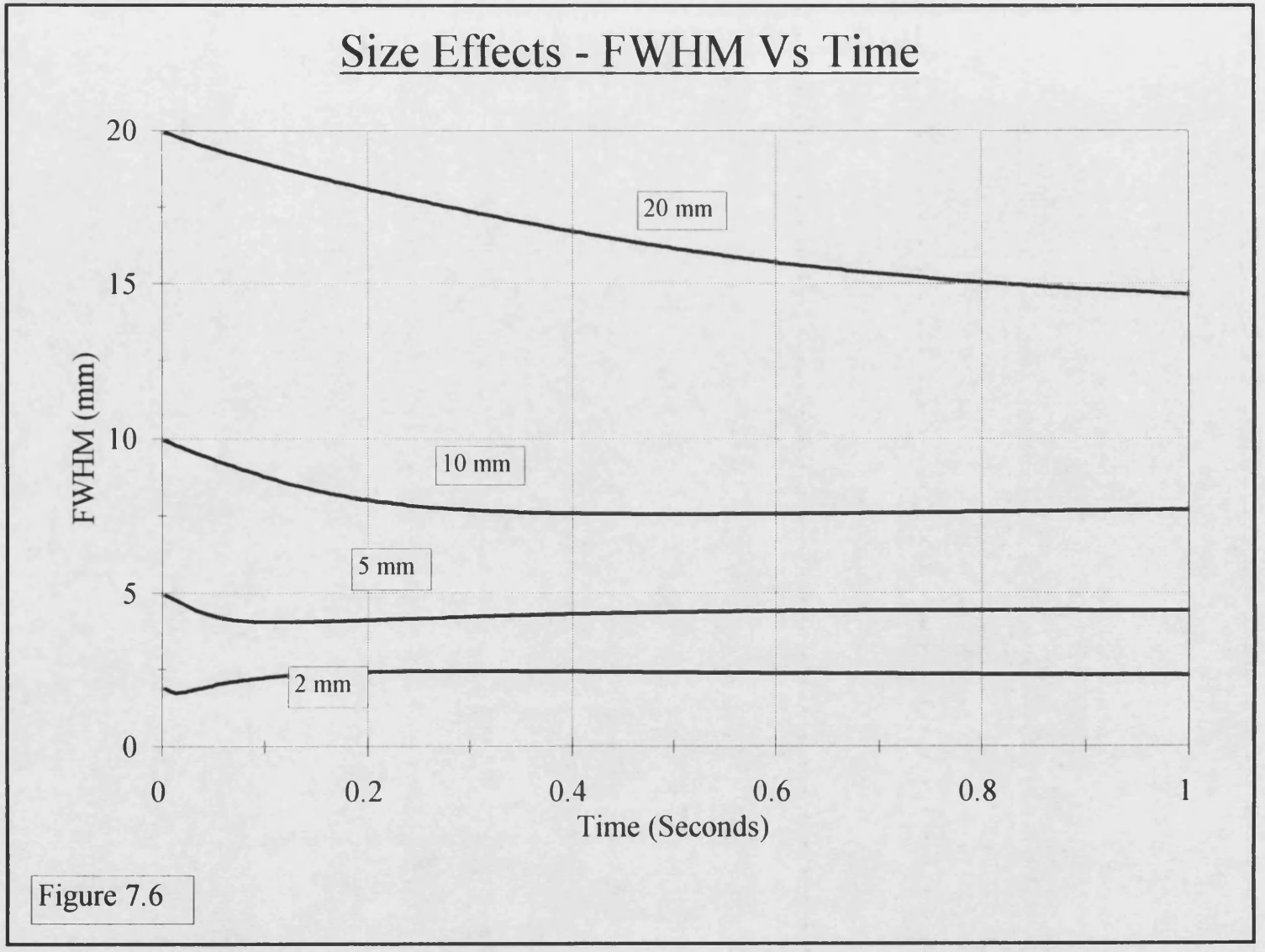
Size Effects - FWHM Vs Time
20
15
10
5
0
FWHM (mm)
20 mm
10 mm
5 mm
2 mm
0
0.2
0.4
0.6
0.8
1
Time (Seconds)

Figure 7.6

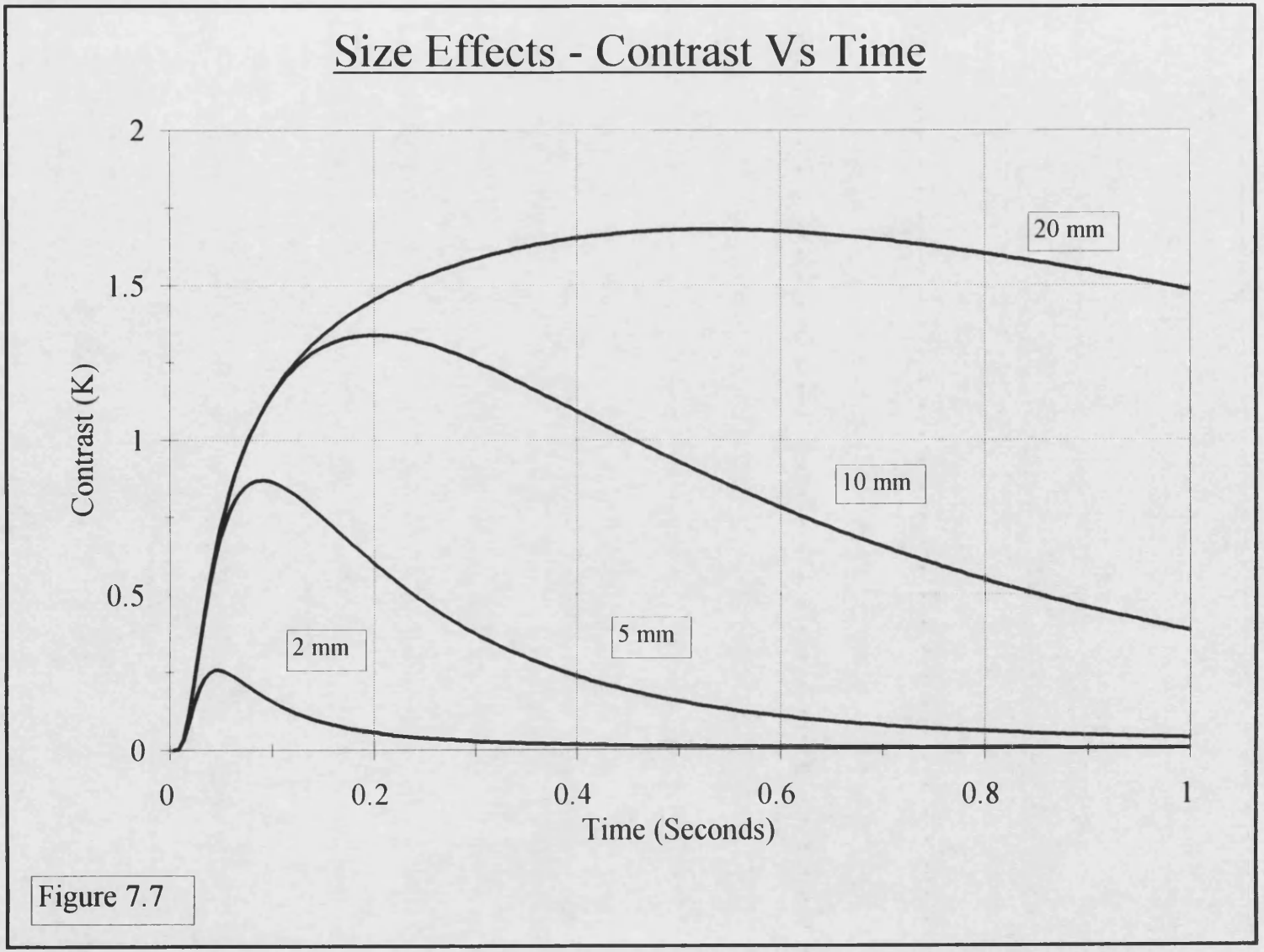
Size Effects - Contrast Vs Time
Contrast (K)
Time (Seconds)
0
0.5
1
1.5
2
0
0.2
0.4
0.6
0.8
1
20 mm
10 mm
5 mm
2 mm

Figure 7.7

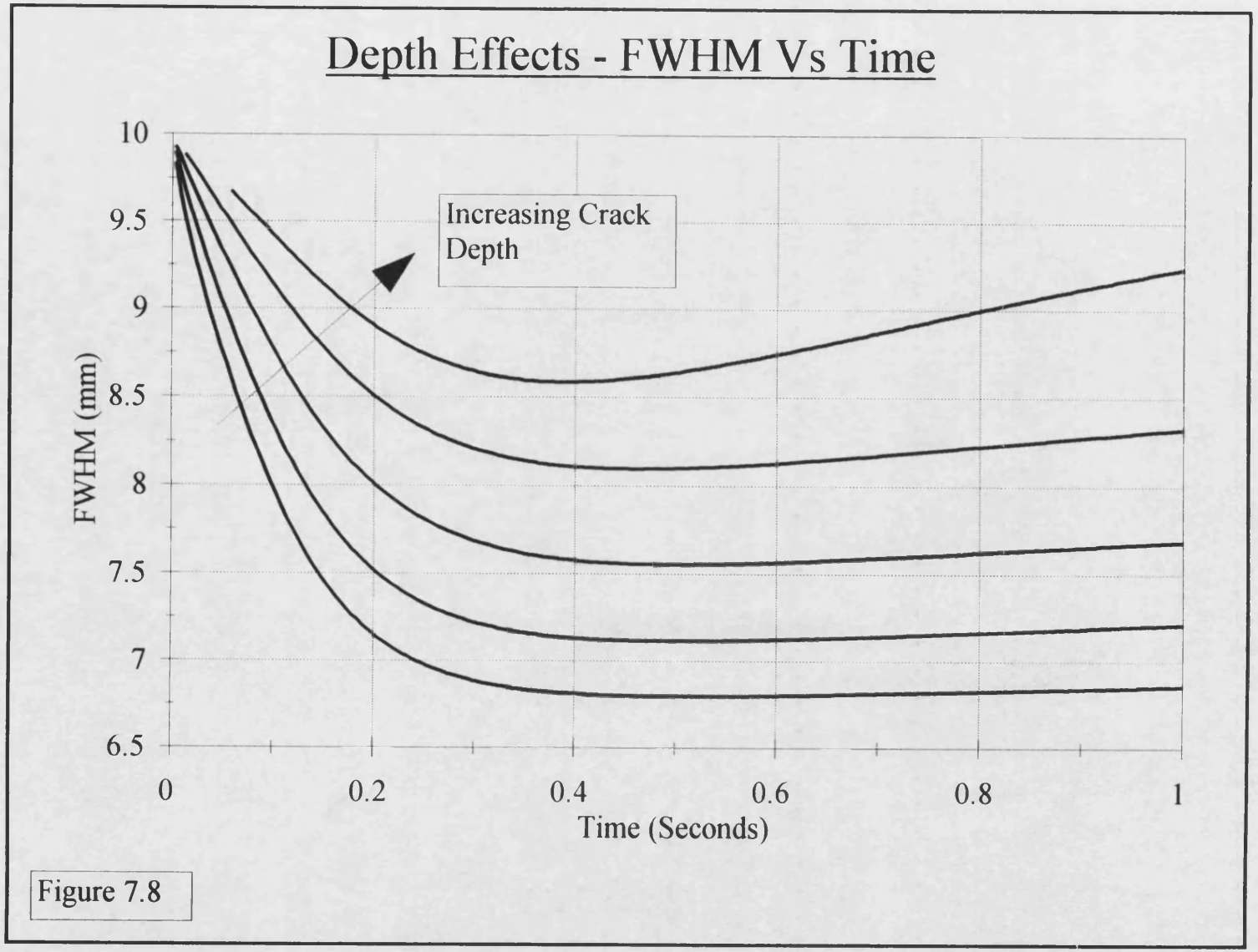
Depth Effects - FWHM Vs Time
10
9.5
9
8.5
8
7.5
7
6.5
FWHM (mm)
Increasing Crack Depth
0
0.2
0.4
0.6
0.8
1
Time (Seconds)

Figure 7.8

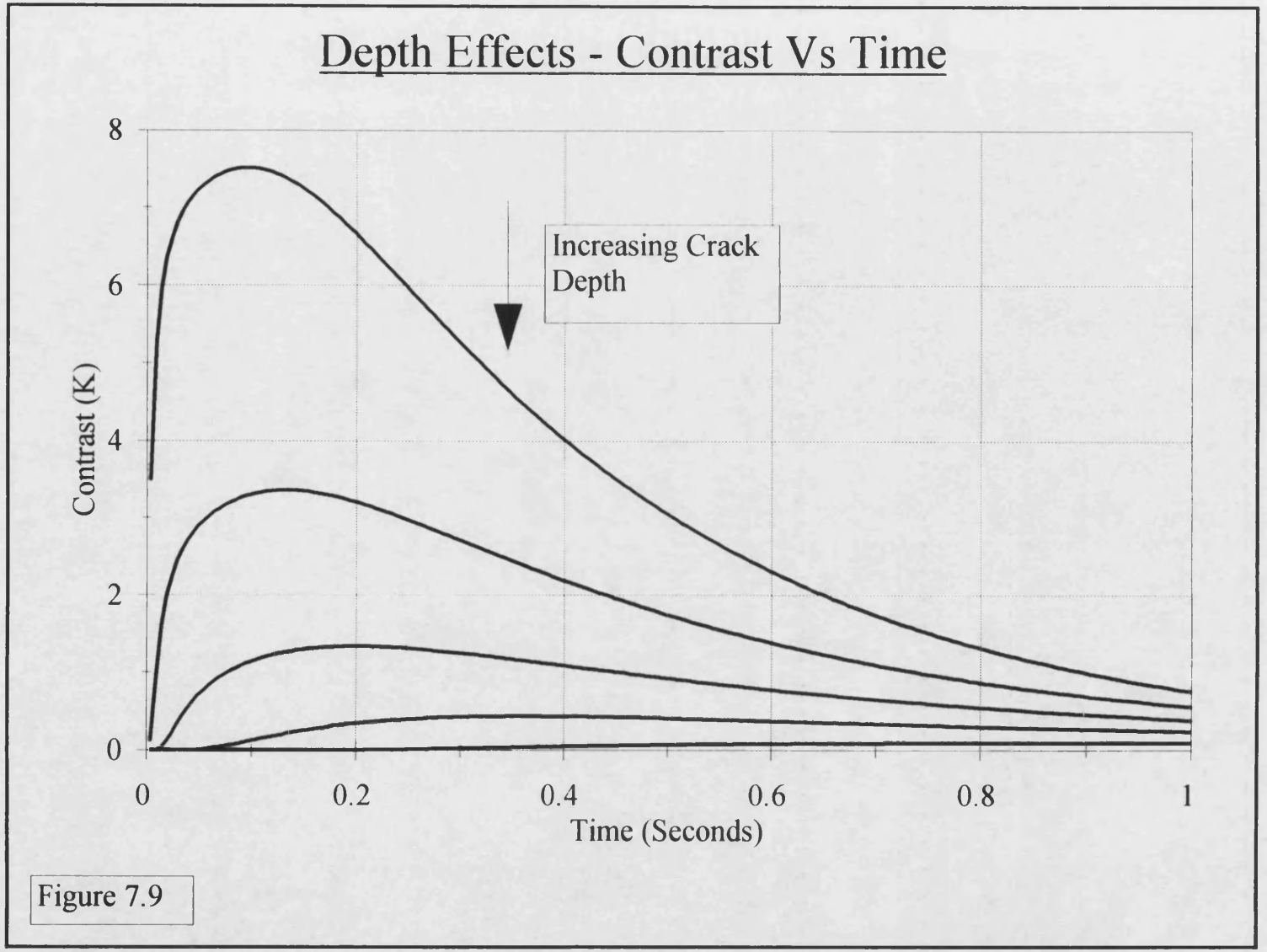
Depth Effects - Contrast Vs Time
Increasing Crack Depth
Contrast (K)
Time (Seconds)
0
2
4
6
8
0
0.2
0.4
0.6
0.8
1

Figure 7.9

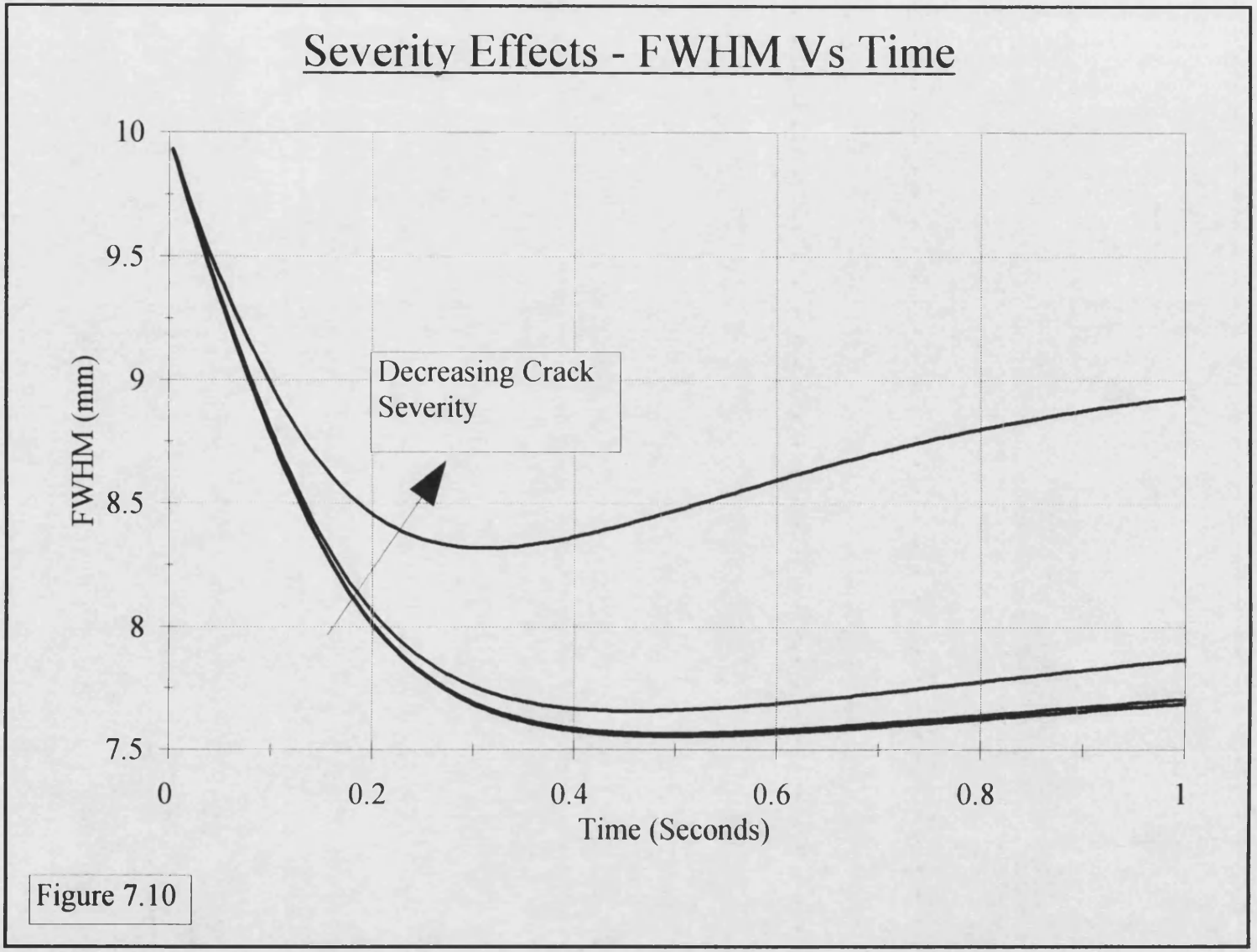
Severity Effects - FWHM Vs Time
10
9.5
9
8.5
8
7.5
FWHM (mm)
Decreasing Crack Severity
0
0.2
0.4
0.6
0.8
1
Time (Seconds)

Figure 7.10

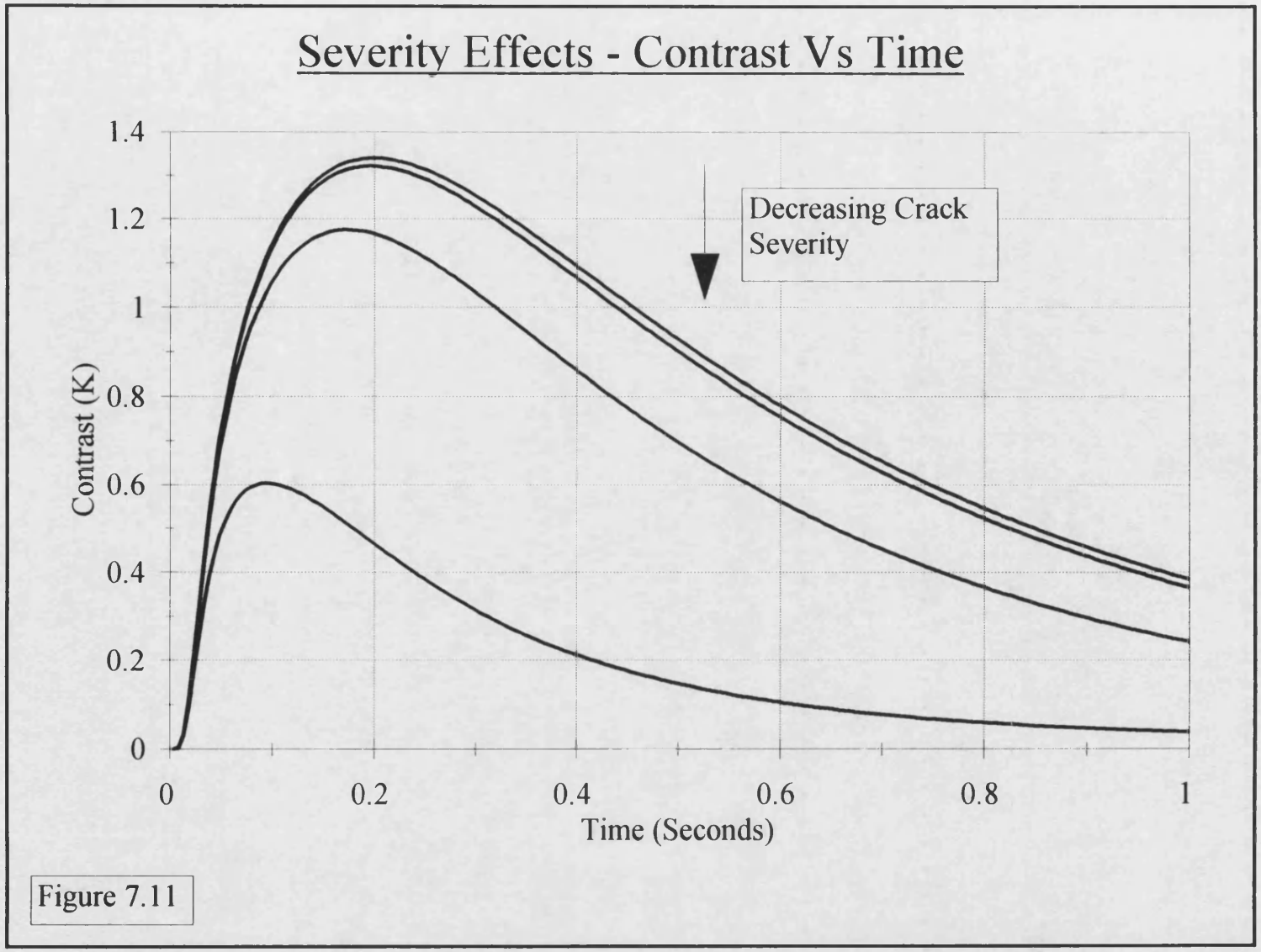
Severity Effects - Contrast Vs Time
1.4
1.2
1
0.8
0.6
0.4
0.2
0
Contrast (K)
Decreasing Crack Severity
0
0.2
0.4
0.6
0.8
1
Time (Seconds)

Figure 7.11

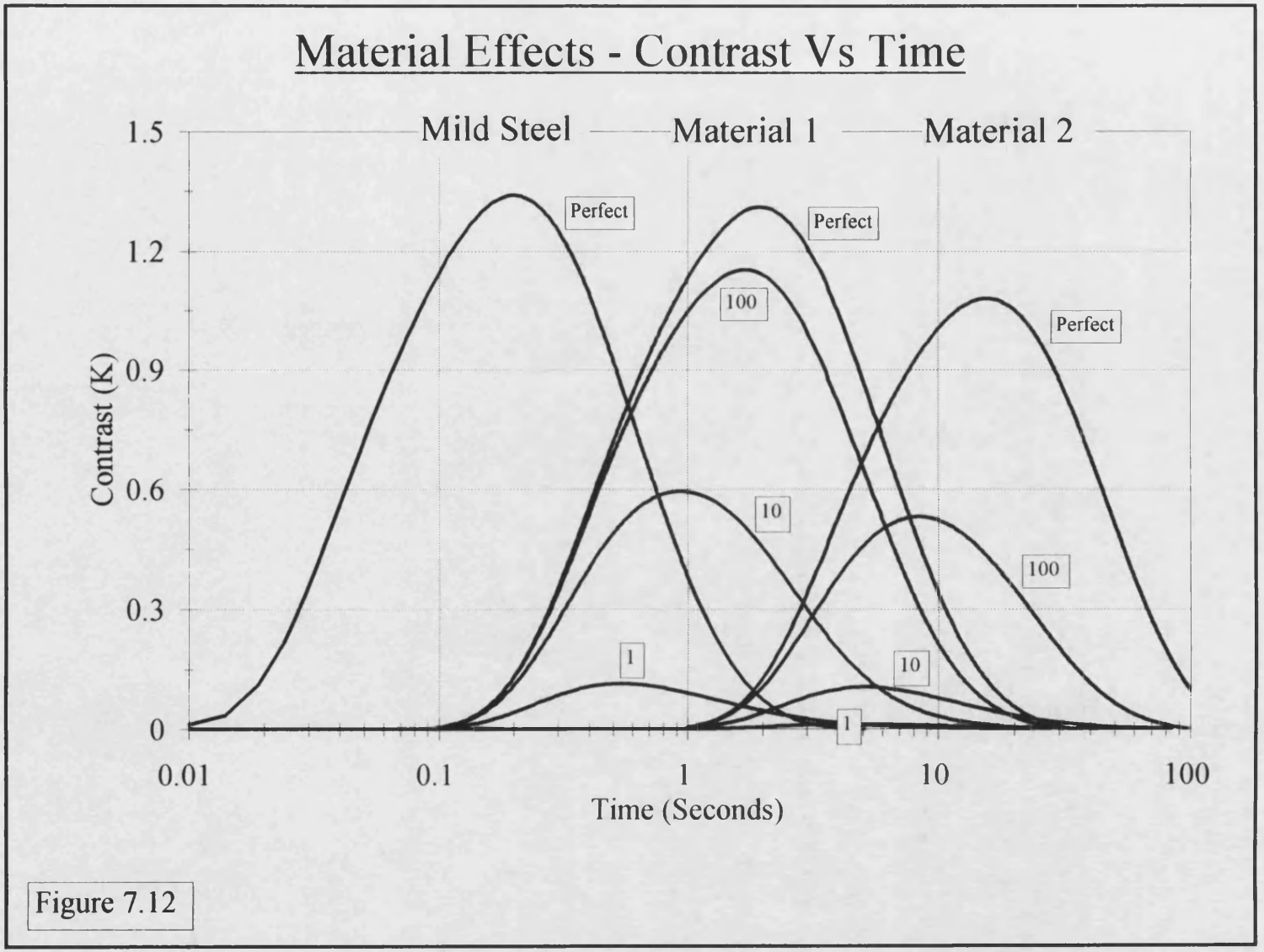
Material Effects - Contrast Vs Time
Mild Steel
Material 1
Material 2
1.5
1.2
0.9
0.6
0.3
0
Contrast (K)
Perfect
Perfect
Perfect
100
100
10
10
1
1
0.01
0.1
1
10
100
Time (Seconds)

Figure 7.12

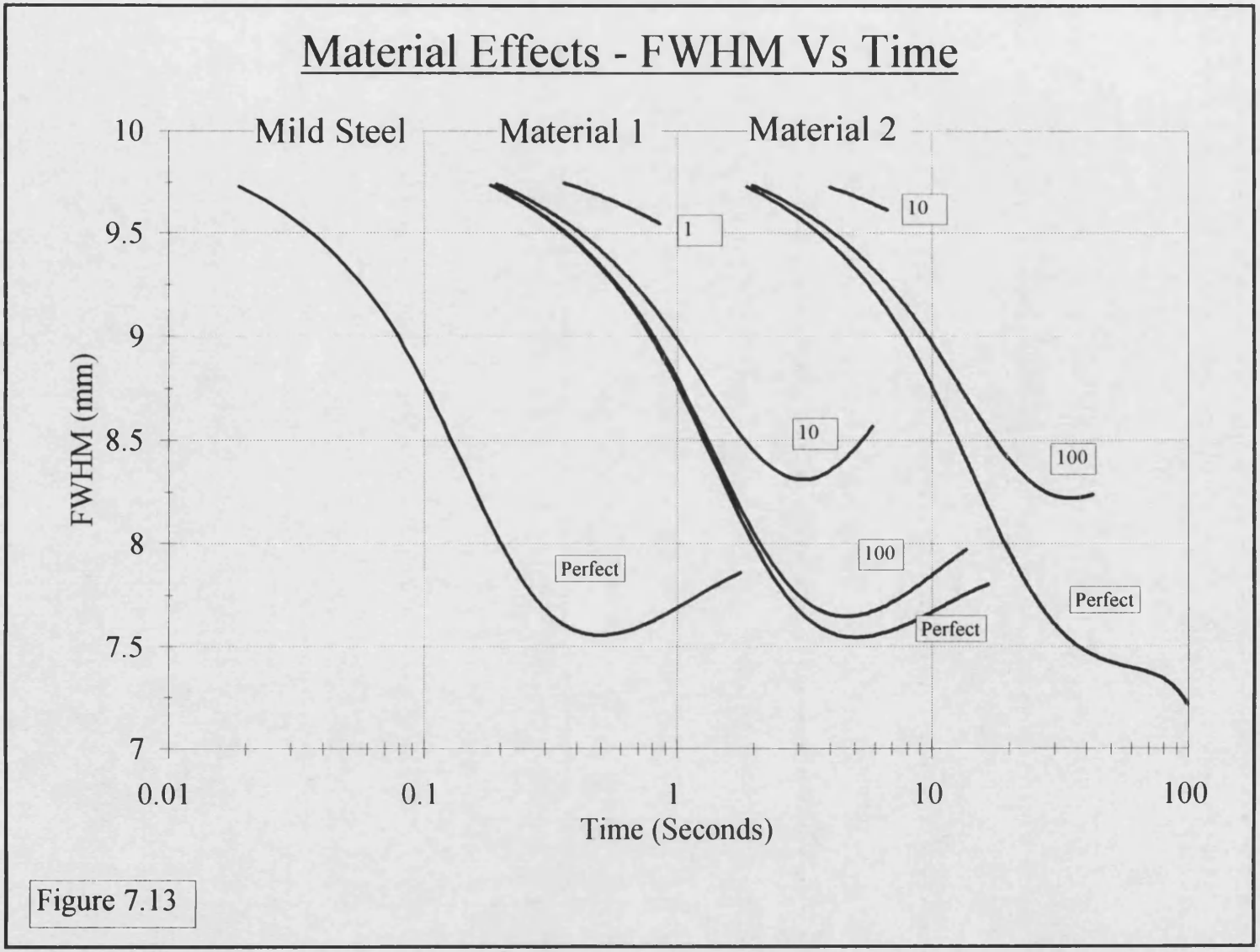
Material Effects - FWHM Vs Time
Mild Steel
Material 1
Material 2
10
9.5
9
8.5
8
7.5
7
FWHM (mm)
0.01
0.1
1
10
100
Time (Seconds)
1
10
10
100
Perfect
100
Perfect
Perfect

Figure 7.13

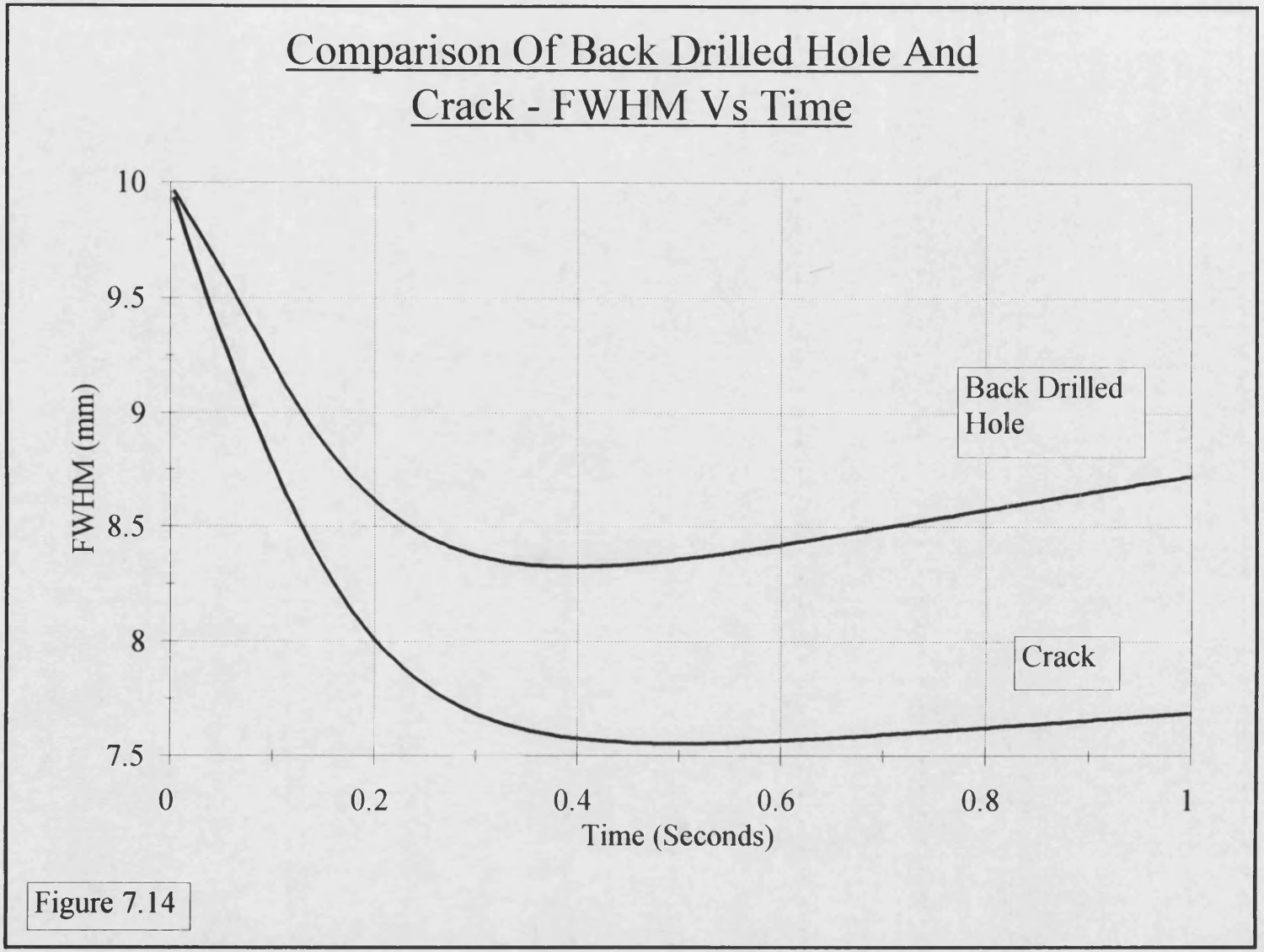
Comparison Of Back Drilled Hole And Crack - FWHM Vs Time
10
9.5
9
8.5
8
7.5
FWHM (mm)
0
0.2
0.4
0.6
0.8
1
Time (Seconds)
Back Drilled Hole
Crack

Figure 7.14

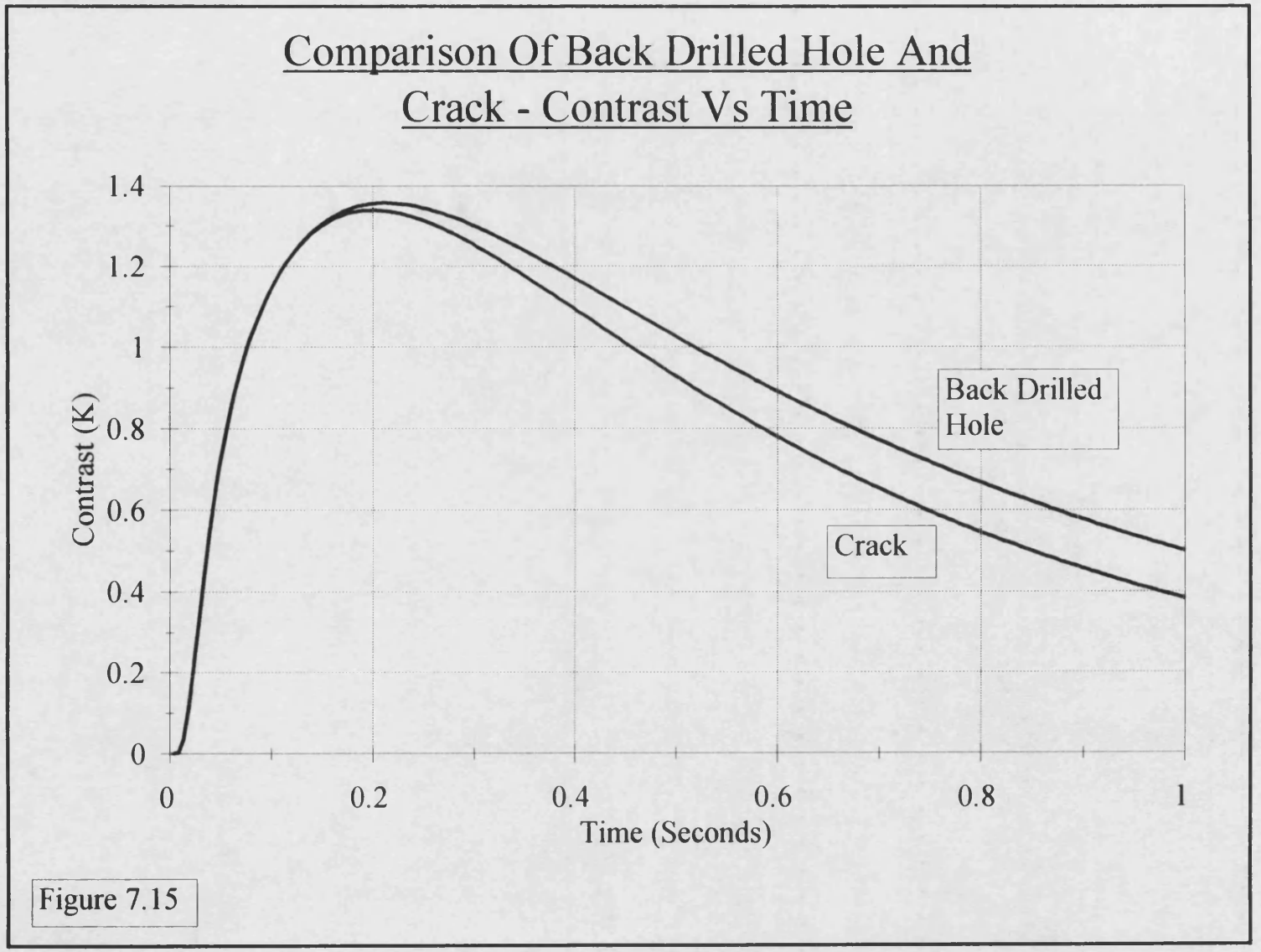
Comparison Of Back Drilled Hole And Crack - Contrast Vs Time
1.4
1.2
1
0.8
0.6
0.4
0.2
0
Contrast (K)
0
0.2
0.4
0.6
0.8
1
Time (Seconds)
Back Drilled Hole
Crack

Figure 7.15

Frame 1

Frame 2

Frame 3

Frame 4

Frame 5

Frames 1-5 Of Heat Flow Animation

Figure 7.16

Frame 6

Frame 7

Frame 8

Frame 9

Frame 10

Frames 6-10 Of Heat Flow Animation

Figure 7.17

Chapter 8

Neural Network Processing Of Transient Thermography Data

As was shown in chapter 7, each of the parameters associated with a defect (depth, size and severity) effect the transient thermal response recorded in a PVT experiment. If there were only one unknown parameter, then it may be possible to deduce it from the data. If however there is no prior knowledge of the defect, as is the case in NDE, it becomes an extremely difficult task to deduce all of the defect parameters, as their individual effects interact. Attempts have been made to devise schemes for calculating some or all of the defect parameters from experimental data [60-62,64-69,72-74], but these tend to rely on complex inversion procedures that can be time consuming. A commercially available software package has also been developed [106].

Due to the complexity of formulating an accurate analytical method for calculating the defect parameters, interest is now being shown in the use of neural network processing for this task [75,76]. Using a neural network is very simple, training data from known defect samples is fed into the network, which is trained to give the defect parameters as outputs. When the training is complete, the network can be used on new data. The user of the network need not have any knowledge of thermal techniques, however care must be taken with the results.

There are very many papers and books available on the subject of neural networks and their applications, two examples of which are [107,108], the first being a recent review article, the second a more in depth analysis. Before discussing the use of neural networks for the processing of transient thermography data, a review of the basics of single perceptron and multilayer perceptrons networks is given.

8.1 Neural Networks

Research in the field of neural networks was initially inspired by studies of information processing in biological systems (e.g. the human brain). It was recognised that the processing mechanism differed from the approach taken in todays conventional computers. The massive parallelism of the human brain, with around 10^{11} processing units (neurons), each working very slowly, but combining to produce an incredible processing power, is dramatically different from the architecture of modern single

processor computers. It should be noted that there are many different network models, for example radial basis function and Hopfield networks. Only single perceptron and multilayer perceptron networks are considered here, as they are generally accepted as the simplest form of network. Multilayer perceptron networks are also the most widely used for practical applications.

8.1.1 The Perceptron

The perceptron is the most basic form of neural network, and consists of a single neuron (processing unit). The model of the neuron was developed by McCulloch and Pitts back in 1943. Figure 8.1 shows a schematic diagram of a perceptron. The inputs to the neuron consist of the p input values $x_1, x_2, \ldots, x_p$, and a biasing input x_0 fixed at -1. Each of the inputs, including the bias input x_0, is multiplied by an associated weight $w_0, w_1, \ldots, w_p$, and then summed to form a total v. The output y of the neuron is then given by applying the non-linear activation function φ to the total input v. The biasing input x_0 has the effect of shifting (biasing) the total v either positively or negatively (depending on the weight w_0) for input into the activation function.

Mathematically this can be expressed as :

$$v = \sum_{i=0}^{p} x_i w_i \tag{8.1}$$

$$y = \varphi(v) = \varphi\left(\sum_{i=0}^{p} x_i w_i\right) \tag{8.2}$$

Three examples of possible non-linear activation functions are shown in figure 8.2. The first is a simple threshold function :

$$\varphi(v) = \begin{cases} 1 \text{ if } v \geq 0 \\ 0 \text{ if } v < 0 \end{cases} \qquad \text{Threshold Function} \tag{8.3}$$

The second is a piecewise linear function :

$$\varphi(v) = \begin{cases} 1 \text{ if } v \geq 0.5 \\ v + 0.5 \text{ if } 0.5 > v > -0.5 \\ 0 \text{ if } v \leq -0.5 \end{cases} \qquad \text{Piecewise Linear Function} \tag{8.4}$$

The third is the most commonly used function, and is called the Sigmoid function. Note that this function is differentiable (smooth) whereas the others are not. This property will be of great importance when multilayer perceptrons are considered :

$$\varphi(v) = \frac{1}{1+e^{-av}} \qquad \text{Sigmoid Function} \qquad (8.5)$$

The perceptron can be mathematically regarded as being a non-linear function, mapping the input variables $x_1, x_2, ..., x_p$ into a single output variable y. If the threshold function is used as the activation function, the output of the perceptron will be either 0 or 1. Neural networks are often applied to problems of pattern recognition. It can be shown [108] that a single perceptron model can be used to classify two patterns that are linearly separable. By this it is meant that in the p-dimensional space of the input variables $x_1, x_2, ..., x_p$, the patterns to which the input data is to be classified can be separated by a hyperplane. In two dimensions, the input variables x_1 and x_2 form an x-y pair on a 2-D Cartesian grid. Inputs associated with class 1 always lies on one side of a separating line (decision boundary), and inputs associated with class 2 always lie on the other side of the boundary (see figure 8.3). In training a perceptron, the weights $w_0, w_1, ..., w_p$ are adjusted so that the separating line (plane) lies between the pattern classes.

8.1.2 Perceptron Training

Consider now the problem outlined above of finding the decision boundary between two linearly separable patterns. The output of the perceptron (using the threshold function) is to be 0 when the inputs correspond to class 1, and 1 when the inputs correspond to class 2. Before discussing the training algorithm, it is preferable to define a shorthand notation that will greatly simplify it's presentation. The inputs $x_0, x_1, ..., x_p$ can be thought of as constituting the components of a vector $\mathbf{x}$. Similarly the weights $w_0, w_1, ..., w_p$ can be thought of as the components of a vector $\mathbf{w}$. Using this terminology, the total v to which the activation function φ is applied is given by :

$$v = \mathbf{w}^T\mathbf{x} \qquad (8.6)$$

Where the superscript T implies that the transpose of vector $\mathbf{w}$ is to be taken before calculating the matrix product of the pair. Taking the transpose of vector (matrix) $\mathbf{w}$ generates a $1xp$ row vector, which is then multiplied by the px1 column vector $\mathbf{x}$ to obtain a single element (scalar quantity) v.

To train the perceptron, it is necessary to have a training set of input vectors [$\mathbf{x}(1)$, $\mathbf{x}(2)$, ..., $\mathbf{x}(N)$], for which the classification of each is known (i.e. for each input vector in the training set, it is known to which class it belongs). Initially, all elements of the weight vector $\mathbf{w}$ are set to zero. The first input vector $\mathbf{x}(1)$ is then applied to the perceptron, and the associated output class calculated. If the input vector is correctly classified, then the weight vector is left unchanged, if it is not correctly classified it is adjusted as follows :

a) If the output was 0 (indicating class 1), and the input vector actually corresponded to class 2, the weight vector is modified to :

$$\mathbf{w}_{New} = \mathbf{w}_{Old} + \eta\mathbf{x}(1) \tag{8.7}$$

Where η is called the learning rate parameter ($\eta > 0$), and controls how fast the weight vector is modified. This change to the weight vector $\mathbf{w}$ has the effect of increasing the weight for positive input elements and reducing the weight for negative input elements. If the input vector $\mathbf{x}(1)$ was applied again, the output of the perceptron would be more likely to classify the input vector correctly.

b) If the output was 1 (indicating class 2), and the input vector actually corresponded to class 1, the weight vector is modified to :

$$\mathbf{w}_{New} = \mathbf{w}_{Old} - \eta\mathbf{x}(1) \tag{8.8}$$

This change has the effect of decreasing the weight for positive input elements and increasing the weight for negative input elements.

Once any alterations have been made to $\mathbf{w}$, the next input vector $\mathbf{x}(2)$ is applied to the perceptron, followed by $\mathbf{x}(3)$, $\mathbf{x}(4)$ etc. The general case of applying the n^{th} input vector $\mathbf{x}(n)$ results in the following modifications to $\mathbf{w}$:

a) If the input vector $\mathbf{x}(n)$ is correctly classified, the weight vector $\mathbf{w}$ is left unchanged.

b) If the output was 0 (indicating class 1), and the input vector actually corresponded to class 2, the weight vector is modified to :

$$\mathbf{w}_{New} = \mathbf{w}_{Old} + \eta\mathbf{x}(n) \tag{8.9}$$

c) If the output was 1 (indicating class 2), and the input vector actually corresponded to class 1, the weight vector is modified to :

$$\mathbf{w}_{New} = \mathbf{w}_{Old} - \eta\mathbf{x}(n) \tag{8.10}$$

Once all the input vectors have been applied to the perceptron, the training cycles through the training set again. Between each cycle of the training set, the order of presentation of the set is randomised, as this helps to speed the training process. Each pass through the set reduces the number of incorrectly classified input vectors. When all the input vectors in the training set are classified correctly, the training is complete. Note that it has been assumed that the training data *is* linearly separable. If it is not, it will not be possible to reach a stage where all inputs are correctly characterised. A proof that this training algorithm will generate a weight vector **w** capable of correctly classifying input vectors corresponding to two linearly separable patterns in a finite number of iterations can be found in [108]. Note that if the Sigmoid function was used as the activation function instead of the threshold function, the outputs would not be quantised 0s and 1s.

8.1.3 The Multilayer Perceptron

Figure 8.4 shows the architecture of a multilayer perceptron. This example has two hidden layers of neurons (circles), and is fully connected (i.e. each input or neuron is connected to every neuron in the next layer). A multilayer perceptron can have any number of hidden layers greater than or equal to one, and full connectivity is not required. It is important to note that in this architecture there is no feedback i.e. there are no connections from right to left, and no inter-layer connections. Signal flow through the network is from left to right only (except during training - see below and appendix B). This type of network is known as a multilayer feedforward network. As might be expected from this architecture, the training of such a network (adjustment of the weights) is rather more involved than the single perceptron case. A widely adopted training method is known as the error back propagation algorithm, and is discussed below.

8.1.4 Multilayer Perceptron Training - Error Back Propagation

The basic idea of back propagation training is simple, although a full derivation of the algorithm is lengthy. To avoid undue clutter here in the main text, a derivation of the error back propagation algorithm can be found in appendix B, with just an overview of

the method given here. It is recommended that this section be read first to give a flavour of the method before tackling the derivation.

In simple terms, the algorithm consists of making two passes through the network for each example in the training set, a forward pass, and a backward error propagation pass. The training set consists of a set of N pairs of vectors [(**x**(1),**d**(1)),(**x**(2),**d**(2)), ...,(**x**(N),**d**(N))]. The **x**(i)s are the input vectors, and the **d**(i)s are the required output vectors. Note that in this case there can be more than 1 output neuron, and so an output vector is calculated rather than a single number.

The training algorithm proceeds as follows :

1. All the weights in the network are initialised to small random values.

2. The examples in the training set are presented to the network. For each example, steps 3 and 4 are carried out.

3. Forward Computation. Consider training example **n** being presented to the network. The input vector **x**(n) is applied to the input layer of the network. The total input $v_j^{(l)}$ to a neuron j, in layer l, is then computed layer by layer using the formula (see figure 8.5 showing the inputs and output of a general hidden layer neuron j) :

$$v_j^{(l)}(n) = \sum_{i=0}^{p} w_{ji}^{(l)}(n) y_i^{(l-1)}(n) \tag{8.11}$$

This is analogous to equation 8.1 for the total input to a single perceptron, but is generalised so that it can be applied to any neuron, in any layer of a multilayer perceptron network. $w_{ji}^{(l)}$(n) is the weight associated with input $y_i^{(l-1)}$(n) to neuron j. Input $y_i^{(l-1)}$(n) is the output of neuron i when considering any layer other than the first hidden layer, or is the input element x_i(n) when considering the first hidden layer.

The output of neuron j in layer l ($y_j^{(l)}$(n)) is calculated analogously to the single perceptron case by applying the activation function φ to the total input $v_j^{(l)}$. Assuming the use of the Sigmoid function given by equation 8.5 (with a = 1), this is given by :

$$y_j^{(l)}(n) = \frac{1}{1+e^{(-v_j^{(l)}(n))}} \tag{8.12}$$

If neuron j is in the output layer, then the output of the neuron constitutes a part of the output vector **o**(n). In this case :

$$o_j(n) = y_j^{(l)}(n) \tag{8.13}$$

Once all the computations have been made, for every neuron in each layer of the network, the complete output vector **o**(n) is available.

4. Backward Computation. The error e_j(n) for an output layer neuron j, can now be found by subtracting the output vector element o_j(n) from the desired response for that element from the required output vector **d**(n). i.e. :

$$e_j(n) = d_j(n) - o_j(n) \tag{8.14}$$

Quantities $\delta_j^{(l)}$ known as the local gradients (see appendix B) are now evaluated using the equations below :

$$\delta_j^{(l)}(n) = e_j(n)o_j(n)\left\{1 - o_j(n)\right\} \quad \text{For neuron j in output layer} \tag{8.15}$$

$$\delta_j^{(l)}(n) = y_j^{(l)}(n)\left\{1 - y_j^{(l)}(n)\right\}\sum_{\mathbf{k}} \delta_{\mathbf{k}}^{(l+1)}(n)w_{kj}^{(l+1)}(n) \quad \text{For neuron j in hidden layer} \tag{8.16}$$

Note that in these equations, the partial derivative of the activation function (that occurs in the expressions for the local gradients) has been explicitly evaluated for the Sigmoid function.

Finally, the weights are modified using the formula :

$$w_{ji}^{(l)}(n+1) = w_{ji}^{(l)}(n) + \alpha\left\{w_{ji}^{(l)}(n) - w_{ji}^{(l)}(n-1)\right\} + \eta\delta_j^{(l)}(n)y_i^{(l-1)}(n) \tag{8.17}$$

Where η is the learning rate parameter, and α is the momentum parameter.

5. The training continues until the entire training set has been presented to the network. The order of the examples is then randomised, and presented again. A full presentation of the entire training set is often called an epoch. The training stops when the average error over the entire training set is below a given level, when the change in the weights in an epoch falls below a certain level, or when a set number of epochs has been presented.

8.2 Applying A Neural Network Approach To Defect Characterisation

The previous sections of this chapter have given a brief introduction to perceptron and multilayer perceptron networks, without reference to a specific application. It is now necessary to consider how one applies these ideas to the problem of defect characterisation from transient thermography data. It is necessary to consider such questions as :

1. How many, and representing what physically measurable parameters, are the inputs to the network going to be ?

2. How many hidden layers should the network be comprised of, and how many neurons should be in each layer ?

3. Should the network be fully connected ?

4. How many, and representing what defect characteristics, should the outputs of the network be ?

5. How is the training data to be generated - experiment or simulation ?

N.B. It is usual to normalise both the inputs and outputs of the training set data before training the network. This is done so that the use of the Sigmoid function (outputs limited to only between 0 and 1 (see figure 8.2)) can be used without modification. Obviously, if this is done, data input into the network after training needs to be normalised in an identical fashion to the training data. The output data also needs to be 'un-normalised' with reference to the manner in which the training data outputs were normalised.

There are two distinct approaches that can be taken for the characterisation of defects from transient thermography data. The first, as taken by Bison, Bressan, Di Sarno, Grinzato etal [76], is to use the neural network to analyse a sequence of images on a point by point basis. From the sequence, the time evolution of each individual point in the image is analysed to find the time of maximum contrast t_{max} (with reference to a known non-defect point), and the value of the maximum contrast C_{max}. This is input into what they term a 'flaw detector' network, which determines if the point corresponds to a defect or non-defect position. If the point corresponds to a defect position, a filtered (smoothed) contrast-time profile of the point (with 50 time values) is fed into a second 'estimator' network. The job of this second network is to estimate the depth of

the defect. Their networks were trained to detect and characterise the depth of circular defects in PVC. A mixture of experimental and simulated data was used to train the networks, and then tested experimentally using a new sample with defects buried at different depths. The results were extremely good, accurately determining both the position and depth of the defects.

The approach taken by the author is to limit the application of the neural network only to the task of defect characterisation (not defect location). In this case, experimentally measurable parameters of the defect are input into the network, and it is the network's job to characterise the defect from this. This approach is not so highly automated as the approach of Bison etal, but is likely to be quicker in instances where it is obvious where the defect is located. The specific task to which the network would be applied was for the characterisation of crack defects in mild steel, as much simulation of this problem has already been undertaken.

8.2.1 Network Training Data

It was decided to use the following experimentally measurable defect features as inputs to the network (these are similar to those used by Krapez, Maldague and Cielo [62] in their analytical inversion procedure) :

1. The maximum relative contrast. This is measured in reference to a non defect position, and is defined by :

$$C_{\max} = \frac{T_{Defect}(t_{\max})}{T_{Non-Defect}(t_{\max})} \tag{8.18}$$

Where t_{max} is the time of maximum contrast over the defect, $T_{Defect}(t_{max})$ is the temperature over the centre of the defect at maximum contrast, and $T_{Non\text{-}Defect}(t_{max})$ is the temperature of a non defect point at maximum contrast.

2. Half rise time. The time taken for the point in the centre of the defect to rise to half the maximum contrast level.

3. The value of the FWHM at the half rise time.

4. Half fall time. The time taken for the point in the centre of the defect rise to its maximum contrast and then fall to half the maximum contrast level.

5. The value of the FWHM at the half fall time.

Figure 8.6 shows a pair of typical contrast-time and FWHM-time curves with the half rise and half fall times marked, along with the corresponding FWHM measurements. These inputs were chosen as between them they contain a good deal of information on the time scale of the contrast time relationship, and on the variation of the apparent defect size with time. The half rise and half fall times are also quite easy to determine with reasonable accuracy (it is more accurate to measure the half rise or fall time from a contrast time curve, than the time of maximum contrast).

It was decided, as no facilities were available for the manufacture of defect samples, that all training data (and subsequent test data) would be simulated. For the training data, simulations were made of crack defects with the following diameters, depths and contact resistances :

Crack Diameters : 2, 4, 6, 8, 10 mm

Crack Depths : 0.25, 0.5, 1.0, 1.5, 2.0 mm

Contact Resistances : 10, 100 μm (equivalent thickness of air)

All combinations of these characteristics were simulated, giving a total training set of 50 examples. From the simulations, the input values discussed above were extracted, and fed into the network. The network was trained using the standard back propagation algorithm discussed earlier.

8.2.2 Network Topology

Figure 8.7 shows a schematic diagram of the network topology. The network has five inputs (discussed above), with a single hidden layer of four neurons, and an output layer of two neurons. The network is fully connected. This configuration was arrived at on a trail and error basis - there are no golden rules for determining which network topology will suit a given problem. Generally speaking, the more hidden layers, the more detail will be extracted from the training data. It can be a problem if too many hidden layers are used in a network, in that the network effectively memorises the training data, and looses it's ability to interpolate it's 'knowledge' to new data. For this reason, simple network topologies tend to be more robust with new data. In training a network, there is no guarantee that a good (low error over the training set) solution will be found, even if the problem is theoretically solvable by the training method. For this reason, it is

necessary to train a network several times, as each time a new set of random initial weights will be used, and so a different final solution will be achieved. Obviously, the best (least error) set of weights from a group of training attempts is selected as the final weight set.

A commercially available neural network package called Neudesk, produced by Neural Computer Sciences, was used for the training of the network. Once the network was trained (weights calculated), a separate FORTRAN program was written to evaluate the network output without using Neudesk. This was done so that the normalisation procedure could be applied automatically to input test data, and results produced rescaled automatically. This considerably simplified and speeded up the testing procedure.

Note

Initially it was intended to train the network to give three outputs (a) true defect diameter, (b) defect depth, and (c) defect contact resistance. However, it became apparent when training the network to produce these quantities, that the network would not converge to a set of weights suitable for this task. For this reason the outputs were reduced to only the first two, defect diameter and depth. (If more time were available, it may have been possible to find a new input quantity (or quantities) that contained enough information for the network to determine the contact resistance).

8.3 Results

The network was tested in two distinct ways. The first was to input new data into the network, produced by simulating cracks of size, depth and contact resistance different to those in the training set. This was done to determine the interpolating ability of the network. A second series of tests was devised to determine what effect small errors in the experimental measurements would make. For example - if a small error was made in the determination of the half rise and half fall times - what effect would this have on the calculated defect characteristics. Obviously, if only small errors in the measured input quantities cause massive variations in the network outputs, when practical limitations of experimental accuracy are considered, this method of solution would be useless.

8.3.1 Interpolation Results

Size Interpolation

Simulations were made for crack defects with diameters of 3, 5, 7, 9 and 11 mm, at the same depths and contact resistances as the training data. The network inputs were extracted from the simulated data, and fed into the network as a way of testing the ability of the network to interpolate the defect diameter. The tables below show the true defect parameters, the defect parameters calculated by the network, and the percentage errors of the network parameters compared to the true parameters.

3mm Diameter Test Results

True Diameter (mm)	True Depth (mm)	True CR (≡Width Air μm)	Network Diameter (mm)	Network Depth (mm)	% Error In Diameter	% Error In Depth
3	0.25	100	3.155067	0.244357	5.1689	-2.2572
3	0.5	100	2.977391	0.466877	-0.753633	-6.6246
3	1	100	2.810915	0.979438	-6.302833	-2.0562
3	1.5	100	2.804902	1.534849	-6.503267	2.3232667
3	2	100	2.845039	2.016702	-5.165367	0.8351
3	0.25	10	3.139067	0.250966	4.6355667	0.3864
3	0.5	10	2.964793	0.469542	-1.173567	-6.0916
3	1	10	2.807648	0.976022	-6.411733	-2.3978
3	1.5	10	2.807072	1.528836	-6.430933	1.9224
3	2	10	2.851734	2.009787	-4.9422	0.48935

Maximum Diameter Error = -6.5%, Maximum Depth Error = -6.6%

5mm Diameter Test Results

True Diameter (mm)	True Depth (mm)	True CR (≡Width Air μm)	Network Diameter (mm)	Network Depth (mm)	% Error In Diameter	% Error In Depth
5	0.25	100	4.855601	0.239662	-2.88798	-4.1352
5	0.5	100	4.968184	0.499444	-0.63632	-0.1112
5	1	100	4.949795	0.998226	-1.0041	-0.1774
5	1.5	100	4.866442	1.497188	-2.67116	-0.187467
5	2	100	4.771528	1.99629	-4.56944	-0.1855
5	0.25	10	4.851662	0.256352	-2.96676	2.5408
5	0.5	10	4.950877	0.500537	-0.98246	0.1074
5	1	10	4.942323	0.990873	-1.15354	-0.9127
5	1.5	10	4.870497	1.486333	-2.59006	-0.911133
5	2	10	4.787869	1.981453	-4.24262	-0.92735

Maximum Diameter Error = -4.6%, Maximum Depth Error = -4.1%

7mm Diameter Test Results

True Diameter (mm)	True Depth (mm)	True CR (≡Width Air μm)	Network Diameter (mm)	Network Depth (mm)	% Error In Diameter	% Error In Depth
7	0.25	100	6.987433	0.236239	-0.179529	-5.5044
7	0.5	100	7.08899	0.533946	1.2712857	6.7892
7	1	100	7.102606	1.025205	1.4658	2.5205
7	1.5	100	7.141062	1.499118	2.0151714	-0.0588
7	2	100	7.207447	1.99081	2.9635286	-0.4595
7	0.25	10	6.957383	0.268392	-0.608814	7.3568
7	0.5	10	7.067163	0.535269	0.9594714	7.0538
7	1	10	7.098821	1.012393	1.4117286	1.2393
7	1.5	10	7.143115	1.481644	2.0445	-1.223733
7	2	10	7.220351	1.967786	3.1478714	-1.6107

Maximum Diameter Error = +3.2%, Maximum Depth Error = +7.4%

9mm Diameter Test Results

True Diameter (mm)	True Depth (mm)	True CR (≡Width Air μm)	Network Diameter (mm)	Network Depth (mm)	% Error In Diameter	% Error In Depth
9	0.25	100	9.148193	0.220673	1.6465889	-11.7308
9	0.5	100	9.162973	0.514771	1.8108111	2.9542
9	1	100	9.076782	1.007237	0.8531333	0.7237
9	1.5	100	9.060836	1.520216	0.6759556	1.3477333
9	2	100	9.118828	2.020233	1.3203111	1.01165
9	0.25	10	9.084395	0.268956	0.9377222	7.5824
9	0.5	10	9.13076	0.521308	1.4528889	4.2616
9	1	10	9.079222	0.988827	0.8802444	-1.1173
9	1.5	10	9.06569	1.491601	0.7298889	-0.559933
9	2	10	9.126731	1.987993	1.4081222	-0.60035

Maximum Diameter Error = +1.8%, Maximum Depth Error = -11.8%

11mm Diameter Test Results

Note that this is not really an interpolation test, but an extrapolation test, as a diameter of 11 mm lies outside of the range of the training data.

True Diameter (mm)	True Depth (mm)	True CR (≡Width Air μm)	Network Diameter (mm)	Network Depth (mm)	% Error In Diameter	% Error In Depth
11	0.25	100	10.54717	0.207881	-4.116582	-16.8476
11	0.5	100	10.59895	0.46446	-3.645882	-7.108
11	1	100	10.54218	0.937715	-4.161964	-6.2285
11	1.5	100	10.45490	1.506514	-4.955391	0.4342667
11	2	100	10.36944	2.043604	-5.732336	2.1802
11	0.25	10	10.52330	0.268281	-4.333591	7.3124
11	0.5	10	10.57202	0.480455	-3.890673	-3.909
11	1	10	10.54279	0.9149	-4.156409	-8.51
11	1.5	10	10.46419	1.461044	-4.870945	-2.597067
11	2	10	10.38375	1.997845	-5.6022	-0.107715

Maximum Diameter Error = -5.7%, Maximum Depth Error = -16.8%

Most of the errors in these tests were below ± 5% in both diameter and depth. The largest errors were for the depth determination of shallow defects with large diameter. All but two of the errors were below ± 10%, with one of these for the 11 mm diameter defect (extrapolation rather than interpolation). Neural networks are generally more suitable for interpolation tasks, rather than extrapolating outside of the range of their training data.

Depth Interpolation

Simulations were made for crack defects at depths of 0.75, 1.25, 1.75and 2.25 mm, for the same diameters and contact resistances as the training data. The network inputs were extracted from the simulated data, and fed into the network as a way of testing the ability of the network to interpolate the defect depth. The tables below show the true defect parameters, the defect parameters calculated by the network, and the percentage errors of the network parameters compared to the true parameters.

2mm Diameter - Depth Interpolation Results

True Diameter (mm)	True Depth (mm)	True CR (≡Width Air μm)	Network Diameter (mm)	Network Depth (mm)	% Error In Diameter	% Error In Depth
2	0.75	100	1.9256	0.7152	-3.72	-4.64
2	1.25	100	2.0351	1.2576	1.755	0.608
2	1.75	100	2.2169	1.7757	10.845	1.4685714
2	2.25	100	2.3654	2.2038	18.27	-2.053333
2	0.75	10	1.9231	0.7147	-3.845	-4.706667
2	1.25	10	2.0353	1.2544	1.765	0.352
2	1.75	10	2.2189	1.7722	10.945	1.2685714
2	2.25	10	2.3689	2.2006	18.445	-2.195556

Maximum Diameter Error = +18.5%, Maximum Depth Error = -4.7%

4mm Diameter - Depth Interpolation Results

True Diameter (mm)	True Depth (mm)	True CR (≡Width Air μm)	Network Diameter (mm)	Network Depth (mm)	% Error In Diameter	% Error In Depth
4	0.75	100	3.916	0.7209	-2.1	-3.88
4	1.25	100	3.7991	1.2532	-5.0225	0.256
4	1.75	100	3.7151	1.7684	-7.1225	1.0514286
4	2.25	100	3.6432	2.2417	-8.92	-0.368889
4	0.75	10	3.9046	0.7183	-2.385	-4.226667
4	1.25	10	3.7979	1.2462	-5.0525	-0.304
4	1.75	10	3.7227	1.7585	-6.9325	0.4857143
4	2.25	10	3.6597	2.2304	-8.5075	-0.871111

Maximum Diameter Error = -8.9%, Maximum Depth Error = -3.9%

6mm Diameter - Depth Interpolation Results

True Diameter (mm)	True Depth (mm)	True CR (≡Width Air μm)	Network Diameter (mm)	Network Depth (mm)	% Error In Diameter	% Error In Depth
6	0.75	100	6.0355	0.7729	0.5916667	3.0533333
6	1.25	100	6.0305	1.2527	0.5083333	0.216
6	1.75	100	6.0275	1.738	0.4583333	-0.685714
6	2.25	100	5.9485	2.2337	-0.858333	-0.724444
6	0.75	10	6.0231	0.7653	0.385	2.04
6	1.25	10	6.029	1.2408	0.4833333	-0.736
6	1.75	10	6.0358	1.7217	0.5966667	-1.617143
6	2.25	10	5.9775	2.2134	-0.375	-1.626667

Maximum Diameter Error = -0.9%, Maximum Depth Error = +3.1%

8mm Diameter - Depth Interpolation Results

True Diameter (mm)	True Depth (mm)	True CR (≡Width Air μm)	Network Diameter (mm)	Network Depth (mm)	% Error In Diameter	% Error In Depth
8	0.75	100	8.1517	0.7821	1.89625	4.28
8	1.25	100	8.1305	1.2655	1.63125	1.24
8	1.75	100	8.2123	1.7595	2.65375	0.5428571
8	2.25	100	8.2469	2.2349	3.08625	-0.671111
8	0.75	10	8.1421	0.7725	1.77625	3
8	1.25	10	8.1328	1.2465	1.66	-0.28
8	1.75	10	8.2159	1.7345	2.69875	-0.885714
8	2.25	10	8.2706	2.2067	3.3825	-1.924444

Maximum Diameter Error = +3.4%, Maximum Depth Error = +4.28%

10mm Diameter - Depth Interpolation Results

True Diameter (mm)	True Depth (mm)	True CR (≡Width Air μm)	Network Diameter (mm)	Network Depth (mm)	% Error In Diameter	% Error In Depth
10	0.75	100	9.9426	0.7301	-0.574	-2.653333
10	1.25	100	9.8588	1.245	-1.412	-0.4
10	1.75	100	9.8343	1.7924	-1.657	2.4228571
10	2.25	100	9.8075	2.2535	-1.925	0.1555556
10	0.75	10	9.9342	0.7207	-0.658	-3.906667
10	1.25	10	9.8647	1.2145	-1.353	-2.84
10	1.75	10	9.8404	1.7533	-1.596	0.1885714
10	2.25	10	9.8254	2.2176	-1.746	-1.44

Maximum Diameter Error = -1.9%, Maximum Depth Error = -3.9%

For all but the 2 mm diameter defect, the depth interpolation results are extremely good. Many of the errors are less than ±2%.

Severity Tests

Simulations were made for crack defects with a contact resistance equivalent to 50 μm of air, for the same diameters and depths as the training data. The network inputs were extracted from the simulated data, and fed into the network as a way of testing the ability of the network to cope with a different contact resistance. The tables below show the true defect parameters, the defect parameters calculated by the network, and the percentage errors of the network parameters compared to the true parameters.

2mm Diameter - Severity Test Results

True Diameter (mm)	True Depth (mm)	True CR (≡Width Air μm)	Network Diameter (mm)	Network Depth (mm)	% Error In Diameter	% Error In Depth
2	0.25	50	2.1627	0.2798	8.135	11.92
2	0.5	50	1.9949	0.4887	-0.255	-2.26
2	1	50	1.9562	0.9772	-2.19	-2.28
2	1.5	50	2.1279	1.5281	6.395	1.8733333
2	2	50	2.2967	1.998	14.835	-0.1

Maximum Diameter Error = +14.8%, Maximum Depth Error = +11.9%

4mm Diameter - Severity Test Results

True Diameter (mm)	True Depth (mm)	True CR (≡Width Air μm)	Network Diameter (mm)	Network Depth (mm)	% Error In Diameter	% Error In Depth
4	0.25	50	3.9759	0.2401	-0.6025	-3.96
4	0.5	50	3.9705	0.4758	-0.7375	-4.84
4	1	50	3.8546	0.9835	-3.635	-1.65
4	1.5	50	3.7523	1.515	-6.1925	1
4	2	50	3.6835	2.0098	-7.9125	0.49

Maximum Diameter Error = -7.9%, Maximum Depth Error = -4.8%

6mm Diameter - Severity Test Results

True Diameter (mm)	True Depth (mm)	True CR (≡Width Air μm)	Network Diameter (mm)	Network Depth (mm)	% Error In Diameter	% Error In Depth
6	0.25	50	5.8621	0.2427	-2.298333	-2.92
6	0.5	50	6.0018	0.5225	0.03	4.5
6	1	50	6.0356	1.0138	0.5933333	1.38
6	1.5	50	6.0284	1.4904	0.4733333	-0.64
6	2	50	6.0137	1.9861	0.2283333	-0.695

Maximum Diameter Error = -2.3%, Maximum Depth Error = +4.5%

8mm Diameter - Severity Test Results

True Diameter (mm)	True Depth (mm)	True CR (≡Width Air μm)	Network Diameter (mm)	Network Depth (mm)	% Error In Diameter	% Error In Depth
8	0.25	50	8.1166	0.2344	1.4575	-6.24
8	0.5	50	8.1673	0.5313	2.09125	6.26
8	1	50	8.1295	1.0218	1.61875	2.18
8	1.5	50	8.1609	1.5088	2.01125	0.5866667
8	2	50	8.2576	2.0002	3.22	0.01

Maximum Diameter Error = +3.22%, Maximum Depth Error = +6.3%

10mm Diameter - Severity Test Results

True Diameter (mm)	True Depth (mm)	True CR (≡Width Air μm)	Network Diameter (mm)	Network Depth (mm)	% Error In Diameter	% Error In Depth
10	0.25	50	9.9481	0.22	-0.519	-12
10	0.5	50	9.9775	0.492	-0.225	-1.6
10	1	50	9.8961	0.9752	-1.039	-2.48
10	1.5	50	9.8388	1.5173	-1.612	1.1533333
10	2	50	9.8336	2.0343	-1.664	1.715

Maximum Diameter Error = -1.7%, Maximum Depth Error = -12%

Considering the very limited amount of training data for contact resistance variations, the results are reasonable.

Multiple Interpolation

Simulations were made for crack defects with diameters of 3, 5, 7, 9 and 11 mm, at depths of 0.75, 1.25, 1.75 and 2.25 mm, and with a contact resistance equivalent to 50 microns of air. The network inputs were extracted from the simulated data, and fed into the network as a way of testing the ability of the network to interpolate when all three defect characteristics differ from any member of the training set. The tables below show the true defect parameters, the defect parameters calculated by the network, and the percentage errors of the network parameters compared to the true parameters.

3mm Diameter - Multiple Interpolation Results

True Diameter (mm)	True Depth (mm)	True CR (≡Width Air μm)	Network Diameter (mm)	Network Depth (mm)	% Error In Diameter	% Error In Depth
3	0.75	50	2.8657	0.7073	-4.476667	-5.693333
3	1.25	50	2.7963	1.2631	-6.79	1.048
3	1.75	50	2.8235	1.7848	-5.883333	1.9885714
3	2.25	50	2.8641	2.2319	-4.53	-0.804444

Maximum Diameter Error = -6.8%, Maximum Depth Error = -5.7%

5mm Diameter - Multiple Interpolation Results

True Diameter (mm)	True Depth (mm)	True CR (≡Width Air μm)	Network Diameter (mm)	Network Depth (mm)	% Error In Diameter	% Error In Depth
5	0.75	50	4.9733	0.7474	-0.534	-0.346667
5	1.25	50	4.9094	1.247	-1.812	-0.24
5	1.75	50	4.8239	1.7454	-3.522	-0.262857
5	2.25	50	4.6952	2.2362	-6.096	-0.613333

Maximum Diameter Error = -6.1%, Maximum Depth Error = -0.6%

7mm Diameter - Multiple Interpolation Results

True Diameter (mm)	True Depth (mm)	True CR (≡Width Air μm)	Network Diameter (mm)	Network Depth (mm)	% Error In Diameter	% Error In Depth
7	0.75	50	7.101	0.7853	1.4428571	4.7066667
7	1.25	50	7.1119	1.259	1.5985714	0.72
7	1.75	50	7.1819	1.7412	2.5985714	-0.502857
7	2.25	50	7.1769	2.2286	2.5271429	-0.951111

Maximum Diameter Error = +2.6%, Maximum Depth Error = +4.7%

9mm Diameter - Multiple Interpolation Results

True Diameter (mm)	True Depth (mm)	True CR (≡Width Air μm)	Network Diameter (mm)	Network Depth (mm)	% Error In Diameter	% Error In Depth
9	0.75	50	9.1178	0.7606	1.3088889	1.4133333
9	1.25	50	9.0547	1.2578	0.6077778	0.624
9	1.75	50	9.09	1.7734	1	1.3371429
9	2.25	50	9.1107	2.2379	1.23	-0.537778

Maximum Diameter Error = +1.3%, Maximum Depth Error = +1.4%

11mm Diameter - Multiple Interpolation Results

True Diameter (mm)	True Depth (mm)	True CR (≡Width Air μm)	Network Diameter (mm)	Network Depth (mm)	% Error In Diameter	% Error In Depth
11	0.75	50	10.5764	0.6905	-3.850909	-7.933333
11	1.25	50	10.499	1.2092	-4.554545	-3.264
11	1.75	50	10.4141	1.7849	-5.326364	1.9942857
11	2.25	50	10.3124	2.25	-6.250909	0

Maximum Diameter Error = -6.3%, Maximum Depth Error = -7.9%

These tests are the most difficult for the network. It is seen that the results are extremely good, with errors in many cases lower than for just the diameter or depth interpolation. No error from this test set exceeds ±8%. All these results are extremely encouraging, especially when the limited size (only 50 examples) of the training set is taken into account. If a larger, more finely spaced in terms of diameter, depth and contact resistance training set were used, it would be hoped to produce even better results.

8.3.2 Input Error Sensitivity

To test the sensitivity of the network outputs to small errors in the input data, errors were added and subtracted from the data generated by the simulations. The following errors were considered :

1. A ± 5 ms error in both the half rise, and half fall times. This is to simulate an experimental error in the timing of the sequence with respect to the heating pulse. This is a small amount, but it must be remembered that mild steel is a thermally fast material, and so for shallow defects, this corresponds to a high percentage error.

2. A ± 0.2 mm error in the FWHM at both the half rise and half fall times. This could be due to an uncertainty in the maximum contrast level (see below), which could lead to an error in the measurement of the width of the contrast peak.

3. A ± 10 % error in the maximum relative contrast. This could be caused by a noisy contrast-time curve, making accurate determination difficult.

All these errors were applied to the input data used to train the network. Each type of error was considered independently, to determine the sensitivity of the network outputs to each type of input error in isolation. The results were as follows :

+5 ms Error In Timings

5 ms was added to both the half rise and half fall times of the data used to train the network, all other inputs remaining unchanged. The network was fed with the modified input values, and the outputs analysed. This timing error gave rise to an RMS percentage deviation from the true diameter and depth of 4.1% and 12.7% respectively.

-5 ms Error In Timings

5 ms was subtracted from both the half rise and half fall times of the data used to train the network, all other inputs remaining unchanged. The network was fed with the modified input values, and the outputs analysed. This negative timing error gave rise to an RMS percentage deviation from the true diameter and depth of 4.9% and 10.4% respectively.

+0.2 mm Error In FWHM Measurements

0.2 mm was added to the FWHM measurements at both the half rise and half fall times, all other inputs remaining unchanged. The network was fed with the modified input values, and the outputs analysed. This measurement error gave rise to an RMS percentage deviation from the true diameter and depth of 8.3% and 4.9% respectively.

-0.2 mm Error In FWHM Measurements

0.2 mm was subtracted from the FWHM measurements at both the half rise and half fall times, all other inputs remaining unchanged. The network was fed with the modified input values, and the outputs analysed. This measurement error gave rise to an RMS percentage deviation from the true diameter and depth of 6.2% and 4.7% respectively.

+10 % Error In Maximum Relative Contrast

10 % was added to the maximum relative contrast, all other inputs remaining unchanged. The network was fed with the modified input values, and the outputs analysed. This error gave rise to an RMS percentage deviation from the true diameter and depth of 4.5% and 5.9% respectively.

-10 % Error In Maximum Relative Contrast

10 % was subtracted from the maximum relative contrast, all other inputs remaining unchanged. The network was fed with the modified input values, and the outputs

analysed. This error gave rise to an RMS percentage deviation from the true diameter and depth of 4.3% and 6.3% respectively.

The conclusions from this analysis are as follows :

1. Timing errors have the greatest effect on the depth determination from the network.

2. As might be expected, FWHM measurement errors have the greatest effect on the diameter determination of the network.

3. Errors in the maximum relative contrast have similar effects (percentage wise) on the diameter and depth determinations of the network.

None of the RMS deviations reported above are very large, implying the network outputs are not too sensitive to small errors in the inputs. It seems likely that this type of network could be used for a practical (experimental) defect sizing procedure.

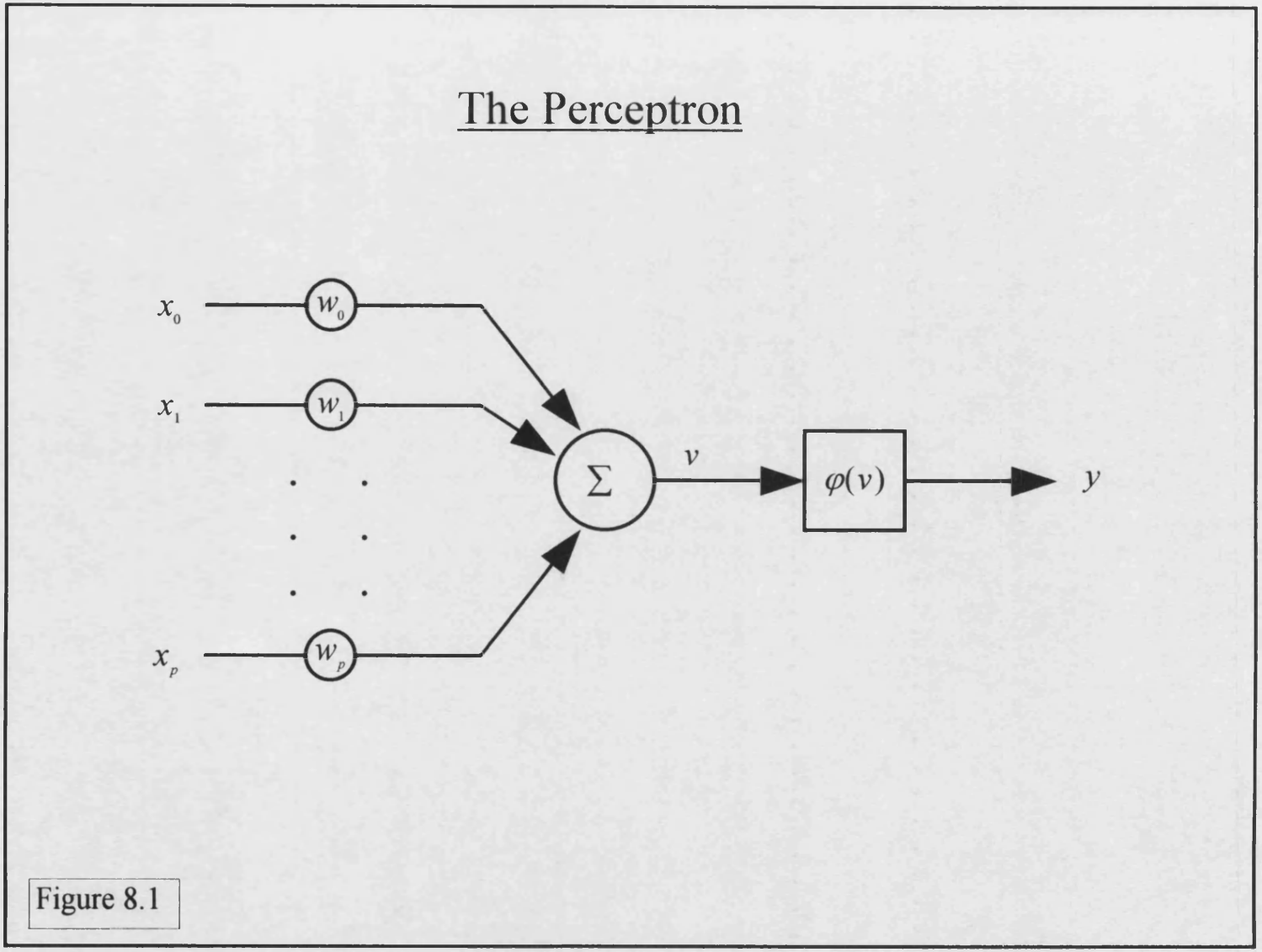

Figure 8.1

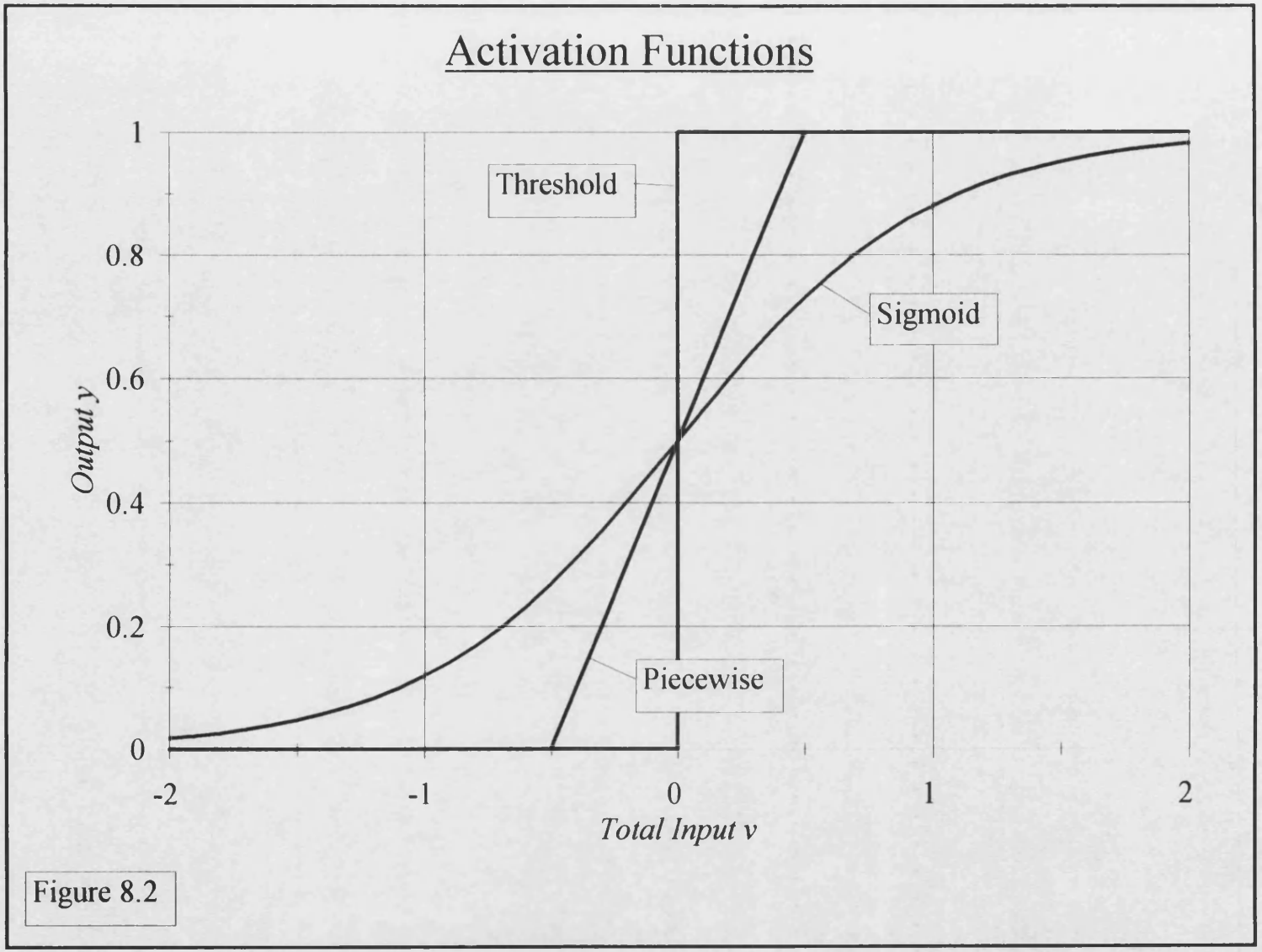
Activation Functions
1
0.8
0.6
0.4
0.2
0
Output y
Threshold
Sigmoid
Piecewise
-2
-1
0
1
2
Total Input v

Figure 8.2

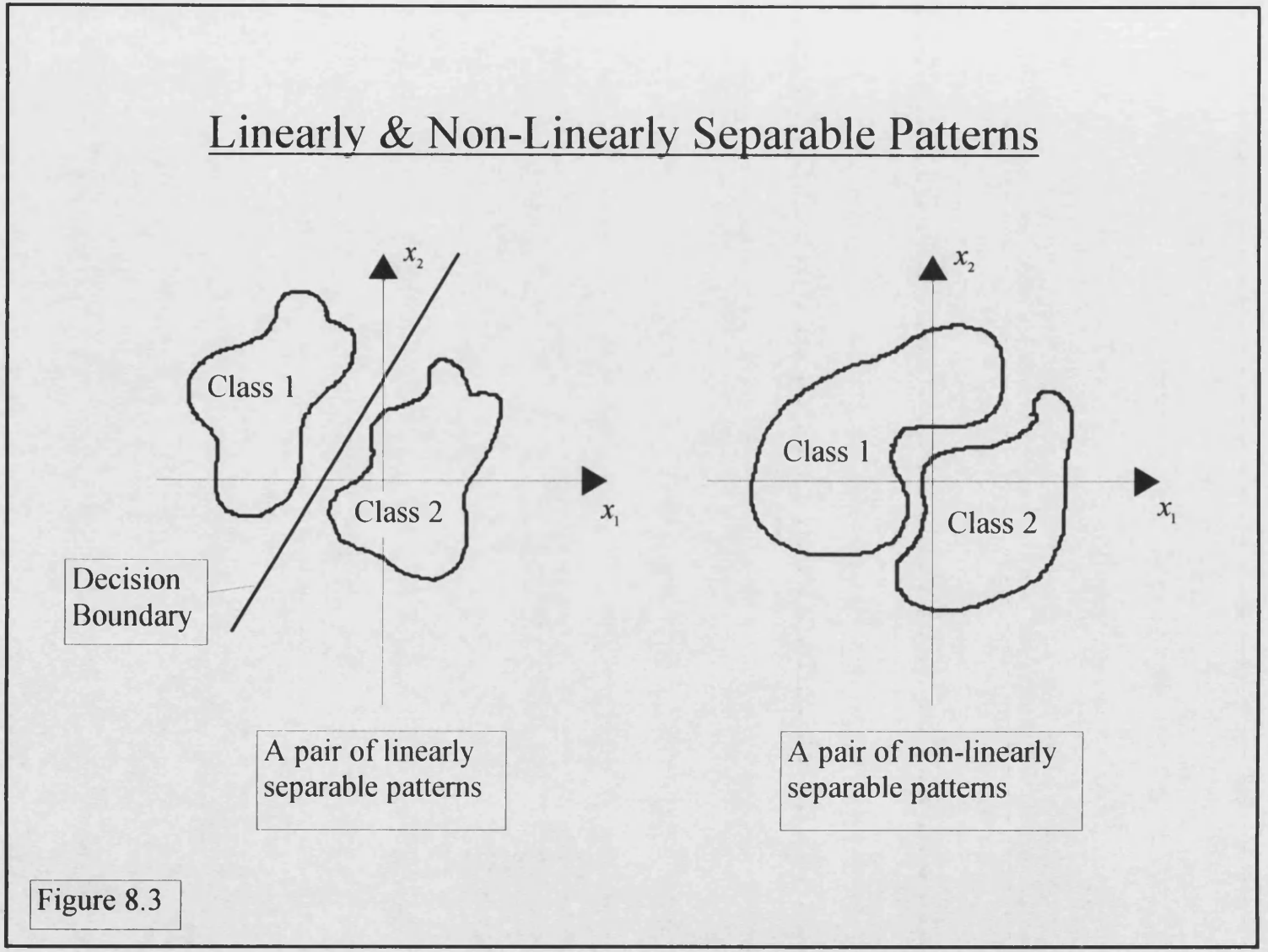
Linearly & Non-Linearly Separable Patterns
x_2
Class 1
Class 2
x_1
Decision Boundary
A pair of linearly separable patterns
x_2
Class 1
Class 2
x_1
A pair of non-linearly separable patterns

Figure 8.3

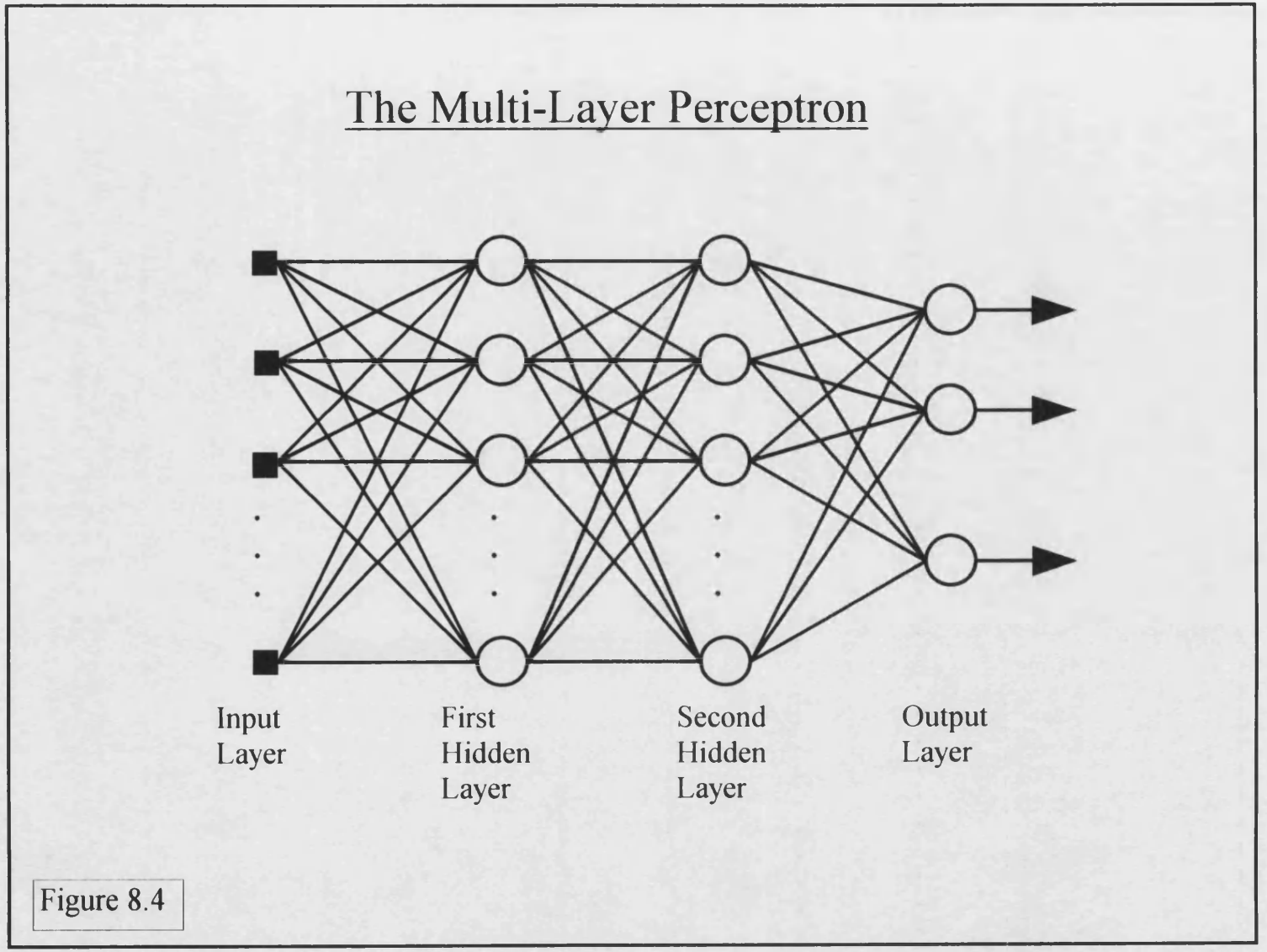
The Multi-Layer Perceptron
Input Layer
First Hidden Layer
Second Hidden Layer
Output Layer

Figure 8.4

The Inputs And Output Of A Hidden Layer Neuron

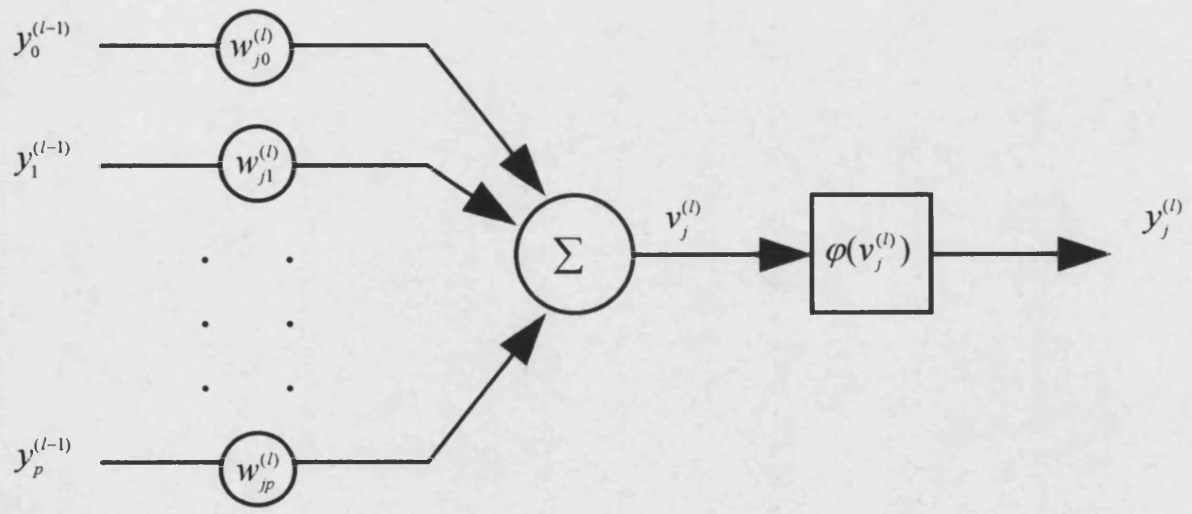

Inputs to neuron j from layer $l-1$

Neuron j

Output of neuron j to layer $l+1$

Figure 8.5

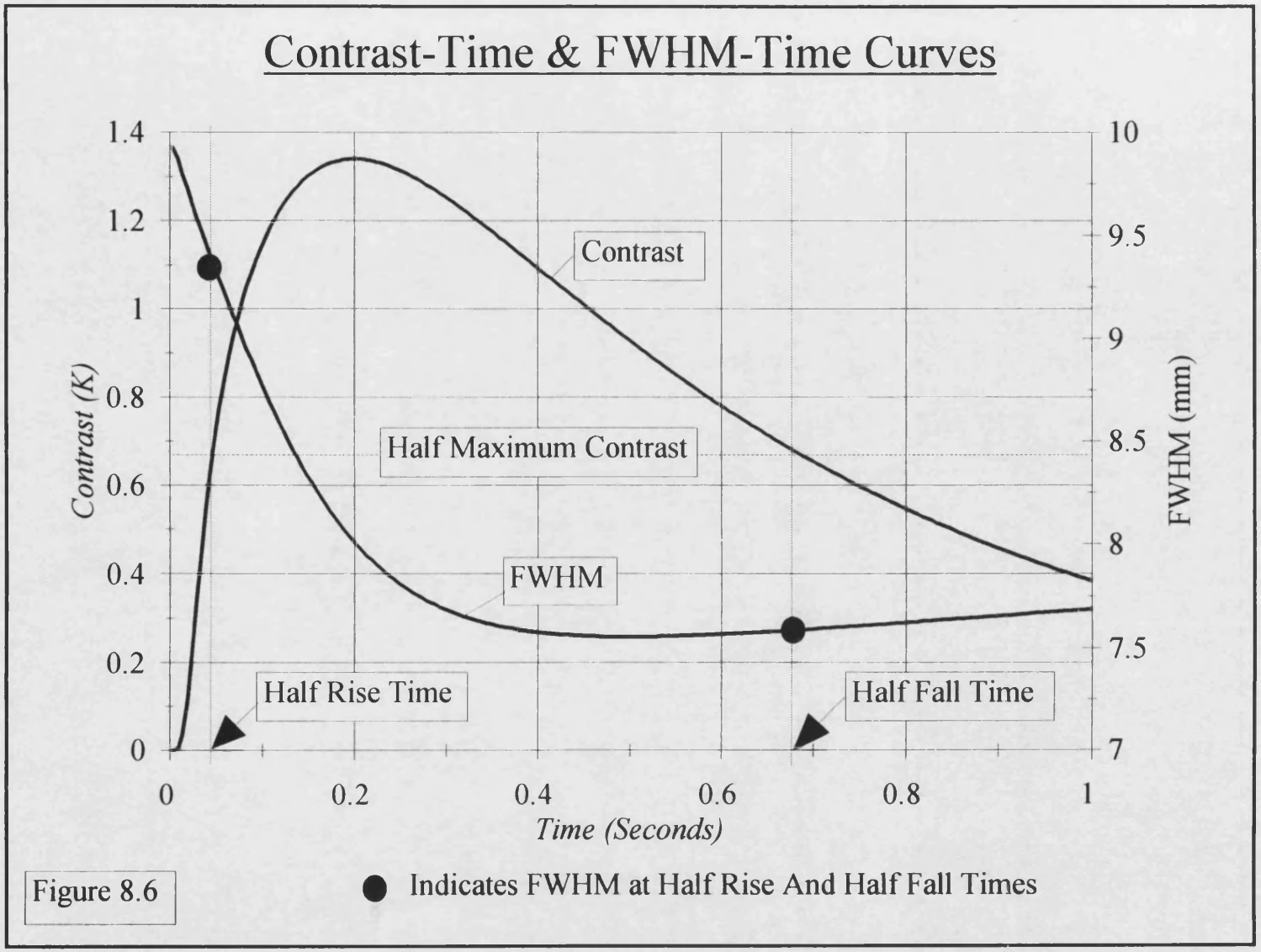
Contrast-Time & FWHM-Time Curves
1.4
1.2
1
0.8
0.6
0.4
0.2
0
Contrast (K)
10
9.5
9
8.5
8
7.5
7
FWHM (mm)
Contrast
Half Maximum Contrast
FWHM
Half Rise Time
Half Fall Time
0
0.2
0.4
0.6
0.8
1
Time (Seconds)
Indicates FWHM at Half Rise And Half Fall Times

Figure 8.6

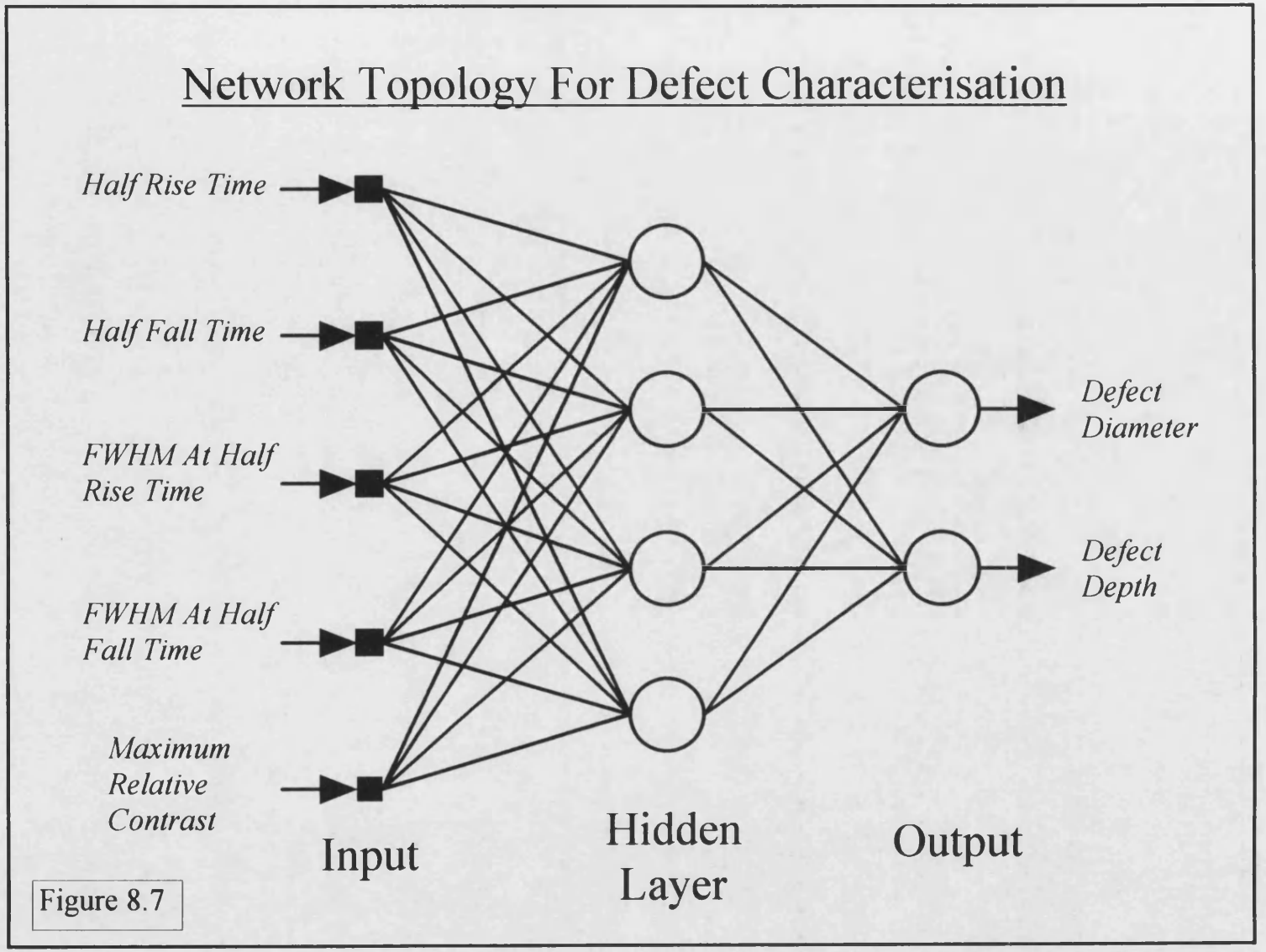
Network Topology For Defect Characterisation
Half Rise Time
Half Fall Time
FWHM At Half Rise Time
FWHM At Half Fall Time
Maximum Relative Contrast
Defect Diameter
Defect Depth
Input
Hidden Layer
Output

Figure 8.7

Chapter 9

Discussion And Conclusions

9.1 Sample Microscopy

Step coated samples 1, 2, 3, 4 and 6 were polished and micrographed as part of the experimental investigation into the thickness and structure of the coatings. It was found that in all cases, the actual coating thickness rarely approached the intended thickness. The structure of the coatings was found to be dependent not only on the technique used to spray them, but also on the coating material. The HVOF sprayed coatings of tungsten carbide of samples 1 and 2 were relatively homogeneous in nature, showing moderate levels of porosity. The HVOF coating of aluminium/silicon alloy of sample 3 on the other hand, showed considerably more inhomogeneity, with high porosity and large blow holes present. The blow holes are thought to be due to the remelting of the aluminium when another pass is made over a previously sprayed part of the coating. This is due to the low melting point of the aluminium. The arc sprayed aluminium/silicon alloy coating of sample 4 was even less homogeneous than the coating of sample 3. Microscopy of sample 6 again revealed the inhomogeneous nature of arc sprayed coatings, this time for a zinc coating. However, the nature of the inhomogeneity of this coating was rather different than that seen for sample 4, no large blow holes are seen in the zinc coating. The thermal spraying of aluminium with either the HVOF or arc spraying techniques seems to present specific difficulties. It would be expected that similar difficulties would be encountered if any other thermal spraying technique was used.

9.2 The Application Of CW-PTR To Sprayed Coatings

9.2.1 HVOF Sprayed Coatings

The application of CW-PTR to the HVOF sprayed tungsten carbide step coatings of samples 1 and 2, showed this technique to be useful for coating thermal property determination, and coating thickness evaluation. The calculated thermal properties of the coatings of the two samples agreed to well within the experimental error of the procedure, however there were large ± errors in the diffusivity determinations. Comparison of coating thicknesses calculated from the inversion of the phase scan data

from CW-PTR scans along the length of the samples, with thickness measurements made with a dial gauge, showed good general agreement. The major feature of a distinct thinning of the coating in the third coating thickness step of each sample was clearly found in both the inverted phase scan and dial gauge data sets.

The technique was found to be unsuitable for use with the HVOF sprayed Aluminium/Silicon alloy coating. It was not possible to determine the thermal properties of this coating, and therefore impossible to invert the phase scan data. This can be attributed to the inhomogeneous nature of this coating, as compared to the coatings of samples 1 and 2. Coating homogeneity appears to be a crucial factor in determining the suitability of the CW-PTR technique for use with a specific coating.

The CW-PTR investigation of the aluminium sprayed sample containing the copper inserts (sample 7), showed the ability of the technique to detect sub-surface features at the depth of the coating/substrate interface (approximately 250μm). Inserts as small as 1mm in diameter were detected. This result was rather unexpected as the technique was found unsuitable for the thermal property determination of the HVOF sprayed aluminium/silicon alloy coating. Similar analysis of the adhesion defect sample (sample 8) failed to reveal the presence of any defects. However, it could be that the method used to create the defects did not work, and that no defects were in fact present.

9.2.2 Arc Sprayed Coatings

It was previously noted that the successful application of the CW-PTR technique is reliant upon the coating structure being relatively homogeneous. The microstructures of the arc sprayed coating (samples 4) were clearly far from this. No success was achieved in determining the coating thermal properties, and so inverting the phase scan data was impossible.

Arc sprayed coatings are often applied to large structures such as bridges and oil rig platforms. The use of this technique for the NDE of such structures would clearly be impractical from the point of view of the time required for inspection. A faster and cheaper method of NDE is required for this type of low quality spray coating.

9.2.3 Plasma Sprayed Coatings

Only one plasma sprayed sample was available, that of an LC1B (nickel chrome carbide) step coating (sample 9). The coating thickness steps of this sample were far thicker than for any of the other samples, and from the CW-PTR phase scans taken along the length of the sample, the steps were far more consistent. The thermal property determination of this coating was much more accurate in terms of the ± error associated with the coating diffusivity than that of either sample 1 or 2 (± 10% for this coating, as compared to ± 44% for the HVOF sprayed coatings). It is difficult to make a direct comparison of these results though, as the coating materials are different. As noted previously, the coating material has a dramatic effect on the homogeneity of the coating structure obtained from a given spraying technique, and hence on the applicability of the CW-PTR technique. However, previous work in the application of CW-PTR to plasma sprayed coatings has indicated that the coatings are generally of a high enough quality for CW-PTR to be viable.

The accurate fitting of the experimental data from both the two HVOF sprayed tungsten carbide coatings and the plasma sprayed LC1B coating, to the simple 1-D thermal wave model, has shown this simple model to be adequate for use for thermal property determination and coating thickness inversion. The inversion procedure is complicated by the fact that the inverting function is not single valued. Complete automation of the inversion procedure is therefore quite difficult.

The CW-PTR technique is very slow to apply to large areas, making it suitable only for use on extremely high quality components, where the cost and time of using the technique can be justified. Safety critical components such as aircraft turbine blades are well suited to this technique.

9.3 Transient Thermography Of Sprayed Coatings

Attempts were made to detect the presence of the copper inserts of sample 7, and the adhesion defects of sample 8, using the single sided transient thermography technique. No defects were detected in either case. There are several important limitations to the use of the transient thermography technique that must be considered. Firstly, the amount of heat supplied must be capable of raising the temperature of the material above a defect to a temperature high enough for the IR camera to detect contrast (a temperature difference greater than 0.2K is required). Secondly, the camera must be

able to grab images before this contrast has disappeared. The camera and heating systems used to test these samples were slow. Not enough heat could be injected into the sample rapidly enough to raise the temperature above the defects high enough, or long enough, for the camera to be able to detect them. This was not helped by the fact that the coatings of samples 7 and 8 were of aluminium, a high thermal diffusivity coating, and hence very fast at equalising temperature variations. The use of a high energy flash heating system, coupled with a high speed thermal camera, may have been able to detect the features (with the caveat that the adhesion defects may not have been present).

The application of the transient thermography technique to the LC1B sample with the back drilled holes (sample 10) was successful. The diffusivity of this coating was much lower than that of the aluminium coatings, meaning the coating responded thermally much slower. The coating was also much thicker, causing the heat to take longer to seep into the substrate. The back drilled holes were easily detected. These results show that it is not always necessary to use extremely expensive high energy flash systems and high speed thermal cameras for the testing of spray coated components.

The application of the transient thermography technique, as with the CW-PTR technique, is limited to materials which have a relatively homogeneous internal structure. A known anisotropy in thermal properties can be catered for, such as the anisotropic thermal conductivity of carbon fibre composites, but random inhomogeneity such as that found in low quality sprayed coatings render the technique unusable.

9.4 Finite Difference Modelling

The numerical finite difference model developed to simulate transient thermography was shown to be capable of accurately modelling experiment. The comparison of modelling results with data from the transient experiments on the LC1B sample with the back drilled holes showed excellent agreement. The model was used to investigate the effect of defect characteristics such as diameter, depth and severity on the transient response following Dirac pulse heating. It was found that for large defects, the FWHM decreased almost linearly with time, in agreement with the results of the analytical Wiener-Hopf solution. Marked deviations from this behaviour were found for smaller defects, something that could not be predicted using the analytical approach, as this lies outside of the range of application of the analytical model. It was found that shallow defects in particular were difficult to size accurately, as their FWHM decreased more rapidly, and by a larger amount, than for the deeper defects.

9.5 Defect Characterisation From Transient Thermography Data

The finite difference simulations of crack and back drilled hole defects in mild steel showed the difficulty of accurately determining the defect characteristics (depth, diameter and severity) from the thermal transient. Due to this difficulty, several groups have started to evaluate the use of neural network processing for the characterisation of defects. A simple multilayer perceptron network was developed that took five inputs of easily measured defect parameters, and interpreted these to give the defect depth and diameter. The network was trained using simulated data, and tested to check the interpolating ability, and input error sensitivity. The results were very promising, with the network interpolating very well between elements of the training set, and showing reasonable insensitivity to simulated experimental errors of the input data. The results were even more encouraging when it is borne in mind the very limited size of the training set (only 50 examples).

For automatic defect detection and characterisation using transient thermography data, neural network processing looks very promising. Two limitations to its application are the need to develop a new network for each type of sample inspected, and the training time (which can be considerable). Both of these problems are not likely to limit interest in this field however, since in an industrial setting, an automated inspection system would be testing a single type of component, and hence once the system was set up, no retraining would be needed. The introduction of this type of processing has brought the day much closer when a fully automated transient thermography testing system will be available.

9.6 Further Work

One area of work that has been neglected in this project is the accurate modelling of the CW-PTR experiment. It has been shown that the simple 1D theory gives a good fit to the experimental data, but the small beam diameter must effect the detected signal. The modelling of the CW-PTR experiment will be far more complex than that of the axi-symmetric transient case discussed in this thesis. It will require a full 3D model to be developed, requiring far more computational power for solution.

Another area of interest for the future must be in the further development of the application of neural network processing to the interpretation of thermographic data. A very simple approach was taken here, which could easily be expanded upon. Further experimentation on the inputs to the network, and network topology, would almost

certainly lead to a network capable to outputting all three defect characteristics (defect depth, diameter and severity). It might however be more profitable to concentrate on the use of the neural network approach for fully automated defect detection and characterisation. At present, the limitations of this approach are the processing time required to train the network, and to extract and process the data from an experiment. With time, this will not be such a problem, as computer processing speeds increase dramatically every few years.

At the present time, with the exception of the aerospace industry, there has been very limited industrial use of thermal NDT. Before companies will be willing to invest in thermal testing, considerable experimental investigation into the use of the techniques for specific tasks must be undertaken. Only when the techniques have been proved capable of solving the specific NDT problems faced by industry will the funding be made available for the development of test apparatus and procedures. It is to be hoped that, as a result of work such as this thesis, thermal NDT will be as commonplace in the future as ultrasonic testing is today.

Appendix A

Code Listing For The Numerical Finite Difference Model

Two distinct versions of the code were developed, the first to simulate finite duration heating pulses (including step-on heating), the second to simulate Dirac delta heating pulses. The main difference between the code of the two versions is the extra code in the Dirac heating model required to calculate the time derivative of the step-on heating response. For this reason only the Dirac heating model code is included, as it can be considered a super-set of the code for the other model. During the lifetime of the development of the code, several iterations (versions) were written. The code presented here represents the final version, and was used to generate all the Dirac pulse heating numerical data presented in this thesis.

The code was written and compiled using the integrated development environment of the PC based Microsoft FORTRAN Powerstation compiler (version 1.0). This is a 32-bit compiler, fully complying to the FORTRAN 77 standard, containing many of the additions to the standard that have now been incorporated into FORTRAN 90. Due to the length of the code, and to aid modularity of design, the code was split into 8 separate source files. In addition to the source files, 2 include files were also used (the incorporation of include files is one of the extensions to the FORTRAN 77 standard).

The source files (with a brief description of their content) were :

CONRESDD.FOR	- Main routine.
IMPRCR.FOR	- Implicit radial (r) direction code.
IMPZCR.FOR	- Implicit depth (z) direction code.
TDMA.FOR	- Tri-diagonal matrix algorithm.
DELTA.FOR	- Calculates pulse response from step-on response.
UPDATE.FOR	- Keeps track of step on temperatures for DELTA.FOR.
OUTPNT.FOR	- Routine to output point data to a file.
OUTROW.FOR	- Routine to output row data to a file.

The include files were :

PARAMS.FI	- Sets maximum array sizes.
GLOB.FI	- Defines all the global variables used in the model.

The contents of the files are now listed in the order in which they appear in the above lists, starting with CONRESDD.FOR. A reduced font size with single line spacing has been used for the code listings to reduce the number of pages required. The code listings were imported directly from the compiler, unfortunately the alignment of the columns of the code has not been accurately maintained.

Code Listing For CONRESDD.FOR

```
C     CONTACT RESISTANCE DELTA PULSE MODEL


C     AUTHOR : M.B. SAINTEY
C     DATE : 14/04/94
C     VERSION : 2.0
C     CODE FOR THE POWERSTATION COMPILER

C     ************************************************************************
C     THIS NEW VERSION HAS TO CHANGED TO INCLUDE A DIFFERENT NODAL SPACING
C     FOR THE REGION WITHIN THE COATING TO ALLOW FOR THIN COATINGS
C     ************************************************************************

C     DEPARTMENT OF MATERIALS SCIENCE
C     UNIVERSITY OF BATH
C     CLAVERTON DOWN
C     BATH
C     AVON
C     ENGLAND

          PROGRAM CONRESDD

C     INCLUDE FILES

      INCLUDE 'PARAMS.FI'
      INCLUDE 'GLOB.FI'

C     ******* DEFINE ALL VARIABLES *******

C     LOCAL VARIABLES

          CHARACTER*12   INPUT, PNTFIL, ROWFIL
          INTEGER    I, J, NI, NUMON
          INTEGER    OPR, COUNTER, PERC
          INTEGER    PNTINT, PNTCNT, ROWINT, ROWCNT
          REAL*8     Q, HF, HB, DT, DT1, KC, KO, KS, PC, PO, PS
          REAL*8     CC, CO, CS, RC, DS
          REAL*8     TIME, DDTIME

 1    FORMAT(1X,'DATA GENERATED USING CONRESDD.EXE - VERSION 2.0')

C     ******* INITIALISE THE T AND TP ARRAYS TO 0 *******

          DO 5 I=1,RSIZE,1
            DO 6 J=1,ZSIZE,1
```

```
                T(I,J) = 0.0
                TP(I,J) = 0.0
 6      CONTINUE
 5    CONTINUE

C     ******* GET NAME OF CONTROL FILE *******

      PRINT*
      PRINT*, 'CONTACT RESISTANCE ADI FDE CALCULATION - DIRAC PULSE'
      PRINT*, '*************************************************'
      PRINT*
      PRINT*, 'VERSION 2.0'
      PRINT*
      PRINT*, 'ENTER NAME OF CONROL FILE  : '
      READ*, INPUT

      OPEN(UNIT=60,FILE=INPUT,STATUS='OLD')

C     ******* READ IN THE CONTROL VARIABLES *******

      READ(60,*) N, M, P, G
      READ(60,*) KC, PC, CC
      READ(60,*) KS, PS, CS
      READ(60,*) KO, PO, CO
      READ(60,*) Q, HF, HB
      READ(60,*) RC
      READ(60,*) DX, DS, DT1
      READ(60,*) NUMON
      READ(60,*) PNTFIL, PNTINT
      READ(60,*) LPR1, LPZ1
      READ(60,*) LPR2, LPZ2
      READ(60,*) LPR3, LPZ3
      READ(60,*) LPR4, LPZ4
      READ(60,*) OPR, ROWFIL, ROWINT
      READ(60,*) ROW1, ROW2

      CLOSE(60)

C     ******* WRITE DATA READ IN TO SCREEN BEFORE COMMENCING *******


      PRINT*
      PRINT*, 'TOT RADIAL PTS = ',N,'  TOT DEPTH PTS = ',M
      PRINT*, 'CR RADIAL PTS = ',P,' PTS ABOVE CR = ',G
      PRINT*, 'THERMAL CONDUCTIVITY (COATING) = ',KC
      PRINT*, 'DENSITY (COATING) = ',PC
      PRINT*, 'SPECIFIC HEAT CAPACITY (COATING)= ',CC
      PRINT*, 'THERMAL CONDUCTIVITY (SUBSTRATE) = ',KS
      PRINT*, 'DENSITY (SUBSTRATE) = ',PS
      PRINT*, 'SPECIFIC HEAT CAPACITY (SUBSTRATE)= ',CS
      PRINT*, 'THERMAL CONDUCTIVITY (OTHER) = ',KO
      PRINT*, 'DENSITY (OTHER) = ',PO
      PRINT*, 'SPECIFIC HEAT CAPACITY (OTHER)= ',CO
      PRINT*, 'PLANE HEAT FLUX = ',Q
      PRINT*, 'FRONT SURFACE HEAT TRANSFER CFT = ',HF
      PRINT*, 'BACK SURFACE HEAT TRANSFER CFT = ',HB
      PRINT*, 'CONTACT RESISTANCE = ',RC
      PRINT*, 'NODAL SPACINGS = ',DX, DS
      PRINT*, 'TIME INCREMENT = ',DT1
```

```
      PRINT*, 'NUMBER OF ITERATIONS WITH HEAT ON = ',NUMON
      PRINT*, 'HEATING TIME = ',(DBLE(NUMON)*DT1)
      PRINT*, 'POINT OUTPUT FILENAME = ',PNTFIL
      PRINT*, 'OUTPUT DATA EVERY ',PNTINT,' ITERATIONS'
      PRINT*, 'POINT 1', LPR1, LPZ1
      PRINT*, 'POINT 2', LPR2, LPZ2
      PRINT*, 'POINT 3', LPR3, LPZ3
      PRINT*, 'POINT 4', LPR4, LPZ4
      IF(OPR.EQ.1) THEN
        PRINT*, 'OUTPUT RADIAL TEMP PROFILE FILENAME = ',ROWFIL
        PRINT*, 'OUTPUT ROW EVERY ',ROWINT,' ITERATIONS'
      ENDIF

C     ******* OPEN THE FILES FOR OUTPUT BEFORE CALCULATION COMMENCES *******

      OPEN(UNIT=61,FILE=PNTFIL,STATUS='NEW')
      WRITE(61,1)
      IF(OPR.EQ.1) THEN
        OPEN(UNIT=62,FILE=ROWFIL,STATUS='NEW')
        WRITE(62,1)
      ENDIF

C     ******* CALCULATE SOME USEFUL PARAMETERS *******

      HD = DX/2.0
      KCOP = ((DX+DS)*KC*KO)/((DS*KO)+(2.0*RC*KC*KO)+(DX*KC))
      KCSP = ((DX+DS)*KC*KS)/((DX*KC)+(DS*KS))
      PCAV = ((PO*CO)+(PS*CS))/2.0
      BIF = (HF*DX)/KC
      BIBO = (HB*DX)/KO
      BIBS = (HB*DX)/KS
      RN = (DBLE(N)-1.0)*DX
      RP = (DBLE(P)-1.0)*DX
      TA = 0.0
      TIME = 0.0


C     ******* HEAT THE SPECIMIN *******

C     SETTLE WITH 20 PASSES WITH TIME STEP DT1/20

      DT = DT1/20.0
      FC = (KC*DT)/(PC*CC*DX*DX)
      FCZ = (KC*DT)/(PC*CC*DS*DS)
      FO = (KO*DT)/(PO*CO*DX*DX)
      FS = (KS*DT)/(PS*CS*DX*DX)
      FCOZ = (2.0*KCOP*DT)/(PC*CC*(DX+DS)*DS)
      FOCZ = (2.0*KCOP*DT)/(PO*CO*(DX+DS)*DX)
      FCSZ = (2.0*KCSP*DT)/(PC*CC*(DX+DS)*DS)
      FSCZ = (2.0*KCSP*DT)/(PS*CS*(DX+DS)*DX)
      F5 = ((KCOP+KCSP)*DT)/(DX*(DX+DS)*PCAV)
      F2 = ((KO+KS)/2.0)*(DT/(DX*DX*PCAV))
      F3 = (KO*DT*(RP-HD))/(RP*DX*DX*PCAV)
      F4 = (KS*DT*(RP+HD))/(RP*DX*DX*PCAV)
      BTAV = (HB*DT)/(DX*PCAV)
      A1 = (Q*DS*FCZ)/KC
      DO 50 NI=1,20,1
        CALL IMPRCR()
        CALL IMPZCR()
```

```
          IF(NI.EQ.1) THEN
            PNT1(0) = T(LPR1,LPZ1)
            PNT2(0) = T(LPR2,LPZ2)
            PNT3(0) = T(LPR3,LPZ3)
            PNT4(0) = T(LPR4,LPZ4)
            DO 60 I=1,N,1
              RW1(I,0) = T(I,ROW1)
              RW2(I,0) = T(I,ROW2)
60        CONTINUE
          TSTP(0) = DT
        ELSE IF(NI.EQ.2) THEN
          PNT1(1) = PNT1(0)
          PNT1(0) = T(LPR1,LPZ1)
          PNT2(1) = PNT2(0)
          PNT2(0) = T(LPR2,LPZ2)
          PNT3(1) = PNT3(0)
          PNT3(0) = T(LPR3,LPZ3)
          PNT4(1) = PNT4(0)
          PNT4(0) = T(LPR4,LPZ4)
          DO 70 I=1,N,1
            RW1(1,I) = RW1(0,I)
                RW1(0,I) = T(I,ROW1)
            RW2(1,I) = RW2(0,I)
                RW2(0,I) = T(I,ROW2)
70        CONTINUE
          TSTP(1) = TSTP(0)
          TSTP(0) = DT
          TSTP(2) = TSTP(0) + TSTP(1)
        ELSE
          TSTP(1) = TSTP(0)
          TSTP(0) = DT
          TSTP(2) = TSTP(0) + TSTP(1)
          CALL UPDATE()
        ENDIF
50    CONTINUE

C     CHANGE TIME STEP TO DT1

          DT = DT1
          FC = (KC*DT)/(PC*CC*DX*DX)
          FCZ = (KC*DT)/(PC*CC*DS*DS)
          FO = (KO*DT)/(PO*CO*DX*DX)
          FS = (KS*DT)/(PS*CS*DX*DX)
          FCOZ = (2.0*KCOP*DT)/(PC*CC*(DX+DS)*DS)
          FOCZ = (2.0*KCOP*DT)/(PO*CO*(DX+DS)*DX)
          FCSZ = (2.0*KCSP*DT)/(PC*CC*(DX+DS)*DS)
          FSCZ = (2.0*KCSP*DT)/(PS*CS*(DX+DS)*DX)
          F5 = ((KCOP+KCSP)*DT)/(DX*(DX+DS)*PCAV)
          F2 = ((KO+KS)/2.0)*(DT/(DX*DX*PCAV))
          F3 = (KO*DT*(RP-HD))/(RP*DX*DX*PCAV)
          F4 = (KS*DT*(RP+HD))/(RP*DX*DX*PCAV)
          BTAV = (HB*DT)/(DX*PCAV)
          A1 = (Q*DS*FCZ)/KC
          PNTCNT = 1
          ROWCNT = 1
          TIME = DT1
          COUNTER = 1
          PERC = 0
```

```
C   HEATING LOOP WITH TIME STEP DT1
C   START AT NI=2 SINCE 20 PASSES AT DT1/20 = 1 PASS AT DT1

      DO 100 NI=2,NUMON,1

        CALL IMPRCR()
        CALL IMPZCR()
      TSTP(1) = TSTP(0)
      TSTP(0) = DT
      TSTP(2) = TSTP(0) + TSTP(1)
      CALL UPDATE()
          PNTCNT = PNTCNT + 1
          ROWCNT = ROWCNT + 1
          TIME = TIME + DT
          DDTIME = TIME - DT
          IF(PNTCNT.GE.PNTINT) THEN
                    CALL OUTPNT(DDTIME)
                    PNTCNT = 0
          ENDIF
          IF((OPR.EQ.1).AND.(ROWCNT.GE.ROWINT)) THEN
                    CALL OUTROW(DDTIME)
            ROWCNT = 0
          ENDIF
          COUNTER = COUNTER + 1
          IF(COUNTER.EQ.((NUMON)/10)) THEN
            COUNTER = 0
            PERC = PERC + 10
            PRINT*, 'COMPLETED ',PERC,' %'
          ENDIF

100  CONTINUE


      CLOSE(61)
      IF(OPR.EQ.1) THEN
        CLOSE(62)
      ENDIF

      END
```

Code Listing For IMPRCR.FOR

```
C   IMPLICIT R DIRECTION FOR ADI MODEL OF THE CONTACT RESISTANCE
C   MODEL

C   LAST EDITED : 14/04/94
C   VERSION 2.0

C   ***************************************************************
C   HAS THE ADDITION OF A DIFFERENT GRID SPACING WITHIN THE COATING
C   ***************************************************************

C   ***************************************************************
C   ********************** R IMPLICIT *****************************
C   ***************************************************************
```

```
      SUBROUTINE    IMPRCR()

C   INCLUDE FILES

    INCLUDE 'PARAMS.FI'
    INCLUDE 'GLOB.FI'

C   LOCAL VARIABLES
      INTEGER   I, J
      REAL*8    A(MAXSIZE), B(MAXSIZE), C(MAXSIZE), D(MAXSIZE)
      REAL*8    R, FCM, FCP, FOM, FOP, FSM, FSP

C   ******* TOP HEATED ROW *******

      B(1) = 0.0
      D(1) = 2.0*FC + 1.0
      A(1) = -2.0*FC
      C(1) = A1 + FCZ*T(1,2) + (1.0-BIF*FCZ-FCZ)*T(1,1) + BIF*FCZ*TA
      DO 20 I=2,N-1,1
        R = (DBLE(I)-1.0)*DX
            FCM = FC*(R-HD)/R
            FCP = FC*(R+HD)/R
            B(I) = -1.0*FCM
            D(I) = 2.0*(1.0+FC)
            A(I) = -1.0*FCP
            C(I) = 2.0*A1 + 2.0*FCZ*T(I,2) +
     /      2.0*(1.0-BIF*FCZ-FCZ)*T(I,1) + 2.0*BIF*FCZ*TA
20    CONTINUE
      FCM = FC*(RN-HD)/RN
      B(N) = -1.0*FCM
      D(N) = 1.0 + FCM
      A(N) = 0.0
      C(N) = A1 + FCZ*T(N,2) + (1.0-BIF*FCZ-FCZ)*T(N,1) + BIF*FCZ*TA
      CALL TDMA(N,A,B,C,D)
      DO 30 I=1,N,1
            TP(I,1) = C(I)
30    CONTINUE

C   ******* WITHIN THE COATING LAYER *******

      DO 40 J=2,G-1,1
            B(1) = 0.0
            D(1) = 2.0*(1.0+(2.0*FC))
            A(1) = -4.0*FC
            C(1) = FCZ*T(1,J-1) + FCZ*T(1,J+1) + 2.0*(1.0-FCZ)*T(1,J)
            DO 50 I=2,N-1,1
              R = (DBLE(I)-1.0)*DX
              FCM = FC*(R-HD)/R
              FCP = FC*(R+HD)/R
              B(I) = -1.0*FCM
              D(I) = 2.0*(1.0+FC)
              A(I) = -1.0*FCP
              C(I) = FCZ*T(I,J-1) + FCZ*T(I,J+1) + 2.0*(1.0-FCZ)*T(I,J)
50      CONTINUE
            FCM = FC*(RN-HD)/RN
            B(N) = -2.0*FCM
            D(N) = 2.0*(1.0+FCM)
```

```
                A(N) = 0.0
                C(N) = FCZ*T(N,J-1) + FCZ*T(N,J+1) + 2.0*(1.0-FCZ)*T(N,J)
                CALL TDMA(N,A,B,C,D)
                DO 60 I=1,N,1
                  TP(I,J) = C(I)
60    CONTINUE
40  CONTINUE

C     ******* ROW IMEDIATELY ABOVE THE CONTACT RESISTANCE AND SUBSTRATE
*******

        B(1) = 0.0
        D(1) = 2.0*(1.0 + 2.0*FC)
        A(1) = -4.0*FC
        C(1) = FCZ*T(1,G-1) + FCOZ*T(1,G+1) + (2.0-FCZ-FCOZ)*T(1,G)
        DO 70 I=2,P-1,1
                R = (DBLE(I)-1.0)*DX
                FCM = FC*(R-HD)/R
                FCP = FC*(R+HD)/R
                B(I) = -1.0*FCM
                D(I) = 2.0*(1.0+FC)
                A(I) = -1.0*FCP
                C(I) = FCZ*T(I,G-1) + FCOZ*T(I,G+1) + (2.0-FCZ-FCOZ)*T(I,G)
70  CONTINUE
        FCM = FC*(RP-HD)/RP
        FCP = FC*(RP+HD)/RP
        B(P) = -1.0*FCM
        D(P) = 2.0*(1.0+FC)
        A(P) = -1.0*FCP
        C(P) = FCZ*T(P,G-1) + ((FCOZ+FCSZ)/2.0)*T(P,G+1) +
     /          (2.0-FCZ-((FCOZ+FCSZ)/2.0))*T(P,G)
        DO 80 I=P+1,N-1,1
                R = (DBLE(I)-1.0)*DX
                FCM = FC*(R-HD)/R
                FCP = FC*(R+HD)/R
                B(I) = -1.0*FCM
                D(I) = 2.0*(1.0+FC)
                A(I) = -1.0*FCP
                C(I) = FCZ*T(I,G-1) + FCSZ*T(I,G+1) + (2.0-FCZ-FCSZ)*T(I,G)
80  CONTINUE
        FCM = FC*(RN-HD)/RN
        B(N) = -2.0*FCM
        D(N) = 2.0*(1.0+FCM)
        A(N) = 0.0
        C(N) = FCZ*T(N,G-1) + FCSZ*T(N,G+1) + (2.0-FCZ-FCSZ)*T(N,G)
        CALL TDMA(N,A,B,C,D)
        DO 90 I=1,N,1
                TP(I,G) = C(I)
90  CONTINUE


C     ******* ROW IMEDIATELY BELOW THE CONTACT RESISTANCE *******

        B(1) = 0.0
        D(1) = 2.0*(1.0 + 2.0*FO)
        A(1) = -4.0*FO
        C(1) = FOCZ*T(1,G) + FO*T(1,G+2) + (2.0-FOCZ-FO)*T(1,G+1)
        DO 100 I=2,P-1,1
                R = (DBLE(I)-1.0)*DX
```

```
                FOM = FO*(R-HD)/R
                FOP = FO*(R+HD)/R
                B(I) = -1.0*FOM
                D(I) = 2.0*(1.0+FO)
                A(I) = -1.0*FOP
                C(I) = FOCZ*T(I,G) + FO*T(I,G+2) + (2.0-FOCZ-FO)*T(I,G+1)
100 CONTINUE
        B(P) = -1.0*F3
        D(P) = 2.0+F3+F4
        A(P) = -1.0*F4
        C(P) = F2*T(P,G+2) + F5*T(P,G) + (2.0-F5-F2)*T(P,G+1)
        DO 110 I=P+1,N-1,1
                R = (DBLE(I)-1.0)*DX
                FSM = FS*(R-HD)/R
                FSP = FS*(R+HD)/R
                B(I) = -1.0*FSM
                D(I) = 2.0*(1.0+FS)
                A(I) = -1.0*FSP
                C(I) = FSCZ*T(I,G) + FS*T(I,G+2) + (2.0-FSCZ-FS)*T(I,G+1)
110 CONTINUE
        FSM = FS*(RN-HD)/RN
        B(N) = -2.0*FSM
        D(N) = 2.0*(1.0+FSM)
        A(N) = 0.0
        C(N) = FSCZ*T(N,G) + FS*T(N,G+2) + (2.0-FSCZ-FS)*T(N,G+1)
        CALL TDMA(N,A,B,C,D)
        DO 120 I=1,N,1
                TP(I,G+1) = C(I)
120 CONTINUE


C    ******* ROWS BELOW THE CONTACT RESISTANCE *******

        DO 130 J=G+2,M-1,1
                B(1) = 0.0
                D(1) = 2.0*(1.0+(2.0*FO))
                A(1) = -4.0*FO
                C(1) = FO*T(1,J-1) + FO*T(1,J+1) + 2.0*(1.0-FO)*T(1,J)
                DO 140 I=2,P-1,1
                  R = (DBLE(I)-1.0)*DX
                  FOM = FO*(R-HD)/R
                  FOP = FO*(R+HD)/R
                  B(I) = -1.0*FOM
                  D(I) = 2.0*(1.0+FO)
                  A(I) = -1.0*FOP
                  C(I) = FO*T(I,J-1) + FO*T(I,J+1) + 2.0*(1.0-FO)*T(I,J)
140     CONTINUE
                B(P) = -1.0*F3
                D(P) = 2.0+F3+F4
                A(P) = -1.0*F4
                C(P) = F2*T(P,J-1) + F2*T(P,J+1) + 2.0*(1.0-F2)*T(P,J)
                DO 150 I=P+1,N-1,1
                  R = (DBLE(I)-1.0)*DX
            FSM = FS*(R-HD)/R
                  FSP = FS*(R+HD)/R
                  B(I) = -1.0*FSM
                  D(I) = 2.0*(1.0+FS)
                  A(I) = -1.0*FSP
                  C(I) = FS*T(I,J-1) + FS*T(I,J+1) + 2.0*(1.0-FS)*T(I,J)
```

```
150    CONTINUE
       FSM = FS*(RN-HD)/RN
       B(N) = -2.0*FSM
       D(N) = 2.0*(1.0+FSM)
       A(N) = 0.0
       C(N) = FS*T(N,J-1) + FS*T(N,J+1) + 2.0*(1.0-FS)*T(N,J)
                    CALL TDMA(N,A,B,C,D)
                    DO 160 I=1,N,1
                       TP(I,J) = C(I)
160    CONTINUE
130 CONTINUE


C    ******* BOTTOM ROW *******

         B(1) = 0.0
         D(1) = 1.0 + 2.0*FO
         A(1) = -2.0*FO
         C(1) = BIBO*FO*TA + FO*T(1,M-1) + (1.0-FO-(BIBO*FO))*T(1,M)
         DO 170 I=2,P-1,1
                    R = (DBLE(I)-1.0)*DX
                    FOM = FO*(R-HD)/R
                    FOP = FO*(R+HD)/R
                    B(I) = -1.0*FOM
                    D(I) = 2.0*(1.0+FO)
                    A(I) = -1.0*FOP
                    C(I) = 2.0*FO*T(I,M-1) + 2.0*BIBO*FO*TA
  /                  + 2.0*(1.0-FO-(BIBO*FO))*T(I,M)
170 CONTINUE
         B(P) = -1.0*F3
         D(P) = 2.0+F3+F4
         A(P) = -1.0*F4
         C(P) = 2.0*F2*T(P,M-1) + 2.0*BTAV*TA + 2.0*(1.0-F2-BTAV)*T(P,M)
         DO 180 I=P+1,N-1,1
                    R = (DBLE(I)-1.0)*DX
                    FSM = FS*(R-HD)/R
                    FSP = FS*(R+HD)/R
                    B(I) = -1.0*FSM
                    D(I) = 2.0*(1.0+FS)
                    A(I) = -1.0*FSP
                    C(I) = 2.0*FS*T(I,M-1) + 2.0*BIBS*FS*TA
  /                  + 2.0*(1.0-FS-(BIBS*FS))*T(I,M)
180 CONTINUE
         FSM = FS*(RN-HD)/RN
         B(N) = -1.0*FSM
         D(N) = 1.0 + FSM
         A(N) = 0.0
         C(N) = FS*T(N,M-1) + BIBS*FS*TA + (1.0-FS-(BIBS*FS))*T(N,M)
         CALL TDMA(N,A,B,C,D)
         DO 190 I=1,N,1
                    TP(I,M) = C(I)
190 CONTINUE

C    ******* COPY CONTENTS OF TP TO T *******

         DO 200 I=1,N,1
                    DO 210 J=1,M,1
                       T(I,J) = TP(I,J)
210    CONTINUE
```

```
200 CONTINUE

      RETURN


      END
```

Code Listing For IMPZCR.FOR

```
C   IMPLICIT X DIRECTION FOR ADI MODEL OF THE CONTACT RESISTANCE
C   MODEL

C   LAST EDITED : 14/04/94
C   VERSION 2.0

C   ****************************************************************
C   HAS THE ADDITION OF A DIFFERENT GRID SPACING WITHIN THE COATING
C   ****************************************************************


C   ****************************************************************
C   ************************* IMPLICIT Z ************************
C   ****************************************************************

      SUBROUTINE    IMPZCR()


C   INCLUDE FILES

    INCLUDE 'PARAMS.FI'
    INCLUDE 'GLOB.FI'


C   LOCAL VARIABLES
      INTEGER       I, J
      REAL*8    A(MAXSIZE), B(MAXSIZE), C(MAXSIZE), D(MAXSIZE)
      REAL*8    R, FCM, FCP, FOM, FOP, FSM, FSP

C   ******* AXIS *******

      B(1) = 0.0
      D(1) = FCZ + 1.0 + BIF*FCZ
      A(1) = -1.0*FCZ
      C(1) = A1 + 2.0*FC*T(2,1) + (1.0-(2.0*FC))*T(1,1) + BIF*FCZ*TA
      DO 10 J=2,G-1,1
            B(J) = -1.0*FCZ
            D(J) = 2.0*(1.0+FCZ)
            A(J) = -1.0*FCZ
            C(J) = 4.0*FC*T(2,J) + 2.0*(1.0-(2.0*FC))*T(1,J)
10  CONTINUE
      B(G) = -1.0*FCZ
      D(G) = 2.0 + FCZ + FCOZ
      A(G) = -1.0*FCOZ
      C(G) = 4.0*FC*T(2,G) + 2.0*(1.0-(2.0*FC))*T(1,G)
      B(G+1) = -1.0*FOCZ
```

```
      D(G+1) = 2.0 + FOCZ + FO
      A(G+1) = -1.0*FO
      C(G+1) = 4.0*FO*T(2,G+1) + 2.0*(1.0-(2.0*FO))*T(1,G+1)
      DO 20 J=G+2,M-1,1
            B(J) = -1.0*FO
            D(J) = 2.0*(1.0+FO)
            A(J) = -1.0*FO
        C(J) = 4.0*FO*T(2,J) + 2.0*(1.0-(2.0*FO))*T(1,J)
20  CONTINUE
      B(M) = -1.0*FO
      D(M) = 1.0 + FO + (BIBO*FO)
      A(M) = 0.0
      C(M) = 2.0*FO*T(2,M) + (1.0-(2.0*FO))*T(1,M) + BIBO*FO*TA
      CALL TDMA(M,A,B,C,D)
      DO 30 J=1,M,1
            TP(1,J) = C(J)
30  CONTINUE

C   ******* COLUMNS INCLUDING THE CONTACT RESISTANCE *******

      DO 40 I=2,P-1,1
            R = (DBLE(I)-1.0)*DX
            FCM = FC*(R-HD)/R
            FCP = FC*(R+HD)/R
            FOM = FO*(R-HD)/R
            FOP = FO*(R+HD)/R
            B(1) = 0.0
            D(1) = 2.0*(1.0+FCZ+BIF*FCZ)
            A(1) = -2.0*FCZ
            C(1) = 2.0*A1 + FCM*T(I-1,1) + FCP*T(I+1,1)
     /        + 2.0*(1.0-FC)*T(I,1) + 2.0*BIF*FCZ*TA
            DO 50 J=2,G-1,1
              B(J) = -1.0*FCZ
              D(J) = 2.0*(1.0+FCZ)
              A(J) = -1.0*FCZ
              C(J) = FCM*T(I-1,J) + FCP*T(I+1,J)
     /        + 2.0*(1.0-FC)*T(I,J)
50    CONTINUE
            B(G) = -1.0*FCZ
            D(G) = 2.0 + FCZ + FCOZ
            A(G) = -1.0*FCOZ
            C(G) = FCM*T(I-1,G) + FCP*T(I+1,G) + 2.0*(1.0-FC)*T(I,G)
            B(G+1) = -1.0*FOCZ
            D(G+1) = 2.0 + FOCZ + FO
            A(G+1) = -1.0*FO
            C(G+1) = FOM*T(I-1,G+1) + FOP*T(I+1,G+1) +
     /       2.0*(1.0-FO)*T(I,G+1)
            DO 60 J=G+2,M-1,1
              B(J) = -1.0*FO
              D(J) = 2.0*(1.0+FO)
              A(J) = -1.0*FO
              C(J) = FOM*T(I-1,J) + FOP*T(I+1,J)
     /        + 2.0*(1.0-FO)*T(I,J)
60    CONTINUE
            B(M) = -2.0*FO
            D(M) = 2.0*(1.0 + FO + BIBO*FO)
            A(M) = 0.0
            C(M) = FOM*T(I-1,M) + FOP*T(I+1,M) + 2.0*(1.0-FO)*T(I,M)
     /       + 2.0*BIBO*FO*TA
```

```
                CALL TDMA(M,A,B,C,D)
                DO 70 J=1,M,1
                  TP(I,J) = C(J)
70    CONTINUE
40  CONTINUE

C   ******* COL' CONTAINING THE EDGE OF THE CONTACT RESISTANCE *******

        FCM = FC*(RP-HD)/RP
        FCP = FC*(RP+HD)/RP
        B(1) = 0.0
        D(1) = 2.0*(1.0+FCZ+BIF*FCZ)
        A(1) = -2.0*FCZ
        C(1) = 2.0*A1 + FCM*T(P-1,1) + FCP*T(P+1,1)
     /    + 2.0*(1.0-FC)*T(P,1) + 2.0*BIF*FCZ*TA
        DO 80 J=2,G-1,1
                B(J) = -1.0*FCZ
                D(J) = 2.0*(1.0+FCZ)
                A(J) = -1.0*FCZ
                C(J) = FCM*T(P-1,J) + FCP*T(P+1,J) + 2.0*(1.0-FC)*T(P,J)
80  CONTINUE
        B(G) = -1.0*FCZ
        D(G) = 2.0 + FCZ + ((FCOZ+FCSZ)/2.0)
        A(G) = -1.0*((FCOZ+FCSZ)/2.0)
        C(G) = FCM*T(P-1,G) + FCP*T(P+1,G) + 2.0*(1.0-FC)*T(P,G)
        B(G+1) = -1.0*F5
        D(G+1) = 2.0 + F5 + F2
        A(G+1) = -1.0*F2
        C(G+1) = F3*T(P-1,G+1) + F4*T(P+1,G+1) +
     /          (2.0-F3-F4)*T(P,G+1)
        DO 90 J=G+2,M-1,1
                B(J) = -1.0*F2
                D(J) = 2.0*(1.0+F2)
                A(J) = -1.0*F2
                C(J) = F3*T(P-1,J) + F4*T(P+1,J) + (2.0-F3-F4)*T(P,J)
90  CONTINUE
        B(M) = -2.0*F2
        D(M) = 2.0*(1.0 + F2 + BTAV)
        A(M) = 0.0
        C(M) = F3*T(P-1,M) + F4*T(P+1,M) + (2.0-F3-F4)*T(P,M)
     /          + 2.0*BTAV*TA

        CALL TDMA(M,A,B,C,D)
        DO 100 J=1,M,1
                TP(P,J) = C(J)
100 CONTINUE

C   ******* COL'S OUTSIDE OF THE RADIUS OF THE CONTACT RESISTANCE *******

        DO 110 I=P+1,N-1,1
                R = (DBLE(I)-1.0)*DX
                FCM = FC*(R-HD)/R
                FCP = FC*(R+HD)/R
                FSM = FS*(R-HD)/R
                FSP = FS*(R+HD)/R
                B(1) = 0.0
                D(1) = 2.0*(1.0+FCZ+BIF*FCZ)
                A(1) = -2.0*FCZ
                C(1) = 2.0*A1 + FCM*T(I-1,1) + FCP*T(I+1,1)
```

```
     /          + 2.0*(1.0-FC)*T(I,1) + 2.0*BIF*FCZ*TA
                DO 120 J=2,G-1,1
                  B(J) = -1.0*FCZ
                  D(J) = 2.0*(1.0+FCZ)
                  A(J) = -1.0*FCZ
                  C(J) = FCM*T(I-1,J) + FCP*T(I+1,J)
     /          + 2.0*(1.0-FC)*T(I,J)
  120 CONTINUE
                B(G) = -1.0*FCZ
                D(G) = 2.0 + FCZ + FCSZ
                A(G) = -1.0*FCSZ
                C(G) = FCM*T(I-1,G) + FCP*T(I+1,G) + 2.0*(1.0-FC)*T(I,G)
                B(G+1) = -1.0*FSCZ
                D(G+1) = 2.0 + FSCZ + FS
                A(G+1) = -1.0*FS
                C(G+1) = FSM*T(I-1,G+1) + FSP*T(I+1,G+1) +
     /                     2.0*(1.0-FS)*T(I,G+1)
                DO 130 J=G+2,M-1,1
                  B(J) = -1.0*FS
                  D(J) = 2.0*(1.0+FS)
                  A(J) = -1.0*FS
                  C(J) = FSM*T(I-1,J) + FSP*T(I+1,J)
     /          + 2.0*(1.0-FS)*T(I,J)
  130 CONTINUE
                B(M) = -2.0*FS
                D(M) = 2.0*(1.0+FS+BIBS*FS)
                A(M) = 0.0
                C(M) = FSM*T(I-1,M) + FSP*T(I+1,M) + 2.0*(1.0-FS)*T(I,M)
     /           + 2.0*BIBS*FS*TA
                CALL TDMA(M,A,B,C,D)
                DO 140 J=1,M,1
                  TP(I,J) = C(J)
  140 CONTINUE
  110 CONTINUE

C     ******* OUTSIDE LAGGED SURFACE *******

        FCM = FC*(RN-HD)/RN
        FSM = FS*(RN-HD)/RN
        B(1) = 0.0
        D(1) = 1.0 + FCZ + BIF*FCZ
        A(1) = -1.0*FCZ
        C(1) = A1 + FCM*T(N-1,1) + (1.0-FCM)*T(N,1) + BIF*FCZ*TA
        DO 150 J=2,G-1,1
                B(J) = -1.0*FCZ
                D(J) = 2.0*(1.0+FCZ)
                A(J) = -1.0*FCZ
                C(J) = 2.0*FCM*T(N-1,J) + 2.0*(1.0-FCM)*T(N,J)
  150 CONTINUE
        B(G) = -1.0*FCZ
        D(G) = 2.0 + FCZ + FCSZ
        A(G) = -1.0*FCSZ
        C(G) = 2.0*FCM*T(N-1,G) + 2.0*(1.0-FCM)*T(N,G)
        B(G+1) = -1.0*FSCZ
        D(G+1) = 2.0 + FSCZ + FS
        A(G+1) = -1.0*FS
        C(G+1) = 2.0*FSM*T(N-1,G+1) + 2.0*(1.0-FSM)*T(N,G+1)
        DO 160 J=G+2,M-1,1
                B(J) = -1.0*FS
```

```
                D(J) = 2.0*(1.0+FS)
                A(J) = -1.0*FS
                C(J) = 2.0*FSM*T(N-1,J) + 2.0*(1.0-FSM)*T(N,J)
160  CONTINUE
        B(M) = -1.0*FS
        D(M) = 1.0 + FS + BIBS*FS
        A(M) = 0.0
        C(M) = FSM*T(N-1,M) + (1.0-FSM)*T(N,M) + BIBS*FS*TA
        CALL TDMA(M,A,B,C,D)
        DO 170 J=1,M,1
                TP(N,J) = C(J)
170  CONTINUE

C    ******* COPY CONTENTS OF TP TO T *******

        DO 180 I=1,N,1
                DO 190 J=1,M,1
                  T(I,J) = TP(I,J)
190     CONTINUE
180  CONTINUE

        RETURN

        END
```

Code Listing For TDMA.FOR

```
C     SUBROUTINE TO SOLVE TRI-DIAGONAL SYSTEMS OF EQUATIONS

C     AUTHOR : M.B. SAINTEY
C     DATE : 16/06/93
C     VERSION : 2.0
C     CODE FOR THE POWERSTATION COMPILER

C     DEPARTMENT OF MATERIALS SCIENCE
C     UNIVERSITY OF BATH
C     CLAVERTON DOWN
C     BATH
C     AVON
C     ENGLAND

        SUBROUTINE     TDMA(N,A,B,C,D)

C    INCLUDE THE PARAMS FILE

    INCLUDE 'PARAMS.FI'

    INTEGER N
        INTEGER I
        REAL*8  R
        REAL*8  A(MAXSIZE), B(MAXSIZE), C(MAXSIZE), D(MAXSIZE)


C     N = NUMBER OF NODAL POINTS
C     B() CONTAINS THE CFT'S OF THE BELOW DIAGONAL ELEMENTS
```

```
C     D() CONTAINS THE CFT'S OF THE DIAGONAL ELEMENTS
C     A() CONTAINS THE CFT'S OF THE ABOVE DIAGONAL ELEMENTS
C     C() CONTAINS THE CONSTANT TERMS

C     THE SOLUTIONS WILL BE STORED IN THE C() MATRIX

C     ELIMINATE THE BELOW DIAGONAL ELEMENTS (GAUSSIAN ELIMINATION)

          DO 10 I=2,N,1
                    R = B(I)/D(I-1)
                    D(I) = D(I) - (R * A(I-1))
                    C(I) = C(I) - (R * C(I-1))
 10   CONTINUE

C     BACK SUBSTITUTE TO GET THE SOLUTION (STORE IN THE C() MATRIX)

          C(N) = C(N)/D(N)

          DO 20 I=N-1,1,-1
                    C(I) = ( C(I) - (A(I)*C(I+1)) )/D(I)
 20   CONTINUE

          RETURN

          END
```

Code Listing For DELTA.FOR

```
C     FILE: DELTA.FOR
C     SUBROUTINE OF FINITE DIFFERENCE MODEL

C     ROUTINE TO CALCULATE THE DELTA PULSE

C     DATE LAST MODIFIED : 17/06/93.
C     CODE FOR THE POWERSTATION COMPILER

C     AUTHOR: M.B.SAINTEY
C          DEPT MATERIALS SCIENCE
C          UNIVERSITY OF BATH.

          SUBROUTINE   DELTA(TP1DD,TP2DD,TP3DD,TP4DD,TR1DD,TR2DD)

C     INCLUDE FILES

     INCLUDE 'PARAMS.FI'
     INCLUDE 'GLOB.FI'

C     DECLARE LOCAL VARIABLES

     INTEGER I
          REAL*8  TP1DD, TP2DD, TP3DD, TP4DD, TR1DD(RSIZE), TR2DD(RSIZE)


C     AT PRESENT ONLY HAVE STEP ON TEMPS
C     CALCULATING DELTA PULSE TEMPS BY NUMERICALLY DIFFERENTIATING
```

```
C    TSTP(2) = TIME BETWEEN TEMPS 0 AND 2

     TP1DD = (PNT1(0)-PNT1(2))/TSTP(2)
     TP2DD = (PNT2(0)-PNT2(2))/TSTP(2)
     TP3DD = (PNT3(0)-PNT3(2))/TSTP(2)
     TP4DD = (PNT4(0)-PNT4(2))/TSTP(2)

     DO 10 I=1,N,1
       TR1DD(I) = (RW1(0,I)-RW1(2,I))/TSTP(2)
       TR2DD(I) = (RW2(0,I)-RW2(2,I))/TSTP(2)
10   CONTINUE

     RETURN
     END
```

Code Listing For UPDATE.FOR

```
C    SUBROUTINE FOR UPDATING THE PREVIOUS TEMPS AT POINTS
C    AND ROWS TO BE OUTPUT

C    CAN ONLY BE CALLED AFTER AT LEAST 3 STEPS + INITIALISATION
C    OF THE POINT AND ROW ARRAYS

C    AUTHOR : M.B. SAINTEY
C    DATE : 17/06/93
C    VERSION : 1.0
C    CODE FOR THE POWERSTATION COMPILER

C    DEPARTMENT OF MATERIALS SCIENCE
C    UNIVERSITY OF BATH
C    CLAVERTON DOWN
C    BATH
C    AVON
C    ENGLAND

     SUBROUTINE  UPDATE()

C    INCLUDE FILES

     INCLUDE 'PARAMS.FI'
     INCLUDE 'GLOB.FI'

     INTEGER I

C    UPDATE FOR POINT 1 (LPR1,LPZ1)

     PNT1(2) = PNT1(1)
     PNT1(1) = PNT1(0)
     PNT1(0) = T(LPR1,LPZ1)

C    UPDATE FOR POINT 2 (LPR2,LPZ2)

     PNT2(2) = PNT2(1)
     PNT2(1) = PNT2(0)
     PNT2(0) = T(LPR2,LPZ2)
```

```
C    UPDATE FOR POINT 3 (LPR3,LPZ3)

     PNT3(2) = PNT3(1)
     PNT3(1) = PNT3(0)
     PNT3(0) = T(LPR3,LPZ3)

C    UPDATE FOR POINT 4 (LPR4,LPZ4)

     PNT4(2) = PNT4(1)
     PNT4(1) = PNT4(0)
     PNT4(0) = T(LPR4,LPZ4)

C    UPDATE FOR ROWS

     DO 10 I=1,N,1
       RW1(2,I) = RW1(1,I)
       RW1(1,I) = RW1(0,I)
       RW1(0,I) = T(I,ROW1)
       RW2(2,I) = RW2(1,I)
       RW2(1,I) = RW2(0,I)
       RW2(0,I) = T(I,ROW2)
10   CONTINUE

     RETURN
     END
```

Code Listing For OUTPNT.FOR

```
C     FILE: OUTPNT.F   DELTA PULSE VERSION
C     SUBROUTINE OF FINITE DIFFERENCE MODEL
C     OUTPUT ROUTINE FOR LOGGED POINT DATA

C     DATE LAST MODIFIED : 17/06/93.
C     CODE FOR THE POWERSTATION COMPILER

C     AUTHOR: M.B.SAINTEY
C          DEPT MATERIALS SCIENCE
C          UNIVERSITY OF BATH.

        SUBROUTINE     OUTPNT(DDTIME)

C    INCLUDE FILES

     INCLUDE 'PARAMS.FI'
     INCLUDE 'GLOB.FI'

C    DECLARE LOCAL VARIABLES

        INTEGER I
        REAL*8  DDTIME
        REAL*8  CONTRA, HH, FWHH, RATIO, INTERP
        REAL*8  TP1DD, TP2DD, TP3DD, TP4DD, TR1DD(RSIZE), TR2DD(RSIZE)

C    DEFINE THE OUTPUT FORMAT FOR THE DATA
```

```
1    FORMAT(1X,F10.5,2X,5(',',2X,F15.10,2X))


C    AT PRESENT ONLY HAVE STEP ON TEMPS
C    CALL ROUTINE FOR CALCULATING DELTA PULSE TEMPS

     CALL DELTA(TP1DD,TP2DD,TP3DD,TP4DD,TR1DD,TR2DD)

C    CALCULATE THE CONTRAST, AND THE FWHH USING LINEAR INTERPOLATION
C    CALCULATE FOR ROW1, USUALLY SET TO UPPER SURFACE
         CONTRA = TR1DD(1) - TR1DD(N)
C    ONLY CALCULATE THE FWHH IF CONTRAST > 0.001K, ELSE SET TO 0
         IF(CONTRA.GT.0.00000001) THEN
           HH = TR1DD(N) + (CONTRA/2.0)
           I=1
10       IF(TR1DD(I).GT.HH) THEN
                       I = I + 1
                       GOTO 10
           ENDIF
C    I IS THE FIRST RADIAL POSITION WITH T < HH
C    TO FIND FWHH MORE ACCUATELY, USE LINEAR INTERPOLATION
           RATIO = (TR1DD(I-1)-HH)/(HH-TR1DD(I))
           INTERP = RATIO/(RATIO+1.0)
C     FWHH IN mm's
           FWHH = 2000.0*DX*(DBLE(I-1)+INTERP-1.0)
         ELSE
           FWHH = 0.0
         ENDIF

C    WRITE THE OUTPUT TO FILE

         WRITE(61,1) DDTIME, TP1DD, TP2DD, TP3DD, TP4DD, FWHH

         RETURN
         END
```

Code Listing For OUTROW.FOR

```
C    FILE: OUTROW.F
C    SUBROUTINE OF FINITE DIFFERENCE MODEL
C    OUTPUT ROUTINE FOR LOGGED ROW DATA

C    DATE LAST MODIFIED : 16/06/93.
C    CODE FOR THE POWERSTATION COMPILER

C    AUTHOR: M.B.SAINTEY
C         DEPT MATERIALS SCIENCE
C         UNIVERSITY OF BATH.

       SUBROUTINE    OUTROW(DDTIME)

C    INCLUDE FILES

     INCLUDE 'PARAMS.FI'
```

```
      INCLUDE 'GLOB.FI'

C     DECLARE LOCAL VARIABLES

      INTEGER I
          REAL*8    DDTIME
          REAL*8  TP1DD, TP2DD, TP3DD, TP4DD, TR1DD(RSIZE), TR2DD(RSIZE)


C     DEFINE THE OUTPUT FORMAT FOR THE DATA

1     FORMAT(1X,F15.10)
2     FORMAT(1X,F15.10,3X,',',3X,F15.10)
3     FORMAT(1X,'11111 ********** END OF ROW **********')

C     AT PRESENT ONLY HAVE STEP ON TEMPS
C     CALL ROUTINE FOR CALCULATING DELTA PULSE TEMPS

      CALL DELTA(TP1DD,TP2DD,TP3DD,TP4DD,TR1DD,TR2DD)


C      WRITE THE DATA

          WRITE(62,1) DDTIME
          DO 10 I=1,N,1
            WRITE(62,2) TR1DD(I), TR2DD(I)
10      CONTINUE
          WRITE(62,3)

          RETURN
          END
```

Listing For PARAMS.FI

```
C     PARAMS FILE
C     HAVE NOT USED ANY METACOMMANDS OR 'INTERFACE TO' STATEMENTS


C     ENSURE THAT ALL VARIABLES ARE DEFINED

      IMPLICIT NONE

      INTEGER RSIZE, ZSIZE, MAXSIZE

      PARAMETER (RSIZE = 301, ZSIZE = 301, MAXSIZE = 301)
```

Listing For GLOB.FI

```
C     INCLUDE FILE FOR THE CONTACT RESISTANCE ADI SIMULATION DELTA PULSE
C                 ------------------          -----------
C     LAST EDITED :  14/04/94
C     VERSION 2.0
C
```

```
C   M.B. SAINTEY
C
C
C   USED TO DEFINE ALL THE GLOBAL VARIABLES

C   GLOBAL VARIABLES

        INTEGER N, M, G, P
        REAL*8  T(RSIZE,ZSIZE), TP(RSIZE,ZSIZE)
        REAL*8  DX, HD, BIBO, BIBS, BIF, A1, RN, RP, TA, FC, FS, FO
        REAL*8  KCOP, KCSP, FCOZ, FOCZ, FCSZ, FSCZ, FCZ, PCAV
        REAL*8  F5, F2, F3, F4, BTAV
        INTEGER LPR1, LPZ1,LPR2,LPZ2,LPR3,LPZ3,LPR4,LPZ4,ROW1,ROW2

C   THE NEXT LOT OF VARIABLES ARE USED TO KEEP TRACK OF PREVIOUS TEMPS
C   TO ENABLE DIFFERENTIATION TO FIND THE TEMP AFTER A DELTA PULSE

        REAL*8  PNT1(0:2), PNT2(0:2), PNT3(0:2), PNT4(0:4)
        REAL*8  RW1(0:2,RSIZE), RW2(0:2,RSIZE), TSTP(0:2)

C   DEFINE THE COMMON BLOCKS

        COMMON  /VARS1/N, M, G, P
        COMMON  /VARS2/T, TP
        COMMON  /VARS3/DX, HD, BIBO, BIBS, BIF, A1, RN, RP, TA,FC,FS,FO
        COMMON  /VARS4/LPR1,LPZ1,LPR2,LPZ2,LPR3,LPZ3,LPR4,LPZ4,ROW1,ROW2
        COMMON  /VARS5/PNT1, PNT2, PNT3, PNT4, RW1, RW2, TSTP
        COMMON  /VARS6/KCOP, KCSP, FCOZ, FOCZ, FCSZ, FSCZ, FCZ, PCAV
        COMMON  /VARS7/F5, F2, F3, F4, BTAV
```

The model is run with the use of a control file. The format of the control file is described below :

Control File Format

```
N    M    P    G
KC   PC   CC
KS   PS   CS
KO   PO   CO
Q    HF   HB
RC
DX   DS   DT1
NUMON
PNTFIL   PNTINT
LPR1   LRZ1
LPR2   LPZ2
LPR3   LPZ3
LPR4   LPZ4
```

OPR ROWFIL ROWINT
ROW1 ROW2

Where :

N = Total number of nodes along radius (int)
M = Total number of nodes in depth (int)
P = Number of nodes along radius of contact resistance (int)
G = Number of nodes in depth above contact resistance (int)
KC = Thermal conductivity of coating (real)
PC = Density of coating (real)
CC = Specific heat capacity of coating (real)
KS = Thermal conductivity of substrate (real)
PS = Density of substrate (real)
CS = Specific heat capacity of substrate (real)
KO = Thermal conductivity of other (real)
PO = Density of other (real)
CO = Specific heat capacity of other (real
Q = Applied heat flux (continuous) (real)
HF = Front surface heat transfer coefficient (real)
HB = Rear surface heat transfer coefficient (real)
RC = Contact resistance (real)
DX = Standard nodal spacing, DS = Coating nodal spacing (both real)
DT1 = Time step (real)
NUMON = Total number of time steps to consider (int)
PNTFIL = Filename for point output data (char)
PNTINT = Number of time steps between each point data output (int)
LPR1 = Radial node position for output point 1 (int) (similarly for 2, 3 and 4)
LRZ1 = Depth node position for output point 1 (int) (similarly for 2, 3 and 4)
OPR = Set to 1 for if row output data required, 0 else (int)
ROWFIL = Filename for row output data (char)
ROWINT = Number of time steps between each row data output (int)
ROW1 = Depth nodal position for output row1 (int)
ROW2 = Depth nodal position for output row2 (int)

Appendix B

Derivation Of The Multilayer Perceptron Error Back Propagation Algorithm

This derivation of the algorithm is based on the derivation in [108]. The following notation is used :

- Indices i, j, an k refer to different neurons in the network.
- Iteration n refers to the n^{th} training pattern of the training set. The training set contains a total of N examples.
- $e_j(n)$ refers to the error signal at the output of neuron j at iteration n.
- $d_j(n)$ refers to the desired response for the output of neuron j at iteration n.
- $y_j(n)$ refers to the calculated output of nueron j at iteration n.
- $w_{ji}(n)$ denotes the weight connecting the output of neuron i to the input of neuron j at iteration n. The correction applied to this weight during training at iteration n is denoted by $\Delta w_{ji}(n)$.
- The total sum of the inputs to neuron j at iteration n is denoted by $v_j(n)$. The non-linear activation function $\varphi_j()$ of neuron j is applied to this value.
- The i^{th} element of the n^{th} training input vector $\mathbf{x}(n)$ is denoted by $x_i(n)$.
- The k^{th} element of the n^{th} overall output vector $\mathbf{o}(n)$ is denoted by $o_k(n)$.
- η denotes the learning rate parameter.

Derivation

The error signal at the output of neuron j at iteration n is defined as :

$$e_j(n) = d_j(n) - y_j(n) \tag{B1}$$

Define the instantaneous value of the squared error for neuron j as :

$$\text{Instantaneous Squared Error For Neuron j} = \frac{1}{2}e_j^2(n) \tag{B2}$$

Defining the sum of the instantaneous squared errors over all neurons in the output layer as $E(n)$, this can be written as :

$$E(n) = \frac{1}{2} \sum_{\substack{Output \\ Layer}} e_j^2(n) \tag{B3}$$

The average squared error over the whole training set of N examples is given by :

$$E_{av} = \frac{1}{N} \sum_{n=1}^{N} E(n) \tag{B4}$$

The instantaneous errors, and hence the average squared error, is a function of the free parameters of the network i.e. it is a function of the weights w_{ij}. The idea of the learning process is to minimise this error by adjusting the weights. One method of proceeding with the minimisation is to update the weights after the presentation of each member of the training set. This is only an estimate of the changes that would be made if the minimisation was based on the true average squared error for the whole set, but is far simpler to apply.

Considering the sum of the inputs to a neuron j for iteration n, using the notation defined above, this can be expressed as :

$$v_j(n) = \sum_{i=0}^{P} w_{ji}(n) y_i(n) \tag{B5}$$

Where there are a total of p inputs to neuron j excluding the biasing input (taken here as index i=0). The output of neuron j at iteration n is given by :

$$y_j(n) = \varphi_j(v_j(n)) \tag{B6}$$

In attempting to calculate an adjustment Δw_{ji}(n) to be made to the weight w_{ji}(n), it is necessary to determine what effect on the instantaneous error E(n) each weight has. This is done in the usual way by evaluating the partial derivative of the instantaneous error with respect to the weight. By the chain rule of partial differentiation, this can be expressed as :

$$\frac{\partial E(n)}{\partial w_{ji}(n)} = \frac{\partial E(n)}{\partial e_j(n)} \frac{\partial e_j(n)}{\partial y_j(n)} \frac{\partial y_j(n)}{\partial v_j(n)} \frac{\partial v_j(n)}{\partial w_{ji}(n)} \tag{B7}$$

This has been done as now each partial derivative in the chain on the RHS of (B7) can be readily evaluated.

Differentiating both sides of (B3) with respect to e_j(n) :

$$\frac{\partial E(n)}{\partial e_j(n)} = e_j(n) \tag{B8}$$

Differentiating both sides of (B1) with respect to y_j(n) :

$$\frac{\partial e_j(n)}{\partial y_j(n)} = -1 \tag{B9}$$

Differentiating both sides of (B6) with respect to v_j(n) :

$$\frac{\partial y_j(n)}{\partial v_j(n)} = \varphi_j'(v_j(n)) \tag{B10}$$

Where the prime indicates differentiation with respect to the argument of the function. To evaluate the final part of the chain, differentiate (B5) with respect to w_{ij}(n) :

$$\frac{\partial v_j(n)}{\partial w_{ji}(n)} = y_i(n) \tag{B11}$$

Putting all these together, the final equation for the dependence of the instantaneous error E(n) on the weight w_{ij}(n) is given by :

$$\frac{\partial E(n)}{\partial w_{ji}(n)} = -e_j(n)\varphi_j'(v_j(n))y_i(n) \tag{B12}$$

This can be envisaged as the gradient in weight space of the instantaneous error for input iteration n with respect to the weight w_{ij}(n). An appropriate adjustment to the weight can now be defined as :

$$\Delta w_{ji}(n) = -\eta \frac{\partial E(n)}{\partial w_{ji}(n)} \tag{B13}$$

This has the effect of adjusting the weight by an amount proportional to the learning rate parameter η. This has the effect of decreasing the instantaneous error by moving the weight value in the opposite direction to the error gradient in weight space. This method of adjusting the weights is known as the method of steepest descent, as the weights are always adjusted in the opposite (negative) direction to the gradient in weight space.

By defining a value known as the local gradient $\delta_j(n)$ by :

$$\delta_j(n) = -\frac{\partial E(n)}{\partial e_j(n)} \frac{\partial e_j(n)}{\partial y_j(n)} \frac{\partial y_j(n)}{\partial v_j(n)} = e_j(n)\varphi_j'(v_j(n)) \tag{B14}$$

(B13) can now be expressed as :

$$\Delta w_{ji}(n) = \eta \delta_j(n) y_i(n) \tag{B15}$$

The local gradient $\delta_j(n)$ is dependent upon the error value $e_j(n)$, and so the key part in the evaluation of $\Delta w_{ji}(n)$ is the evaluation of this error. This is a simple task for output neurons as they have a desired output with which to compare the computed output, to generate an error using equation (B1).

For neurons in the hidden layers however, this is not so easy. They have no desired value with which they can be compared, and so a more protracted method is required. The error for a hidden neuron has to be evaluated recursively in terms of the errors of all the neurons to which it is connected. Using the first equality of equation (B14), and missing out the differentiation with respect to $e_j(n)$ in the chain, the local gradient for a hidden neuron j can be expressed as :

$$\delta_j(n) = -\frac{\partial E(n)}{\partial y_j(n)} \frac{\partial y_j(n)}{\partial v_j(n)} \tag{B16}$$

Using equation (B10), this can be expressed as :

$$\delta_j(n) = -\frac{\partial E(n)}{\partial y_j(n)} \varphi_j'(v_j(n)) \tag{B17}$$

Rewriting equation (B3) using the index k to represent neurons in the output layer (to avoid confusion with index j now being used for a hidden neuron) :

$$E(n) = \frac{1}{2} \sum_k e_k^2(n) \tag{B18}$$

Using this expression, the partial derivative of equation (B17) can be evaluated :

$$\frac{\partial E(n)}{\partial y_j(n)} = \sum_k e_k(n) \frac{\partial e_k(n)}{\partial y_j(n)} \tag{B19}$$

Using the chain rule for the partial derivative in (B19), this can be rewritten as :

$$\frac{\partial E(n)}{\partial y_j(n)} = \sum_k e_k(n) \frac{\partial e_k(n)}{\partial v_k(n)} \frac{\partial v_k(n)}{\partial y_j(n)} \tag{B20}$$

As the index k denotes a neuron in the output layer, from (B1) :

$$e_k(n) = d_k(n) - y_k(n) \tag{B21}$$

Which using (B6) can be expressed as :

$$e_k(n) = d_k(n) - \varphi_k(v_k(n)) \tag{B22}$$

The first partial derivative of equation (B20) can therefore be expressed as :

$$\frac{\partial e_k(n)}{\partial v_k(n)} = -\varphi_k'(v_k(n)) \tag{B23}$$

From (B5) :

$$v_k(n) = \sum_{j=0}^{q} w_{kj}(n) y_j(n) \tag{B24}$$

Where q is the total number of inputs excluding the bias (the bias is taken as input j=0) input into neuron k. Differentiating this with respect to y_j(n) produces the second partial derivative of (B20) :

$$\frac{\partial v_k(n)}{\partial y_j(n)} = w_{kj}(n) \tag{B25}$$

Putting (B23) and (B25) into (B20) :

$$\frac{\partial E(n)}{\partial y_j(n)} = -\sum_k e_k(n) \varphi_k'(v_k(n)) w_{kj}(n) \tag{B26}$$

Using the definition of the local gradient given by the right hand equality of equation (B14) :

$$\frac{\partial E(n)}{\partial y_j(n)} = -\sum_k \delta_k(n) w_{kj}(n) \tag{B27}$$

Finally, inserting (B27) into expression (B17) for the local gradient of a hidden layer neuron j :

$$\delta_j(n) = \varphi_j'(v_j(n)) \sum_k \delta_k(n) w_{kj}(n) \tag{B28}$$

From this equation it is seen that the local gradient for a hidden layer neuron is given by the product of (a) the sum of the local gradients of the output layer neurons multiplied by their respective weights, with (b) the gradient of the activation function of the hidden layer neuron. This is why a note was made earlier of the importance of the differentiability of the activation function φ. Equation (B28) is strictly true for neurons in the first hidden layer back from the output layer. For a hidden layer neuron further back in the network, equation (B28) still holds true, but with the index k now running over the elements of the next right most neuron layer. Calculating the respective local gradients, and hence weight adjustments, thus proceeds from the output layer neurons, to the hidden layer closest to the output layer, backwards through the network until all the neuron layers have been considered. Hence the name error back propagation.

As yet, nothing has been said about the value of the learning rate parameter η. If η is large, small errors produce a large change to the weight, obviously a situation that will be unstable. On the other hand, if η is too small, it will take a great number of iterations for the weights to move towards the minimum error condition. A method of increasing the rate of learning, and reducing the likelihood of an unstable (oscillatory) path to the minimum error, is to add a momentum term in the weight change expression (B15) :

$$\Delta w_{ji}(n) = \alpha \Delta w_{ji}(n-1) + \eta \delta_j(n) y_i(n) \tag{B29}$$

The momentum term $\alpha \Delta w_{ij}(n\text{-}1)$ has the effect of increasing the magnitude of the change in the weight if the previous change $\Delta w_{ij}(n\text{-}1)$ was in the same direction as the current change $\eta \delta_j(n) y_i(n)$, and inhibiting the change if the current change is opposite in direction to the previous change. This attempts to stop oscillations in the weights from developing.

The training can be stopped when the average error over the whole training set is below a predetermined level, if the changes in the weights per cycle of the training set fall

below a certain level, or if the number of cycles of the training data reaches a certain level.

References

[1] R.L. Cox, D.P. Almond, H. Reiter
'Ultrasonic Testing Of Plasma Sprayed Coatings'
NDT International, December 1980. pp. 291-295.

[2] V.A. Troitskii, V.I. Zagrebel'nyi, L.I. Sychev
'Comparison Of Ultrasonic Echo And Thermal Inspection Methods'
Tekhnicheskaya Diagnostika i Nerazhrushayushchii Kontrol (1990). Vol. 2, No. 2, pp. 50-55.

[3] R. Kawase, H. Haraguchi, T. Hamamoto
'Non-Destructive Evaluation Method For Thermal Sprayed Ceramic Coatings Using Ultrasonic Waves'
Proceedings Of The 4th National Thermal Spray Conference, Pittsburgh, PA, USA. 4th-10th May 1991.

[4] R. Krull, M. Gribi
'Non-Destructive Testing Of Ceramic Coatings'
European Journal Of NDT (1993). Vol. 3, No. 1, pp. 2-5.

[5] R.L. Cox, D.P. Almond, H. Reiter
'Ultrasonic Attenuation In Plasma Sprayed Coating Materials'
Ultrasonics, January 1981. pp. 17-22.

[6] P.M. Patel, D.P. Almond
'Thermal Wave Testing Of Plasma-Sprayed Coatings And A Comparison Of The Effects Of Coating Microstructure On The Propagation Of Thermal And Ultrasonic Waves'
Journal Of Materials Science (1985). Vol. 20, pp. 955-966.

[7] R. Halmshaw
'Non-Destructive Testing'
Published by Edward Arnold (1987). ISBN : 0 7131 3634 0.

[8] A.G. Bell
'Upon The Production Of Sound By Radiant Energy'
Phil. Mag. April 1881. Vol. xi, pp.510-528.

[9] A. Rosencwaig, A. Gersho
'Theory Of The Photoacoustic Effect With Solids'
Journal Of Applied Physics (1976). Vol. 47, No. 1, pp 64-69.

[10] P.E. Nordal, S.O. Kanstad
'Photothermal Radiometry'
Physica Scripta (1979). Vol. 20, pp.659-662.

[11] G. Busse
'Photothermal Transmission Probing Of A Metal'
Infrared Physics (1980). Vol. 20, pp.419-422.

[12] G. Busse
'Optoacoustic And Photothermal Material Inspection Techniques'
Applied Optics (1982). Vol. 21, No. 1, pp. 107-110.

[13] A. Lehto, M. Jokinen, J. Jaarinen, T.Tiusanen, M. Luukkala
'Alternating Beam Method (ABM) In Photothermal Microscopy (PTM) And Photoacoustic Microscopy (PAM)'
Electronics Letters (1981). Vol. 17, No. 15, pp. 540-541.

[14] G. Busse, P. Eyerer
'Thermal Wave Remote And Non-Destructive Inspection Of Polymers'
Appl. Phys. Lett (1983). Vol. 43, No. 4, pp. 355-357.

[15] S. Aithal, G. Rousset, L. Bertrand, P. Cielo, S. Dallaire
'Photoacoustic Characterisation Of Subsurface Defects In Plasma Sprayed Coatings'
Thin Solid Films 119(1984). pp. 153-158.

[16] D.P. Almond, I.M. Pickup, P.M. Patel, H. Reiter
'The Non-Destructive Evaluation Of Surface Coatings By Photothermal Imaging'
J. Materials For Energy Systems (1985). Vol. 6, No. 4, pp. 287-292.

[17] D.P. Almond, P.M. Patel, I.M. Pickup, H. Reiter
'An Evaluation Of The Suitability Of Thermal Wave Interferometry For The Testing Of Plasma Sprayed Coatings'
NDT International, February 1985. pp. 17-24.

[18] P.M. Patel, D.P. Almond, H. Reiter
'Thermal Wave Detection And Characterisation Of Subsurface Defects'
Appl. Phys. B (1987). Vol. 43, pp.9-15.

[19] D.P. Almond, P.M. Patel, H. Reiter
'The Testing Of Plasma Sprayed Coatings By Thermal Wave Interferometry'
Materials Evaluation (1987). Vol. 45, pp. 471-475.

[20] P.M. Patel, D.P. Almond, J.D. Morris
'Potential Applications Of Thermal Wave Interferometry For Non-Destructive Evaluation And Characterisation Of Surface Coated Components'
European Journal Of NDT (1991). Vol. 1, No. 2, pp. 64-76.

[21] C.A. Bennett, R.R. Patty
'Thermal Wave Interferometry: A Potential Application Of The Photoacoustic Effect'
Applied Optics (1982). Vol. 21, No. 1, pp. 49-54.

[22] A.C. Bento, S.R. Brown, D.P. Almond, I.G. Turner
'Thermal Wave Non-Destructive Thickness Measurements Of Hydroxyapatite Coatings Applied To Prosthetic Hip Stems'
Journal Of Materials Science : Materials In Medicine (To Be Published).

[23] H.G. Walther, W. Karpen
'Monitoring Of Paint Adhesion On Polymers Using Photothermal Detection'
Proceedings Of Quantitative Thermography (QIRT 92). Eurotherm Seminar 27, pp.388-392.

[24] P. Cielo
'Pulsed Photothermal Evaluation Of Layered Materials'
J. Appl. Phys. (1984). Vol. 56, No. 1, pp. 230-234.

[25] D.L. Balageas, J.-C. Krapez, P. Cielo
'Pulsed Photothermal Modelling Of Layered Materials'
J. Appl. Phys. (1986). Vol. 59, No. 2, pp. 348-357.

[26] S.K. Lau, D.P. Almond, P.M. Patel
'Transient Thermal Wave Techniques For The Evaluation Of Surface Coatings'
J. Phys. D: Appl. Phys. (1991). Vol. 24, pp. 428-436.

[27] J. Hartikainen
'Inspection Of Plasma Sprayed Coatings Using Fast Infrared Scanning Technique'
Rev. Sci. Instrum. (1989). Vol. 60, No. 7, pp. 1334-1337.

[28] J. Hartikainen
'Fast Photothermal Measurement System For Inspection Of Weak Adhesion Defects'
Appl. Phys. Lett. (1989). Vol. 55, No. 12, pp. 1188-1190.

[29] J. Varis, J. Hartikainen, R. Lehtiniemi, M. Luukala
'A Simple Transportable Imaging System For Fast Non-Destructive Testing'
Proceedings Of Quantitative Thermography (QIRT 92). Eurotherm Seminar 27, pp.235-238.

[30] J. Hartikainen, R. Lehtiniemi, J. Rantala, J. Varis, M. Luukala
'Fast Infrared Line Scanning Method And Its Applications'
Review Of Progress In Quantitative Non-Destructive Evaluation Vol. 13 (1994). pp. 401-408.

[31] W.N. Reynolds, J.M. Milne, J.W. Child
'Transient Thermography'
European Patent : 0 089 760
United Kingdom Atomic Energy Authority

[32] D.P. Bentz, J.W. Martin
'Thermographic Imaging Of Surface Finish Defects In Coatings On Metal Substrates'
Materials Evaluation, February 1992. pp. 242-246.

[33] J.K. Kaiser
'Millimetre Wave Heating For Thermographic Inspection Of Carbon Fibre Reinforced Composites'
Materials Evaluation, May 1994. pp. 597-599.

[34] D.W. Wilson, J.A. Charles
'Thermographic Detection Of Adhesive Bond And Interlaminar Flaws In Composites'
Experimental Mechanics, July 1981. pp. 276-280.

[35] A.J. Rogovsky
'Ultrasonic And Thermographic Methods For NDE Of Composite Tubular Parts'
Materials Evaluation, April 1985. pp. 547-555.

[36] W.N. Reynolds
'Thermographic Methods Applied To Industrial Materials'
Canadian Journal Of Physics (1986). Vol. 64, pp. 1150-1154.

[37] P. Cielo, X. Maldague, A.A. Déom, R. Lewak
'Thermographic Non-Destructive Evaluation Of Industrial Materials And Structures'
Materials Evaluation, April 1987. pp. 452-465.

[38] P.V. McLaughlin, M.G. Mirchandani, P.V. Ciekurs
'Infrared Thermographic Flaw Detection In Composite Laminates'
Transactions Of The ASME : Journal Of Engineering Materials And Technology (1987). Vol. 109, pp. 146-150.

[39] M. Connolly, D. Copley
'Thermographic Inspection Of Composite Materials'
Materials Evaluation, December 1990. pp. 1461-1463.

[40] T. Jones, H. Berger
'Thermographic Detection Of Impact damage In Graphite-Epoxy Composites'
Materials Evaluation, December 1992. pp. 1446-1453.

[41] D. Maillet, A.S. Houlbert, S. Didierjean, A.S. Lamine, A. Degiovanni
'Non-Destructive Thermal Evaluation Of Delaminations In A Laminate : Part I - Identification By Measurement Of Thermal Contrast'
Composites Science And Technology (1993). Vol. 47, pp. 137-153.

[42] D. Maillet, A.S. Houlbert, S. Didierjean, A.S. Lamine, A. Degiovanni
'Non-Destructive Thermal Evaluation Of Delaminations In A Laminate : Part II - The Experimental Laplace Transforms Method'
Composites Science And Technology (1993). Vol. 47, pp. 155-172.

[43] D. David, J.Y. Marin, M. Dessendre, I. Avenas-Payan, B. Lelièvre, H. Trétout
'Sequoia : Artificial Intelligence Applied To The Infrared Thermography Inspection Of Composite Aerospace Structures'
Review Of Progress In Quantitative Non-Destructive Evaluation Vol. 13 (1994). pp. 903-910.

[44] A.C. Ramamurthy, T. Ahmed, L.D. Favro, R.L. Thomas, D.K. Hsu
'Low Velocity Foreign Object Damage To Composites And Automotive Paint Finishes : A Thermal Wave Study'
Review Of Progress In Quantitative Non-Destructive Evaluation Vol. 13 (1994). pp. 455-460.

[45] R. Monti, G. Mannara
'Non-Destructive Testing Of Honeycomb Structures By Computerised Thermographic Systems'
Acta Astronautica (1985). Vol. 12, No. 6, pp. 405-414.

[46] C. Hobbs, A. Temple
'The Inspection Of Aerospace Structures Using Transient Thermography'
British Journal Of NDT (1993). Vol. 35, No. 4, pp. 183-189.

[47] L.D. Favro, P.K. Kuo, R.L. Thomas, S.M. Shepard
'Thermal Wave Imaging For Ageing Aircraft Inspection'
Materials Evaluation, December 1993. pp. 1386-1389.

[48] C. Brett, D.P. Woodings
'The Application Of Transient Thermography To The Inspection Of Protective Coatings In FGD Plant'
Insight (1994). Vol. 36, No. 4, pp. 202-205.

[49] H. Kaasinen
'Assessing The Quality Of The Waterproofing Of Bridges Using Thermography'
British Journal Of NDT (1993). Vol. 35, No. 6, pp. 301-304

[50] D. Harris, M. Kelly
'The Potential For NDE Of Thermal Sprayed Coatings Using Infrared Video Thermography'
Proceedings Of The National Thermal Spraying Conference 1987. 14th-17th September, Orlando, Florida.

[51] J.W. Maclachlan Spicer, W.D. Kerns, L.C. Aamodt, J.C. Murphy
'Measurement Of Coating Physical Properties And Detection Of Coating Disbonds By Time Resolved Infrared Radiometry'
Journal Of Non-Destructive Evaluation (1989). Vol. 8, No. 2, pp. 107-120.

[52] J.C. Murphy, J.W. Maclachlan Spicer, R. Osiander, W.D. Kerns, L.C. Aamodt
'Quantitative Non-Destructive Evaluation Of Coatings By Thermal Wave Imaging'
Review Of Progress In Quantitative Non-Destructive Evaluation Vol. 13 (1994). pp. 417-425.

[53] G.J. Trezek, S. Balk
'Provocative Techniques In Thermal NDT Imaging'
Materials Evaluation, August 1976. pp. 172-176.

[54] C.M. Sayers
'Detectability Of Defects By Thermal Non-Destructive Testing'
British Journal Of NDT, January 1984. pp. 28-33.

[55] S.F. Burch, J.T. Burton, S.J. Cocking
'Detection Of Defects By Transient Thermography : A Comparison Of Predictions From Two Computer Codes With Experimental Results'
British Journal Of NDT, January 1984. pp. 36-39.

[56] P.M. Patel, S.K. Lau, D.P. Almond
'Numerical Computation Of Transient And Steady-State Periodic Thermal Wave Distribution In Homogeneous Media'
Review Of Progress In Quantitative Non-Destructive Evaluation Vol. 9 (1990). pp. 517-524.

[57] M.P. Connolly
'A Review Of Factors Influencing Defect Detection In Infrared Thermography : Applications To Coated Materials'
Journal Of Non-Destructive Evaluation (1991). Vol. 10, No. 3, pp. 89-96.

[58] J. Rantala, J. Hartikainen
'Numerical Estimation Of The Spatial Resolution Of Thermal NDT Techniques Based On Flash Heating'
Research In Non-Destructive Evaluation (1991). Vol. 3, pp. 125-139.

[59] G. Walle, J. Burgschweiger, U. Netzelmann
'Numerical Modelling Of The Defect Response In Pulsed Video Thermography On Samples With Finite Optical Penetration'
Proceedings Of Quantitative Thermography (QIRT 94). Eurotherm Seminar 42, pp.238-243.

[60] X. Maldague, J.C. Krapez, D. Poussart
'Thermographic Non-destructive Evaluation (NDE) : An Algorithm For Automatic Defect Extraction In Infrared Images'
IEEE Transactions On Systems, Man & Cybernetics, Vol. 20, No. 3, pp. 722-725 (1990).

[61] J.-C. Krapez, P. Cielo
'Thermographic Non-destructive Evaluation : Data Inversion Procedures Part I: 1-D Analysis'
Res. Nondestr. Eval, 1991, pp. 81-100. Springer Verlag, New York Inc.

[62] J.-C. Krapez, X. Maldague, P. Cielo
'Thermographic Non-destructive Evaluation : Data Inversion Procedures Part II: 2-D Analysis And Experimental Results'
Res. Nondestr. Eval, 1991, pp. 101-124. Springer Verlag, New York Inc.

[63] A.G. Protasov, V.M. Sineglazov
'Determination Of The Geometrical Parameters Of Defects By Thermal Inspection Methods'
Tekhnicheskaya Diagnostika i Nerazhrushayushchii Kontrol (1991). Vol. 3, No. 2, pp. 30-33.

[64] J.-C. Krapez, D.M. Boscher, P.M. Delpech, A.A. Déom, G. Gardette, D.L. Balageas
'Time-Resolved Pulsed Stimulated Infrared Thermography Applied To Carbon-Epoxy Non Destructive Evaluation'
Proceedings Of Quantitative Infrared Thermography (QIRT 92). Eurotherm Seminar 27. pp. 195-200.

[65] P.M. Delpech, D.M. Boscher, F. Lepoutre, A.A. Déom, D.L. Balageas
'Time-Resolved Pulsed Stimulated Infrared Thermography Applied To Carbon-Carbon Non Destructive Evaluation'
Proceedings Of Quantitative Infrared Thermography (QIRT 92). Eurotherm Seminar 27. pp. 201-206.

[66] M. Bonnet, H. Maigre, M, Manaa
'Numerical Reconstruction Of Interfacial Defects And Interface Thermal Resistances Using Thermal Measurements'
Proceedings Of Quantitative Infrared Thermography (QIRT 92). Eurotherm Seminar 27. pp. 266-271.

[67] R.L. Thomas, L.D. Favro, D.J. Crowther, P.K. Kuo
'Inversion Of Thermal Wave Infrared Images'
Proceedings Of Quantitative Infrared Thermography (QIRT 92). Eurotherm Seminar 27. pp. 278-282.

[68] V.A. Storozhenko
'Quantitative Infrared Thermography Application For Thermal Defectometry'
Proceedings Of Quantitative Infrared Thermography (QIRT 92). Eurotherm Seminar 27. pp. 283-287.

[69] P.M. Delpech, J.-C. Krapez, D.L. Balageas
'Thermal Defectometry Using The Temperature Decay Rate Method'
Proceedings Of Quantitative Infrared Thermography (QIRT 94). Eurotherm Seminar 42. pp. 220-225.

[70] D.P. Almond, S.K. Lau
'Edge Effects And A Method Of Defect Sizing For Transient Thermography'
Appl. Phys. Lett (1993). Vol.62, No. 25, pp. 3369-3371.

[71] D.P. Almond, S.K. Lau
'Defect Sizing By Transient Thermography I : An Analytical Approach'
J. Phys. D: Appl. Phys. (1994). Vol. 27, pp. 1063-1069.

[72] D.P. Almond, M.B. Saintey, S.K. Lau
'Edge-Effects And Defect Sizing By Transient Thermography'
Proceedings Of Quantitative Infrared Thermography (QIRT 94). Eurotherm Seminar 42. pp. 247-252.

[73] J.-C. Krapez, D.L. Balageas
'Early Detection Of Thermal Contrast In Pulsed Stimulated Infrared Thermography'
Proceedings Of Quantitative Infrared Thermography (QIRT 94). Eurotherm Seminar 42. pp. 260-266.

[74] T.T.N. Lan, K. Haupt, U. Seidel, H.G. Walther
'Reconstruction Of Thermal Defects From Photothermal Images'
Proceedings Of Quantitative Infrared Thermography (QIRT 94). Eurotherm Seminar 42. pp. 267-272.

[75] D.R. Prabhu, W.P. Winfree
'Neural Network Processing Of Thermal NDE Data For Corrosion Detection'
Review Of Progress In Quantitative Non-Destructive Evaluation Vol. 12 (1993). pp. 775-782.

[76] P.G. Bison, C. Bressan, R. Di Sarno, E. Grinzato, S. Marinetti, G. Manduchi
'Thermal NDE Of Delaminations In Plastic Materials By Neural Network Processing'
Proceedings Of Quantitative Infrared Thermography (QIRT 94). Eurotherm Seminar 42. pp. 214-219.

[77] E. Grinzato, S. Marinetti, P.G. Bison, G. Manduchi
'Application Of Neural Networks To Thermographic Data Reduction'
Paper Presented At The Quantitative Thermography Meeting Of The Societe Francaise Des Thermiciens, In Paris, France, On 7th December 1994.

[78] G. Busse, M. Bauer, W. Rippel, D. Wu
'Lock-in Vibrothermal Inspection Of Polymer Composites'
Proceedings Of Quantitative Infrared Thermography (QIRT 92). Eurotherm Seminar 27. pp. 154-159.

[79] D. Wu, W. Karpen, G. Busse
'Lock-in Thermography For Multiplex Photothermal Non-Destructive Evaluation'
Proceedings Of Quantitative Infrared Thermography (QIRT 92). Eurotherm Seminar 27. pp. 371-376.

[80] W. Karpen, D. Wu, R. Steegmüller, G. Busse
'Depth Profiling Of Orientation In Laminates With Local Lockin Thermography'
Proceedings Of Quantitative Infrared Thermography (QIRT 94). Eurotherm Seminar 42. pp. 281-286.

[81] M. Nacitas, P.Levesque, D.L. Balageas
'Lock-In Infrared Thermography Applied To The Characterisation Of Electromagnetic Fields'
Proceedings Of Quantitative Infrared Thermography (QIRT 94). Eurotherm Seminar 42. pp. 287-292.

[82] D. Wu
'Lockin Thermography For Defect Characterisation In Veneered Wood'
Proceedings Of Quantitative Infrared Thermography (QIRT 94). Eurotherm Seminar 42. pp. 298-302.

[83] H.D. Stevens, Z. Babiak, M. Wewel
'Recent Developments In Arc Spraying'
IEEE Transactions On Plasma Science. 1990, Vol. 18, No. 6, pp. 974-979.

[84] H. Herman
'Plasma Sprayed Coatings'
Scientific American. September 1988, pp. 78-83.

[85] D.W. Parker, G.L. Kutner
'HVOF Spray Technology - Poised For Growth'
Advanced Materials And Processes. 1991, Vol. 4, pp. 68-74.

[86] G. Arfken
'Mathematical Methods For Physicists (Third Edition)'
Academic Press Inc. ISBN : 0 12 059810 8.

[87] H.S. Carslaw, J.C. Jaeger
'Conduction Of Heat In Solids (Second Edition)'
Oxford Science Publications. ISBN : 0 19 853368 3.

[88] S.K. Lau, D.P. Almond, J.M. Milne
'A Quantitative Analysis Of Pulsed Video Thermography'
NDT&E International. 1991, Vol. 24, No. 4, pp.195-202.

[89] B. Noble
'Methods Based On The Wiener-Hopf Technique'
Pergamon Press, London, 1958.

[90] D.R. Croft, J.A.R. Stone
'Heat Transfer Calculations Using Finite Difference Equations'
PAVIC Publications, Sheffield City Polytechnic. ISBN : 086 339 1206.

[91] G.D. Smith
'Numerical Solution Of Partial Differential Equations'
Oxford University Press (1965). ISBN : 0 19 859611 1.

[92] J. Crank, P. Nicolson
'A Practical Method For Numerical Evaluation Of Solutions Of Partial Differential Equations Of The Heat Conduction Type'
Proceedings Of The Cambridge Philosophical Society, 1947. Vol. 43, No. 1, pp.50-67.

[93] D.W. Peaceman, H.H. Rachford
'The Numerical Solution Of Parabolic And Elliptic Differential Equations'
J. Soc. Indust. Appl. Math, 1955. Vol. 3, No. 1, pp.28-41.

[94] S.G. Burnay, T.L. Williams, C.H.N. Jones
'Applications Of Thermal Imaging'
Adam Hilger imprint by IOP publishing Ltd. ISBN : 0-85274-421-8.

[95] Chambers Science And Technology Dictionary
W&R Chambers Ltd 1991. ISBN : 0-550-13239-2.

[96] Mullard Technical Publication M80-0043
'802CPY And 825CPY High-Performance Self-Poling TGS Pyroelectric Infrared Detectors'
Mullard Limited, Mullard House, Torrington House, London, WC1E 7HD.

[97] P.M. Patel
'An Evaluation Of Photothermal Radiometry For NDT Of Plasma Sprayed Coatings'
PhD. Thesis, Bath University, 1988.

[98] T.L. Williams, R. Hunt
'Testing Thermal Imaging Systems'
Proceedings Of The Society Of Photo-Optical Instrumentation Engineers (SPIE), 1981. Vol. 274, pp.273-279.

[99] T.L. Williams, N.T. Davidson, S. Wocial
'Objective Measurement Of MRTD'
SPIE, 1988. Vol. 916, pp.92-98.

[100] T.L. Williams, N.T. Davidson
'Recent Advances In Testing Of Thermal Imagers'
SPIE, 1989. Vol. 1110, pp.220-231.

[101] T.L. Williams
'Objective MRTD Measurement - An Update'
SPIE, 1990. Vol. 1320, pp.420-430.

[102] T.L. Williams
'The MTF Of Thermal Imaging Cameras - Its Relevance And Measurement'
Proceedings Of Quantitative Infrared Thermography (QIRT 92). Eurotherm Seminar 27. pp. 51-56.

[103] A.C. Bento, D.P. Almond
'Accuracy Of Thermal Wave Interferometry For The Evaluation Of Thermophysical Properties : Applied To Plasma Sprayed Coatings'
To Be Published.

[104] G.A. Georgiou, M.B. Saintey, A.M. Lank, D.P. Almond
'The Mathematical Modelling Of Thermal Wave NDT Of Sprayed Coatings'
Proceedings Of The 14th International Thermal Spray Conference, Kobe, Japan, 22nd-26th May, 1995.

[105] M.B Saintey, D.P. Almond
'Defect Sizing By Transient Thermography II : A Numerical Treatment'
Submitted April 1995 For Publication In J. Phys. D: Appl. Phys.

[106] V.Vavilov, D. Kourtenkov, E. Grinzato, P. Bison, S. Marinetti, C. Bressan
'Inversion Of Experimental Data And Thermal Tomography Using "Termo.heat" and "Termidge" Software'
Proceedings Of Quantitative Infrared Thermography (QIRT 94). Eurotherm Seminar 42. pp. 273-278.

[107] C.M. Bishop
'Neural Networks And Their Applications'
Rev. Sci. Instrum., June 1994. Vol. 65, No. 6, pp. 1803-1832.

[108] S. Haykin
'Neural Networks - A Comprehensive Foundation'
Macmillan College Publishing Company, 1994. ISBN : 0 02 352761 7.